DISSERTATION

SYNTHESIS AND CHARACTERIZATION OF LOW-DIMENSIONAL PARAMAGNETIC ACETYLIDE COMPLEXES

Submitted by

Wesley A. Hoffert

Department of Chemistry

In partial fulfillment of the requirements

For the degree of Doctor of Philosophy

Colorado State University

Fort Collins, Colorado

Spring 2011

Doctoral Committee:

Advisor: Matthew Shores

Oren Anderson
Amy Prieto
Travis Bailey
Carl Patton

ABSTRACT

SYNTHESIS AND CHARACTERIZATION OF LOW-DIMENSIONAL PARAMAGNETIC ACETYLIDE COMPLEXES

The work described herein involves efforts to prepare transition metal acetylide assemblies with low-dimensional topologies. Among the possible alkynyl ligands, I focus on complexes of ethynylbenzenes and butadiyne.

In Chapter 1, my research is placed in the context of designing single molecule magnets (SMMs) with enhanced working temperatures. The maximum temperature at which a SMM retains its magnetization depends on the ground state spin (*S*) and the magnetic zero-field spiltting (*D*). Optimizing both of these terms could be achieved by preparing multinuclear transition metal acetylides. However, techniques for the synthesis of paramagnetic metal acetylides are still being developed. Specifically, differential substitution of axial ligands by acetylides in pseudo-octahedral complexes has proven to be difficult, and the development of new synthetic methods to address this problem is a focus of several research groups. Recent results describing the preparation and magnetic properties of relevant assemblies are highlighted.

In Chapter 2, the syntheses and characterizations of a family of diamagnetic ethynylbenzene complexes containing (cyclam)Co^{III} (cyclam = 1,4,8,11-tetraazacyclotetradecane) units are presented. The complexes are prepared by

dehydrohalogenation in methanol, and the resulting Co^{III} first coordination sphere includes acetylide and chloride ligands at the axial coordination sites. These complexes are intended to be structural models for metallodendrimer building blocks. As chloride salts, the low solubility of the chloro acetylide complexes precludes the use of reaction conditions needed for further chloride substitution. To investigate the use of alternative synthetic protocols in organic solvents, anion exchange is performed with a mononuclear complex to afford [(cyclam)CoCl(C_2Ph)](BPh_4). This complex reacts with LiC_2Ph in tetrahydrofuran to yield [(cyclam)Co(C_2Ph)$_2$](BPh_4), demonstrating the feasibility of stepwise acetylide substitution. Successful syntheses of paramagnetic Co^{II} analogues are thwarted by ligand dissociation upon electrochemical reduction.

Efforts to incorporate paramagnetic d^5 Fe^{III} ions into ethynylbenzene-bridged clusters are presented in Chapter 3. Mono-, di-, and tri-nuclear complexes containing $[(dmpe)_2FeCl]^-$ (dmpe = 1,2-bis(dimethylphosphino)ethane) units are prepared and characterized structurally and magnetically. Consistent with spin topology rules, antiferromagnetic coupling is observed for [(dmpe)$_4$Fe$_2$Cl$_2$(μ-*p*-DEB)]($BAr^F{}_4$)$_2$ (*p*-H_2DEB = 1,4-diethynylbenzene, $BAr^F{}_4$ = tetrakis[3,5-bis(trifluoromethyl)tetraphenyl]borate), with $J = -132$ cm^{-1}. Ferromagnetic coupling is observed for [(dmpe)$_4$Fe$_2$Cl$_2$(μ-*m*-DEB)]($BAr^F{}_4$)$_2$ (J = 20 cm^{-1}) and [(dmpe)$_4$Fe$_2$Cl$_2$(TEB)](OTf)$_3$ (H_3TEB = 1,3,5-triethynylbenzene, OTf = trifluoromethanesulfonate) ($J_{12} = J_{13} = 11$ cm^{-1}, $J_{23} = 61$ cm^{-1}). DFT calculations on $[(dmpe)_2FeCl(C_2H)]^+$ are used to elucidate the orientation of the singly occupied d orbital relative to the ancillary phosphine ligands. From this information, the structural and

electronic origins of the magnetic coupling strength in this family of complexes can be rationalized.

The work presented in Chapter 4 is a departure from complexes with bridging acetylide ligands. Attempting to prepare dendritic building blocks with octahedral d^4 Cr^{II} ions led to the isolation of a redox-related family of dinitrogen-bridged chromium acetylide complexes containing the $[RC_2Cr(\mu\text{-}N_2)CrC_2R]^{n+}$ (R = Ph–, $^{i}Pr_3Si$–; n = 0, 1, 2) backbone. Magnetic data collected for the n = 0 and n = 2 complexes are consistent with high-spin triplet and quintet ground states, respectively. The mixed-valent complex (n = 1) exhibits temperature dependent magnetic behavior consistent with a quartet ⇌ doublet two-center spin equilibrium. Electronic structure calculations performed on the full n = 0 and n = 2 complexes suggest that the high-spin states arise from singly occupied orthogonal π* orbitals coupled with a variable occupation of dδ orbitals. Significant N–N and Cr–N π-bonding pins the occupation of the π manifold, leading to variable occupation of the dδ space. In contrast, the n = 1 complex is not well described by a B3LYP hybrid density functional model. A CAS-SORCI study on a simplified model of the mixed valent complex reproduces the observed Hund's rule violation for the S = ½ ground state and places the lowest quartet 1.45 kcal/mol above the doublet ground state.

Finally, the preparation and properties of a series of wire-like molecules containing redox-active $(dmpe)_2Fe$ units bridged by oligo-yne ligands are presented in Chapter 5. By using synthetic conditions where methanol is present, we isolate and structurally characterize an unusual tri-nodal ene-triyne complex $[(dmpe)_6Fe_3Cl_2(C_8H)](PF_6)$. The one-electron oxidized congener exhibits electronic delocalization necessary for molecular circuitry. Strictly aprotic conditions were used to synthesize $[(dmpe)_4Fe_2Cl_2(\mu\text{-}C_4)](PF_6)$.

Owing to the shorter iron-iron distance relative to $[(dmpe)_6Fe_3Cl_2(C_8H)](PF_6)_2$, the electronic delocalization in this complex is enhanced. Chemical oxidation was used to prepare $[(dmpe)_4Fe_2Cl_2(\mu\text{-}C_4)](PF_6)_2$. The magnetic data are consistent with a thermally activated singlet ⇌ triplet spin equilibrium.

ACKNOWLEDGEMENTS

The work presented here would not have been possible without the help of several individuals and organizations, and to them I owe a great deal of gratitude.

I thank Colorado State University and the ACS Petroleum Research Fund for financial support while pursuing my Ph.D. Sometimes I stop and think about how fortunate I was to get paid to pursue this degree, and without these organizations, it would not have been possible.

Individually, I thank my advisor, Matt Shores, for guidance, support, and friendship. I joined his group not knowing what I was in for, but I have no regrets. He is one of the most driven people I know, and future exciting results that will come from his group will happen largely because of his tireless dedication to his students and to his discipline. I also thank my undergraduate mentors, Allan van Asselt and Timothy Hubin, who first showed me just how cool inorganic chemistry could be. My high school chemistry teacher, Jan Bryson, also helped me realize my love for the central science.

Past and current members of the group deserve a great deal of thanks. Dr. Md. K. Kabir initially helped me understand how to do research even when I was bumbling around the lab in my first year. Another postdoc, Dr. Zhaoping Ni, was an invaluable resource to me in all matters of magnetism, and I wish him the best of luck with his independent career in China. I spent the majority of graduate school with fellow students Brian Newell, Ashley McDaniel, and Stephanie Fiedler, and the many hours we spent

together were thoroughly enjoyable. Thank you for reading manuscripts, answering questions, and being excellent labmates in general. To Christina Klug, who is no longer a "zero-year," I wish you luck in your future endeavors. The staff at the CIF deserves thanks for training me and troubleshooting instrument issues. Susie Miller was especially helpful in showing me how single crystals should be selected, mounted, and analyzed with the APEX and SMART diffractometers. I know that these skills will continue to be valuable even after I leave CSU.

While out of the lab, I made several lifelong friends during my time in Fort Collins, and I thank them for their continued words of support and prayers. Isaac and Laura Bartholomew, Skylar and Jaime Brower, Rob and Hannah Breshears all helped to prop me up when I felt like falling down, and I am deeply appreciative for that.

My parents and parents-in law have loved and supported me throughout this process, and I can't tell them enough how valuable that was. Finally, I thank my wife, Elissa, for "following" me here, and this work is dedicated to her. Her relentless love and support has kept me going during this process, and hopefully this work at least partially reflects her devotion to me.

AUTOBIOGRAPHY

Wesley Alan Hoffert was born on May 15th, 1981 in Wheat Ridge, Colorado, to parents Timothy and Nina Hoffert. He attended high school in Golden, CO, graduating in 1999. After spending one year at Manchester College in North Manchester, IN, he attended McPherson College in McPherson, KS, earning a B.S. in chemistry in 2003. During his collegiate career Wesley ran cross country and track and was awarded all-conference honors in those sports. In 2002, he was recognized as an NAIA academic All-American. After college, Wesley worked as a pharmaceutical quality assurance chemist for Hospira in McPherson, KS. In 2005, he began his Ph.D. work at Colorado State University, where he studied inorganic chemistry with Prof. Matthew P. Shores. Wesley earned his doctorate in 2011, and will be taking his talents to Richland, WA to continue doing research with Dr. Jenny Yang at Pacific Northwest National Laboratories.

Wesley met his wife, Elissa, while attending McPherson College. They were married on October 4, 2003 in Abilene, KS. He enjoys the outdoors, and especially loves mountain biking. He is also an avid reader and a die-hard fan of the Colorado Rockies.

DEDICATION

I dedicate this work to my wife, Elissa Hoffert, who has supported me unflinchingly throughout my doctoral work.

TABLE OF CONTENTS

LIST OF FIGURES AND SCHEMES

LIST OF TABLES

Chapter 1. Paramagnetic Acetylide Clusters: Enhancing Magnetic Coupling and Topological Anisotropy for Molecular Magnets

1.1 Introduction

As magnetic data storage density continues to increase, bit dimensions are approaching a critical small size, known as the superparamagnetic limit. Below this limit, thermal effects can induce random flips of the magnetization, which is obviously inadequate for data storage. Engineers continue to discover methods to push beyond "maximum" theoretical storage densities with commercially available magnetic storage density at 84 billion bits per cm^2 as of March 2010.[1] However, it is apparent that a new approach will eventually be needed to keep up with technological demands. One possibility is to use molecular magnets as binary storage bits that are far smaller than the domain sizes of metallic alloys that are currently employed. For example, the estimated storage density for a device based on single molecule magnets (SMMs) is 30 trillion bits per cm^2.[2] Although the phenomenon of single molecule magnetism was discovered in the early 1990s at temperatures below 4 K,[3] ensuing research efforts have only raised the working temperature of these species to approximately 7 K.[4] Needless to say, the synthetic manipulation of the parameters responsible for SMM behavior has proven to be especially challenging. Approaches to maximizing the working temperature for SMMs can be understood with the help of the energy diagram depicted in Figure 1.1.[5]

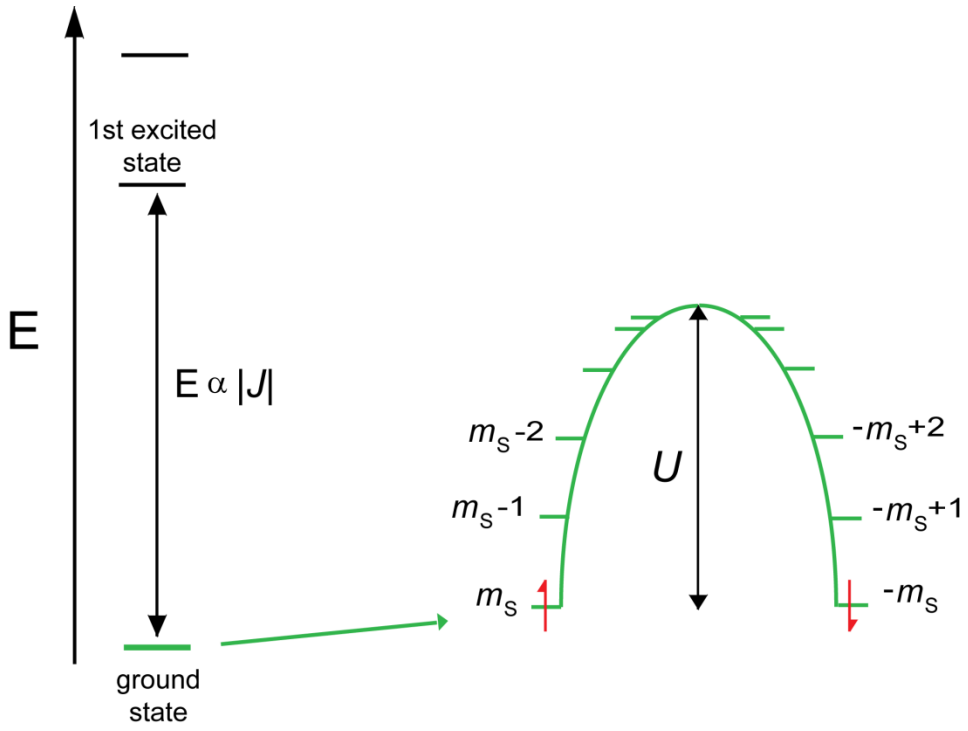

Figure 1.1. Idealized energy diagram for a SMM. The arrows in the $\pm m_s$ levels represent the orientation of *S* relative to the easy-axis of the cluster. Adapted from ref. 5.

First, strong exchange coupling (large $|J|$) is needed to isolate the ground state from higher energy spin states. In cases of low or moderate J coupling, thermal energy allows for excited states to mix with the ground state, thereby providing a route for electrons to "relax" into non-SMM manifolds. Within a high-spin ground state (S), the presence of negative molecular easy-axis magnetic anisotropy (D) can produce a thermal barrier between spin microstates of opposite sign. The "height" of this barrier (U) is simply given by $S^2|D|$ or $(S^2\text{-}¼)|D|$, depending on whether the overall spin of the complex is integer or half-integer, respectively. A large U (in practice, significantly greater than k_BT) would be required to observe magnetic bistability at room temperature.

Chemists have made significant progress in manipulating S and J by preparing high nuclearity clusters[6] and high-spin molecules.[5, 7] Although it appears that extremely high spin systems often display small magnetic anisotropies,[7b] giant spin systems are not absolutely necessary to observe SMM behavior at higher temperatures: a molecular system with a well-isolated $S = 15$ ground state spin and $D = –1$ cm$^{–1}$ would give a barrier U larger than k_BT at ambient conditions. Such a ground spin state is already achievable, but controlling the magnetic anisotropy term D is much more challenging. The recent discoveries of SMM behavior in mononuclear U(III)[8] ($S = 3/2$) and Fe(II)[9] ($S = 2$) complexes highlight the significance of the magnetic anisotropy relative to spin state. Historically, sizeable molecular magnetic anisotropies in less exotic compounds are typically accessed through the judicious choice of metal ions and serendipity.

In order to capitalize on the individual ionic contributions to the molecular magnetic anisotropy, the topological anisotropy should be maximized. In this regard, one- and two-dimensional paramagnetic clusters are attractive candidates for single molecule magnets.

Recent efforts in this area have employed cyanide as a bridging ligand. Depending on the choice of ancillary ligand set(s), the cyanide ligand is useful for the rational synthesis of a number of cluster topologies owing to its predictable coordination geometry.[10] However, cyanide-based SMMs are limited by the ability of the ligand to mediate superexchange. For first row transition metals, cyanide complexes typically display $|J|$ values on the order of 10 cm^{-1} under the convention of the spin Hamiltonian in Equation 1.1.[10a]

$$\hat{H} = -2J(S_A \cdot S_B) \qquad \text{(Equation 1.1)}$$

Increasing the working temperature of single molecule magnets will require bridging ligands that give rise to better-isolated ground states. In this regard, acetylide-bridged complexes should enjoy significantly larger J values than cyanide-bridged complexes due to greater metal-ligand overlap. The topological constraints enforced by the acetylide moiety also offer the possibility of preparing low-dimensional paramagnetic clusters, some types of which are represented in Scheme 1.1.

The chemistry of diamagnetic transition metal-acetylide complexes is rich and well-established.[11] These species are usually pursued for their technological potential. For example, metallo-dendrimers based on ethynylbenzene bridging ligands have been investigated for their non-linear optical properties, and linear redox-active C_n-bridged species are envisioned as components of molecule-based electronics.[12] The synthesis of these materials is usually accomplished in a straightforward manner, which allows for stepwise ligand substitution reactions to proceed in high yields. For example Pt^{II} acetylide complexes of the type $[(R_3P)_2PtCl(C_2R')]$ can be prepared using a dehydrohalogenation approach by mixing stoichiometric $[(R_3P)_2PtCl_2]$ with an acetylene in the presence of an organic base. Other methods for preparing diamagnetic acetylides

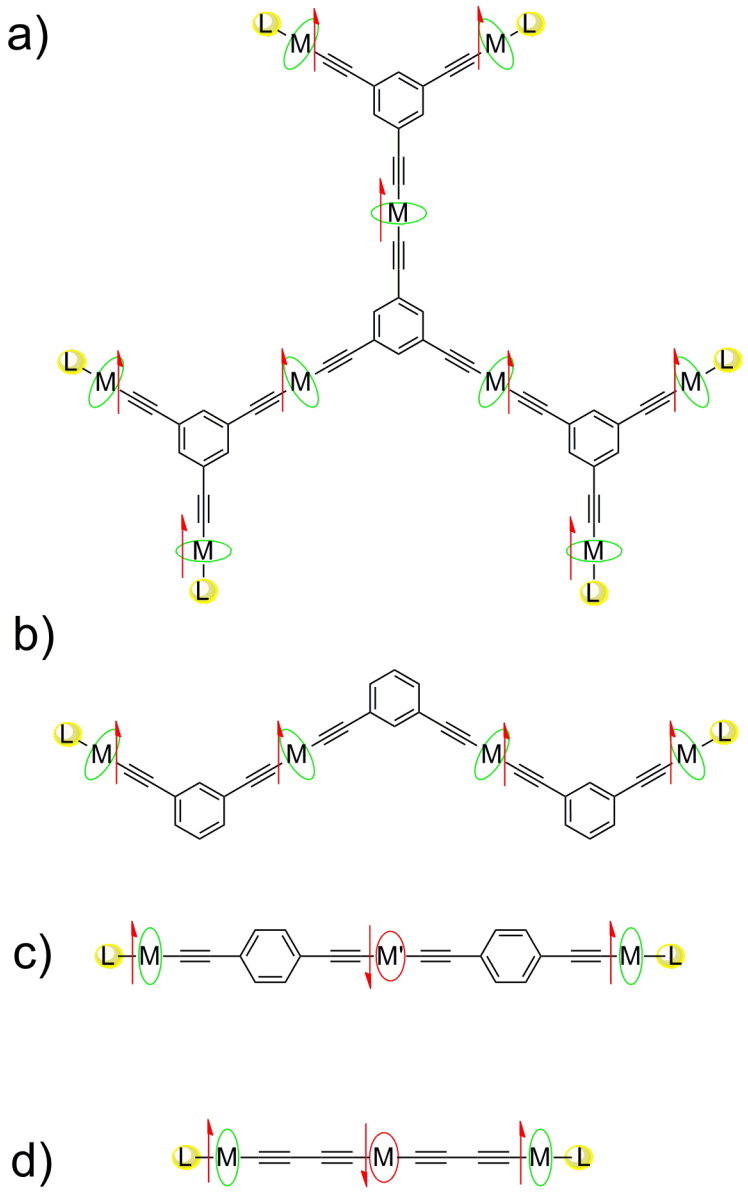

Scheme 1.1. New two- (a) and one-dimensional (b, c, d) paramagnetic metal-acetylide targets featuring topological anisotropies important for observing SMM behavior. The magnetic coupling in (d) is depicted here as antiferromagnetic, but in some cases, ferromagnetic coupling has been observed for dinuclear species.

also exist, and these have been extensively reviewed.[12-13]

The same methods that are used to synthesize Ru- and Pt-containing acetylide complexes are generally incompatible with paramagnetic ions, which tend to be more reactive than their filled-shell counterparts. Even so, a surge in interest in the properties of paramagnetic acetylide complexes warrants an appraisal of the recent developments in this area as they apply to the advancement of the field of molecular magnetism. Since the field of paramagnetic acetylides is relatively young, the tools needed to prepare the species depicted in Scheme 1.1 are still being developed. Here, I present an overview of recent results involving magnetically and structurally characterized transition metal assemblies bridged by alkynyl-type ligands.

1.2 Paramagnetic Oligo-yne-Based Molecular Wires

The preparation of paramagnetic assemblies based on sp carbon linkages usually involves the synthesis of a diamagnetic complex with redox-active metal groups. These metal centers (typically Fe, Ru, or Re) can then be oxidized individually to afford mixed-valent or homo-valent compounds.[13-14] Although species with a range of bridge lengths have been examined, C_4 and C_8 linkers have garnered the most attention. Typically, characterization of these types of molecules is focused on the measurement of the electronic coupling parameter, V_{ab}, which provides an estimate of the degree of single-electron delocalization. This measurement requires the generation of a mixed-valent congener, and subsequent near-infrared spectroscopic measurements are interpreted in terms of Hush theory to calculate V_{ab}.[15] However, it is theoretically possible to relate the energy of V_{ab} to the magnitude of J for antiferromagnetically coupled systems since both interactions involve the same orbital pathway. Several relationships have been proposed,

including the one shown in Equation 1.2 where $\bar{\nu}$ is the energy of the metal-metal charge transfer.[16]

$$J_{ab} = (V_{ab})^2 / \bar{\nu}_{MMCT} \qquad \text{(Equation 1.2)}$$

Predictably, electronic coupling decreases as the length of the bridging ligand increases. Furthermore, molecular rigidity decreases as the bridge is lengthened. Both of these effects would be expected to be detrimental to the formation of an isolated anisotropic ground state, meaning that chain lengths beyond 4 carbon atoms provide diminishing returns with regard to electronic communication. Related to this, Alvarez has examined the issue of long-distance magnetic coupling in dicycanamidobenzene-bridged compounds using broken symmetry DFT/B3LYP calculations. With a highly rigid pentacene-type bridging ligand, robust antiferromagnetic coupling (J = –337 cm^{-1}) is predicted in a Cr^{III}_2 complex despite a metal-metal distance of 25 Å.[17] This result highlights the importance of ligand rigidity in optimizing intramolecular interactions and supports the observation of diminished electronic coupling in C_n-bridged complexes (n > 4), where structural "flimsiness" gives rise to a breakdown of the orbital communication pathway. As for shorter carbon-based bridging ligands, some examples of diacetylide (C_2^{2-})-bridged complexes are known,[18] but the challenges involved in the preparation of these species have been exceptionally difficult to overcome. This is probably due to the inherent difficulty in generating stable C_2^{2-} in solvents compatible with metal complex starting materials. Therefore, discussion here will be restricted to C_4-bridged complexes.

Antiferromagnetic coupling through a rigid C_4 ligand can be very robust owing to the availability of two orthogonal pπ* networks on the bridging ligand. However, high-spin ground states have also been realized in di-radical complexes bridged by wire-like

ligands.[19] The presence of these limiting cases can occur within the same compound and is manifested as a thermally-activated $S = 1 \rightleftharpoons S = 0$ spin equilibrium. Lapinte reported an example of this situation in the case of $[(dppe)_2(Cp^*)_2Fe_2(\mu\text{-}C_4)](PF_6)_2$.[20] In cases like this, strong electronic delocalization leads to a HOMO in which m_s levels are split and the spin equilibrium can be interpreted as a case of molecular zero-field splitting. Moreover, in 2004, Berke used DFT to calculate the dependence of metal rotamer conformation on the singlet-triplet energy gap (and hence the observed ground state) in a diacetylide-bridged dinuclear Mn complex. Those calculations indicated that the population of the triplet or singlet states depended on the degree of metal dπ-ligand pπ orbital overlap.[18a] Similar issues can be expected for C_4-bridged compounds, so the ability to tune the rotational conformation of metal nodes should lead to deeper understanding and control of the magnetic properties in these types of complexes. This might be accomplished by varying the extent of steric bulk on the ancillary and bridging ligands, thereby changing the preferred metal coordination conformation.

In sum, the strong intramolecular coupling imparted by carbon-rich bridging ligands makes them attractive for assembling single-chain species. Furthermore, antiferromagnetic interactions in large, mixed-metal linear clusters would be expected to lead to well-isolated ground states with a high degree of magnetic anisotropy.

1.3 Di-Ruthenium Based Complexes

Diruthenium complexes have been explored as building blocks for magnetic materials, and the large zero-field splitting observed for these species makes them intriguing candidates for molecular magnets.[21] A wide array of compounds based on diruthenium units has been studied in depth, and there are several excellent reviews on

the subject.[12, 22] Synthetically, one advantage of using Ru_2 units in the preparation of oligo-yne complexes is the ability to tune the reactivity at the axial positions by adjusting the level of steric bulk on the ancillary ligands. Ren took advantage of this property to assemble a tri-nodal complex connected by C_4^{2-} ligands.[23] Under basic conditions, two equivalents of a mono-alkynyl Ru_2 complex react with a Ru_2 di-nitrato complex to form a neutral, linear trimeric species with a Ru_2^{5+}–Ru_2^{6+}–Ru_2^{5+} configuration. The compound was purified by recrystallization, and the X-ray structure is shown in Figure 1.2.

The magnetic susceptibility at room temperature is consistent with the presence of two non-coupled $S = 3/2$ centers (the Ru_2^{5+} groups) and an $S = 1$ center (the middle Ru_2^{6+} group). However, the data at low temperature suggest that the central Ru_2^{6+} unit undergoes a spin transition to an $S = 0$ state.[24] Along with the large magnetic anisotropy and the expected antiferromagnetic interaction between the central node and the endgroups, the combination of so many electronic effects could not be modeled with a simple spin Hamiltonian. Therefore, DFT/B3LYP calculations were employed to better understand the magnetism exhibited by the trimeric complex. From the relative energies of the ground- and first excited state, the antiferromagnetic interaction between the Ru_2^{5+} endgroups was calculated to be -0.2 cm^{-1}, suggesting that the central Ru_2^{6+} unit acts as an insulator in its singlet state. The energetic difference between the second and third excited states yields a calculated coupling constant between the central and end Ru_2^{n+} moieties of -72 cm^{-1}. The robust antiferromagnetic interaction exhibited by this complex suggests that high-spin ground states in these types of complexes could be achieved by substituting a central unit that contains a non-zero ground state. Going forward, lessons learned from the magnetic and electronic calculations reported by Ren can be applied to

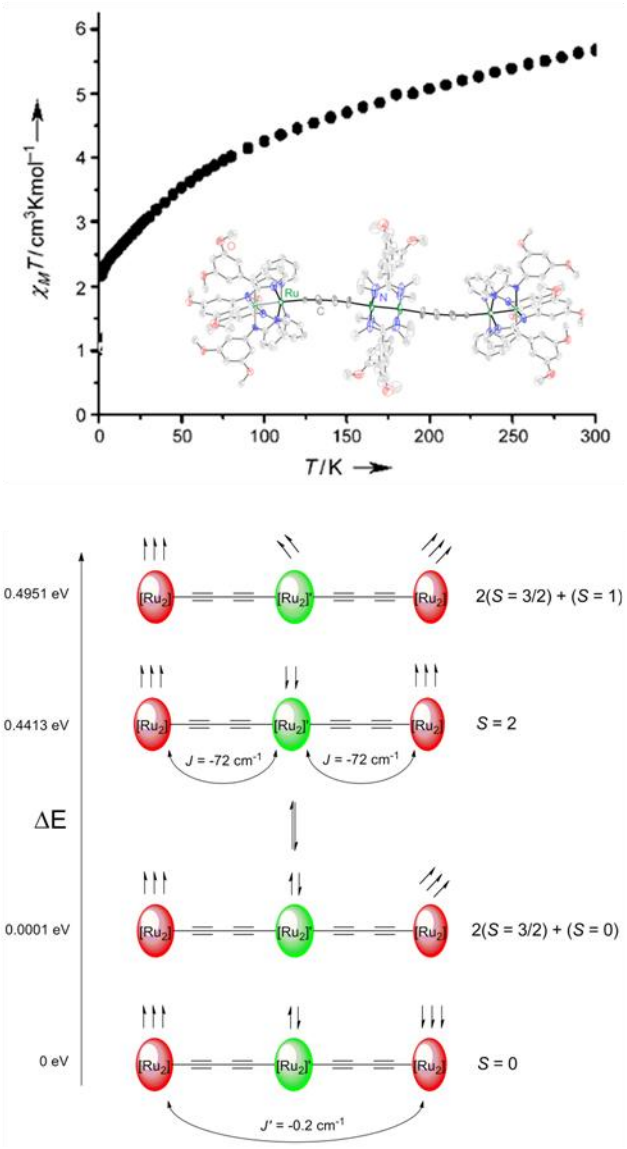

Figure 1.2. Top: variable temperature magnetic susceptibility data for trinodal Ru_2 complex. Inset: X-ray crystal structure with hydrogen atoms omitted for clarity and thermal ellipsoids rendered at 40% probability. Bottom: *J* scheme and calculated relative energies that account for the susceptibility data. Red ellipses denote Ru_2^{5+} units and green ellipses denote Ru_2^{6+} units. Figure adapted from ref. 23.

larger assembles where spin and magnetic anisotropy can be built up in a rational manner.

1.4 Pseudo-octahedral $W^{IV/V}$ Complexes

Targeting modular wire-like systems capable of single-electron conductance, Berke and coworkers isolated a di-tungsten C_4-bridged complex with substitutionally labile iodo ligands at the axial positions.[25] The neutral $W^{IV}(\mu\text{-}C_4)$ complex was synthesized in three steps starting with $[(dppe)(CO)_3(THF)W^0]$ (Scheme 1.2).[26] The X-ray structure (Figure 1.3), vibrational spectroscopy, and diamagnetism of $[(dppe)_4W_2I_2(\mu\text{-}C_4)]$ confirmed the di-carbynic nature of the bridging ligand (i.e. $W^{IV}{\equiv}C{-}C{\equiv}C{-}C{\equiv}W^{IV}$, C_4^{6-}) as opposed to a di-acetylenic structure ($W^{II}{-}C{\equiv}C{-}C{\equiv}C{-}W^{II}$, C_4^{2-}). The cyclic voltammogram indicated that the complex could be reversibly oxidized by up to two electrons, a feature held in common with other C_4-bridged complexes.[14d, 20]

Although the mono-oxidized dimeric complex was not expected to reveal novel magnetic behavior, the spectroscopic characteristics of the mixed-valent species can offer insight into the degree of magnetic coupling expected for further oxidized analogues. A comparison of IR and EPR spectra for the homo-valent systems versus the mixed valent one indicated that electron transfer between W termini occurs between the time scales for these spectroscopic methods (10^{-13} s and 10^{-9} s, respectively). The authors concluded that this is consistent with a medium level of electron delocalization, and this contrasts with the fully delocalized Robin-Day class III behavior exhibited by other strongly coupled C_4^{n-}-bridged transition metal analogues with Fe- and Ru-containing endgroups.[14d, 19a]

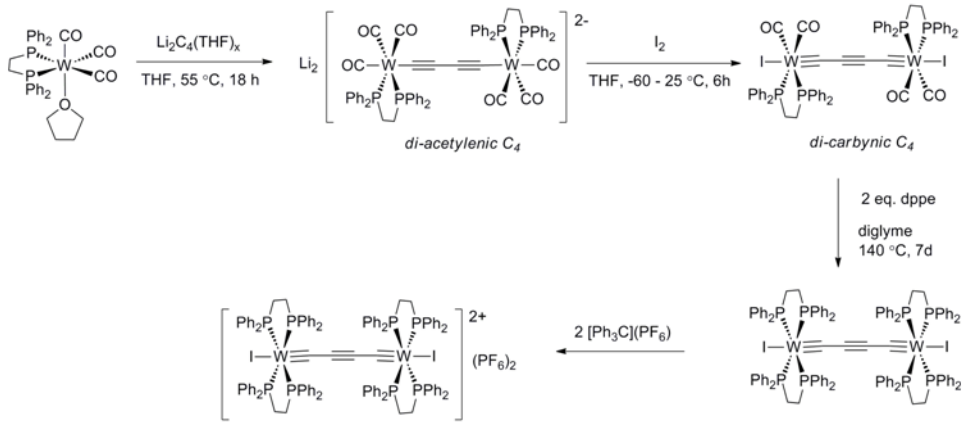

Scheme 1.2. Syntheses of neutral and di-oxidized C_4-bridged tungsten complexes. Adapted from ref 23.

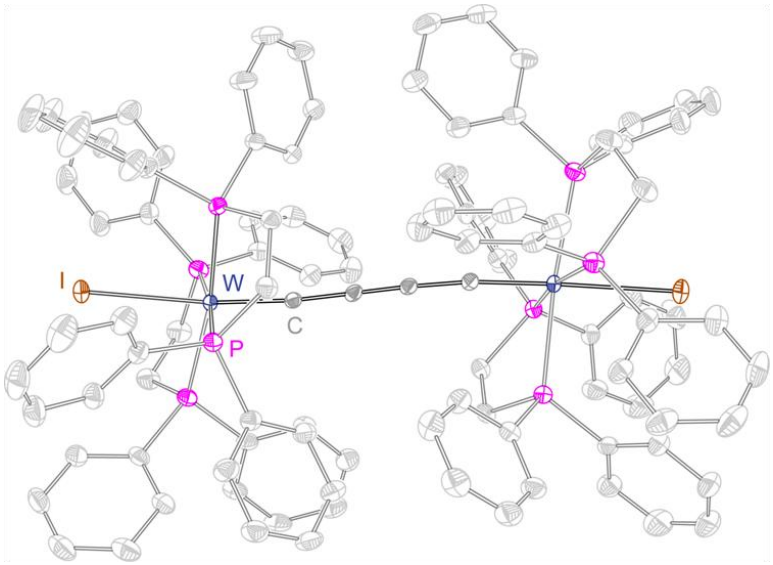

Figure 1.3. X-ray structure of $[(dppe)_4W_2I_2(\mu\text{-}C_4)]$ with thermal ellipsoids rendered at 40% probability. Hydrogen atoms removed for clarity. Figure adapted from ref 23.

From this, weaker magnetic coupling for this W_2 di-radical system would be predicted when compared to a structurally similar first-row metal complex.

Di-oxidation of the complex with trityl hexafluorophosphate yields the complex $[(dppe)_4W_2I_2(\mu\text{-}C_4)](PF_6)_2$. Although this complex was not characterized crystallographically, the similarity of the IR spectra between the neutral and cationic forms of the compound suggests that the carbynic structure of the bridging ligand is preserved. A qualitative molecular orbital analysis of a $XP_4W{\equiv}C{-}C$ fragment implies that the oxidation likely occurs at the non-bonding W dδ orbitals, which would account for the lack of structural differences between the neutral and oxidized species. At room temperature, the magnetic susceptibility of the complex is consistent with the presence of two magnetically isolated S = ½ centers (Figure 1.4). Upon cooling, χ_M decreases abruptly below 150 K and is essentially negligible below 20 K. After accounting for the presence of a paramagnetic impurity, fitting the data to an S = ½ dimer model leads to a J value of −167 cm^{-1} with g = 1.98. The antiferromagnetic interaction here is quite strong, but it should be noted that the interaction is weaker than previously reported C_4^{n-}-bridged complexes with pseudo-octahedral second ($[Ru_2C_4]^{2+}$) and third row ($[Re_2C_4]^{2+}$) transition metal ions,[14c] which are diamagnetic at room temperature.

1.5 Increasing the Nuclearity of Molecular Wires by a Building Block Approach

The axially coordinated iodo ligands allow for a way to augment the nuclearity of the core W_2 complex. Although the W–I bond is quite strong, substituting the iodide by acetylide was accomplished by mixing the starting complex with catalytic CuI and excess amounts of TlOTf and LiC_4SiMe_3.[27] The chromatographically purified compound could then be functionalized with redox-active Fe^{II} endgroups in three steps (Figure 1.5). The

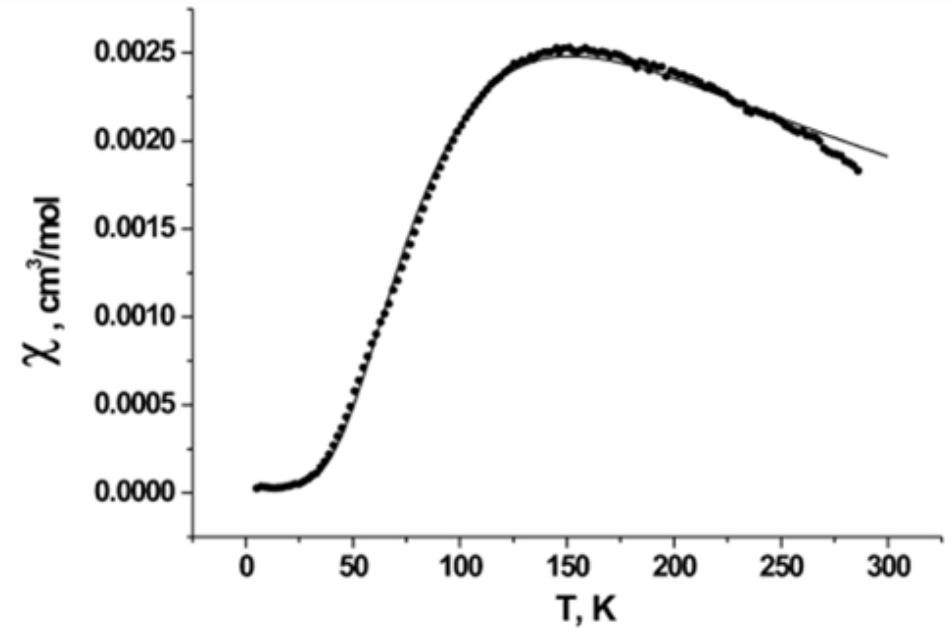

Figure 1.4. Molar susceptibility versus temperature and fit (smoothed line) for $[(dppe)_4W_2I_2(\mu\text{-}C_4)](PF_6)_2$. Figure adapted from ref. 25.

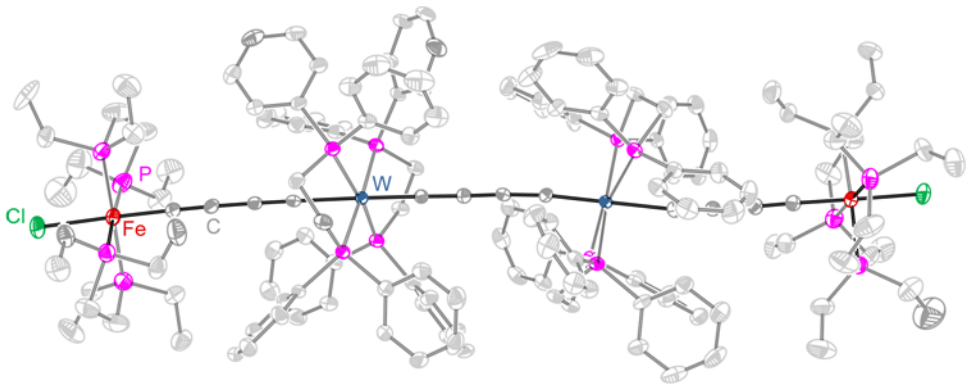

Figure 1.5. X-ray crystal structure of $[(depe)_4(dppe)_4Fe_2W_2Cl_2(\mu\text{-}C_4)_3]$ with thermal ellipsoids rendered at 40% probability. Hydrogen atoms are omitted for clarity. Figure adapted from ref. 27.

cyclic voltammogram of the compound contained three redox waves. Two one-electron waves corresponded to the $Fe^{III/II}$ redox couples, and the third wave represented the two-electron oxidation of both W^{IV} centers. A one-electron oxidized analogue of the complex was isolated, and the electronic coupling parameter, V_{ab}, was estimated using the Hush approximation to be 680 cm^{-1}. Compared to the coupling parameter for $[(dppe)_2I_2W_2(\mu\text{-}C_4)](PF_6)$ (ca. –250 cm^{-1}),[25] this value indicates that electronic delocalization between the distant Fe termini is significantly enhanced relative to the mixed valent W_2 complex. This finding is highly interesting, considering the longer electron transfer pathway and the presence of two W^{IV} interruptions along the electron transfer pathway. Although the two-, three- and four-electron-oxidized analogues were not isolated, the initial results obtained by Berke suggest that the strong intramolecular coupling offered by carbon-rich ligands could be used to prepare paramagnetic clusters with well-isolated ground states, which is a necessary requirement for increasing the working temperature of SMMs.

1.6 The Appeal of Ethynylbenzene Bridging Ligands

The use of ethynylbenzene bridging ligands to prepare highly anisotropic paramagnetic molecules is appealing for several reasons. The rigid linkage can be used to constrain the molecular topology in either one or two dimensions, in accord with the use of a di- or tri-topic bidging ligand.[28] For molecules containing several metal ions with large ionic magnetic anisotropies, a low dimensional arrangement is necessary in order to prevent cancellation of individual *D* tensors. In practice, the parallel alignment of many Jahn-Teller axes within a single cluster is a good example of the magnetic advantage of low dimensionality, and this is the reason cited for the large magnetic anisotropy observed for $Mn_{12}OAc$.[3] Theoreticians have explored this concept in detail and have

provided synthetic chemists with several metal-ligand arrangements as candidates for SMMs.[29] As shown in Figure 1.6, the colinear alignment of several easy axes ($D_{ion} < 0$) or the orthogonal alignment of hard axes ($D_{ion} > 0$) is predicted to produce clusters with large, negative D_{mol} values. The latter arrangement has been employed to observe slow magnetic relaxation in $[Fe_3Cr(L)_2(dpm)_6]\cdot Et_2O$ (H_3L = 2-hydroxymethyl-2-phenylpropane-1,3-diol, Hdpm = dipivaloylmethane).[30] The architectures mentioned here could be designed using di- and triethynylbenzene bridges, but high-spin molecules bridged by these ligands have yet to be reported.

Apart from the anisotropy advantages imparted by the ethynylbenzene ligands, the sign of the intramolecular magnetic coupling (J) is predictable. In short, *o*- and *p*-phenylene bridges are known antiferromagnetic couplers while *m*-phenylene bridges give rise to ferromagnetic coupling.[31] A spin polarization mechanism accounts for these rules, and Lapinte confirmed that they could be applied to metal acetylide complexes in the late 1990s.[32] Since then, work in this area has focused on understanding and manipulating the magnitude of J in di- and tri-radical systems. This foundational knowledge will be especially important as molecules with more spin are synthesized and characterized, but current synthetic techniques have only allowed for the isolation of ethynylbenzene complexes of LS d^5 Fe^{III} ions. These complexes have appeared in multiple reviews,[11, 33] but recent developments concerning the intramolecular interactions for these species merit further emphasis.

1.7 Fe^{III} Diethynylbenzene Complexes

Paramagnetic arylethynyl-bridged clusters involving [(dppe)Fe(Cp*)] endgroups have been known for some time. These reactive complexes are prone to form impurities upon

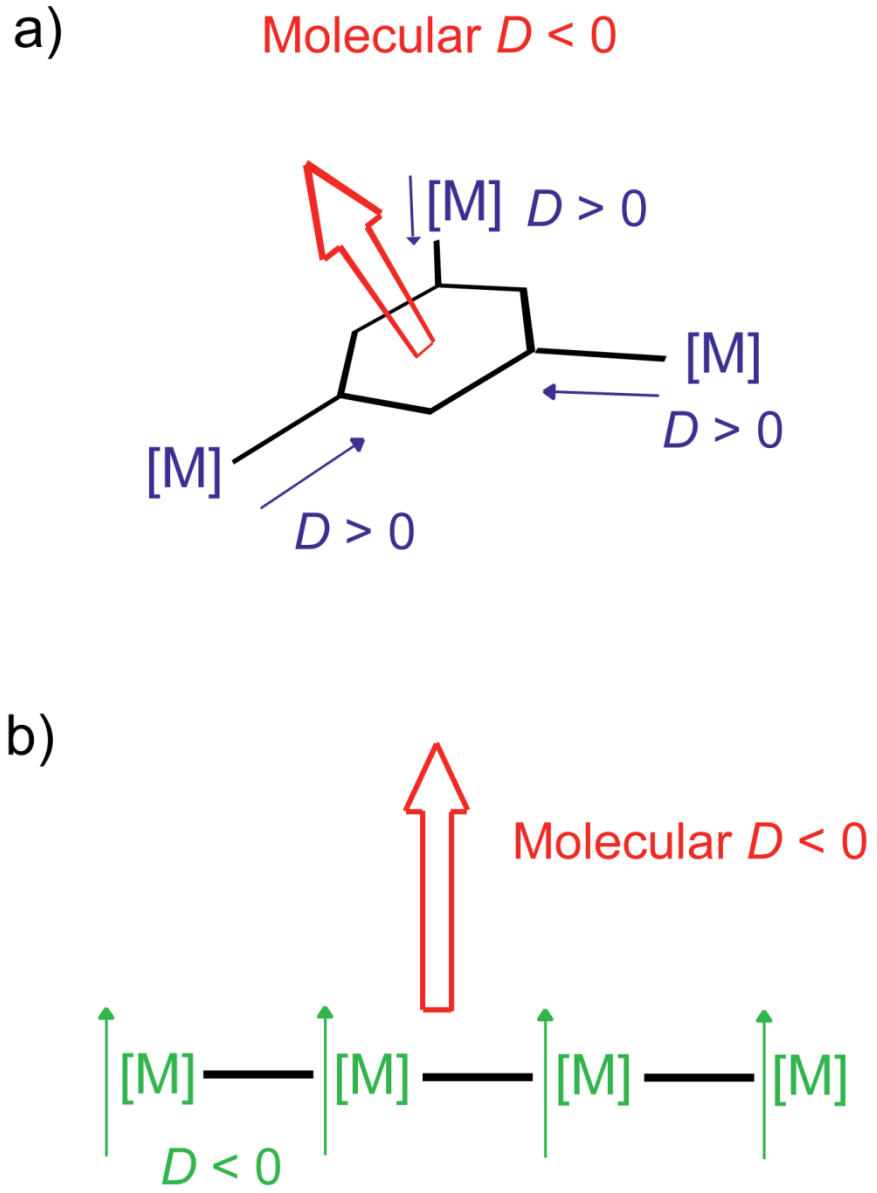

Figure 1.6. Topological arrangements for acetylide-bridged transition metal complexes that result in easy-axis molecular magnetic anisotropy: a) orthogonal arrangement of easy-plane magnetic ions with and b) collinear arrangement of easy-axis magnetic ions.

exposure to air,[34] so determinations of the intramolecular magnetic couplings are highly variable.[35] In 2009, Paul reinvestigated the magnetic properties of a family of dinuclear di-radical systems because the previously published J values seemed too weak in comparison to similar compounds.[36] Crystalline $[(dppe)_2Fe_2(Cp^*)_2(\mu\text{-}p\text{-}DEB)](PF_6)_2$ and amorphous $[(dppe)_2Fe_2(Cp^*)_2(\mu\text{-}m\text{-}DEB)](PF_6)_2$ were isolated and were subjected to variable temperature SQUID magnetometry. As shown in Figure 1.7, $\chi_M T$ for $[(dppe)_2Fe_2(Cp^*)_2(\mu\text{-}p\text{-}DEB)](PF_6)_2$ decreases from a value of ca. 0.37 $cm^3 \cdot K \cdot mol^{-1}$ at 300 K to 0 $cm^3 \cdot K \cdot mol^{-1}$ at temperatures below ca. 75 K. This trend indicates a robust antiferromagnetic interaction between the S = ½ spin centers, and the data were fit with a modified Bleaney-Bowers expression to extract a J value of –191 cm^{-1} with an 11% S = ½ impurity and g = 2.04. In contrast, the invariance of $\chi_M T$ with temperature for $[(dppe)_2Fe_2(Cp^*)_2(\mu\text{-}m\text{-}DEB)](PF_6)_2$ at 1.4 $cm^3 \cdot K \cdot mol^{-1}$ suggests that the triplet state in this complex is populated even at 300 K, and a lower bound estimate of J = 150 cm^{-1} was made assuming a g value of = 2.37. In contrast, Berben reported a fit of the temperature-dependent susceptibility for structurally similar $[(dmpe)_4Fe_2Cl_2(\mu\text{-}m\text{-}DEB)](PF_6)_2$, finding J = 41 cm^{-1}.[37]

The J values obtained by Paul provide a reason for optimism that well-isolated ground states may exist in larger systems based on *m*-DEB and *p*-DEB. However, these data (especially the data for the *m*-DEB complex) should be treated with caution for a few reasons: (1) ferromagnetic interactions are typically weaker than antiferromagnetic interactions within a family of similar compounds; (2) the g value for the *m*-DEB complex (2.37) is relatively large for a first-row transition-metal complex, especially considering that similar compounds exhibit g values much closer to 2.00; (3) in the

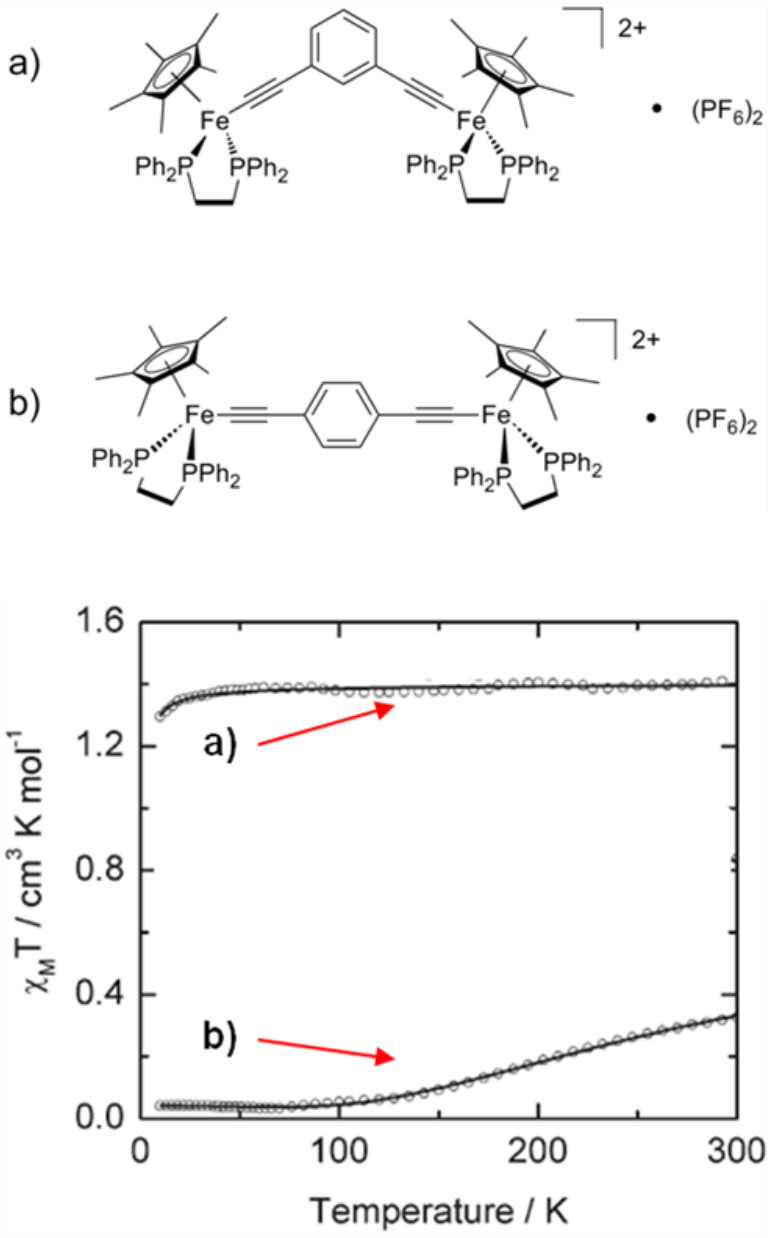

Figure 1.7. a) $[(dppe)_4Fe_2(Cp^*)_2(\mu\text{-}m\text{-DEB})](PF_6)_2$ and b) $[(dppe)_4Fe_2(Cp^*)_2(\mu\text{-}p\text{-DEB})](PF_6)_2$ (top). Bottom: corresponding variable temperature magnetic susceptibility data and fits. Figure adapted from ref 36.

original report for this compound,[32] X-band EPR spectroscopy at 77 K revealed a broad signal centered at g = 2.10. Since triplet systems are usually accompanied by large ZFS effects, the observation of an EPR signal is usually not possible with the low energies and magnetic fields available with X-band techniques.[38] In the original paper, fits to a separate data set for $[(dppe)_2Fe_2(Cp^*)_2(\mu\text{-}m\text{-DEB})](PF_6)_2$ are consistent with $J = 65$ cm^{-1} and g = 2.10. The broad signal in the EPR spectrum represents the $\Delta m_s = 1$ transition arising from the presence of degenerate, uncoupled $S = ½$ centers at 77 K. In light of the cautions explained above, this interpretation is, in all likelihood, far closer to reality.

The strong antiferromagnetic (AF) interaction present in *p*-DEB bridged systems arises due to the quinoidal-type contribution to the valence bond structure. In this arrangement, the energetic gain associated with the resonance structure is partially offset by the cost of losing aromaticity within the phenylene system.[39] Thus, enhancing AF interactions in *p*-DEB based systems has been explored by appending the bridging ligand with additional phenyl rings. Lapinte synthesized the 1,4-diethynylnapthalene (DEN)[40] and 9,10-diethynylanthracene (DEA)[41]-bridged complexes (Figure 1.8). The value of $\chi_M T$ at 300 for the DEN-bridged complex is much lower than the predicted spin-only value for two uncoupled $S = ½$ centers with g near 2.00 (0.23 cm^3·K·mol^{-1} vs. 0.75 cm^3·K·mol^{-1}). Cooling the sample results in a steady decrease in $\chi_M T$ and the value reaches zero at approximately 100 K. Fitting the data with the Bleaney-Bowers relationship results in $J = -517$ cm^{-1} with $g = 2.16$. In comparison, the susceptibility for the DEA-bridged complex is negligible at 293 K, which precludes a determination of J from a fitting procedure. However, the authors carried out broken symmetry DFT calculations and estimated the singlet-triplet energy gap to be at least 1200 cm^{-1}, corresponding to $J \approx -600$ cm^{-1}.

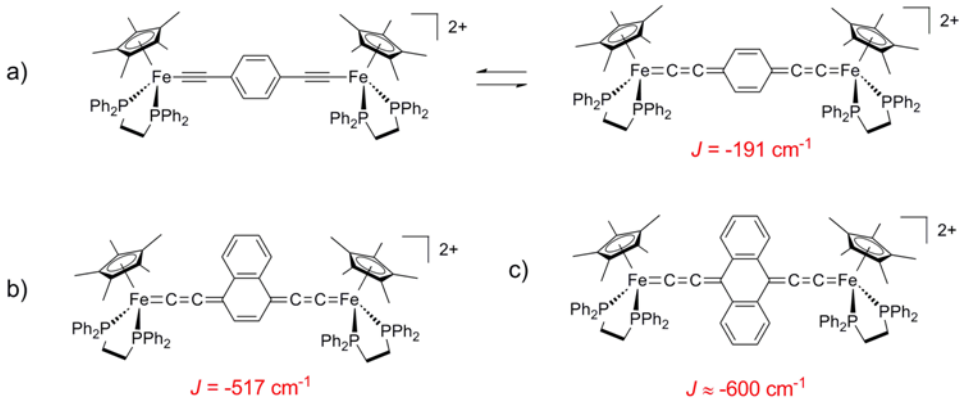

Figure 1.8. Quinodal contributions to resonance structures and antiferromagnetic coupling constants for a) $[(dppe)_4Fe_2(Cp^*)_2(\mu\text{-}p\text{-}DEB)](PF_6)_2$ b) $[(dppe)_4Fe_2(Cp^*)_2(\mu\text{-}1,4\text{-}DEN)](PF_6)_2$ c) $[(dppe)_4Fe_2(Cp^*)_2(\mu\text{-}9,10\text{-}DEA)](PF_6)_2$.

1.8 Conclusions

It is apparent from the magnetically characterized species presented here that carbon-rich linkers can be exceptional ligands for supplying ferro- and antiferromagnetic interactions in polymetallic clusters. This feature is vital to improving the working temperature of SMMs since excited state mixing reduces the population of the best double minimum energy manifold for SMM behavior. Synthetic advances in paramagnetic acetylide chemistry have been used by Ren and Berke to isolate wire-like complexes that incorporate Ru_2, W, and Fe units. X-ray structures of these linear molecules indicate that the low-dimensionality needed to conserve magnetic anisotropy is maintained even as the number of nodes is increased.

Magnetic investigations of diethynylbenzene-bridged complexes of LS Fe^{III} ions indicate that the bridging ligands impart strong intermolecular interactions. Further, the type and strength of magnetic coupling is tunable by ligand topology. In the *para*-bridged AF cases, the superexchange interaction can be optimized by extending the delocalized π system through the phenylene part of the bridging ligand as illustrated by the trend in the benzene < naphthalene < anthracene series. For ferromagnetically coupled *meta*-ethynylbenzene complexes, the variability in the magnetic data makes it difficult to ascertain the exact capabilities of the ligand. However, conservative fits of the magnetic data make it clear that significant coupling interactions should be expected.

1.9 Outlook

These results are promising in the context of synthesizing clusters that behave as SMMs at technologically reasonable temperatures. Further research efforts as they relate to the synthesis and characterization of novel transition metal-acetylide clusters are

described herein. The main focus of this work is to develop the methodology needed to prepare paramagnetic metallodendrimers based on ethynylbenzene bridging ligands. In Chapter 2, the preparation of several Co^{III}(cyclam) ethynylbenzene complexes is presented, and the ability to perform stepwise ligand substitution is demonstrated. The inclusion of paramagnetic Fe^{III} ions into arylacetylide-bridged assemblies is described in Chapter 3, and the influence of ancillary ligand conformation on the magnetic coupling is explored. Efforts to incorporate Cr^{II} ions into similar ethynylbenzene complexes resulted in the isolation of a family of dinitrogen-bridged species, and the unusual electronic and magnetic properties of these complexes are discussed in Chapter 4. In Chapter 5, the syntheses and properties of Fe-containing complexes bridged by one-dimensional carbon chains are described. Finally, like many areas of research, inorganic synthesis is incredibly challenging. In the course of his time at Colorado State, the author has explored additional synthetic avenues that deserve additional attention. Thus, some preliminary results and suggestions for future research are presented in the Appendix.

1.10 References and Notes

1. Toshiba Introduces Industry's Highest Areal Density 2.5-inch 750GB Hard Disk Drives. http://www.toshiba.co.jp/about/press/2010_03/pr2501.htm (accessed January 7, 2010).
2. (a) Winpenny, R. E. P., *Single Molecule Magnets and Related Phenomena*. Springer: Berlin, 2006; Vol. 122, p 262; (b) Ritter, S. K., *Chemical & Engineering News* **2004,** *82*, 29-32.
3. Sessoli, R.; Gatteschi, D.; Caneschi, A.; Novak, M. A., *Nature* **1993,** *365*, 141-143.
4. Lin, P.-H.; Burchell, T. J.; Ungur, L.; Chibotaru, L. F.; Wernsdorfer, W.; Murugesu, M., *Angew. Chem. Int. Ed.* **2009,** *48*, 9489-9492.
5. Marvaud, V.; Herrera, J. M.; Barilero, T.; Tuyeras, F.; Garde, R.; Scuiller, A.; Decroix, C.; Cantuel, M.; Desplanches, C., *Monatsh. Chem.* **2003,** *134*, 149-163.

6. Tasiopoulos, A. J.; Vinslava, A.; Wernsdorfer, W.; Abboud, K. A.; Christou, G., *Angew. Chem. Int. Ed.* **2004,** *43*, 2117-2121.

7. (a) Murugesu, M.; Habrych, M.; Wernsdorfer, W.; Abboud, K. A.; Christou, G., *J. Am. Chem. Soc.* **2004,** *126*, 4766-4767; (b) Ako, A. M.; Hewitt, I. J.; Mereacre, V.; Clérac, R.; Wernsdorfer, W.; Anson, C. E.; Powell, A. K., *Angew. Chem. Int. Ed.* **2006,** *45*, 4926-4929; (c) Stamatatos, T. C.; Abboud, K. A.; Wernsdorfer, W.; Christou, G., *Angew. Chem. Int. Ed.* **2007,** *46*, 884-888.

8. (a) Rinehart, J. D.; Long, J. R., *J. Am. Chem. Soc.* **2009,** *131*, 12558-12559; (b) Rinehart, J. D.; Meihaus, K. R.; Long, J. R., *J. Am. Chem. Soc.* **2010,** *132*, 7572-7573.

9. (a) Harman, W. H.; Harris, T. D.; Freedman, D. E.; Fong, H.; Chang, A.; Rinehart, J. D.; Ozarowski, A.; Sougrati, M. T.; Grandjean, F.; Long, G. J.; Long, J. R.; Chang, C. J., *J. Am. Chem. Soc.* **2010,** *132*, 18115-18126; (b) Freedman, D. E.; Harman, W. H.; Harris, T. D.; Long, G. J.; Chang, C. J.; Long, J. R., *J. Am. Chem. Soc.* **2010,** *132*, 1224-1225.

10. (a) Berseth, P. A.; Sokol, J. J.; Shores, M. P.; Heinrich, J. L.; Long, J. R., *J. Am. Chem. Soc.* **2000,** *122*, 9655-9662; (b) Shores, M. P.; Sokol, J. J.; Long, J. R., *J. Am. Chem. Soc.* **2002,** *124*, 2279-2292.

11. Long, N. J.; Williams, C. K., *Angew. Chem. Int. Ed.* **2003,** *42*, 2586-2617.

12. Ren, T., *Organometallics* **2005,** *24*, 4854-4870.

13. (a) Szafert, S.; Gladysz, J. A., *Chem. Rev.* **2003,** *103*, 4175-4206; (b) Szafert, S.; Gladysz, J. A., *Chem. Rev.* **2006,** *106*, PR1-PR33.

14. (a) Brady, M.; Weng, W.; Zhou, Y.; Seyler, J. W.; Amoroso, A. J.; Arif, A. M.; Böhme, M.; Frenking, G.; Gladysz, J. A., *J. Am. Chem. Soc.* **1997,** *119*, 775-788; (b) Dembinski, R.; Bartik, T.; Bartik, B.; Jaeger, M.; Gladysz, J. A., *J. Am. Chem. Soc.* **2000,** *122*, 810-822; (c) Paul, F.; Meyer, W. E.; Toupet, L.; Jiao, H.; Gladysz, J. A.; Lapinte, C., *J. Am. Chem. Soc.* **2000,** *122*, 9405-9414; (d) Bruce, M. I.; Costuas, K.; Davin, T.; Ellis, B. G.; Halet, J.-F.; Lapinte, C.; Low, P. J.; Smith, M. E.; Skelton, B. W.; Toupet, L.; White, A. H., *Organometallics* **2005,** *24*, 3864-3881; (e) Coat, F.; Guillevic, M.-A.; Toupet, L.; Paul, F.; Lapinte, C., *Organometallics* **1997,** *16*, 5988-5998.

15. Hush, N. S., Intervalence-Transfer Absorption. Part 2. Theoretical Considerations and Spectroscopic Data. In *Prog. Inorg. Chem.*, Cotton, F. A., Ed. 1967; pp 391-444.

16. (a) Naklicki, M. L.; White, C. A.; Plante, L. L.; Evans, C. E. B.; Crutchley, R. J., *Inorg. Chem.* **1998,** *37*, 1880-1885; (b) Fabre, M.; Bonvoisin, J., *J. Am. Chem. Soc.* **2007,** *129*, 1434-1444; (c) Nelsen, S. F.; Ismagilov, R. F.; Teki, Y., *J. Am. Chem. Soc.* **1998,** *120*, 2200-2201.

17. Ruiz, E.; Rodríguez-Fortea, A.; Alvarez, S., *Inorg. Chem.* **2003,** *42*, 4881-4884.

18. (a) Kheradmandan, S.; Venkatesan, K.; Blacque, O.; Schmalle, H. W.; Berke, H., *Chem. Eur. J.* **2004,** *10*, 4872-4885; (b) Bullock, R. M.; Lemke, F. R.; Szalda, D. J., *J. Am. Chem. Soc.* **1990,** *112*, 3244-3245; (c) Ogawa, H.; Onitsuka, K.; Joh, T.; Takahashi, S.; Yamamoto, Y.; Yamazaki, H., *Organometallics* **1988,** *7*, 2257-2260.

19. (a) Lapinte, C., *J. Organomet. Chem.* **2008,** *693*, 793-801; (b) Kheradmandan, S.; Heinze, K.; Schmalle, H. W.; Berke, H., *Angew. Chem. Int. Ed.* **1999,** *38*, 2270-2273.

20. Le Narvor, N.; Toupet, L.; Lapinte, C., *J. Am. Chem. Soc.* **1995,** *117*, 7129-7138.

21. (a) Chen, W.-Z.; Cotton, F. A.; Dalal, N. S.; Murillo, C. A.; Ramsey, C. M.; Ren, T.; Wang, X., *J. Am. Chem. Soc.* **2005,** *127*, 12691-12696; (b) Kennon, B. S.; Her, J.-H.; Stephens, P. W.; Miller, J. S., *Inorg. Chem.* **2009,** *48*, 6117-6123; (c) Miller, J. S.; Manson, J. L., *Acc. Chem. Res.* **2001,** *34*, 563-570; (d) Shum, W. W.; Liao, Y.; Miller, J. S., *J. Phys. Chem. A* **2004,** *108*, 7460-7462; (e) Vos, T. E.; Liao, Y.; Shum, W. W.; Her, J.-H.; Stephens, P. W.; Reiff, W. M.; Miller, J. S., *J. Am. Chem. Soc.* **2004,** *126*, 11630-11639.

22. (a) Ren, T., *Coord. Chem. Rev.* **1998,** *175*, 43-58; (b) Hurst, S. K.; Ren, T., *J. Organomet. Chem.* **2003,** *670*, 188-197.

23. Ying, J.-W.; Liu, I. P.-C.; Xi, B.; Song, Y.; Campana, C.; Zuo, J.-L.; Ren, T., *Angew. Chem. Int. Ed.* **2010,** *49*, 954-957.

24. Barral, M. C.; Herrero, S.; Jiménez-Aparicio, R.; Torres, M. R.; Urbanos, F. A., *Angew. Chem. Int. Ed.* **2005,** *44*, 305-307.

25. Semenov, S. N.; Blacque, O.; Fox, T.; Venkatesan, K.; Berke, H., *J. Am. Chem. Soc.* **2010,** *132*, 3115-3127.

26. (a) Semenov, S. N.; Blacque, O.; Fox, T.; Venkatesan, K.; Berke, H., *Angew. Chem. Int. Ed.* **2009,** *48*, 5203-5206; (b) Semenov, S. N.; Blacque, O.; Fox, T.; Venkatesan, K.; Berke, H., *Organometallics* **2010,** *29*, 6321-6328.

27. Semenov, S. N.; Taghipourian, S. F.; Blacque, O.; Fox, T.; Venkatesan, K.; Berke, H., *J. Am. Chem. Soc.* **2010,** *132*, 7584-7585.

28. Albinati, A.; Leoni, P.; Marchetti, L.; Rizzato, S., *Angew. Chem. Int. Ed.* **2003,** *42*, 5990-5993.

29. (a) Oshio, H.; Nakano, M., *Chem. Eur. J.* **2005,** *11*, 5178-5185; (b) Cirera, J.; Ruiz, E.; Alvarez, S.; Neese, F.; Kortus, J., *Chem. Eur. J.* **2009,** *15*, 4078-4087.

30. Tancini, E.; Rodriguez-Douton, M. J.; Sorace, L.; Barra, A.-L.; Sessoli, R.; Cornia, A., *Chem. Eur. J.* **2010,** *16*, 10482-10493.

31. (a) Ung, V. n. A.; Cargill Thompson, A. M. W.; Bardwell, D. A.; Gatteschi, D.; Jeffery, J. C.; McCleverty, J. A.; Totti, F.; Ward, M. D., *Inorg. Chem.* **1997,** *36*, 3447-3454; (b) Ovchinnikov, A. A., *Theor. Chim. Acta* **1978,** *47*, 297-304.

32. Weyland, T.; Costuas, K.; Mari, A.; Halet, J. F.; Lapinte, C., *Organometallics* **1998,** *17*, 5569-5579.

33. Paul, F.; Lapinte, C., In *Unusual Structures and Physical Properties in Organometallic Chemistry*, Gielen, M.; Willem, R.; Wrackmeyer, B., Eds. John Wiley and Sons: West Sussex, 2002.

34. Paul, F.; Toupet, L.; Roisnel, T.; Hamon, P.; Lapinte, C., *C. R. Chimie* **2005,** *8*, 1174-1185.

35. (a) Roué, S.; Le Stang, S.; Toupet, L.; Lapinte, C., *C. R. Chimie* **2003,** *6*, 353-366; (b) Le Narvor, N.; Lapinte, C., *C. R. Acad. Sci., Ser. IIC: Chim.* **1998,** *1*, 745-749; (c) Weyland, T.; Costuas, K.; Mari, A.; Halet, J.-F.; Lapinte, C., *Organometallics* **1998,** *17*, 5569-5579.

36. Paul, F. d. r.; Bondon, A.; da Costa, G. g.; Malvolti, F.; Sinbandhit, S.; Cador, O.; Costuas, K.; Toupet, L.; Boillot, M.-L., *Inorg. Chem.* **2009,** *48*, 10608-10624.

37. Berben, L. A. Ph.D.Thesis, University of California, Berkeley, 2005.

38. Drago, R. S., *Physical Methods for Chemists*. 2nd ed.; Surfside: Gainesville, 1992.

39. Montgomery, L. K.; Huffman, J. C.; Jurczak, E. A.; Grendze, M. P., *J. Am. Chem. Soc.* **1986,** *108*, 6004-6011.

40. Tanaka, Y.; Shaw-Taberlet, J. A.; Justaud, F. d. r.; Cador, O.; Roisnel, T.; Akita, M.; Hamon, J.-R.; Lapinte, C., *Organometallics* **2009,** *28*, 4656-4669.

41. de Montigny, F.; Argouarch, G.; Costuas, K.; Halet, J.-F.; Roisnel, T.; Toupet, L.; Lapinte, C., *Organometallics* **2005,** *24*, 4558-4572.

Chapter 2. Synthesis and Characterization of Ethynylbenzene Complexes of Co^{III}

2.1 Introduction

Inorganic chemists have long been concerned with being able to assemble transition metal clusters using a "building block" approach.[1] Small ligands such as oxide,[2] hydroxide,[3] and cyanide[4] have proven to be effective directors of multimetallic cluster self-assembly, but there is interest in the synthesis of metal clusters bridged by a framework of larger ligands with delocalized π orbitals.[5] Such molecules have been suggested as potential components of non-linear optical devices,[6] and more recently, magnetic materials.[7] Polyethynylbenzene bridging ligands have been attractive in this regard: Takahashi and coworkers have synthesized metallodendrimers with up to 45 square planar Pt^{II}-containing units bridged by the triply deprotonated trianion of 1,3,5-triethynylbenzene (H_3TEB).[8] Humphrey and coworkers later reported the preparation and properties of TEB^{3-}-based dendrimers that incorporated nine octahedral Ru^{2+} ions. Both types of molecules were synthesized by stepwise replacement of *trans*-chloride ligands; isolation of products with good monodispersity relied on the high inertness of the metal ions with mixed ligands at sites *trans* to each other. For this reason, Pt^{II} and Ru^{II} are ideal candidates for incorporation into metallodendrimers, as many examples of heteroleptic complexes exist for those ions. However, interesting properties are predicted for first-row transition metal analogues, not the least of which are related to their paramagnetism.

We are interested in synthesizing paramagnetic first row transition metal complexes bridged by rigid σ-donors like TEB^{3-}. This ligand has been shown to engender ferromagnetic coupling between ligated metal ions because of the mutually *meta* bridged connectivity,[9] and the two-dimensional topology imparted by the rigid ligand is expected to encourage magnetic anisotropy.[10] Prior to attempting the synthesis of air- and moisture-sensitive paramagnetic complexes, we wanted to prepare a stable structural analogue of a first-row complex that could be easily studied with conventional techniques such as ^{1}H NMR, making Co^{III} complexes an ideal choice. Earlier work from Giese established that Grignard reagents could be used to prepare monomeric Co^{III} chloro-acetylide complexes.[11] The syntheses of mono- and bis-acetylide Co^{III} complexes was also studied by Lewis and coworkers.[12] They discovered that trialkylstannyl acetylene precursors reacted with neutral $[Co^{III}N_4Cl_2]$ complexes in organic solvents in the presence of catalytic CuI to form monomeric metal-acetylide compounds. Depending on reaction stoichiometry, polymeric compounds could also be prepared by heating equimolar amounts of the dichloro Co^{III} precursor and ditopic *para*-bis(trimethyltin)diethynylbenzene.[12] Although these results demonstrate the feasibility of synthesizing mono- and bis-σ-acetylide Co^{III} complexes, we wanted to explore a route that allowed for the preparation of metallodendrimer building blocks that could be combined in a stepwise manner. Herein, we present the syntheses, X-ray structures, and spectroscopic and electrochemical characterizations of a series of diamagnetic Co^{III}(cyclam)-based chloro-acetylide complexes synthesized using a dehydrohalogenation synthetic strategy. The stepwise preparation of a di-substituted bis-acetylide complex is

also described, which demonstrates the possibility of using related octahedral first-row transition metal complexes as synthons for paramagnetic metallodendrimers.

2.2 Division of Labor

Initial synthesis and characterization of **2.1** was performed by REU student Sara Mosley. Dr. Md. K. Kabir prepared $[(cyclam)_2Co_2Cl_2(\mu\text{-}p\text{-DEB})]Cl_2$ and performed initial spectroscopic measurements.

2.3 Experimental Section

2.3.1 Preparation of Compounds. Unless otherwise noted, all manipulations were performed in air. The compounds $[(cyclam)CoCl_2]Cl$[13] and 1,3,5-triethynylbenzene[14] (H_3TEB) were prepared as described elsewhere. Triethylamine was freshly distilled before use. All other reagents were purchased commercially and were used without further purification.

***trans*-[(cyclam)CoCl(C_2Ph)]BPh_4 (2.1).** Triethylamine (1.62 mL, 11.6 mmol) was added to a green methanolic (10 mL) solution of $[(cyclam)CoCl_2]Cl$ (213 mg, 0.582 mmol) and phenylacetylene (61 μL, 0.55 mmol) in a 100 mL round-bottomed flask, causing the solution color to darken. The flask was fitted with a condenser tube, and the solution was heated at reflux for 24 hours, during which time the solution color turned red-orange. The solvent was removed by rotary evaporation, and the resulting red-brown residue was washed with diethyl ether (10 mL) and dried under vacuum to yield 231 mg of the crude chloride salt as a red-brown solid. This solid was dissolved in *ca.* 10 mL methanol and was added to a methanolic (3 mL) solution of $NaBPh_4$ (184 mg, 0.536 mmol), causing an orange solid to precipitate. This solid was isolated by filtration, washed with methanol (3 × 3 mL) and diethyl ether (3 × 3 mL) to afford 251 mg of the

final product in 64% yield (based on phenylacetylene). Crystals suitable for X-ray diffraction were grown by diffusion of diethyl ether vapor into a concentrated solution of **2.1** in tetrahydrofuran. Absorption spectrum (THF): λ_{max} (ε_M) 227 (43500), 258 (33300), 326 (sh, 10600), 381 (sh, 1400) 486 nm (1100 $M^{-1}\cdot cm^{-1}$). IR: $\nu_{C\equiv C}$ 2125 cm^{-1}. ^1H NMR ($(CD_3)_2CO$): δ 7.37-7.22 (m, 13H, B-C_6H_5, CCC_6H_5), 6.93 (t, 8H, B-C_6H_5), 6.78 (t, 4H, B-C_6H_5), 5.06 (br, 2H, N-*H*), 4.92 (br, 2H, N-*H*), 3.03-2.59 (m, 16H, CH_2), 1.74-1.64 ppm (m, 8H, CH_2). ESI^+-MS (acetone): *m/z* 395.20 ([**2.1**–BPh_4]$^+$). Anal. Calcd. for $C_{42}H_{49}N_4BClCo$: C, 70.55; H, 6.91; N, 7.84. Found: C, 70.37; H, 7.14; N, 7.79.

***trans, trans*-[(cyclam)$_2$Co$_2$Cl$_2$(μ-*p*-DEB)](BPh$_4$)$_2$ (2.2b)**. Triethylamine (1.32 mL, 9.44 mmol) was added to a green methanolic (10 mL) solution of [(cyclam)$CoCl_2$]Cl (181 mg, 0.495 mmol) and freshly sublimed *p*-H_2DEB (29.7 mg, 0.236 mmol) in a 50 mL round-bottomed flask, causing the solution to darken. The flask was fitted with a condenser tube and the solution was heated at reflux for 24 hours, during which time the solution color turned red-orange. The solvent was removed by rotary evaporation, and the resulting red-brown residue was washed with diethyl ether (10 mL) and dried under vacuum to yield 196 mg of crude *trans, trans*-[(cyclam)$_2$Co$_2$Cl$_2$(μ-p-DEB)]Cl$_2$ (**2.2a**) as an orange solid. This solid was dissolved in *ca*. 10 mL methanol and was added to a methanolic (3 mL) solution of $NaBPh_4$ (256 mg (0.748 mmol), causing an orange solid to precipitate. This solid was isolated by filtration, washed with methanol (3 × 3 mL) and diethyl ether (3 × 3 mL). The compound was recrystallized by slow diffusion of diethyl ether into a concentrated solution of **2.2b** in acetone to afford 151 mg of the final product in 47% yield (based on *p*-H_2DEB). Crystals of the chloride salt suitable for X-ray diffraction could be grown by diethyl ether vapor diffusion into a concentrated solution

of crude $[(cyclam)_2Co_2Cl_2(\mu\text{-}p\text{-DEB})]Cl_2$ (**2.2a**) in MeOH. Absorption spectrum (acetone): λ_{max} (ε_M) 327 (3720), 386 (sh) (940) 488 (440 $M^{-1}\cdot cm^{-1}$). IR: $\nu_{C\equiv C}$ 2133 cm^{-1}. ^1H NMR ($(CD_3)_2CO$): δ 7.34 (br, 20H, B-C_6H_5 and CC(Ar-*H*)CC, 6.93 (t, 16H, B-C_6H_5), 6.78 (t, 8H, B-C_6H_5), 4.93 (br, 8H, N-*H*), 3.07-2.54 (m, 32H, CH_2), 1.704 ppm (m, 4H, CH_2). ESI^+–MS (acetone): m/z 1031.47 ([**2.2b**–BPh_4]$^+$), 356.13 ([**2.2b**–2 BPh_4]$^{2+}$). Anal. Calcd. for $C_{84}H_{104}N_8B_2Cl_2Co_2O_2$ (**2.2b**·$2C_3H_6O$): C, 68.72; H, 7.14; N, 7.63. Found: C, 68.56; H, 7.06; N, 7.36.

***trans, trans, trans*-[(cyclam)$_3$Co$_3$Cl$_3$(TEB)](BPh$_4$)$_3$ (2.3b)**. Triethylamine (1.70 mL, 12.3 mmol) was added to a green methanolic (10 mL) solution of [(cyclam)$CoCl_2$]Cl (239 mg, 0.655 mmol) and freshly sublimed H_3TEB (30.7 mg, 0.205 mmol) in a 100 mL round-bottomed flask, causing the solution color to darken. The flask was fitted with a condenser tube and the solution was refluxed for 24 hours, during which time the solution color turned red-orange. The solvent was removed by rotary evaporation, and the resulting red-brown residue was washed with diethyl ether (10 mL) and dried under vacuum to yield 271 mg of crude $[(cyclam)_3Co_3Cl_3(TEB)]Cl_3$ (**2.3a**) as an orange solid. This solid was dissolved in *ca*. 10 mL methanol and was poured into a methanolic (5 mL) solution of $NaBPh_4$ (326 mg (0.953 mmol), causing a salmon-colored solid to precipitate. This solid was isolated by filtration, washed with methanol (3 × 3 mL) and diethyl ether (3 × 3 mL) and dried in air to afford 234 mg of the final product in 57% yield (based on H_3TEB). Crystals of the chloride salt suitable for X-ray diffraction were grown by diethyl ether vapor diffusion into a concentrated solution of $[(cyclam)_3Co_3Cl_3(TEB)]Cl_3$ in MeOH. Absorption spectrum (acetone): λ_{max} (ε_M) 329 (3300), 384 (sh, 575) 485 nm (420 $M^{-1}\cdot cm^{-1}$). IR: $\nu_{C\equiv C}$ 2114 cm^{-1}. ^1H NMR (CD_3CN): δ 7.33 (s, 3H, Ar-*H*), 7.27 (m, 24H,

B-C_6H_5), 7.00 (t, 24H, B-C_6H_5), 6.84 (t, 12H, B-C_6H_5), 4.50 (br, 6H, N-*H*), 4.39 (br, 6H, N-*H*), 2.88-2.39 (m, 48H, CH_2), 1.44 ppm (m, 12H, CH_2). ESI-MS^+ (acetone): m/z 1667.60 ([**2.3b**–BPh_4]$^+$), 674.80 ([**2.3b**–2 BPh_4]$^{2+}$), 343.90 ([**2.3b**–3 BPh_4]$^{3+}$). Anal. Calcd. for $C_{114}H_{135}N_{12}B_3Cl_3Co_3$: C, 68.84; H, 6.84; N, 8.45. Found: C, 68.58; H, 6.83; N, 8.19.

***trans, trans*-[(cyclam)$_2$Co$_2$Cl$_2$(HTEB)]Cl$_2$ (2.4)**. Triethylamine (0.34 mL, 2.42 mmol) was added to a green methanolic (10 mL) solution of [(cyclam)$CoCl_2$]Cl (233 mg, 0.637 mmol) and freshly sublimed H_3TEB (45.5 mg, 0.303 mmol) in a 100 mL round-bottomed flask, causing the solution color to darken. The flask was fitted with a condenser tube and the solution was refluxed for 24 hours, during which time the solution turned orange-brown. The solvent was removed by rotary evaporation, and the resulting red-brown residue was washed with 10 mL of absolute ethanol, causing an orange solid to precipitate. The solid was isolated by filtration, washed with ethanol (3 × 3 mL) and diethyl ether (3 × 3 mL) and dried in air to afford 92.1 mg of the final product in 38% yield. Single crystals suitable for X-ray analysis were grown by diffusing diethyl ether vapor into a concentrated solution of **2.4** in methanol. Absorption spectrum (MeCN): λ_{max} (ε_M) 229 (58780), 264 (46270), 277 (42840), 381 (sh, 298), 482 nm (214 M^{-1} cm^{-1}). IR: $\nu_{C\equiv C}$ 2123 cm^{-1}, ν_{CC-H} 3313 cm^{-1}. ^{1}H NMR (CD_3OD): 7.55 (s, 1H, Ar–*H*), 7.45 (s, 2H, Ar–*H*), 5.18 (br s, 8H, N–*H*), 3.12-2.52 (br m, 32H, CH_2) 2.02 (br t, 4H, CH_2), 1.68 ppm (br m, 4H, CH_2). ESI-MS^+ (MeOH): m/z 771.20 (**2.4**–Cl^+), 368.12 (**2.4**–2Cl^{2+}). Anal. Calcd. for $C_{34}H_{60}Cl_4Co_2N_8O_2$ (**2.4**·2 MeOH): C, 46.80; H, 6.93; N, 12.84. Found: C, 45.38; H, 6.70; N, 12.48. Integration values from the cyclam prtotons in the ^{1}H NMR suggest that a small amount of [(cyclam)$CoCl_2$]Cl may be present. Allowing for this

possibility gives a rational explanation for the combustion analysis results. Anal. Calcd. for $C_{37}H_{68.8}Cl_{4.6}Co_{2.2}N_{8.8}O_3$ (**2.4**·3MeOH·0.2[(cyclam)$CoCl_2$]Cl): C, 45.45; H, 7.09; N, 12.61.

***trans*-[(cyclam)Co(C_2Ph)$_2$](BPh_4) (2.5)**. Under an atmosphere of dinitrogen, LiC_2Ph was generated by adding *n*-BuLi (0.07 mL of a 1.6 molar solution in hexanes, 0.112 mmol) to a solution of phenylacetylene (13.1 μL, 12.1 mg, 0.119 mmol) in diethyl ether (3 mL). After stirring for 5 minutes, the ethereal solution was added to an orange solution of **2.1** (77.3 mg, 0.108 mmol) in tetrahydrofuran (5 mL). After 1 hour of stirring, the solvent was removed *in vacuo* to afford a brown residue. Washing with pentane afforded a yellow/brown solid which was isolated by filtration and washed with diethyl ether (3 × 3 mL) to yield 88 mg of crude yellow solid. The product was recrystallized by slow diffusion of diethyl ether vapor into concentrated solutions of **2.5** in tetrahydrofuran. The yellow needle crystals that formed after one day were isolated by filtration, washed with diethyl ether (3 × 3 mL), and dried under dinitrogen to afford 53.8 mg of the final product (64%). Absorption spectrum (MeCN): λ_{max} (ε_M) 268 (28200), 363 (sh, 270), 463 nm (84 $M^{-1}\cdot cm^{-1}$). IR: $\nu_{C\equiv C}$ 2100 cm^{-1}. ^{1}H NMR (CD_3CN): δ 7.33 (s, 3H, Ar-*H*), 7.27 (m, 24H, B-C_6H_5), 7.00 (t, 24H, B-C_6H_5), 6.84 (t, 12H, B-C_6H_5), 4.50 (br, 6H, N-*H*), 4.39 (br, 6H, N-*H*), 2.88-2.39 (m, 48H, CH_2), 1.44 ppm (m, 12H, CH_2). ESI-MS^+ (acetone): m/z 461.07 (**2.5**–BPh_4^+). Anal. Calcd. for $C_{56}H_{66}BCoN_4O_{1.5}$ (**2.5**·1.5THF): C, 75.67; H, 7.48; N, 6.30. Found: C, 75.64; H, 7.26; N, 6.52.

2.3.2 X-ray Structure Determinations. Structures were determined for the compounds listed in Table 2.1. Single crystals were coated in Paratone oil, supported on cryoloops, transferred to a Bruker Kappa Apex 2 CCD diffractometer, and cooled under a

Table 2.1. Crystallographic data[a] for compounds [(cyclam)CoCl(C_2Ph)]BPh_4 (**2.1**), [(cyclam)$_2$$Co_2Cl_2$(μ-*p*-DEB)]$Cl_2$·2MeOH (**2.2a**·2MeOH), [(cyclam)$_3$$Co_3Cl_3$(TEB)]$Cl_3$·5MeOH (**2.3a**·5MeOH), [(cyclam)$_2$$Co_2Cl_2$(HTEB)]$Cl_2$·1.8MeOH (**2.4**·1.8MeOH), [1,3-{(cyclam)CoCl(C_2)}-5-(C_2H)$_{0.88}$$Br_{0.12}$-benzene]$(BPh_4)_2$ · 4 acetone and [(cyclam)Co(C_2Ph)$_2$]BPh_4·2THF (**2.5**·2THF).

	2.1	**2.2a**·2MeOH	**2.3a**·5MeOH	**2.4**·1.8MeOH	[Co_2TEB/Br]($BPh_4)_2$·4 acetone	**2.5**·2THF
crystal code	msn209	mk001	msn214b	ms07	msn229a	msn216
formula	$C_{42}H_{49}BClCoN_4$	$C_{32}H_{60}Cl_4Co_2O_2N_8$	$C_{47}H_{95}Cl_6Co_3N_{12}O_5$	$C_{35.6}H_{66.4}Cl_4Co_2N_8O_{3.6}$	$C_{91.76}H_{114.89}B_2Br_{0.12}Cl_2Co_2N_8O_4$	$C_{58}H_{70}BCoN_4O_2$
fw	715.04	848.55	1297.84	923.83	1613.55	924.92
color, habit	orange needle	orange prism	orange prism	orange prism	orange prism	yellow needle
T, K	120(2)	100(2)	120(2)	100(2)	120(2)	120(2)
space group	$P2_1/c$	$P2_1/c$	$P\bar{1}$	$C2/c$	$P\bar{1}$	$P2_1/c$
Z	4	2	2	4	2	4
a, Å	16.0376(4)	14.3852(3)	8.617(1)	18.421(4)	10.1434(4)	15.911(1)
b, Å	21.5470(5)	9.6749(2)	15.070(2)	9.769(2)	17.1412(7)	18.464(1)
c, Å	21.1968(5)	17.4624(4)	24.676(3)	29.691(5)	25.525(1)	17.139(1)
α, deg	90	90	72.656(3)	90	92.609(1)	90
β, deg	92.266(1)	119.535(1)	89.289(4)	123.411(9)	96.864(1)	97.391(2)
γ, deg	90	90	80.701(4)	90	104.323(1)	90
V, Å^3	7319.1(3)	2114.52(8)	3016.4(6)	4460.4(2)	4526.2(3)	4993.8(5)
d_{calc}, g/cm^3	1.298	1.433	1.429	1.376	1.259	1.230
GOF	0.996	1.038	1.084	1.095	1.026	1.067
R_1 (wR_2)[b], %[c]	4.58 (11.14)	3.98 (9.83)	5.21 (13.96)	7.50 (18.34)	3.76(9.89)	4.33 (11.46)
R_1 (wR_2)[b], %[d]	6.96 (12.83)	5.55 (10.49)	7.01 (15.15)	14.88 (21.30)	5.47(11.07)	8.61 (14.38)

[a] Obtained with graphite-monochromated Mo Kα (λ = 0.71073 Å) radiation.
[b] $R_1 = \sum||F_o| - |F_c||/\sum|F_o|$, $wR_2 = \{\sum[w(F_o^2 - F_c^2)^2]/\sum[w(F_o^2)^2]\}^{1/2}$. [c] For data where $I>2\sigma(I)$. [d] For all data.

stream of dinitrogen. All data collections were performed at 100 K or 120 K with Mo Kα radiation (λ = 0.71073 Å) and a graphite monochromator. Initial lattice parameters were determined from a minimum of 190 reflections harvested from 36 frames, and data sets were collected targeting complete coverage and four-fold redundancy. Data were integrated and corrected for absorption effects with the Apex 2 software package.[15] Structures were solved by direct methods with the aid of successive Fourier difference maps and were refined against all data using the SHELXTL software package.[16] Displacement parameters for all non-hydrogen atoms were refined anisotropically. Hydrogen atoms were assigned to ideal positions and were refined using a riding model where the isotropic displacement parameters were set at 1.2 times those of the attached carbon or nitrogen atoms (1.5 times for methyl protons).

The refined structure solution for **2.4** was not fully satisfactory due to marginal crystal quality. Attempting to improve the diffraction data quality, tetraphenylborate anion metathesis was performed with **2.4**. The resulting material was recrystallized by slow diffusion of diethyl ether vapor into a solution of the compound in acetone. Upon structural refinement, the crystal was found to contain a 88/12 acetylene/bromine compositional disorder.

In the structure of **2.5**·2THF, the β-acetylenic carbon atoms in each complex exhibited abnormally small thermal ellipsoids with respect to their nearest neighbors. Thus, the atoms were treated with the EADP command to constrain their parameters to those of the α-acetylenic carbon atoms.

2.3.3 Other Physical Measurements. Absorption spectra were obtained in quartz cuvettes with a Hewlett-Packard 8453 spectrophotometer. Infrared spectra were measured

with a Nicolet 380 FT-IR using the Smart Performer ZnSe ATR accessory. ^{1}H NMR spectra were recorded using a Varian INOVA instrument operating at 300 MHz. Cyclic voltammetry experiments were performed in 0.1 molar solutions of $(Bu_4N)PF_6$ in tetrahydrofuran or acetonitrile. The voltammograms were recorded with either a CH Instruments 1230A or 660C potentiostat using a 0.25 mm Pt disk working electrode, Ag/Ag^+ reference electrode, and a Pt mesh auxiliary electrode. All voltammograms shown were measured with a scan rate of 0.1 V/s. Reported potentials are referenced to the $[Cp_2Fe]^+/[Cp_2Fe]$ redox couple and were determined by adding ferrocene as an internal standard at the conclusion of each electrochemical experiment. Elemental analyses were performed by Robertson Microlit Laboratories in Madison, NJ.

2.4 Results and Discussion

2.4.1 Syntheses and characterizations of Co^{III} acetylide complexes. Our approach to making "0^{th}" generation metallodendrimers is based on a dehydrohalogenation strategy that has been employed in the synthesis of other Co^{3+}, Fe^{2+}, and Ru^{2+} containing metal-acetylide complexes. For Ru-containing complexes, the reaction has been shown to proceed by way of a metal-vinylidine intermediate, which reacts readily with a base to afford the metal acetylide. Shown in Scheme 2.1, *trans*-$[Co(cyclam)Cl_2]Cl$ reacts directly with an arylacetylide ligand using triethylamine as the base, yielding the chloro-acetylide complexes as orange solids in acceptable yield. In order to drive the ligand substitution reactions in the syntheses of **2.1**, **2.2a**, and **2.3a** to completion, it was necessary to use a slight stoichiometric excess[17] of $[(cyclam)CoCl_2]Cl$; as evidenced by the isolation of **2.4**, Co^{3+}-deficient reaction mixtures lead to "incomplete" substitution. Obtaining pure bulk samples of the chloride salts of all complexes presented herein was not possible, likely

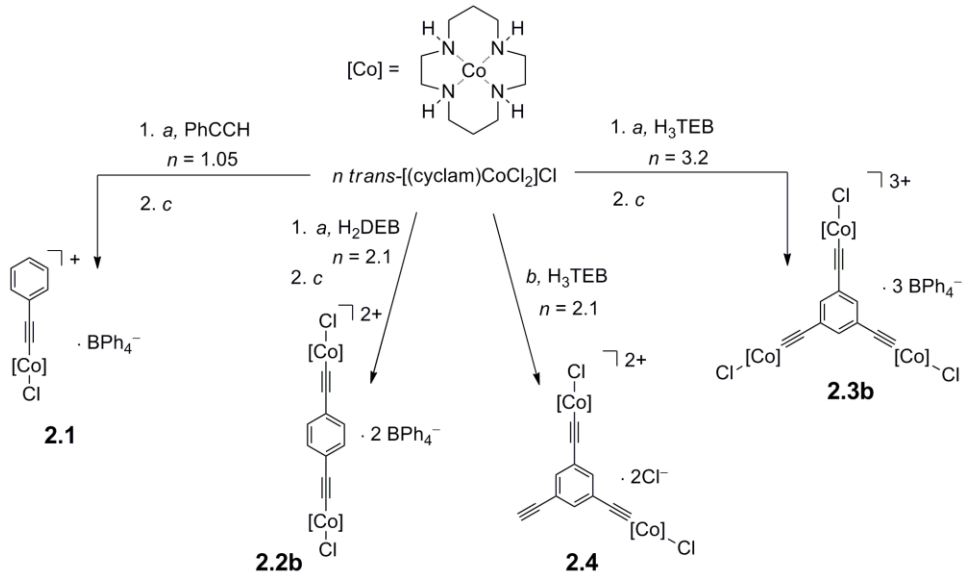

Scheme 2.1. Synthetic conditions used for the preparation of Co^{3+} acetylide complexes **2.1**, **2.2b**, **2.3b**, and **2.4**. Reaction conditions: *a* = MeOH, excess Et_3N, reflux 24 hrs; *b* = MeOH, 4 eq. Et_3N per Co^{3+}, reflux 24 hrs; *c* = excess $NaBPh_4$, MeOH

owing to the similar solubility properties of the acetylide complexes, surplus [(cyclam)$CoCl_2$]Cl, and triethylammonium hydrochloride, which forms as the conjugate acid byproduct of dehydrohalogenation. Although recrystallization of the chloride salts could be used to obtain a few X-ray quality crystals, crystalline samples subjected to combustion analysis were not acceptably pure. Occasionally, crops of crystals of **2.4** contained a green material, indicating excess [(cyclam)$CoCl_2$]Cl. In order to impart differential solubility between the product and impurities, tetraphenylborate anion metathesis was performed, allowing for workup to be performed in less polar solvents like tetrahydrofuran. Slow diffusion of diethyl ether vapor into THF solutions of the tetraphenylborate salts produced crystalline samples that were found to be analytically pure.

The increased solubility of the tetraphenylborate salts in nonpolar solvents like tetrahydrofuran allows for the application of different ligand substitution methods beyond dehydrohalogenation. A common way to exchange halide ligands for acetylides proceeds through alkali metal acetylide ligands,[5a] which are only stable in ethereal solvents. The synthesis of **2.5** was achieved by combining a slight excess of lithium phenylacetylide with **2.1** in THF (Scheme 2.2). The product was isolated from the lithium chloride by-product by recrystallization. The isolation of **2.5** is the first known example of stepwise acetylide ligand substitution in a Co^{III} system. In a related case, Field demonstrated differential reactivity at a low-spin Fe^{II} center by using sequential dehydrohalogenation and photochemical reactions starting with [$(dmpe)_2FeCl(CH_3)$] (dmpe = 1,2-bis(dimethylphosphino)ethane).

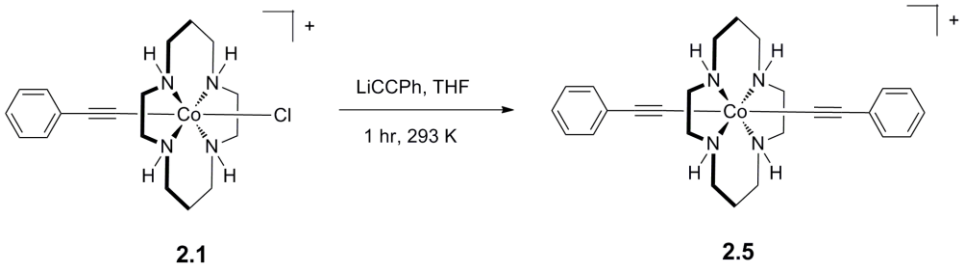

Scheme 2.2 Synthesis of bis-acetylide complex **2.5** from chloro acetylide complex **2.1**. The tetraphenylborate anion allows the complex in **2.1** to be soluble in tetrahydrofuran.

The synthesis of dinuclear **2.4** was achieved by mixing 2.1 equivalents of [(cyclam)$CoCl_2$]Cl with H_3TEB and 4 equivalents of triethylamine per Co in methanol solution. Unlike trinuclear **2.3a**, [(cyclam)$_2Co_2Cl_2$(HTEB)]Cl_2 is sparingly soluble in ethanol; rinsing the product in this solvent essentially removes all triethylammonuim hydrochloride and undesired mono- and tri-nuclear Co^{3+} acetylide species. Presumably, mono-, di- and trinuclear complexes are all formed during the reaction, but the reaction stoichiometry favors the formation of **2.4**. Analytically pure samples of **2.4** could not be obtained, presumably because of incomplete removal of [(cyclam)$CoCl_2$]Cl.

The wedge-like topology of **2.4** would appear to lend itself to schematic assembly of metallodendrimers when combined with one-third of an equivalent of trinuclear **2.3**. However, successful attempts to lithiate the acetylene moiety of a tetraphenylborate analogue of **2.4** were thwarted by the presence of the amine hydrogens on the cyclam ligands which appear to be more reactive toward *n*-BuLi than the acetylene hydrogen. Although a direct comparison of the pKa values for the relevant protons is not available, a measured amine pKa for [(cyclam)Co(CO_3)]$^+$ in H_2O (10.76) is significantly lower than that for phenylacetylene in dimethylsulfoxide (28.7).[18]

The IR spectra of **2.1**, **2.2b**, and **2.3b** each contain a single absorbance between 2114 and 2133 cm^{-1} that corresponds to the stretching frequency of the acetylide ligand when coordinated to the Co^{3+} ion. In **2.4**, two separate absorbances should be visible due to the different acetylene environments; however a single broad peak at 2123 cm^{-1} masks the contribution from the non-bridging acetylene which absorbs at 2109 cm^{-1} for H_3TEB. However, IR evidence for the non-bridging acetylene in **2.4** is found in the sharp

acetylenic C-H stretch that is observed at 3313 cm^{-1}. For bis-acetylide **2.5**, the acetylide stretching frequency moves to lower energies and is found at 2100 cm^{-1}.

2.4.2 X-ray Crystal Structures of Co^{III} Acetylide Complexes. Crystals of **2.1** suitable for X-ray analysis were obtained by slow diffusion of diethyl ether vapor into a concentrated solution of **2.1** in tetrahydrofuran. The compound crystallizes in the $P2_1/c$ space group with two molecules in the unit cell. The coordination geometry about each Co^{3+} center is essentially octahedral with the equatorial positions occupied by the nitrogen atoms from the cyclam ligand (Figure 2.1). The chloride and acetylide ligands are apically coordinated with metal-ligand distances of *ca*. 2.3 and 1.9 Å, respectively (Table 2.2). Similar local coordination geometries are observed for the di- and tri-nuclear complexes **2.2a** and **2.3a** as for mononuclear **2.1** (Figure 2.1 and 2.2). Crystals of **2.4** were also grown from slow diffusion of diethyl ether into methanol, but the solution of the structure was hampered by large (>20%) R_{int} values at resolutions greater than 1.05 Å.

The structure of the mononuclear bis-acetylide complex **2.5** was also determined by X-ray crystallography (Figure 2.3). The coordination geometry of the Co^{3+} center is similar to the chloro-acetylide complex **2.1** with the exception of the second phenylacetylide ligand in place of the chloride. Only minor differences in bond lengths and angles are observed among the series of chloro-acetylide complexes (Table 2.2). When compared to the X-ray structure of $[Co(cyclam)Cl_2]Cl$,[19] the Co–Cl bond in **2.1**-**2.5** is slightly elongated, which is likely due to the trans influence of the acetylide ligand. Substitution of the second chloride ligand for another acetylide in **2.5** causes a significant elongation in the Co–C bond length compared to **2.1**, along with a concomitant

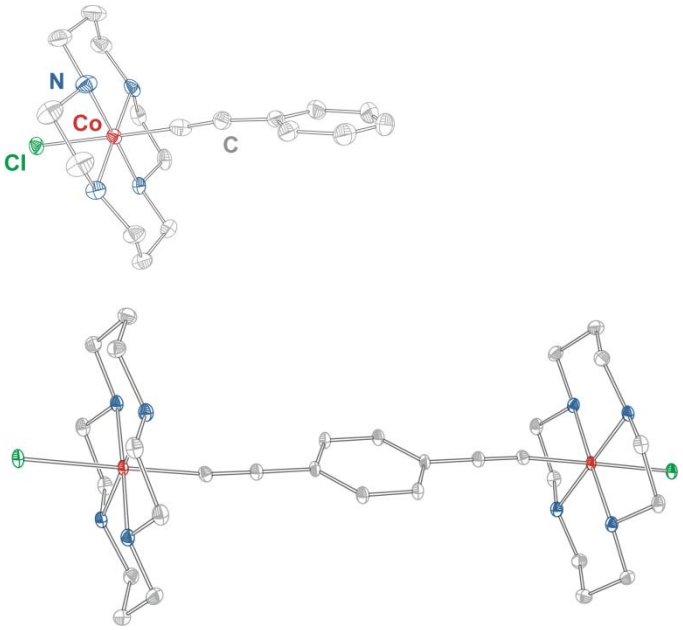

Figure 2.1. X-ray structures of the complex cations in the structures of **2.1** (top), and **2.2a**·2 MeOH (bottom) with thermal ellipsoids rendered at 40% probability. Hydrogen atoms have been omitted for clarity. The complex in **2.2a**·2 MeOH resides on an inversion center. Red, blue green, and gray ellipsoids represent cobalt, nitrogen, chloride, and carbon atoms, respectively.

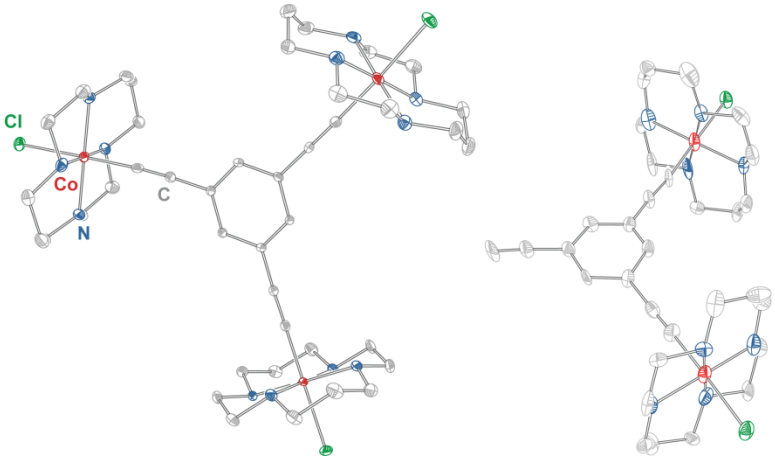

Figure 2.2. X-ray structures of the complex cations in the structures of **2.3a**·5 MeOH (left), and **2.4**·1.8MeOH (right) with thermal ellipsoids rendered at 40% probability. Hydrogen atoms have been omitted for clarity. The complex in **2.4**·1.8 MeOH resides on a two-fold rotation axis.

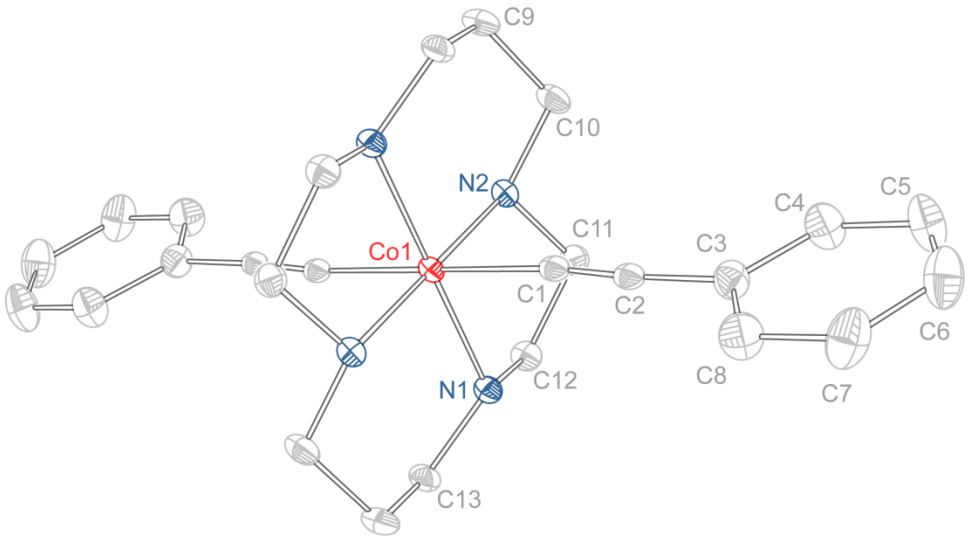

Figure 2.3. X-ray structure of the complex cation in the structure of **2.5**·2THF with thermal ellipsoids rendered at 40% probability. Hydrogen atoms have been omitted for clarity. The complex resides on an inversion center and unique atoms are labeled.

Table 2.2. Selected measured interatomic distances (Å) and angles (deg) for the structures of [(cyclam)$CoCl_2$]Cl,[19] [(cyclam)$CoCl(C_2Ph)$]BPh_4 (**2.1**), [(cyclam)$_2Co_2Cl_2$(μ-*p*-DEB)]Cl_2·2MeOH (**2.2a**·2MeOH), [(cyclam)$_3Co_3Cl_3$-(TEB)]Cl_3·5MeOH (**2.3a**·5MeOH), [(cyclam)$_2Co_2Cl_2$(HTEB)]Cl_2·1.8MeOH (**2.4**·1.8MeOH), and [(cyclam)Co$(C_2Ph)_2$]BPh_4·2THF (**2.5**·2THF).

	[Co(cyclam)Cl_2]Cl[19]	**2.1**[a]	**2.2a**·2 MeOH	**2.3a**·5 MeOH	**2.4**·1.8 MeOH	**2.5**·2 THF[a]
Co–N	1.974[4][b]	1.975[2]	1.979[7]	1.979[6]	1.973[6]	1.983[2]
Co–Cl	2.253[3]	2.3089[5]	2.3123(4)	2.320[5]	2.310[2]	--
Co–C	--	1.898[2]	1.885(2)	1.881[4]	1.868[5]	2.001[3]
C≡C	--	1.160[3]	1.210(2)	1.193[5]	1.184[7]	1.113[4]
C≡CH	--	--	--	--	1.16(1)	--
Co–C≡C	--	174.5[5]	173.4(1)	174.7[3]	174.5[6]	175.5[2]
C–Co–Cl	--	179.0[3]	179.17(5)	178.6[1]	178.6[2]	--

[a] These structures each have two complex residues in the asymmetric unit; bond lengths and angles are averaged from both residues. [b] Square brackets[ ] represent esds for averaged metric parameters.

contraction in the carbon-carbon triple bond. Here, a decrease in the Co–C bonding interaction would be expected to lead to a reduction in M–L π-backbonding, thereby giving a shorter C–C bond.[20]

2.4.3 Cyclic Voltammetry. Although the Co^{3+} complexes serve as structural analogues for paramagnetic dendritic building blocks to be studied in future work, we wished to examine their electrochemical behavior in order to probe the possibility of reducing the Co^{3+} salts to neutral, paramagnetic Co^{2+} complexes. There are several reported examples of Co^{2+}-based single molecule magnets,[21] and we wanted to see if interesting properties would be displayed in the reduced complexes.

In acetonitrile solution, crystals of trinuclear **2.3a** display an irreversible reduction during an initial cathodic scan at –1.52 V. During subsequent scans, a quasi-reversible wave grows in at $E_{1/2}$ = –0.74 V while the wave at –1.52 is diminished (Figure 2.4). We note that a small amount of this wave is detectable even in the first scan. This redox behavior is consistent with a three electron reduction of tri-nuclear **2.3a** at highly negative potentials, followed by dissociation of the (cyclam)$CoCl^{+}$ units from the TEB^{3-} ligand. Increased lability of Co^{2+} ions relative to Co^{3+} is the probable reason for this dissociation. In acetonitrile, the resulting vacant coordination site at the Co^{2+} center is likely occupied by a solvent molecule. This monomeric complex can then be reversibly oxidized, accounting for the quasi-reversible wave at –0.74 V. Supporting this proposed electrochemical reaction, a cyclic voltammogram of [(cyclam)$CoCl_2$]Cl in acetonitrile exhibits a single reversible Co^{3+}/Co^{2+} redox couple at –0.73 V. To investigate whether a less coordinating solvent would prevent ligand dissociation upon reduction, cyclic voltammograms of **2.1** and **2.2b** in tetrahydrofuran were also recorded. However,

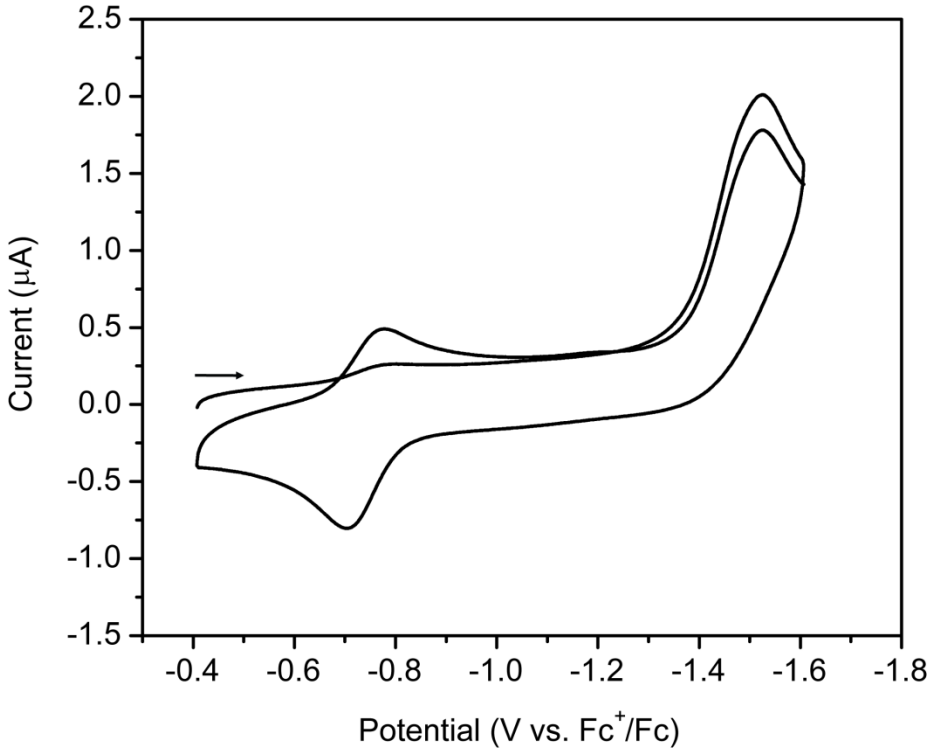

Figure 2.4. Cyclic voltammogram for **2.3a** in acetonitrile. See text for an explanation of the redox behavior.

irreversible reduction peaks were also observed for these salts. The bis-acetylide complex **2.5** also exhibits non-reversible reduction behavior, indicating that replacing a good leaving group (chloride) with phenylacetylide does not allow for reversible reduction behavior.

To our knowledge, there are no electrochemically characterized cobalt acetylide complexes in the literature. The most relevant comparison to be found in the literature is represented by Bianchini and co-workers' study of the redox behavior of trigonal bipyramidal Rh(I) complexes with a $(P)_3(N)(\sigma\text{-}C_2R)$ first coordination sphere.[22] Starting with the Rh^I congener, electrochemical measurements indicate that the one- and two-electron oxidized complexes are electrochemically accessible, but the Rh^{III} complex could only be observed with fast electrochemical scan rates. Obviously, similar behavior is not observed for the Co acetylide complexes presented herein. Better acetylide- and phosphine-metal ligand overlap for the lower coordination number, second-row rhodium complexes relative to the octahedral cobalt species in addition to the kinetic inertness of second row ions are probable reasons for the differences in stability, so the lack of reversible behavior for **2.1-2.5** comes as no surprise.

2.5 Conclusions and Outlook

The syntheses and structural characterizations of mono-, di-, and tri-nuclear Co^{III}(cyclam) complexes that bear a mixture of ethynylbenzene and chloride ligands at the axial coordination sites has been described. The product nuclearity is dependent on reaction stoichiometry; isolation of **2.4** illustrates that partially substituted products can be obtained by tuning the amount of metal precursor complex and organic base.

Furthermore, the feasibility of stepwise ligand substitution has been demonstrated by using lithium phenylacetylide to react with **2.1** in tetrahydrofuran.

Cyclic voltammograms of all complexes in either acetonitrile or tetrahydrofuran demonstrate that isolation of the paramagnetic Co^{II} analogues is impeded by a secondary reaction (rapid ligand exchange) upon reduction. The electrochemical data is consistent with the Co-acetylide bond breaking at negative potentials and that the appearance of a subsequent reversible redox couple is due to a monomeric $Co^{III/II}$ species. Attempts to prepare larger complexes by combining a lithiated analogue of **2.4** and **2.3** were not successful. This is likely due to the presence of amine hydrogen atoms in all complexes which seem to preferentially react with *n*-BuLi over acetylene hydrogen atoms. The use of protected equatorial ligands such as 1,2-dimethylphosphinoethane (dmpe) for future metallodendritic building blocks, which would prevent such undesirable side reactions, is being explored. Alternatively, replacement of the acetylene moiety in **2.4** with a trialkyltin substituent should allow for the formation of a first-generation dendrimer when combined with **2.4** under CuI-catalyzed conditions.[12] The feasibility of this synthetic route is currently being investigated.

2.6 Acknowledgements

This research was supported by Colorado State University and the ACS Petroleum Research Fund (44691-G3). We thank Dr. Md. K. Kabir and Ms. Sara Mosley for the initial syntheses and characterizations of **2.2a** and **2.1**, respectively. We also thank Prof. C. M. Elliott for assistance with the cyclic voltammetry measurements and interpretations.

2.7 References and Notes

1. (a) Lehn, J.-M., *Supramolecular Chemistry*. VCH Publishers: Weinheim, 1995; (b) Nelson, K. J.; DiPasquale, A. G.; Rheingold, A. L.; Daniels, M. C.; Miller, J. S., *Inorg. Chem.* **2008,** *47*, 7768-7774; (c) Angaridis, P.; Berry, J. F.; Cotton, F. A.; Murillo, C. A.; Wang, X., *J. Am. Chem. Soc.* **2003,** *125*, 10327-10334.

2. (a) Lee, S. C.; Holm, R. H., *Chem. Rev.* **2003,** *104*, 1135-1158; (b) Müller, A.; Peters, F.; Pope, M. T.; Gatteschi, D., *Chem. Rev.* **1998,** *98*, 239-272.

3. (a) Cañada-Vilalta, C.; O'Brien, T. A.; Brechin, E. K.; Pink, M.; Davidson, E. R.; Christou, G., *Inorg. Chem.* **2004,** *43*, 5505-5521; (b) Stamatatos, T. C.; Christou, A. G.; Mukherjee, S.; Poole, K. M.; Lampropoulos, C.; Abboud, K. A.; O'Brien, T. A.; Christou, G., *Inorg. Chem.* **2008,** *47*, 9021-9034.

4. (a) Beltran, L. M. C.; Long, J. R., *Acc. Chem. Res.* **2005,** *38*, 325-334; (b) Ni, Z. H.; Kou, H. Z.; Zhang, L. F.; Ge, C. H.; Cui, A. L.; Wang, R. J.; Li, Y. D.; Sato, O., *Angew. Chem. Int. Ed.* **2005,** *44*, 7742-7745.

5. (a) Long, N.; Williams, C. K., *Angew. Chem. Int. Ed.* **2003,** *42*, 2586-2617; (b) Onitsuka, K.; Takahashi, S., *Top. Curr. Chem* **2003,** *228*, 39-63.

6. Weyland, T.; Ledoux, I.; Brasselet, S.; Zyss, J.; Lapinte, C., *Organometallics* **2000,** *19*, 5235-5237.

7. Paul, F. d. r.; Bondon, A.; da Costa, G. g.; Malvolti, F.; Sinbandhit, S.; Cador, O.; Costuas, K.; Toupet, L.; Boillot, M.-L., *Inorg. Chem.* **2009,** *48*, 10608-10624.

8. Onitsuka, K.; Fujimoto, M.; Ohshiro, N.; Takahashi, S., *Angew. Chem. Int. Ed.* **1999,** *38*, 689-692.

9. Weyland, T.; Costuas, K.; Mari, A.; Halet, J.-F.; Lapinte, C., *Organometallics* **1998,** *17*, 5569-5579.

10. Oshio, H.; Nakano, M., *Chem. Eur. J.* **2005,** *11*, 5178-5185.

11. Giese, B.; Zehnder, M.; Neuburger, M.; Trach, F., *J. Organomet. Chem.* **1991,** *412*, 415-423.

12. Khan, M. S.; Pasha, N. A.; Kakkar, A. K.; Raithby, P. R.; Lewis, J.; Fuhrmann, K.; Friend, R. H., *J. Mater. Chem.* **1992,** *2*, 759-760.

13. Bosnich, B.; Poon, C. K.; Tobe, M. L., *Inorg. Chem.* **1965,** *4*, 1102-1108.

14. Weber, E.; Hecker, M.; Koepp, E.; Orlia, W.; Czugler, M.; Csöregh, I., *J. Chem. Soc., Perkin Trans. 2* **1988**, 1251 - 1257.

15. *APEX 2*, Bruker Analytical X-Ray Systems, Inc.: Madison, WI, 2008.

16. Sheldrick, G. M. *SHELXTL*, Bruker AXS: Madison, WI, 2004.

17. Weyland, T.; Lapinte, C.; Frapper, G.; Calhorda, M. J.; Halet, J.-F.; Toupet, L., *Organometallics* **1997,** *16*, 2024-2031.

18. (a) Dasgupta, T. P., *Inorg. Chim. Acta* **1976,** *20*, 33-36; (b) Bordwell, F. G., *Acc. Chem. Res.* **1988,** *21*, 456-463.

19. Ivanikova, R.; Svoboda, I.; Fuess, H.; Maslejova, A., *Acta Crystallogr. Sect E.* **2006,** *62*, m1553-m1554.

20. (a) Wong, C.-Y.; Che, C.-M.; Chan, M. C. W.; Han, J.; Leung, K.-H.; Phillips, D. L.; Wong, K.-Y.; Zhu, N., *J. Am. Chem. Soc.* **2005,** *127*, 13997-14007; (b) Wong, W. Y.; Ho, C. L., *Coord. Chem. Rev.* **2006,** *250*, 2627-2690.

21. (a) Galloway, K. W.; Whyte, A. M.; Wernsdorfer, W.; Sanchez-Benitez, J.; Kamenev, K. V.; Parkin, A.; Peacock, R. D.; Murrie, M., *Inorg. Chem.* **2008,** *47*, 7438-7442; (b) Wu, D.; Guo, D.; Song, Y.; Huang, W.; Duan, C.; Meng, Q.; Sato, O., *Inorg. Chem.* **2009,** *48*, 854-860; (c) Yoshihara, D.; Karasawa, S.; Koga, N., *J. Am. Chem. Soc.* **2008,** *130*, 10460-10461.

22. Bianchini, C.; Meli, A.; Peruzzini, M.; Vacca, A.; Laschi, F.; Zanello, P.; Ottaviani, F. M., *Organometallics* **1990,** *9*, 360-371.

Chapter 3. Geometry Influence on Magnetic Exchange Coupling in Fe(III) Ethynylbenzene Dendritic Building Blocks

3.1 Introduction

Searching for increased processor speeds, larger data storage densities and improved material and energy efficiencies, recent efforts involving molecule-based materials have focused on the synthesis and characterization of molecular species where charge and/or spin can be controlled. Using carbon-rich ligands as bridges for metal-ion species is promising in that they are tunable by well-established synthetic organic methods, and often display good orbital and energetic overlap with the nodes. Relevant to technological applications are poly-yne ligands bridging redox-active metal centers: they have been shown to be exceptional conduits for electricity at the nanoscale, and this discovery in turn has energized the relatively new field of molecular electronics.[1]

Enhancing intramolecular communication is also vital to the development of nanoscale magnets. Research in single-molecule magnet (SMM) clusters has progressed from the discovery of slow magnetic relaxation in a $Mn_{12}O_{12}$ molecule[2] to the isolation of hundreds of other molecular species that show similar properties.[3] The origin of this phenomenon is rooted in the combined presence of a well-isolated, high-spin ground state (*S*) and a negative molecular easy-axis magnetic anisotropy (*D*). In order to avoid populating low-spin excited states, the magnetic exchange constants (*J*) should be as large as possible. In this regard, using rigid, highly conjugated bridging ligands can

engender robust ferro- and antiferromagnetic coupling over long distances owing to tailor-made orbital communication pathways.[4]

While strong intramolecular communication has been predicted and measured for di- and trinuclear organometallic complexes, the synthetic tools needed to generate high spin states in compounds with bridging organometallic ligands are still being developed. Since high spin behavior is a prerequisite for SMM behavior, this is a research area in need of attention. We note that SMM behavior was recently observed for the first time in an organometallic Dy^{III}_2 species, but to our knowledge no SMMs are known where magnetic communication occurs through an all-carbon linkage.[5] Nevertheless, aryl alkynyl ligands based on 1,3,5-triethynylbenzene (H_3TEB) avail themselves as apt candidates with regard to generating high-spin ground state and negative zero-field splitting parameters.[6] Ethynylbenzene ligands like TEB^{3-} have been employed as bridging ligands in second- and third-row transition metal-containing dendrimers because of their rigidity and amenability for regular spatial arrangement of many diamagnetic transition metals around the C_6H_3 core.[7] Relevant to the incorporation of first-row transition metals into TEB-based dendrimers, Field and others have prepared Fe^{II} and Fe^{III} σ-acetylide complexes with a (P_4)(σ-C)(Cl) first coordination sphere and have studied their electrochemical and intervalence charge transfer properties.[8,9,10] Since these types of species contain the necessary coordination geometry for stepwise ligand substitution, an examination of the magnetic properties for the individual "building blocks" is needed so that the properties of larger assemblies can be more easily understood.

Although some paramagnetic ethynylbenzene-bridged complexes are known, the coordination environments of the metal ions are not suitable for incorporation into larger

assemblies. Nonetheless, these ligands have been demonstrated to permit significant spin communication between transition metal centers, although the strength of coupling appears to be dependent on subtle factors. Lapinte and co-workers have synthesized an impressive array of paramagnetic [(η_5-C_5Me_5)(dppe)Fe^{III}]-containing complexes with various acetylide connecting ligands in order to study their magnetic and charge transfer properties.[11] The temperature-dependent magnetic susceptibility for [$(dppe)_3(Cp^*)_3Fe^{III}_3(TEB)](PF_6)_3$ (dppe = 1,2-bis(diphenylphosphino)ethane) was analyzed using Bleaney-Bowers formalism to extract magnetic coupling constants of 9.6 cm^{-1} and 4.4 cm^{-1} owing to the putative isosceles triangle topology of the molecule.[11b] The strength of ferromagnetic coupling was also evaluated for [$(dppe)_2(Cp^*)_2Fe^{III}_2$(*m*-DEB)]$(PF_6)_2$, and the coupling constant was found to be 65 cm^{-1}, which is significantly higher than that found in the tri-nuclear complex. More recently, Paul and coworkers re-investigated the magnetic behavior for [$(dppe)_2(Cp^*)_2Fe^{III}_2$(*m*-DEB)]$(PF_6)_2$, and found that the triplet ground state was fully populated at 300 K, implying a ferromagnetic exchange strength of at least 150 cm^{-1}.[12] Differences in magnetic exchange coupling values have been attributed to impurities,[11a, 13] varying coordination geometries and relative orientations of spin-containing orbitals.[14] Berben has also studied the ability of *m*-DEB to mediate ferromagnetic exchange: the fit of the magnetic susceptibility of *trans,trans*-[$(dmpe)_4Fe_2Cl_2$(*m*-DEB)]$(PF_6)_2$ is consistent with a coupling constant of 41 cm^{-1}, a value that is in line with Lapinte's earliest report.[15] All of these results suggest that the robust magnetic coupling imparted by alkynylbenzene bridging ligands should give rise to high-spin molecules with anisotropic low-dimensional shapes, provided that

paramagnetic dendritic "building blocks" containing substitutionally labile axial ligands can be prepared.

Given the variance found in the magnetic and theoretical treatments applied to a relatively small number of ethynylbenzene-bridged complexes, a systematic study of the factors involved in magnetic exchange is warranted. Herein, we present the syntheses, magnetic characterizations, and computational investigations of a family of di- and tri-nuclear complexes containing $[(dmpe)_2Fe^{III}Cl]$ units connected by DEB^{2-} and TEB^{3-} bridging ligands. We compare magnetic data of the new complexes with the previously reported structurally similar species, and place all the complexes in the same computational framework so that subtle differences in complex geometries can be related to the observed magnetic properties.

3.2 Division of Labor

Syntheses and characterizations of all compounds were performed by Wesley Hoffert. Prof. Anthony Rappé carried out all DFT calculations and created the plots presented in Figure 3.16.

3.3 Experimental Section

3.3.1 Preparation of Compounds. Manipulations were performed inside a dinitrogen-filled glovebox (MBRAUN Labmaster 130). Pentane was distilled over sodium metal and subjected to three freeze-pump-thaw cycles prior to use. Other solvents were sparged with dinitrogen, passed over alumina, and degassed prior to use. The preparations of $[(dmpe)_4Fe_2Cl_2(\mu\text{-}p\text{-}DEB)]$ (dmpe = 1,2-bis(dimethylphosphino)ethane, $p\text{-}H_2DEB$ = 1,4-diethynylbenzene),[8b] $[(dmpe)_2FeCl(C_2Ph)]$,[8b] $[(dmpe)_2FeCl(C_2SiMe_3)](PF_6)$,[15] $[(dmpe)_4Fe_2Cl_2(\mu\text{-}m\text{-}DEB)]$,[15] $[(dmpe)_2FeCl_2]$,[16] $[Cp_2Fe]BAr^F{}_4$ ($BAr^F{}_4$ = tetrakis-

[(3,5-trifluoromethyl)phenyl]borate),[17] $[Cp_2Fe]PF_6$,[18] $[Cp^*_2Fe]PF_6$,[18] and H_3TEB[19] have been described elsewhere. All other reagents were purchased commercially and were used without further purification.

***trans*-[(dmpe)$_2$FeCl(C$_2$Ph)](OTf) (3.1).** A solution of AgOTf (33.4 mg, 0.130 mmol) in 5 mL of acetonitrile was added to a solution of $[(dmpe)_2FeCl(C_2Ph)]$ (61.1 mg, 0.124 mmol) in 5 mL of dichloromethane. The solution color immediately turned dark blue-green. After stirring for 1 hour, the solution was filtered and the filtrate was dried *in vacuo*. The resulting solid was recrystallized by slow diffusion of diethyl ether vapor into a concentrated solution of the crude product in dichloromethane. After 1 day, large dark blue-green crystals were isolated by filtration, washed with diethyl ether (3 × 5 mL) and dried under vacuum for 1 hr at 293 K to afford 65 mg of product (0.101 mmol, 82%). IR (mineral oil mull) $\nu_{C\equiv C}$ 2031 cm^{-1}. ^1H NMR (CD_2Cl_2) δ –27.85 (br, 2H, *m*-Ar–*H*), –20.35 (br, 16H, –PC*H*$_3$, –PC*H*$_2$), –23.74 (br, 12H, –PC*H*$_3$), –24.38 (br, 4H, –PC*H*$_2$), –27.32 (br, 2H, *o*-Ar–*H*), –28.06 (br, 1H, *p*-Ar–*H*). ES^+-MS (CH_2Cl_2): *m/z* 492 ([**3.1**–OTf]$^+$). Absorption spectrum (CH_2Cl_2): λ_{max} (ε_M) 361 (sh, 4930), 411 (1240), 544 (sh, 800), 606 (3290), 732 (9490 $M^{-1}\cdot cm^{-1}$). Anal. Calcd. for $C_{21}H_{37}ClF_3FeO_3P_4S$: C, 39.30; H, 5.81. Found: C, 39.30; H, 5.68.

[(dmpe)$_4$Fe$_2$Cl$_2$(μ-*p*-DEB)](BAr$^F_4$)$_2$ (3.2). A solution of $[Cp_2Fe]BAr^F_4$ (107 mg, 0.102 mmol) in 5 mL of dichloromethane was added to a solution of $[Cl_2(dmpe)_4Fe_2(\mu\text{-}p\text{-}DEB)]$ (46 mg, 0.051 mmol) in 5 mL of dichloromethane. The solution color immediately turned dark green. After stirring for 10 min, the solvent was removed *in vacuo*. Pentane (5 mL) was added to precipitate a green solid. The solid was isolated by filtration, washed with pentane (3 × 5 mL) to remove residual $[Cp_2Fe]$, and was recrystallized by

slow diffusion of pentane vapor into a concentrated solution of the crude product in dichloromethane. After 1 day, dark green crystals were isolated by filtration, washed with pentane (3 × 3 mL), and dried under vacuum for 1 hour at 293 K to afford 109 mg of product (0.041 mmol, 81%). Crystals suitable for X-ray analysis were obtained by allowing a solution of **3.2** in a 3:1 (v/v) mixture of pentane:dichloromethane to stand in a –40˚C freezer for 3 days. IR (mineral oil mull): ν_{CC} 2017 cm^{-1}. ^{1}H NMR (CD_2Cl_2): δ 7.49 (br, 16H, BAr–*H*), 7.44 (br, 8H, BAr–*H*), –1.22 (br, 4H, Ar-*H*), –14.99 (br, 24H, –PCH_3), –15.22 (br, 8H, –PCH_2), –18.11 (br, 32H, –PCH_2, –PCH_3). Absorption spectrum (CH_2Cl_2): λ_{max} (ε_M) 403 (10278), 475 (8442), 606 (4624), 747 (23210), 837 (15184 $M^{-1}\cdot cm^{-1}$). Anal. Calcd. for $C_{98}H_{92}B_2Cl_2F_{48}P_8Fe_2$: C, 44.69; H, 3.52. Found: C, 44.47; H, 3.55.

[(dmpe)$_6$Fe$_3$Cl$_3$(μ_3-TEB)] (3.3). Freshly distilled triethylamine (0.2 mL, 1.43 mmol) was added to a solution of [(dmpe)$_2$FeCl$_2$] (117 mg, 0.274 mmol) and freshly sublimed H_3TEB (13.7 mg, 0.0913 mmol) in methanol (12 mL). The solution color immediately turned orange. After 1 hour, an orange solid precipitated, which was isolated by filtration, washed with methanol (3 × 3 mL) and pentane (3 × 3 mL) then dried *in vacuo* for 1 hour at 293 K to afford 52 mg of product (0.039 mmol, 43% based on H_3TEB). IR (mineral oil mull): ν_{CC} 2035 cm^{-1}. ^{1}H NMR (C_6D_6): δ 6.50 (s, 3H, Ar–*H*), 1.60 (br, 24H, –PCH_2), 1.39 (br, 72H, –PCH_3). ^{31}P NMR (C_6D_6): δ 66.33 (s, 12P, Fe–*P*). ^{13}C NMR (C_6D_6): δ 130.26 (s, 3C, C_{Ar}H), 127.21 (s, 3C, C_{Ar}C≡C), 120.84 (s, 3C, C≡*C*–Fe), 84.82 (d, 3C, *C*≡C–Fe), 30.64 (p, 12C, *C*H_2), 16.02 (s, 12C, *C*H_3), 13.76 (s, 12C, *C*H_3). ES^+-MS (DCM): *m/z* 1320.00 ([**3.3**]$^+$). Absorption spectrum (CH_2Cl_2): λ_{max} (ε_M) 248 (122500),

363 (77500) 466 nm (1800 $M^{-1}\cdot cm^{-1}$). Anal. Calcd. for $C_{48}H_{99}Cl_3P_{12}Fe_3$: C, 43.61; H, 7.55. Found: C, 43.34; H, 7.29.

$[(dmpe)_6Fe_3Cl_3(\mu_3\text{-TEB})](OTf)_3$ (3.4). To an orange slurry of **3.3** (30 mg, 0.023 mmol) in acetonitrile (10 mL) was added a solution of AgOTf (17.5 mg, 0.068 mmol) in acetonitrile (3 mL). The solution immediately turned blue-green. After stirring for 20 minutes, the mixture was filtered to remove silver metal and the solvent was removed from the filtrate *in vacuo*. The solid was stirred with diethyl ether (10 mL) for 30 minutes at 293 K. The blue-green solid was isolated by filtration and was recrystallized by slow diffusion of diethyl ether vapor into a concentrated solution of the crude product in dichloromethane. After 1 day, blue-green crystals were isolated by filtration, washed with diethyl ether (3 × 3 mL), and dried *in vacuo* for 1 hr at 293 K to afford 34 mg of product (0.019 mmol, 83%). IR (mineral oil mull) ν_{CC} 2035 cm^{-1}. ^1H NMR (CD_2Cl_2): δ 63.27 (br, 3H, Ar–*H*), –16.69 (br, 36H, –PCH_3), –18.07 (br, 12H, –PCH_2), –21.46 (br, 48H, –PCH_3, –PCH_2). ES^+-MS (MeCN): *m/z* 1617.80 ([**3.4**–OTf]$^+$), 735.57 ([**3.4**–2 OTf]$^{2+}$). Absorption spectrum (CH_2Cl_2): λ_{max} (ε_M) 301 (53600), 401 (sh, 4290), 544 (sh, 1720), 609 (8100), 732 nm (12940 $M^{-1}\cdot cm^{-1}$). Anal. Calcd. for $C_{51}H_{99}Cl_3P_{12}F_9S_3O_9Fe_3$: C, 34.62; H, 5.64. Found: C, 34.58; H, 5.35.

$[(dmpe)_4Fe_2Cl_2(\mu\text{-}m\text{-DEB})](BAr^F{}_4)_2$ (3.5) A solution of $[Cp_2Fe]BAr^F{}_4$ (52.3 mg, 0.050 mmol) in 5 mL of dichloromethane was added to a solution of $[Cl_2(dmpe)_4Fe_2(\mu$-*m*-DEB)] (22.6 mg, 0.025 mmol) in 5 mL of dichloromethane. The solution color immediately turned dark teal. After stirring for 10 min, the solvent was removed *in vacuo*. Pentane (5 mL) was added to precipitate a green solid. The solid was isolated by filtration, washed with pentane (3 × 5 mL) to remove residual $[Cp_2Fe]$, and was

recrystallized by slow diffusion of pentane vapor into a concentrated solution of the crude product in dichloromethane. After 2 days, dark blue crystals were isolated by filtration, washed with pentane (3 × 3 mL), and dried under vacuum for 1 hour at 293 K to afford 53 mg of product (0.020 mmol, 80%). IR (ATR): ν_{CC} 2021 cm^{-1}. ^{1}H NMR (CD_2Cl_2): δ 46.85 (br s, 1H, Ar–*H*), 7.46 (s, 16H, BAr–*H*), 7.41 (s, 8H, BAr–*H*), –19.29 to –20.56 (br m, 32H, –PC*H*$_3$ and –PC*H*$_2$), –21.93 to –22.54 (br m, 8H, –PC*H*$_3$ and –PC*H*$_2$), –24.15 to –24.42 (br m, 24H, –PC*H*$_3$ and –PC*H*$_2$), –55.79 (br s, 1H, Ar–*H*), –57.35 (br s, 2H, Ar–*H*). Anal. Calcd. for $C_{98}H_{92}B_2Cl_2F_{48}P_8Fe_2$: C, 44.69; H, 3.52. Found: C, 44.93; H, 3.40.

3.3.2 X-ray Structure Determinations. Compounds **3.1**, **3.2**, **3.4** and **3.5** were characterized by single crystal X-ray analysis (Table 3.1). Crystals were coated in Paratone oil prior to removal from the glovebox, supported on Cryoloops, and mounted on a Bruker Kappa Apex 2 CCD diffractometer under a stream of cold dinitrogen. All data collections were performed with Mo Kα radiation and a graphite monochromator. Initial lattice parameters were determined from a minimum of 112 reflections harvested from 36 frames; these parameters were later refined against all data. Data sets were collected targeting complete coverage and four-fold redundancy. Data were integrated and corrected for absorption effects with the Apex 2 software package.[20] Structures were solved by direct methods and refined with the SHELXTL software package.[21] Displacement parameters for all non-hydrogen atoms were refined anisotropically with the exception of disordered carbon, phosphorus and fluorine atoms. Hydrogen atoms were added at the ideal positions and were refined using a riding model where the isotropic displacement parameters were set at 1.2 times those of the attached carbon atom

Table 3.1. Crystallographic data[a] for compounds $[(dmpe)_2FeCl(C_2Ph)](OTf)$ (**3.1**), $[(dmpe)_4Fe_2Cl_2(\mu\text{-}p\text{-}DEB)](BAr^F{}_4)_2$ (**3.2**), $[(dmpe)_6Fe_3Cl_3(\mu_3\text{-}TEB)](CF_3SO_3)_3$ (**3.4**), and $[(dmpe)_4Fe_2Cl_2(\mu\text{-}m\text{-}DEB)](BAr^F{}_4)_2$ (**3.5**).

	3.1	**3.2**	**3.4**	**3.5**
crystal code	msn142	msn171	msn232	msn259r
formula	$C_{21}H_{37}ClF_3FeP_8O_3F_3S$	$C_{98}H_{92}B_2Cl_2F_{48}Fe_2P_8$	$C_{50}H_{99}Cl_3F_6Fe_3O_6P_{12}S_2$	$C_{98}H_{92}B_2Cl_2F_{48}Fe_2P_8$
fw	641.75	2633.70	1619.97	2633.70
color, habit	blue prism	green block	blue prism	blue plate
T, K	100(2)	100(2)	120(2)	110(2)
space group	$P2_12_12_1$	$P\bar{1}$	*Pbcm*	$P\bar{1}$
Z	4	1	4	2
a, Å	12.8296(3)	13.4127(7)	15.5873(6)	13.6337(7)
b, Å	14.3749(4)	14.1127(7)	28.0448(12)	13.7837(7)
c, Å	15.8508(4)	17.5241(10)	21.4267(10)	35.560(2)
α, deg	90	66.8130(10)	90	91.684(4)
β, deg	90	67.9560(10)	90	98.743(4)
γ, deg	90	81.356(2)	90	103.264(3)
V, Å^3	2923.3(1)	2826.3(3)	9366.5(7)	6414.3(6)
d_{calc}, g/cm^3	1.458	1.547	1.149	1.364
GOF	1.008	1.049	1.031	2.062
$R_1{}^b$ (wR_2)^c, % ($I>2\sigma(I)$)	2.40 (5.40)	4.08 (10.46)	5.56 (18.34)	17.10 (47.88)

[a] Obtained with graphite-monochromated Mo Kα (λ = 0.71073 Å) radiation. [b] $R_1 = \Sigma||F_o| - |F_c||/ \Sigma|F_o|$. [c] $wR_2 = \{\Sigma[w(F_o^2 - F_c^2)^2/ \Sigma[w(F_o^2)^2]\}^{0.5}$.

(1.5 times for methyl carbons). After several attempts to model extreme anion/solvent disorder in the structures of **3.4** and **3.5** failed, the Platon SQUEEZE routine was applied.[22] For **3.4**, four 636 Å^3 voids were found; each contained 249 electrons. This electron count roughly corresponds to 6 dichloromethane molecules. For **3.5**, one 698 Å^3 (223 electrons) void and two 307 Å^3 voids were modeled by the SQUEEZE operation. These voids are each consistent with 5 and 3 dichloromethane molecules, respectively. The results presented for these compounds in Table 1 reflect solvent-free data. The high residuals in the structure solution of **3.5** may be the result of crystal twinning or absorption effects that have not been properly accounted for.

3.3.3 Magnetic Susceptibility Measurements. Magnetic susceptibility data were collected with a Quantum Design MPMS-XL SQUID magnetometer. In the glovebox, finely ground samples were loaded into gelatin capsules and inserted into straws. The straws were sealed in plastic bags prior to removal from the glovebox, and were quickly loaded into the instrument to minimize exposure to air. Data were corrected for the magnetization of the sample holder by subtracting the susceptibility of an empty container and for diamagnetic contributions of the sample by using Pascal's constants.[23] Theoretical fits to the susceptibility data for **3.2** and **3.5** were obtained using a relative error minimization routine (julX 1.4.1)[24] with a Hamiltonian of the form $\hat{H} = -2J\hat{S}_1 \cdot \hat{S}_2$. The best fits to the data for tri-nuclear **3.4** were obtained with MAGFIT 3.1[25] based on a three center isosceles spin Hamiltonian of the form $\hat{H} = -2J(\hat{S}_1 \cdot \hat{S}_3) - 2J(\hat{S}_2 \cdot \hat{S}_3) - 2J'(\hat{S}_1 \cdot \hat{S}_2)$. Fits of the magnetization data were obtained with the ANISOFIT[26] program and were based on the Hamiltonian $\hat{H} = D\hat{S}_z^2 + E(\hat{S}_x^2 + \hat{S}_y^2) + g_{iso}\beta\vec{S} \cdot \vec{B}$.

3.3.4 Other Physical Measurements. Electronic absorption spectra were obtained in air free cuvettes with a Hewlett-Packard 8453 spectrophotometer. UV-Vis-NIR spectra were recorded in air free cuvettes using a Cary 500 spectrophotometer. Infrared spectra were measured with a Nicolet 380 FT-IR spectrophotometer using either mineral oil mulls sandwiched between NaCl plates or a Smart Performer ZnSe ATR accessory. ^{1}H NMR spectra were recorded on a Varian INOVA instrument operating at 300 MHz. EPR spectra were obtained using a continuous wave X-band Bruker EMX 200U instrument outfitted with a liquid nitrogen cryostat. Compounds were dissolved in a 1:1 mixture of dichloromethane (DCM):1,2-dichloroethane (DCE) in order to form a glass at low temperature. Cyclic voltammetry experiments were done in 0.1 M solutions of $(Bu_4N)PF_6$ in dichloromethane. Voltammograms were recorded with a CH Instruments potentiostat (either model 1230A or 660C) using a 0.25 mm Pt disk working electrode, Ag/Ag^+ reference electrode, and a Pt mesh auxiliary electrode. All voltammograms shown were measured with a scan rate of 0.1 V/s. Reported potentials are referenced to the $[Cp_2Fe]^+/[Cp_2Fe]$ redox couple and were determined by adding ferrocene as an internal standard at the conclusion of each electrochemical experiment. Elemental analyses were performed by Robertson Microlit Laboratories in Madison, NJ.

3.3.5 Electronic Structure Calculations. The relative stability and character of the five d orbitals at each magnetic iron center can be assessed from a TD-DFT/NTO analysis of a mononuclear fragment ($[(dmpe)_2FeCl(C_2H)]^+$). Restricted and unrestricted B3LYP hybrid density functional studies[43] were carried out in the G03 suite of electronic structure codes.[44] The LANL2[45] basis sets and effective core potentials were used for Fe and P atoms; the 6-31g* basis was used for the remaining atoms.[46-49]

3.4 Results and Discussion

3.4.1 Syntheses and Characterizations. The preparations of di- and triethynylbenzene-bridged complexes are outlined in Scheme 3.1. The neutral (diferrous) form of complex **3.2**, $[(dmpe)_4Fe^{II}_2Cl_2(p\text{-DEB})]$, was previously described by Field and coworkers;[8b] the synthesis of the trinuclear complex **3.3** is adapted from that report. The hexafluorophosphate analogue of **3.5**, $[(dmpe)_4Fe^{II}_2Cl_2(p\text{-DEB})](PF_6)_2$, has been synthesized by Berben, and a similar synthetic procedure was adopted here. Related compounds with (Cp*)(dppe)Fe units coordinated to bridging ethynylbenzene ligands have also been reported by Lapinte.[11b,11f,27-28] For the preparation of the ferrous compounds, a slight stoichiometric excess of $[(dmpe)_2FeCl_2]$ undergoes solvolysis in methanol to generate $[(dmpe)_2Fe(MeOH)Cl]^+$, which interacts with the ethynylbenzene ligand, presumably forming a vinylidene complex. The vinylic proton is then captured by triethylamine to form the iron acetylide complex product, which precipitates cleanly from the reaction mixture. The purity of **3.3** was verified by combustion analysis, mass spectrometry, ^1H, ^{31}P, and ^{13}C NMR (Figures 3.1-3.3, respectively). The ^1H NMR spectrum contains a sharp resonance corresponding to the aromatic protons in addition to broad resonances from ethylene and methylene protons from the dmpe ligands. A single sharp resonance in the ^{31}P spectrum confirms the *trans* coordination geometry about each Fe(II) ion.

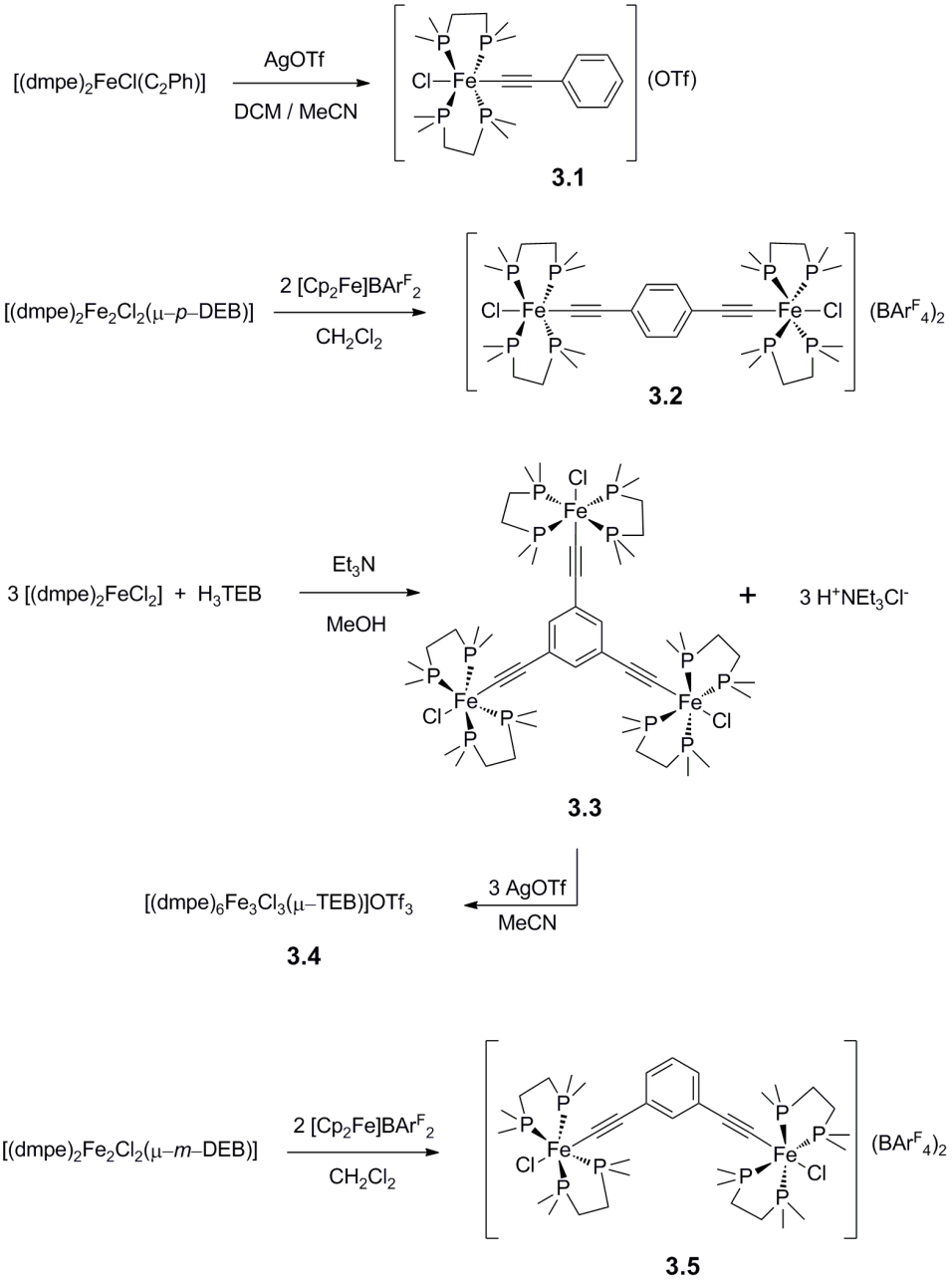

Scheme 3.1. Syntheses of ethynylbenzene complexes **3.1**–**3.5**.

Electrochemical (CV) studies carried out and/or compared to literature allowed the determination of the potentials required for oxidation to Fe(III) species as well as the characterization of the electronic coupling between iron ions. The previously reported electrochemical behavior of $[(dmpe)_4Fe^{II}_2Cl_2(\mu\text{-}p\text{-DEB})]$ showed two reversible one-electron redox waves centered at –0.69 V and –0.49 V vs Fc^+/Fc.[8b] These waves correspond to the formation of the mixed-valent $[Fe^{III}Fe^{II}]$ and diferric $[Fe^{III}Fe^{III}]$ complex cations in solution. Interestingly, the comproportionation constant is much larger in $[(dppe)_2(Cp^*)_2Fe_2(p\text{-DEB})]^{n+}$ ($K_{com} = 2.6 \times 10^4$)[28] than $[(dmpe)_4Cl_2Fe_2(p\text{-DEB})]^{n+}$ ($K_{com} = 2.4 \times 10^3$), indicating stronger Fe-Fe communication in the Cp*-ligated species. Based on the CV data, the BAr^F_4 salt **3.2** was prepared by mixing two equivalents of $[Cp_2Fe]PF_6$ with the neutral $[Fe^{II}_2]$ complex.

For the trinuclear complexes, Lapinte previously reported the isolation of mono- and di-ferric derivatives of $[(dppe)_3Fe_3(Cp^*)_3TEB)]^{n+}$ complexes, owing to the presence of three well-separated redox waves ($\Delta E_{1/2}$ = 0.130 V) for the neutral complex in dichloromethane solution.[27,8b] The *m*-phenylene bridges in **3.3** and **3.5** would be expected to engender weaker coupling than the *p*-phenlyene and Cp* variants,[27-28] due to a contribution of cumulenic/quinoidal character into the overall bonding structure for complexes with a *p*-DEB bridge.[12, 29] Indeed, the CV for **3.3** shows one broad redox wave centered at –0.59 V with a peak-to-peak separation of 186 mV (Figure 3.4). The appearance of shoulders at ca. –0.61 V and –0.64 V indicates that multiple processes occur on the electrochemical time scale, but the lack of resolution is consistent with weaker communication between metal centers. Utilizing the electrochemical data, the triferric complex **3.4** was synthesized by combining **3.3** with three equivalents of AgOTf

in acetonitrile. The purity of **3.4** was confirmed by microanalysis and ^{1}H NMR spectroscopy. The ^{1}H NMR spectrum contains broad, paramagnetically shifted peaks from aromatic, methylene, and ethylene protons, and resonances from **3.3** are not present in the ^{1}H NMR spectrum of **3.4** (Figure 3.5). The mononuclear ferric complex **3.1** was prepared in a similar fashion.

All compounds were characterized with FT-IR spectroscopy. The ethynylbenzene-bridged complexes exhibit a single $\nu_{C\equiv C}$ resonance at lower energies than the corresponding free acetylene ligands. The acetylide stretching frequency in **3.2** decreases to 2017 cm^{-1} compared to 2042 cm^{-1} in the neutral complex. Coincidentally, the stretching frequencies for redox-related **3.3** and **3.4** both occur at 2035 cm^{-1}.

3.4.2 X-ray Structures. The crystal structures of all complexes presented herein reveal pseudo-octahedral coordination geometries around each iron center (Figures 3.6 and 3.7). Equatorial positions are occupied by four phosphorus atoms from the bidentate dmpe ligands while the chloride and bridging acetylide-containing ligands are located at the axial positions. The acetylide ligands in the cations of all of the structures impart a rigid connectivity, leading to essentially linear C-C-Fe angles, where the greatest deviation from linearity is 2.8°. Other relevant bond distances and angles are comparable to related complexes in the literature.[8a, 11g, 28, 30]

For **3.4**, two of the Fe atoms (Fe2 and Fe2a) are related by a crystallographic two-fold rotation axis, and the ethylene carbon atoms of their bidentate dmpe ligands are essentially parallel to the plane of the aromatic bridging ligand. The torsion angle, φ, defined by P···P centroids, Fe ion, and two adjacent aromatic carbons, is 82.2° (see Figure

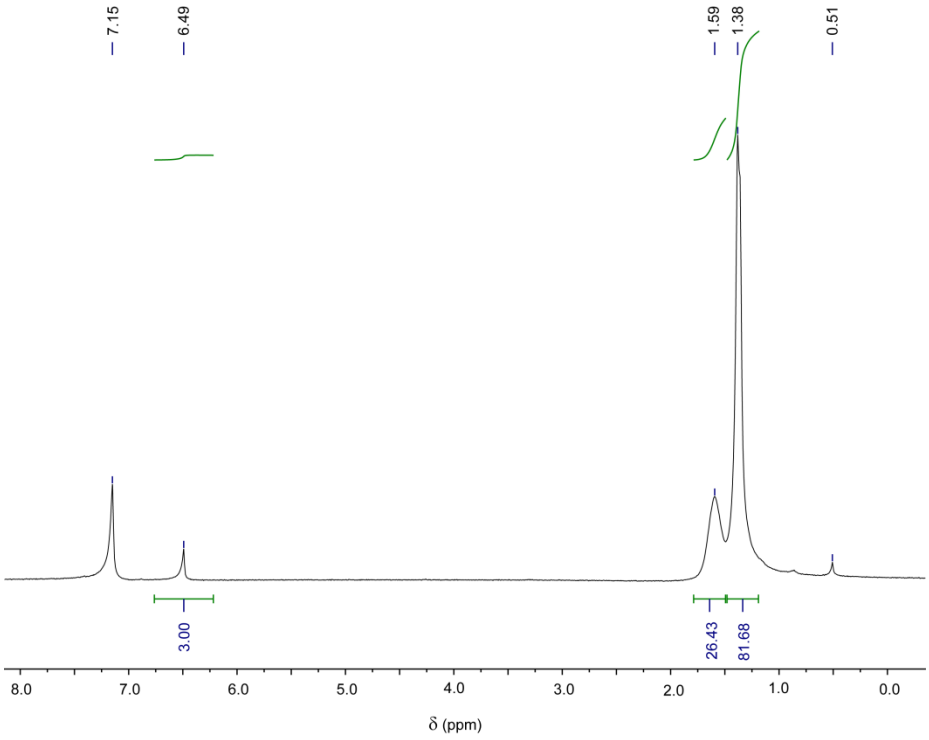

Figure 3.1. ^{1}H NMR spectrum of **3.3** in C_6D_6. The resonance at 0.51 ppm is due to trace methanol and the small resonance at *ca*. 0.85 is due to trace pentane.

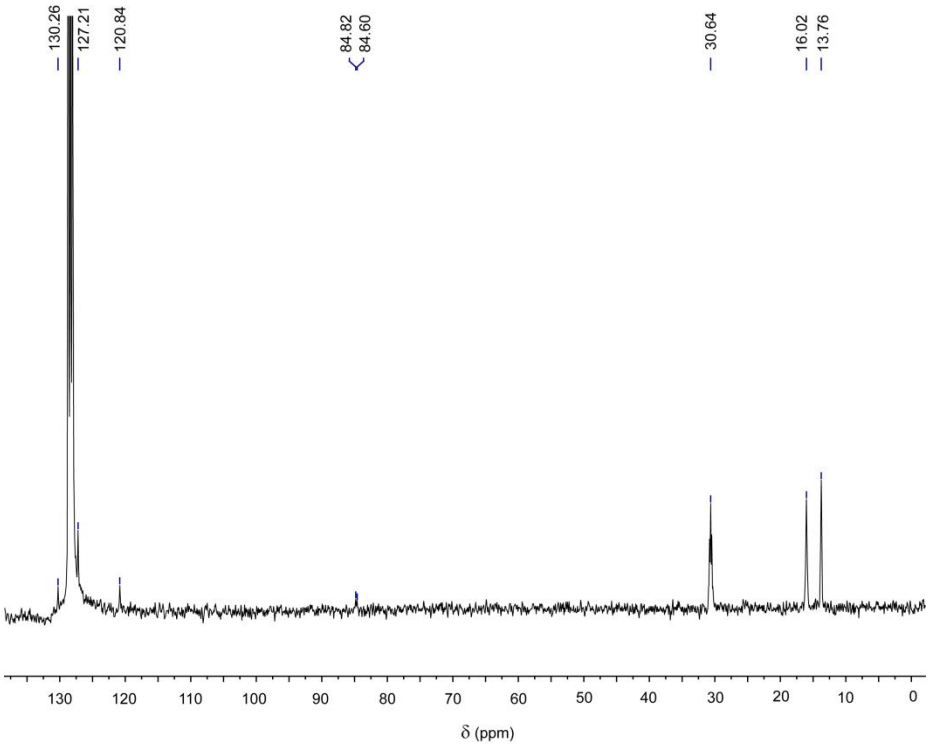

Figure 3.2. ^{13}C NMR spectrum of **3.3** in C_6D_6.

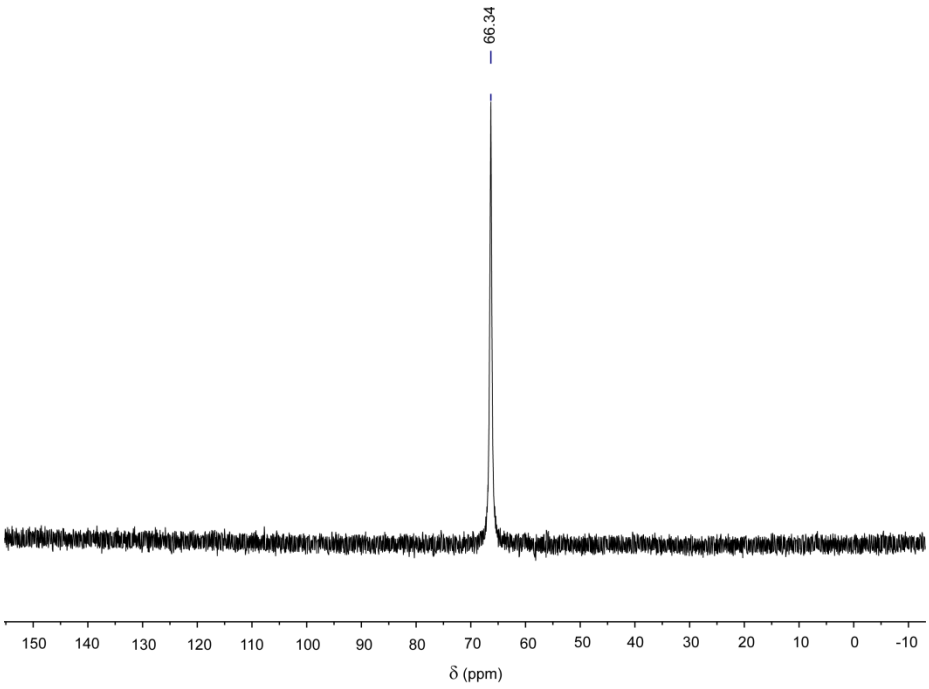

Figure 3.3. ^{31}P NMR spectrum of **3.3** in C_6D_6.

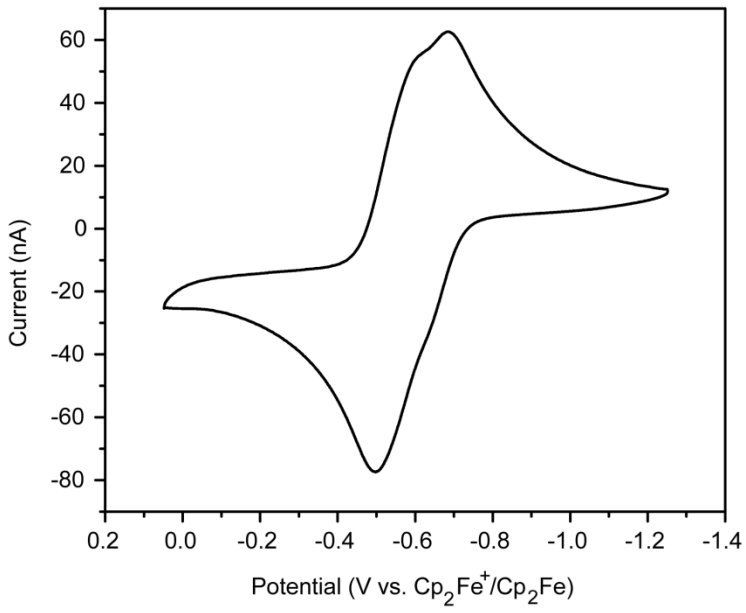

Figure 3.4. Cyclic voltammogram of **3.3** in dichloromethane.

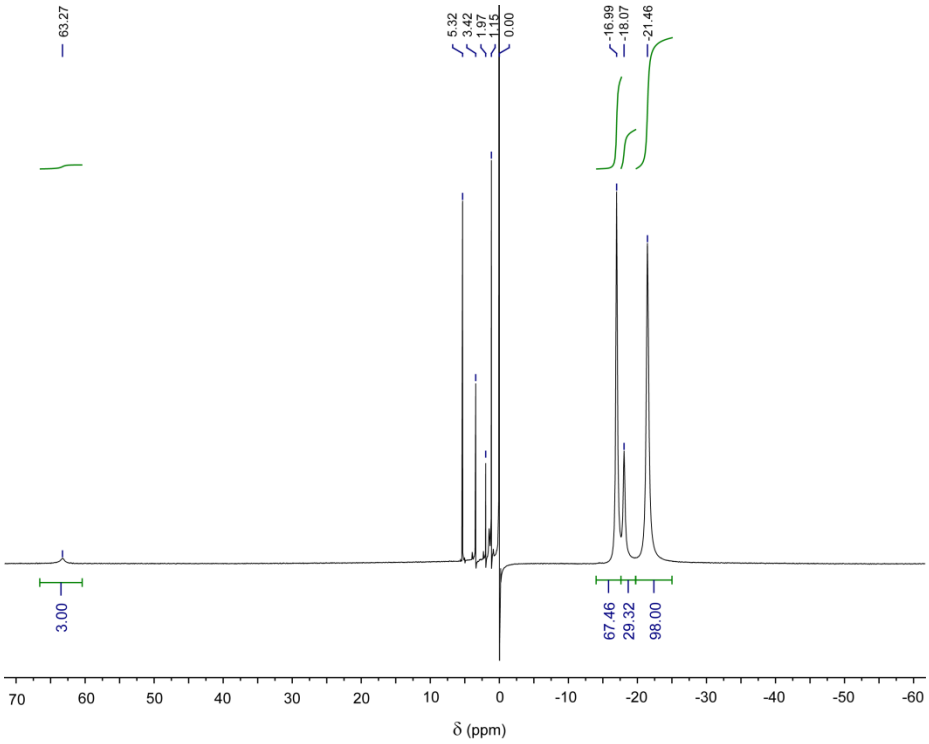

Figure 3.5. ^{1}H NMR spectrum of **3.4** in CD_2Cl_2. The resonances at 3.42 and 1.15 ppm are due to trace amounts of diethyl ether. The resonance at 1.97 ppm is due to a trace amount of acetonitrile.

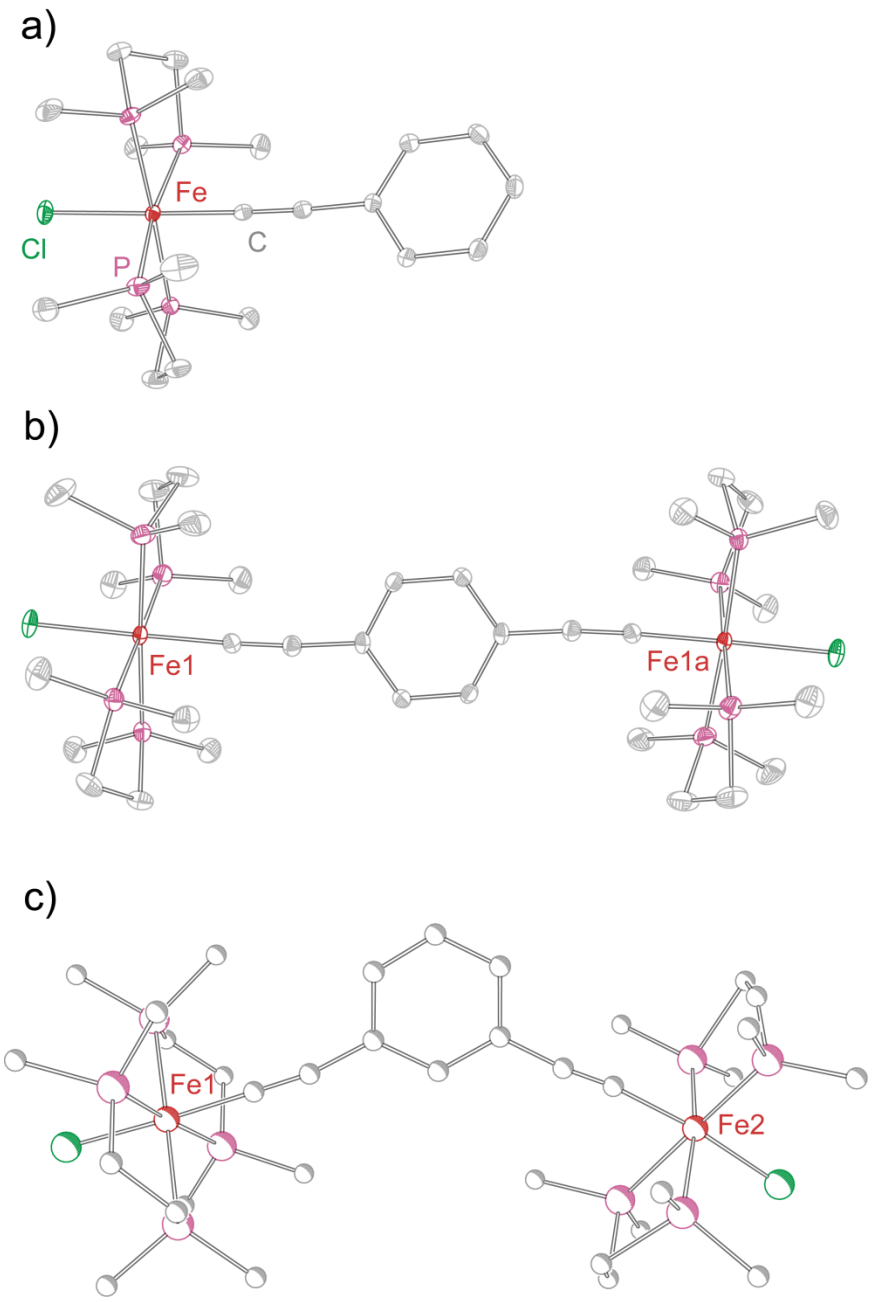

Figure 3.6. X-ray structures of the complex cations in a) **3.1**, b) **3.2**, and c) **3.5** with red, purple, green, and gray ellipsoids/spheres corresponding to Fe, P, Cl, and C atoms, respectively. Thermal ellipsoids in a) and b) are rendered at 40% probability. Hydrogen atoms in all structural plots are omitted for clarity. A thermal ellipsoid plot for **3.5** was not generated due to the occurrence of several non-positive definite atoms.

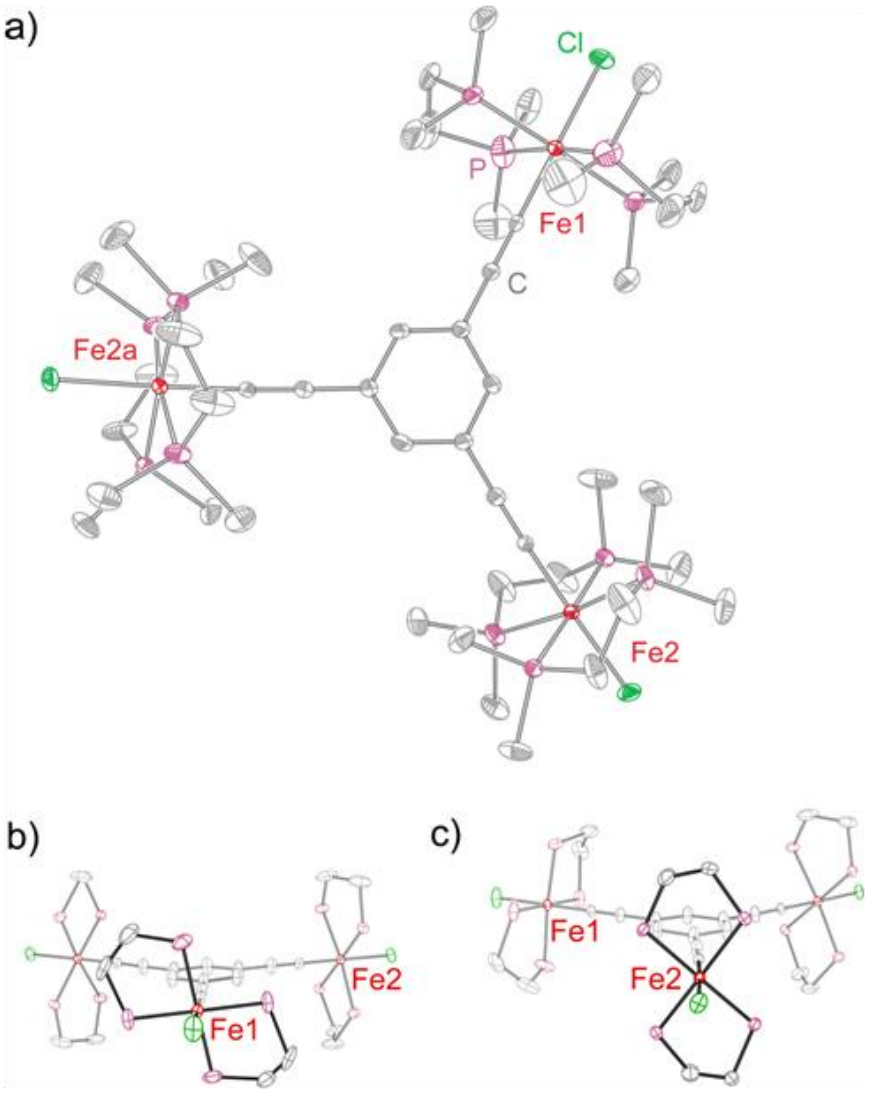

Figure 3.7. a) X-ray structure of the complex cation in **3.4** with hydrogen atoms removed for clarity. Views of the cation down b) the Cl1–Fe1–C_2 axis and c) the Cl2–Fe2–C_2 axis with hydrogen atoms and methyl groups omitted for clarity. See Figure 3.6 for color coding. All thermal ellipsoids are rendered at 40% probability.

3.8 for pictoral definition of φ). In contrast to the environment around Fe2 and Fe2a, the dmpe ligands coordinated to Fe1 are roughly perpendicular to the central phenyl ring: φ here is 36.9°. The Fe atoms reside at the vertices of an isosceles triangle; the Fe1···Fe2 and Fe1···Fe2a distances are 10.184(1) Å while the Fe2···Fe2a distance is 10.389(1) Å. Examination of the packing plot (Figure 3.9) reveals that the cationic complexes are arranged in two-dimensional layers parallel to the crystallographic *ab* plane. These arrays are separated from one another by triflate anions, and the interlayer distance as measured from the aromatic ring is ca. 10.713(2) Å. When viewed down the *c* axis, the cations form infinite stacks that are perfectly eclipsed. The shortest cation-anion distance is 3.3(3) Å and it occurs between one of the Fe1 dmpe ethylene carbons (C14) and an oxygen atom from one of the triflates (O1). The large esd for this interatomic distance is likely the result of libration effects in the triflate molecule. While this is not an obvious hydrogen-bonding interaction, the packing effect nevertheless appears to influence the orientation of the Fe1 dmpe ligands, so that they are twisted out of registry with respect to the dmpe ligands coordinated to Fe2 and Fe2a.

The structure solution for compound **3.5** was sufficient to establish atomic connectivity and to obtain an estimate of relevant structural metrics. However, relatively poor resolution for crystals of **3.5** precludes a rigorous analysis of bond lengths from the X-ray data, and the presence of dmpe ligand disorder cannot be ruled out. Similar crystallographic issues were encountered by Berben, who disclosed the structure of the hexfluorophosphate analogue of **3.5**.[15]

3.4.3 Magnetic Properties. The magnetic susceptibilities for all of the Fe^{III}-containing compounds presented here (Figures 3.10, 3.11, and 3.12) show significant

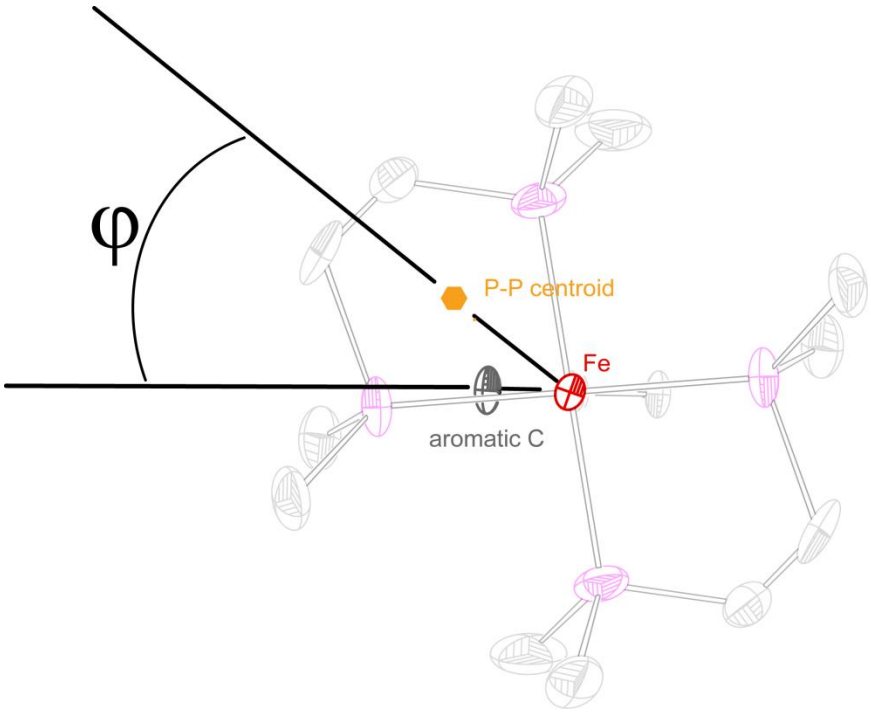

Figure 3.8. Definition of the torsion angle φ using the asymmetric unit of the cationic complex in **3.2** as an example. Here, φ = 28.0°. The view is down the Cl–Fe–C axis. The carbon atoms at the 1 and 4 positions, along with the acetylenic carbon atoms, are obscured by the Fe ellipsoid. Hydrogen atoms and Cl1 are omitted for clarity.

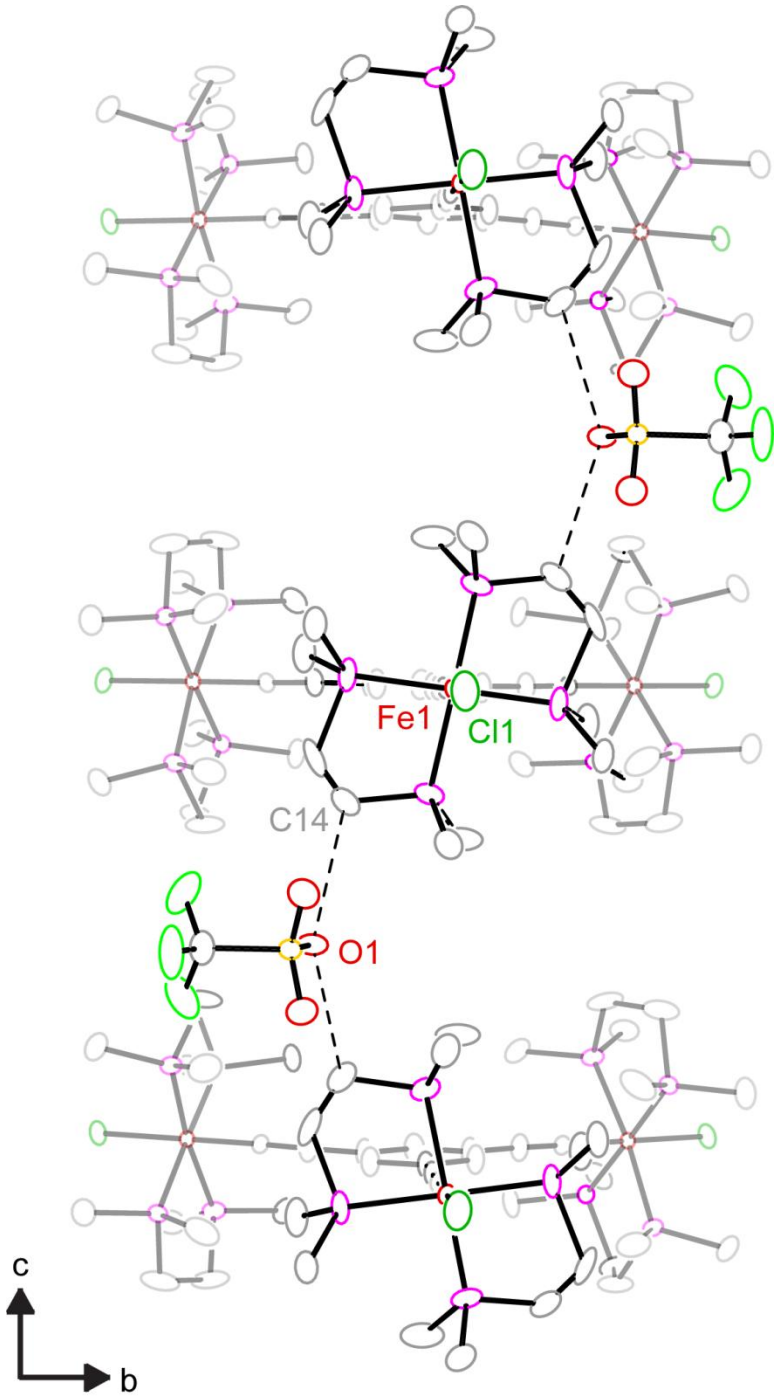

Figure 3.9. Packing diagram for the structure of **3.4** viewed along the *a* crystallographic axis. Dashed lines between O1 and C14 atoms indicate the shortest contacts between the complexes and triflate anions.

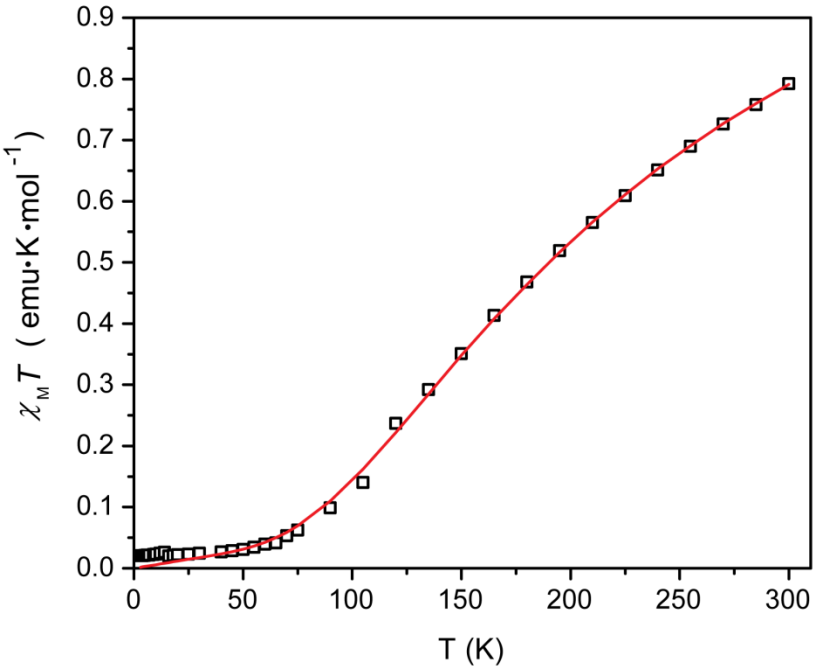

Figure 3.10. Temperature dependent susceptibility data for **3.2** (open squares) and best fit (solid red line).

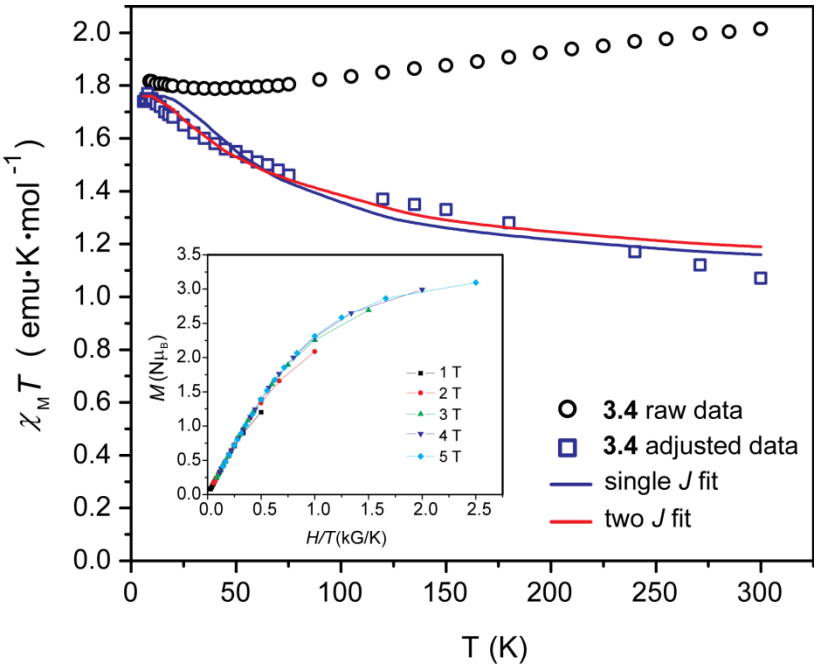

Figure 3.11. Raw (open circles) and TIP-corrected (open squares) magnetic susceptibility data for **3.4** with best fits from one- and two-*J* models. Inset: variable field reduced magnetization data for **3.4**. The solid lines are guides for the eye.

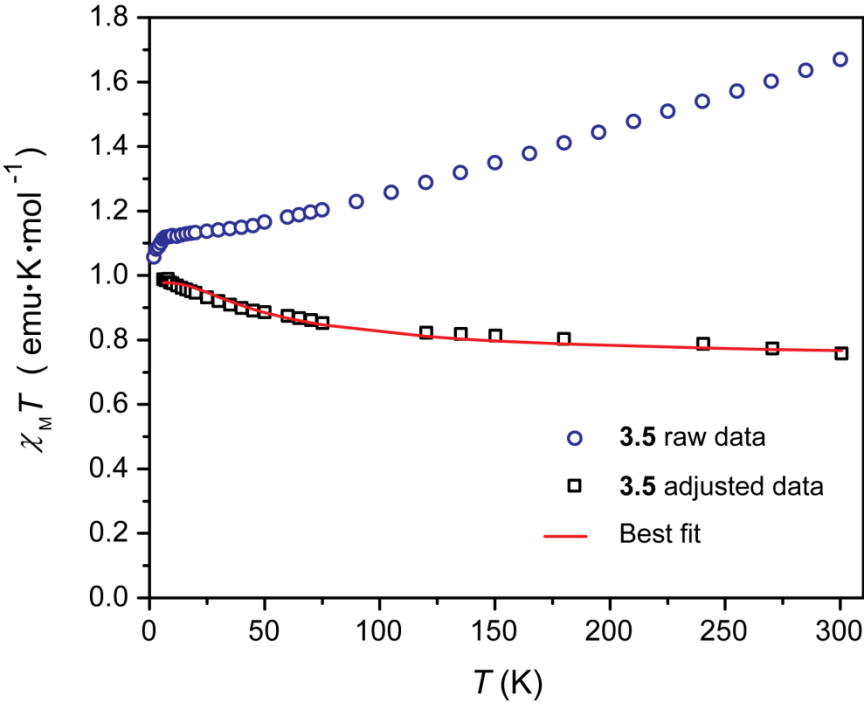

Figure 3.12. Raw (open circles) and corrected (open squares) magnetic susceptibility data for **3.5** with best fit (solid line).

temperature-independent paramagnetism (TIP), manifested as a linear increase in $\chi_M T$ with increasing temperatures and higher-than-expected room temperature susceptibilities for compounds with $g \sim 2$. This issue has been previously noted for pseudo-octahedral Fe^{III} complexes, and its origin has been attributed to either unquenched orbital angular momentum or small amounts of paramagnetic iron impurities present in the sample.[11a, 11e] Considering that we use crushed crystalline samples for magnetic measurements and obtain consistent results from multiple samples prepared at different times, we believe we have minimized paramagnetic impurities, so the magnetic interpretations to be presented reflect intrinsic properties of the pure compounds.

For **3.2** (Figure 3.10), the raw $\chi_M T$ product decreases steadily from 0.79 emu·K·mol^{-1} at 300 K to 0.07 emu·K·mol^{-1} at 75 K, then drops more gradually to 0.02 emu·K·mol^{-1} at 4 K. The trend exhibited by **3.2** indicates that antiferromagnetic (AF) coupling is operative, though the magnitude of $\chi_M T$ is slightly higher than the expected value at 300 K (0.75 emu·K·mol^{-1} is expected for two uncoupled $S = ½$ centers with $g = 2.0$). The best fit to this data affords $J = -132$ cm^{-1} and $g = 2.31$. Fitting the data with a model where g is constrained to smaller, more reasonable values was also possible, and this constraint only had minor effects on the magnitude of $|J|$. While this coupling constant is robust, it is significantly lower than the data for similar Cp*-ligated complexes that have been magnetically characterized.[11g, 12]

For previously reported *p*-DEB-bridged di-radical systems like **3.2**, resonance stabilization has been correlated to the magnitude of antiferromagnetic coupling. Previously characterized Fe^{III} species have had a $(Cp^{*-})(P_2)(C^-)$ first coordination sphere, and the differences in ligands for the complexes discussed here likely influence the

propensity of the Fe^{III} ion to form Fe=C-type interactions.[14b] In addition, the relative orientations of the "magnetic" d orbitals with respect to the aromatic π system will influence observed *J* couplings; this will be explored in more detail below.

For **3.4**, (Figure 3.11) the classical curve shape for a ferromagnetically coupled system is obscured by the involvement of unquenched orbital angular momentum. The susceptibility decreases from 2.00 emu·K·mol^{-1} at 300 K to a local minimum of 1.79 at 40 K, followed by an increase to 1.82 emu·K·mol^{-1} at 10 K. Below 10 K, the susceptibility drops off rapidly, which is either due to a weak intermolecular AF interaction, Zeeman, or zero-field splitting effects. The value of the $\chi_M T$ at 10 K is slightly smaller than the expected spin-only value expected for a ferromagnetically coupled three spin system with $g = 2$ (1.875 emu·K·mol^{-1}).

A similar picture emerges from the raw data for dinuclear **3.5** (Figure 3.12). At 300 K, $\chi_M T$ is 1.67 emu·K·mol^{-1}. Cooling the sample results in a monotonic susceptibility decrease to 1.15 emu·K·mol^{-1} at 40 K. Below 7 K, a more rapid decrease occurs, and $\chi_M T$ is 1.06 emu·K·mol^{-1} at 2 K.

In addition to TIP and orbital contributions, the magnetic susceptibility values for the meta-bridged di- and trinuclear ethynylbenzene-bridged compounds **3.4** and **3.5** (Figures 3.10 and 3.11, respectively) include magnetic exchange components. These contributions are also present in **3.2**, but the effects of TIP are apparently quenched by the strong intramolecular antiferromagnetic interaction. Fits to the raw magnetic data for all compounds presented herein can be obtained using magnetic fitting software. However, to properly evaluate the extent of magnetic communication between metal centers in **3.4** and **3.5**, it is preferable to isolate the spin-only and exchange contributions. For

paramagnetic Fe^{III} phenylacetylide complexes, the orbital contribution is distributed in the d orbitals on the metal center as well as in the aromatic π system of the phenyl ring. When the DEB and TEB bridging ligands mediate magnetic coupling interactions, spin density should delocalize onto π* orbitals on the carbon atoms in the aromatic ring. For the purpose of modeling the exchange interactions, the orbital contributions of the low-spin Fe^{III} ions in compounds **3.4** and **3.5** were eliminated from the data: *n* equivalents of the susceptibility for $[(dmpe)_2FeCl(C_2SiMe_3)](PF_6)$ are subtracted from the raw data, then the ligand susceptibility and the expected spin-only value for *n* low-spin d^5 centers with *g* = 2.00 are added (*n* = 3 for **3.4**, 2 for **3.5**). Similar procedures have been applied to Fe^{III}-contining magnetic data previously in order to more accurately evaluate magnetic coupling interactions in systems where masking effects were present.[15, 31]

The resulting plot for dinuclear **3.5** is shown in Figure 3.12. The value of $\chi_M T$ at 300 K is 0.77 emu·K·mol^{-1}, corresponding to two uncoupled coupled electrons with a *g* value near 2. Upon cooling, the susceptibility gradually increases, reaching a maximum value of 0.98 emu·K·mol^{-1} at 6 K. This behavior is entirely consistent with the population of an *S* = 1 ground state with *g* near 2.00 at low temperature, and fitting the data affords *J* = +20 cm^{-1} with *g* = 1.98. As expected, the data for **3.5** qualititatively match that for $[(dmpe)_4Fe_2Cl_2(\mu\text{-}m\text{-DEB})](PF_6)_2$ obtained by Berben.[15] Magnetic susceptibility data for both compounds was treated identically, yet *J* for the hexafluorophosphate salt is +41 cm^{-1}, more than twice as strong as for **3.5**. X-ray structural data for $[(dmpe)_4Fe_2Cl_2(\mu\text{-}m\text{-DEB})](PF_6)_2$ was not available for analysis, but the ancillary ligand conformations appear to be similar to **3.5**.[15]

The corrected data for **3.4** (Figure 3.11) also show the expected ferromagnetic coupling of Fe^{III} centers. The $\chi_M T$ value at 300 K is 1.07 emu·K·mol^{-1}, which corresponds to three uncoupled S = ½ centers with g = 1.95. Upon cooling, the susceptibility increases gradually, reaching a maximum of 1.77 emu·K·mol^{-1} at 8 K, which is only slightly smaller than the expected susceptibility for an $S = {}^3/_2$ ground state with g = 2.00, corresponding to the g value measured by EPR spectroscopy (Figures 3.13-3.15). Further cooling to 5 K causes a slight decrease in $\chi_M T$ to 1.74 emu·K·mol^{-1}. Considering that the Fe^{III} ions are located at the vertices of an isosceles triangle and that one of the $(dmpe)_2Fe^{III}$ groups is twisted out of registry with respect to the other two, we fit the data assuming two different exchange coupling constants. The best fits to the 2J model (Scheme 3.2b) give $J_{12} = J_{13}$ = 11 cm^{-1} and J_{23} = 61 cm^{-1} with g = 1.94. Treating the data with a single exchange coupling constant (1J model, Scheme 3.2c) between 6 and 300 K yields a significantly different J value (J = 20 cm^{-1}; g = 1.94), and a much poorer fit, especially at low temperature, indicating that the small geometrical perturbations observed in the crystal structure have significant ramifications for the magnetic properties. The fit to the data for **3.4** yields significantly larger J values than determined for Lapinte's TEB-bridged complex, where the two J values were 9.6 cm^{-1} and 4.4 cm^{-1}. Comparing to di-radical Fe^{III} *m*-DEB bridged systems is also telling; coupling constants range from 41 cm^{-1} to apparently 150 cm^{-1}, even though resonance stabilization is not a factor for complexes bridged by a 1,3-phenylene moiety.[11b, 32] Comparison to structurally and magnetically characterized organic tri-radicals is also meaningful: Iwamura has applied an isosceles model to the susceptibility data for 2-

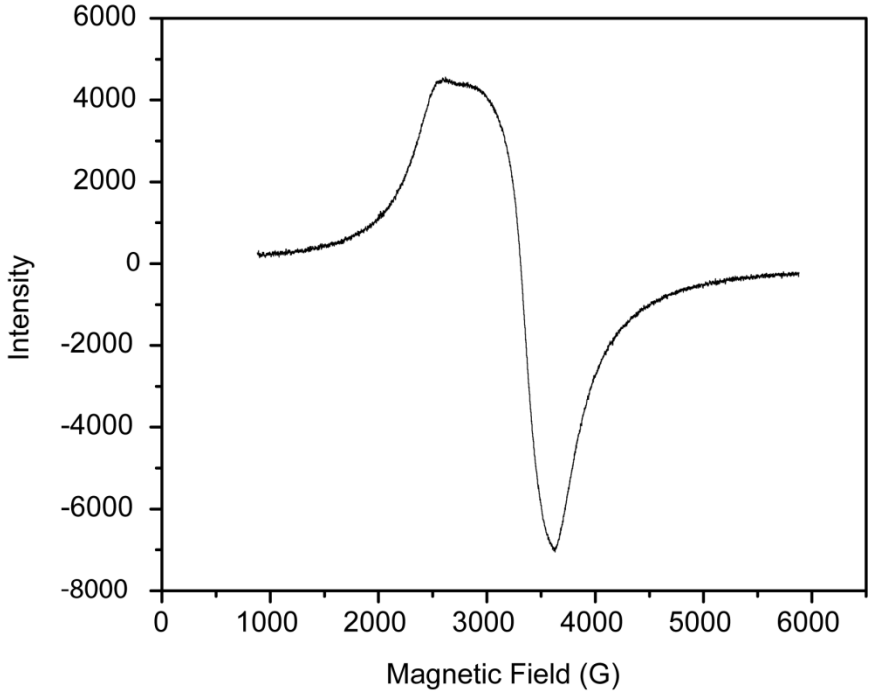

Figure 3.13. X-band EPR spectrum of **3.1** in a frozen dichloromethane:dichloroethane frozen glass at 100 K.

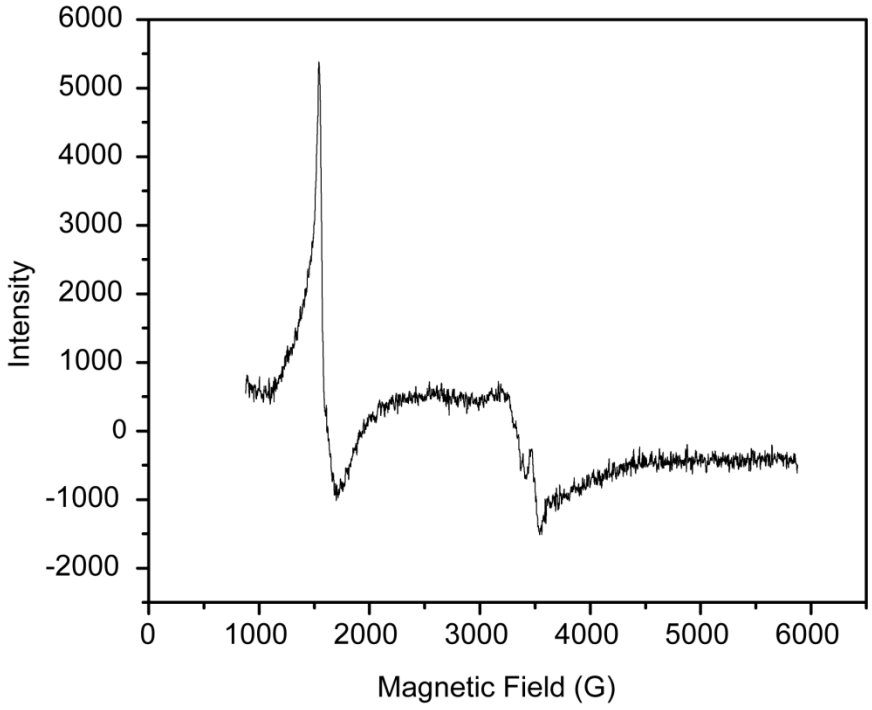

Figure 3.14. X-band EPR spectrum of **3.2** in a frozen dichloromethane:dichloroethane frozen glass at 100 K. The half-field resonance at ca. 1500 G represents a $\Delta m_S = 1$ transition.

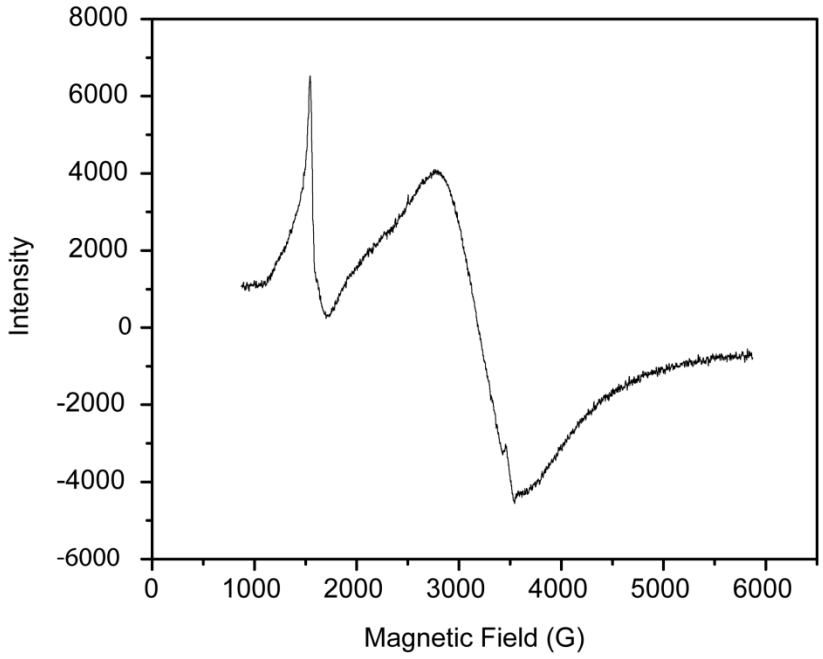

Figure 3.15. X-band EPR spectrum of **3.4** in a frozen dichloromethane:dichloroethane frozen glass at 100 K. The half-field resonance at ca. 1500 G represents a $\Delta m_S = 1$ transition.

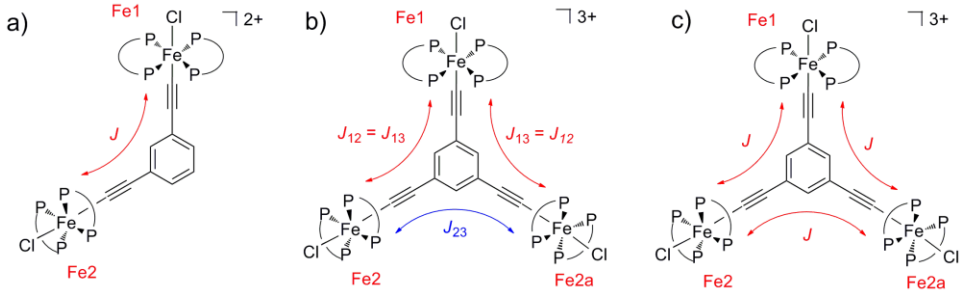

Scheme 3.2. Ferromagnetic exchange pathways for a) **3.5**, b) **3.4** (two *J* model) and c) **3.4** (one *J* model).

methoxy-1,3,5-benzenetriyltris(*N*-*tert*-butyl-nitroxide) to find $J_{12} = J_{13} = 48$ cm^{-1} and $J_{23} = 3$ cm^{-1}.[33]

Magnetization data collected in dc fields up to 5 T further support the assignment of an $S = {}^3/_2$ ground state for **3.4** (Figure 3.11, inset), as the magnetization appears to saturate at approximately 3 $N\mu_B$. The data is also consistent with a nearly isotropic magnetic system, as the isofield magnetization values nearly overlap each other. Preliminary AC susceptibility studies support this conclusion, as no frequency dependence in the susceptibility is observed for **3.4**. The geometric origins of this behavior are explored below.

3.4.4 Magnetostructural Correlations in the TEB-bridged Complexes. A comparison of electrochemical data between **3.3** and $[(dppe)_3(Cp^*)_3Fe_3(TEB)]$ suggests that electronic communication between Fe ions is much weaker in the former than in the latter. That might be thought to translate into weaker magnetic coupling for **3.4** versus $[(dppe)_3(Cp^*)_3Fe_3(TEB)]^{3+}$; for related dinuclear complexes Paul has argued that J scales with the amount of spin that is delocalized on the bridging ligand. Perhaps this helps to explain the behavior of *p*-DEB-bridged species, because the cumulenic resonance form can be transmitted across the bridge, but it is not as helpful for the *m*-DEB- and TEB-bridged complexes, where such resonance cannot be transmitted directly between Fe centers. However, the coupling in **3.4** is clearly much stronger than that found in Lapinte's triferric species.

Although the slight differences in Fe···Fe distances found in the structure of **3.4** justify use of the 2J fitting model, the more significant contributor to the ferromagnetic coupling in the trinuclear complex likely originates from orbital symmetry

considerations. Lapinte has interpreted the antiferromagnetic coupling in polyene-diyl bridged diradicals using criteria developed by Borden, where the degree of overlap between metal dπ and ligand π orbitals has a large influence on the sign and magnitude of magnetic exchange.[11g, 14a, 34] Berke has nicely illustrated the dependence of the singlet-triplet gap on the relative orientation of spin centers in a Mn_2C_2 complex.[14c] However, correlating exchange to geometry has not been considered in detail for the ethynylbenzene systems.

The position of the singly-occupied orbital in the $[Fe^{III}(dmpe)_2X]$ moiety can be established with confidence through computational efforts. The relative stability and character of the five d orbitals at each magnetic iron center can be accessed from a TD-DFT/NTO analysis (Figure 3.16) of the mononuclear fragment $[(dmpe)_2FeCl(C_2H)]^+$. Using a B3LYP LANL2/6-31g* hybrid density functional, the ground state possesses a low spin d^5 configuration with one member of the "t_{2g}" set singly occupied. The singly occupied orbital is π with respect to the four phosphorus centers and is directed between the chelate rings. The lowest energy excitation takes an electron from the doubly occupied perpendicular dπ orbital and places it in the singly occupied dπ orbital. Plots of the natural transition orbitals (NTOs) for this transition are provided in Figure 3.16a with an alternative orientation shown in Figure 3.16b. This excited state is computed to be 7.4 kcal/mol above the ground state. Since this energy roughly corresponds to a 2700 Tesla applied field, the only magnetically accessible state places the unpaired electron in a dπ orbital directed between the chelate rings. Thus, only by changing the relative orientation of the entire $[Fe(dmpe)_2Cl]^+$ fragment relative to the central aryl π system can the magnetic properties of the di- and trinuclear complexes be altered.

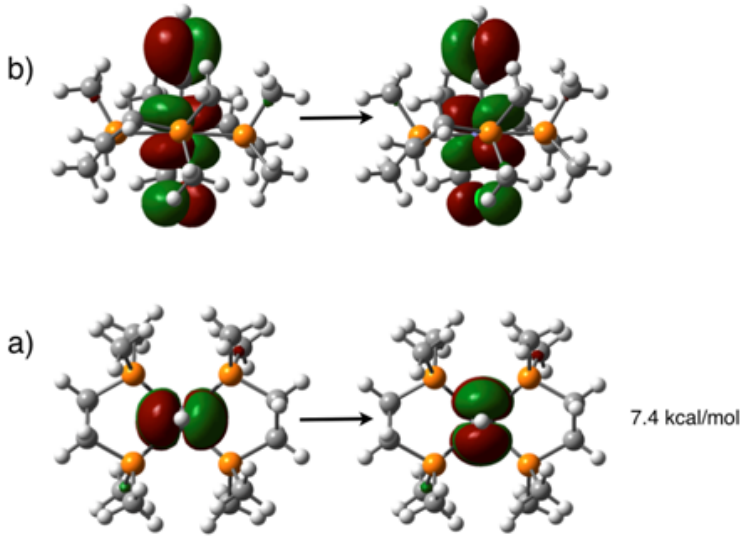

Figure 3.16. Two views (a and b) of the natural transition orbitals involved in the excitation of an electron in a doubly occupied dπ orbital to the singly occupied dπ orbital in $[(dmpe)_2FeCl(C_2H)]^+$.

Considering the origins of well-isolated magnetic ground states in **3.2**, **3.4** and **3.5**, it is reasonable to expect a direct correlation between *J* and the amount of spin density that gets transferred from a Fe^{III} ion to the bridging ligand. Based on the results of DFT analysis, optimal spin-density transfer is anticipated when the magnetic dπ orbital is exactly parallel with the pπ orbitals on the acetylide and aromatic carbon atoms of the ligand. The torsion angle φ (see Section 3.4.2 and Figure 3.8) is partially defined by the P–P centroid, which is related by approximately 90° to the orientation of the dπ magnetic orbital. Thus, optimal spin transfer (and the largest |*J*| values) should occur when φ is 0°. For **3.4,** these geometry effects can be qualitatively understood from the depiction in Figure 3.17. The "all parallel" orbital arrangement shown in Figure 3.17a would be expected to afford the largest coupling since all three unpaired electrons delocalize into the central aryl ring and would reside in strictly orthogonal molecular orbitals. When one or more of the dπ orbitals is taken out of registry with the aryl π system (Figure 3.17, b-d), the ferromagnetic exchange is expected to become significantly weaker, either through reduced delocalization or increased AF coupling or both. Based on its X-ray structure, the bonding picture in **3.4** (and in Lapinte's complex) most resembles the schematic picture shown in Figure 3.17c. Similar thinking also applies to Fe^{III} ethynylbenzene complexes previously characterized by Lapinte and Paul, which allows both families of complexes to be treated with a unified magnetostructural model.

Torsion angles (φ) and reported coupling constants (*J*) are collected for **3.2**, **3.4**, **3.5** and previously characterized paramagnetic metal-ethynylbenzene complexes in Table 3.2. Focusing only on the ferromagnetically coupled complexes presented herein (**3.4** and **3.5**), there appears to be a relationship between φ_{max} and *J* since φ_{max} is essentially a

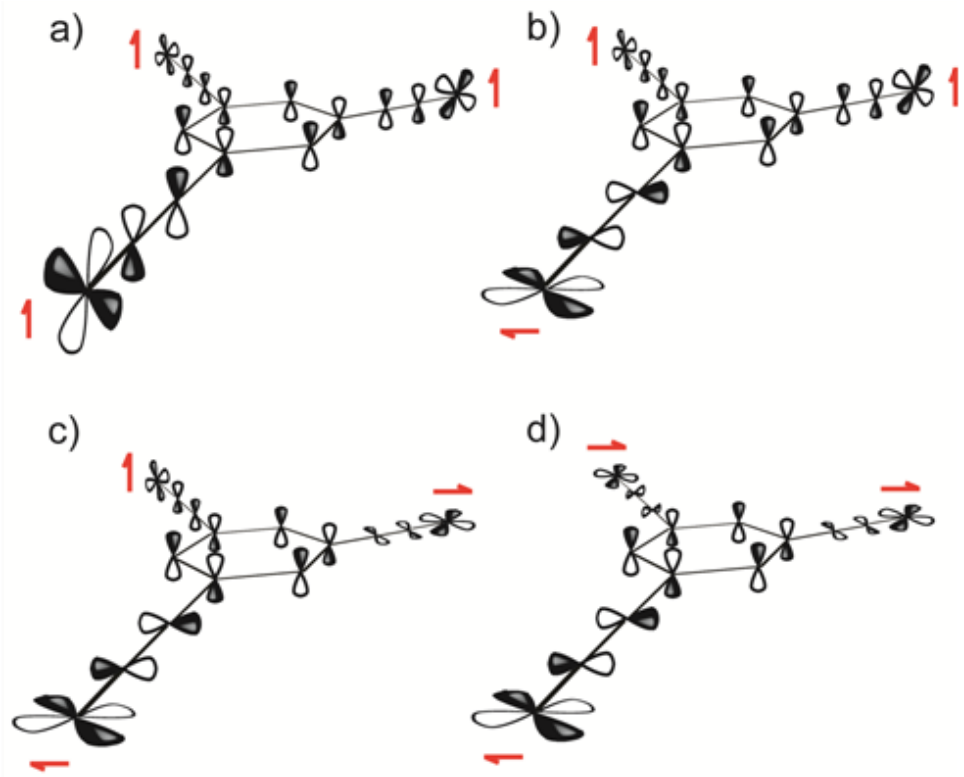

Figure 3.17. Possible orientations of the "magnetic" dπ and acetylide pπ orbitals relative to the aryl π system in the cation of tri-nuclear **3.4**.

Table 3.2. Torsion angles (φ, see text for definition) and reported *J* values for all multi-nuclear complexes presented herein. For comparison, paramagnetic ethynylbenzene data for related [(dppe)(Cp*)Fe^{III}]- and [$(dmpe)_2Fe^{III}Cl$]-containing complexes are also included.

Complex	φ (°)	φ_{avg} (°)	J (cm^{-1})	refs.
3.2	28.1(Fe1) 24.3 (Fe1a)	26.2	−131	this work
3.4	83.2 (Fe1) 36.9 (Fe2)	67.4	$J_{12} = J_{13} = 11.3$; $J_{23} = 61.4$; $J_{avg} = 28$	this work
$[(dmpe)_4Fe_2Cl_2(\mu\text{-}m\text{-DEB})](PF_6)_2$	?[b]	?[b]	+41	20
3.5	85.6	53.5	+20.1	this work
$[(dppe)_2(Cp^*)_2Fe_2(\mu\text{-}p\text{-DEB})](PF_6)_2$	43.2	40.3	−191 (Paul), −1 (Lapinte)	14, 13a
$[(dppe)_2(Cp^*)_2Fe_2(\mu\text{-}m\text{-DEB})](PF_6)_2$	61.7	60.4	>150 (Paul), 65.3 (Lapinte),	14, 13b
$[(dppe)_3(Cp^*)_3Fe_3(TEB)](PF_6)_3$	53.6[a] (Fe1) 0.5[a] (Fe2) 60.7[a] (Fe3)	38.3	$J = 9.6$, $J' = 4.4$, $J_{avg} = 7$	13b

[a] These angles were measured from the tri-ferrous complex $[(dppe)_3(Cp^*)_3Fe_3(TEB)]$.

[b] A CIF file was not available for analysis, and the dmpe ligands are rotationally disordered.

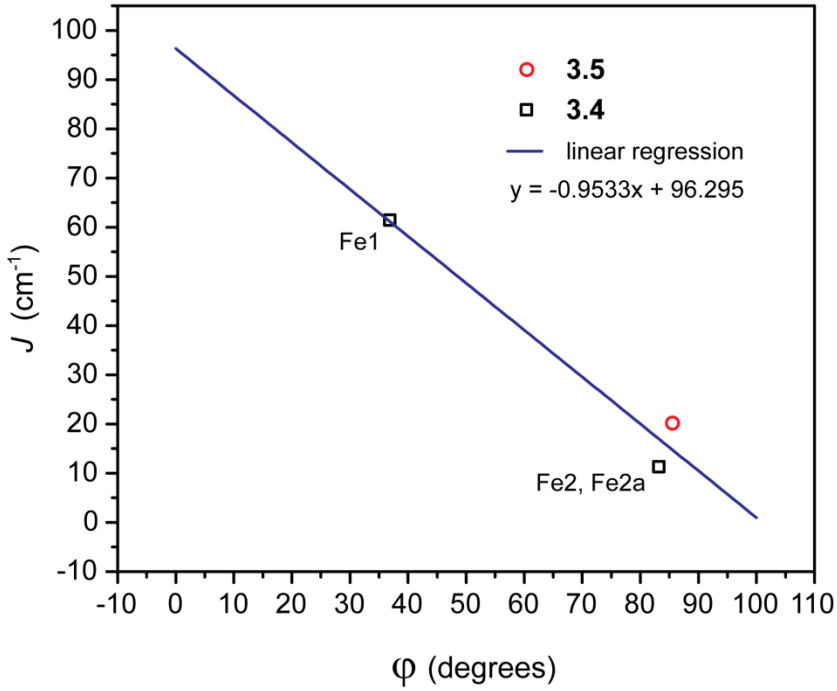

Figure 3.18. Plot of *J* versus φ for **3.4** and **3.5** where intramolecular ferromagnetic coupling is operative. A clear correlation could not be established for the antiferromagnetically coupled complexes.

measure of metal-ligand overlap. Although the sample size here is low, the line of best fit in a plot of φ_{max} vs. $+J$ (Figure 3.18) supports our magnetostructural model, suggesting that a maximum ferromagnetic interaction of 96 cm^{-1} is possible in this family of complexes. However, based on available structural and magnetic data, there is no evidence that this model is operative among complexes that incorporate [(dppe)(Cp*)Fe] units. The reasons for being unable to impose this model onto those complexes are numerous. Notably, large variation in the published *J* values means that at least one of the reported values is incorrect. Additionally, magnetic susceptibility data for $[(dppe)_3(Cp^*)_3Fe_3(TEB)](PF_6)_3$ are not consistent with the discussed $S = {}^3/_2$ ground state,[11b] and structural data for this compound as the tri-ferric salt have not been obtained. Further, differences in the polarization of the metal-ligand bond in $[(dppe)(Cp^*)Fe]^-$ versus $[(dmpe)_2FeCl]^-$ complexes could affect the amount of spin density that is allowed to leak onto the bridging ligand.

3.5 Conclusions and Outlook

The syntheses, structures, and the magnetic properties (and the results of electronic structure calculations) for a series of Fe^{III} ethynylbenzene complexes have been described. Magnetic measurements on **3.4** and **3.5** are consistent with the population of isotropic $S = {}^3/_2$ and $S = 1$ ground states at low temperatures, respectively. In contrast, variable temperature measurements on di-nuclear **3.2** indicate that antiferromagnetic interactions lead to an $S = 0$ ground state. This magnetic behavior is fully consistent with established topology rules. However, the strength of the intramolecular interactions is influenced by more subtle structural features. For instance, the structure and magnetic results for **3.4** are consistent with an isosceles-type interaction, owing to the asymmetry

of the trication and the relative orientations of the $(dmpe)_2Fe$ units coordinated to the bridging ligand. Using DFT calculations, the orbital pathways responsible for the magnetic exchange interactions in Fe^{III} acetylide complexes have been determined. From the orientation of the calculated "magnetic" dπ orbital, a structural handle for these complexes has been established that allows the geometry of ancillary ligand sets to be connected to the strength of intramolecular magnetic interactions. In the ferromagnetically coupled complexes, **3.4** and **3.5**, there appears to be a relationship between the geometry of the "worst" orbital pathway and *J*. Assuming a linear relationship, a maximum ferromagnetic interaction between $[(dmpe)_2FeCl]^-$ units through a 1,3-phenylene bridge of $J = 96\ cm^{-1}$ with optimum ligand geometry is predicted. Attempts to include $[(dppe)(Cp^*)Fe]^-$ ethynylbenzene complexes using this model were hindered by a lack of reliable structural and magnetic data.

Moving forward, the lessons learned here may be applied to tune magnetic interactions in these complexes. Enhanced coupling strengths are foreseen if these orientations could be tuned synthetically. The ability to manipulate *J* could have profound implications for the isolation of high spin, low dimensional metal complexes, potentially resulting in molecular magnets with enhanced properties.

3.6 Acknowledgement

This research was supported by Colorado State University and the ACS Petroleum Research Fund (44691-G3).

3.7 References and Notes

1. (a) Long, N. J.; Williams, C. K., *Angew. Chem. Int. Ed.* **2003,** *42*, 2586-2617; (b) Ren, T., *Organometallics* **2005,** *24*, 4854-4870.

2. Sessoli, R.; Gatteschi, D.; Caneschi, A.; Novak, M. A., *Nature* **1993,** *365*, 141-143.

3. *Single-Molecule Magnets and Related Phenomena.* Springer: Berlin, 2006; Vol. 129, p 262.

4. Ruiz, E.; Rodríguez-Fortea, A.; Alvarez, S., *Inorg. Chem.* **2003,** *42*, 4881-4884.

5. Layfield, R. A.; McDouall, J. J. W.; Sulway, S. A.; Tuna, F.; Collison, D.; Winpenny, R. E. P., *Chem. Eur. J.* **2010,** *16*, 4442-4446.

6. (a) Oshio, H.; Nakano, M., *Chem. Eur. J.* **2005,** *11*, 5178-5185; (b) Cirera, J.; Ruiz, E.; Alvarez, S.; Neese, F.; Kortus, J., *Chem. Eur. J.* **2009,** *15*, 4078-4087; (c) Tancini, E.; Rodriguez-Douton, M. J.; Sorace, L.; Barra, A.-L.; Sessoli, R.; Cornia, A., *Chem. Eur. J.* **2010,** *16*, 10482-10493.

7. (a) Onitsuka, K.; Fujimoto, M.; Kitajima, H.; Ohshiro, N.; Takei, F.; Takahashi, S., *Chem. Eur. J.* **2004,** *10*, 6433-6446; (b) Onitsuka, K.; Fujimoto, M.; Ohshiro, N.; Takahashi, S., *Angew. Chem. Int. Ed.* **1999,** *38*, 689-692; (c) McDonagh, A. M.; Humphrey, M. G.; Samoc, M.; Luther-Davies, B., *Organometallics* **1999,** *18*, 5195-5197; (d) McDonagh, A. M.; Powell, C. E.; Morrall, J. P.; Cifuentes, M. P.; Humphrey, M. G., *Organometallics* **2003,** *22*, 1402-1413.

8. (a) Field, L. D.; George, A. V.; Hambley, T. W., *Inorg. Chem.* **1990,** *29*, 4565-4569; (b) Field, L. D.; George, A. V.; Laschi, F.; Malouf, E. Y.; Zanello, P., *J. Organomet. Chem.* **1992,** *435*, 347-356.

9. We note that replacement of the axial chloride in these complexes is not facile. However, Field and coworkers have achieved stepwise ligand substitution starting with structurally analagous $[(dmpe)_2FeCH_3(C_2R)]$ complexes using photochemical methods. See ref 10.

10. Field, L. D.; Turnbull, A. J.; Turner, P., *J. Am. Chem. Soc.* **2002,** *124*, 3692-3702.

11. (a) Le Narvor, N.; Lapinte, C., *C. R. Acad. Sci., Ser. IIC: Chim.* **1998,** *1*, 745-749; (b) Weyland, T.; Costuas, K.; Mari, A.; Halet, J.-F.; Lapinte, C., *Organometallics* **1998,** *17*, 5569-5579; (c) Packheiser, R.; Ecorchard, P.; Ruffer, T.; Lohan, M.; Brauer, B.; Justaud, F.; Lapinte, C.; Lang, H., *Organometallics* **2008,** *27*, 3444-3457; (d) Packheiser, R.; Lohan, M.; Brauer, B.; Justaud, F.; Lapinte, C.; Lang, H., *J. Organomet. Chem.* **2008,** *693*, 2898-2902; (e) Roué, S.; Le Stang, S.; Toupet, L.; Lapinte, C., *C. R. Chim.* **2003,** *6*, 353-366; (f) Weyland, T.; Ledoux, I.; Brasselet, S.; Zyss, J.; Lapinte, C., *Organometallics* **2000,** *19*, 5235-5237; (g) Paul, F.; Lapinte, C., Magnetic Communication in Binuclear Organometallics. In *Unusual Structures and Physical Properties in Organometallic Chemistry*, Gielen, M.; Willem, R.; Wrackmeyer, B., Eds. Wiley: West Sussex, 2002.

12. Paul, F.; Bondon, A.; da Costa, G.; Malvolti, F.; Sinbandhit, S.; Cador, O.; Costuas, K.; Toupet, L.; Boillot, M.-L., *Inorg. Chem.* **2009,** *48*, 10608-10624.

13. Paul, F.; Toupet, L.; Roisnel, T.; Hamon, P.; Lapinte, C., *C. R. Chim.* **2005,** *8*, 1174-1185.

14. (a) Borden, W. T., *Mol. Cryst. Liq. Cryst.* **1993,** *232*, 195-218; (b) Paul, F.; Lapinte, C., In *Unusual Structures and Physical Properties in Organometallic Chemistry*, Gielen, M.; Willem, R.; Wrackmeyer, B., Eds. John Wiley and Sons: West Sussex, 2002; (c) Kheradmandan, S.; Venkatesan, K.; Blacque, O.; Schmalle, H. W.; Berke, H., *Chem. Eur. J.* **2004,** *10*, 4872-4885.

15. Berben, L. A. Toward acetylide- and N-heterocycle-bridged materials with strong electronic and magnetic coupling. Ph.D., University of California, Berkeley, 2005.

16. Girolami, G. S.; Wilkinson, G.; Galas, A. M. R.; Thorntonpett, M.; Hursthouse, M. B., *J. Chem. Soc. Dalton Trans.* **1985**, 1339-1348.

17. Chávez, I.; Alvarez-Carena, A.; Molins, E.; Roig, A.; Maniukiewicz, W.; Arancibia, A.; Arancibia, V.; Brand, H.; Manríquez, J. M., *J. Organomet. Chem.* **2000,** *601*, 126-132.

18. Connelly, N. G.; Geiger, W. E., *Chem. Rev.* **1996,** *96*, 877-910.

19. Weber, E.; Hecker, M.; Koepp, E.; Orlia, W.; Czugler, M.; Csöregh, I., *J. Chem. Soc., Perkin Trans. 2* **1988**, 1251-1257.

20. *APEX 2*, Bruker Analytical X-Ray Systems, Inc.: Madison, WI, 2008.

21. Sheldrick, G. M. *SHELXTL*, Bruker Analytical X-Ray Systems, Inc.: Madison, WI, 1999.

22. Spek, A. L. *PLATON, A Multipurpose Crystallographic Tool*, Utrecht University: Utrecht, The Netherlands, 2005.

23. Kahn, O., *Molecular Magnetism*. VCH: New York: 1993.

24. Bill, E. *julX*, 1.41; Max Planck Institute for Bioinorganic Chemistry: Mulheim an der Ruhr, 2008 (http://ewww.mpi-muelheim.mpg.de/bac/logins/bill/julX_en.php).

25. Schmitt, E. A. Ph. D. Thesis, University of Illinois at Urbana-Champaign, 1995.

26. Shores, M. P.; Sokol, J. J.; Long, J. R., *J. Am. Chem. Soc.* **2002,** *124*, 2279-2292.

27. Weyland, T.; Lapinte, C.; Frapper, G.; Calhorda, M. J.; Halet, J.-F.; Toupet, L., *Organometallics* **1997,** *16*, 2024-2031.

28. Le Narvor, N.; Lapinte, C., *Organometallics* **1995,** *14*, 634-639.

29. de Montigny, F. d. r.; Argouarch, G.; Costuas, K.; Halet, J.-F. o.; Roisnel, T.; Toupet, L.; Lapinte, C., *Organometallics* **2005,** *24*, 4558-4572.

30. Weyland, T.; Costuas, K.; Mari, A.; Halet, J. F.; Lapinte, C., *Organometallics* **1998,** *17*, 5569-5579.

31. (a) Rinehart, J. D.; Harris, T. D.; Kozimor, S. A.; Bartlett, B. M.; Long, J. R., *Inorg. Chem.* **2009,** *48*, 3382-3395; (b) Newell, B. S.; RappeÌ • , A. K.; Shores, M. P., *Inorg. Chem. 49*, 1595-1606; (c) Lescouězec, R.; Lloret, F.; Julve, M.; Vaissermann, J.; Verdaguer, M., *Inorg. Chem.* **2002,** *41*, 818-826; (d) Colacio, E.; Ghazi, M.; Stoeckli-Evans, H.; Lloret, F.; Moreno, J. M.; Pérez, C., *Inorg. Chem.* **2001,** *40*, 4876-4883.

32. Tanaka, Y.; Shaw-Taberlet, J. A.; Justaud, F. d. r.; Cador, O.; Roisnel, T.; Akita, M.; Hamon, J.-R.; Lapinte, C., *Organometallics* **2009,** *28*, 4656-4669.

33. Kanno, F.; Inoue, K.; Koga, N.; Iwamura, H., *J. Phys. Chem* **1993,** *97*, 13267-13272.

34. (a) Borden, W. T.; Davidson, E. R., *J. Am. Chem. Soc.* **1977,** *99*, 4587-4594; (b) Borden, W. T.; Iwamura, H.; Berson, J. A., *Acc. Chem. Res.* **1994,** *27*, 109-116.

Chapter 4. Unusual Electronic Effects Imparted By Bridging Dinitrogen

4.1 Introduction

A modern focus of coordination chemistry is to ascertain the role(s) of bridging ligands in mediating metal-metal interactions. Advances in the areas of electron transfer, magnetic exchange, and small molecule activation can be attributed in large part to the results of fundamental studies carried out on model M–L–M systems.[1-3] For example, the judicious choice of ligands to link paramagnetic metal centers has profound implications for the ability of a given complex to exist in a well-defined spin ground state.[4] Thus, learning how simple ligands like oxide[5-8] and cyanide[9-14] manage exchange interactions has been critical to the development of molecular magnetism.

Metal complexes of another bridging ligand, dinitrogen, are most often studied for their reactivity. While understanding the electronic structure of transition metal dinitrogen complexes is important for elucidating mechanistic aspects of N_2 activation, it is also critical to probing metal-metal electronic communication and its impact on magnetic communication and electron transfer. Dating from the 1970s,[15,16] physical measurements on metal dinitrogen complexes have contributed significantly to our understanding of mixed valency as well as bridge-mediated/inner-sphere electron transfer processes.

The intramolecular magnetic interactions of paramagnetic $M_2(\mu_2\text{-}\eta^1\text{:}\eta^1\text{-}N_2)$ complexes, including a tetrahedral $V^{III}_2(\mu\text{-}N_2)$ complex[17] and an octahedral $Cr^{I}_2(\mu\text{-}N_2)$ complex[18], have been interpreted in terms of weak antiferromagnetic coupling. In light of the

similarity of dinitrogen to the isoleectronic cyanide bridging ligand, this model makes intuitive sense.[12] However, recent investigations involving N_2-bridged transition metal complexes indicate that non-diamagnetic, high spin electronic ground states exist for tetrahedral $Mo^{III}_2(\mu\text{-}N_2)$[19] and trigonal planar $Co^{I}_2(\mu\text{-}N_2)$ complexes.[20] To correspond with the antiferromagnetic terminology employed by others, we loosely refer to these non-diamagnetic ground states as "ferromagnetically coupled," however a more accurate description would invoke an electronic structure similar to the triplet ground state of dioxygen. The electronic structure that accounts for high spin magnetic behavior in a formally $Fe^{I}_2(\mu\text{-}N_2)$ complex has been described in terms of strong direct antiferromagnetic coupling between Fe^{II} and a diazenido (N_2^{2-}) bridging ligand.[21-23] Recent theoretical calculations involving a $Ni^{I}_2(\mu\text{-}N_2)$ complex predict a triplet ground state, although magnetic measurements made in solution are consistent with the presence of two weakly- or non-coupled S = ½ Ni^{I} ions.[24] There, stepwise potassium metal reduction of the Ni_2 complex occurs at the dinitrogen ligand, and metal-ligand antiferromagnetic coupling is invoked to account for the diamagnetism observed in the di-reduced $K_2Ni_2(\mu\text{-}N_2)$ species.

It is clear from the available reports that interpretations of the measured magnetic properties of dinitrogen-bridged complexes are varied. One source of difficulty is that the few structurally characterized paramagnetic M–N–N–M complexes display myriad coordination geometries as well as a variety of valence bond structures and electron counts, which surely have profound implications for magnetic communication. On a case-by-case basis, magneto-structural correlations drawn from comparisons of metal dinitrogen complexes have been consistent with theory of the day.[17,25-27] However, a

more detailed magneto-structural and theoretical survey of multiple metal dinitrogen complexes with comparable structures but with different electron counts should allow for the drawing of a more complete picture of dinitrogen-mediated magnetic properties, and ultimately lead to a deeper understanding of metal dinitrogen complex electronic structures.

From a theoretical standpoint, there has been a great deal in the electronic structures underpinning dinitrogen activation[28,29] as well as bridge-mediated magnetism.[30-32] Our synthetic entry is more recent: our efforts to prepare Cr^{II} analogues of the complexes described in Chapters 2 and 3 for single-molecule magnet investigations, [4,33,34,35] led to the isolation of a dinitrogen-bridged dinuclear Cr^{I} acetylide complex (**4.1**, Figure 4.1).

The (trimethylsilyl)acetylide analogue of this complex was reported in 2008 by Berben and Kozimor after I had isolated **4.1**.[18,36] There, the magnetic susceptibility data for $[(dmpe)_4Cr_2(C_2SiMe_3)_2(\mu\text{-}N_2)]$ were fit to a model where S = ½ centers weakly couple antiferromagnetically. Cyclic voltammograms obtained for the Me_3Si-containing complex indicated that the oxidized product(s) were stable on the electrochemical time scale. Further, density functional calculations performed on a neutral model complex offered a forecast of a *weakened* dinitrogen bond upon *oxidation* of the Cr^{I} centers.[18]

Intrigued by the potential for redox changes to influence dinitrogen activation, we have set out to isolate and study the $[RC_2Cr(\mu\text{-}N_2)CrC_2R]^{n+}$ species in all its chemically available oxidation states. More generally, the work is motivated by the opportunity to establish magneto-structural and electronic correlations in transition metal complexes bridged by small ligands, which in turn can benchmark theoretical modeling for species

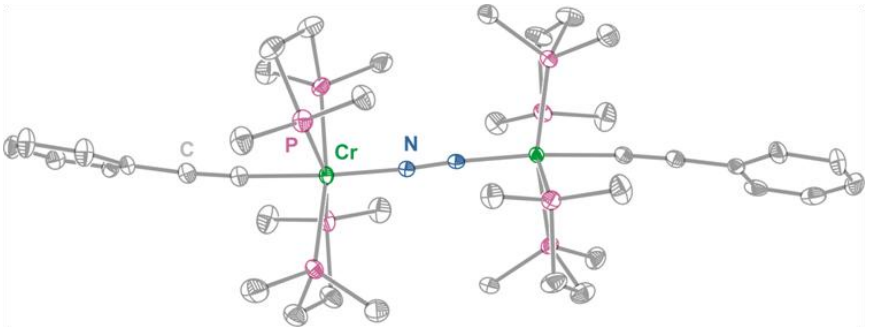

Figure 4.1. Structure of **4.1** rendered with 40% ellipsoids. Green, violet, dark blue and gray ellipsoids represent Cr, P, N, and C atoms, respectively. Hydrogen atoms are omitted for clarity.

with tailored magnetic and electronic properties. Herein, we report the syntheses, characterizations, and initial computational investigations of a structurally related family of $[RC_2Cr(\mu\text{-}N_2)CrC_2R]^{n+}$ (R = Ph, $^{i}Pr_3Si$; n = 0, 1, 2) species, where redox tuning gives rise to significant changes in magnetism, but negligible alteration of the dinitrogen moiety. As will be shown below, experimental data from all three compounds is necessary to *begin* to understand the changes in electronic structure brought about by redox events.

4.2 Division of Labor / Results Dissemination Statement

All experimental work was performed by Wesley Hoffert. Prof. Anthony Rappé carried out the DFT calculations and constructed the spin density and natural orbital plots in Figures 4.12, 4.13, and 4.14. The computed interatomic distances in Table 4.2 were also generated by Prof. Rappé. The bulk of this work was published in *Inorganic Chemistry* in 2010 with the following citation: Hoffert, W. A.; Rappé, A. K.; Shores, M. P., "Unusual Electronic Effects Imparted by Bridging Dinitrogen: an Experimental and Theoretical Investigation." *Inorg. Chem.* **2010,** *49*, 9497-9507. Additional experimental details related to the work presented in this chapter are reported in the Appendix.

4.3 Experimental Section

4.3.1 Preparation of Compounds. Manipulations were performed either inside a dinitrogen-filled glovebox (MBRAUN Labmaster 130) or via Schlenk techniques on dinitrogen manifolds. Pentane was distilled over sodium metal and subjected to three freeze-pump-thaw cycles. Other solvents were sparged with dinitrogen, passed over activated alumina, and degassed prior to use. The preparation of $[(dmpe)_2CrCl_2]$ (dmpe = 1,2-bis(dimethylphosphino)ethane) has been described elsewhere.[37] The reagent

$[CoCp_2]BAr^F_4$ (BAr^F_4 = tetrakis(3,5-bis(trifluoromethylphenyl)borate)) was made by PF_6^- anion metathesis in a manner analogous to the preparation of $[Cp^*_2Fe]BAr^F_4$.[38] All other reagents were purchased commercially and were used without further purification.

$[(dmpe)_4Cr_2(C_2Ph)_2(\mu\text{-}N_2)]$ (4.1). A solution of $[(dmpe)_2CrCl_2]$ (100 mg, 0.236 mmol) in 5 mL of tetrahydrofuran at –78 °C was added to a mixture of phenylacetylene (26 μL, 0.24 mmol) and *n*-BuLi (0.33 mL of a 1.59 M solution in hexanes, 0.53 mmol) in 20 mL of pentane at –78 °C. The green mixture was warmed to 293 K, resulting in a color change to brown. After stirring for 1 hour, the solvent was removed *in vacuo* and the residue was extracted with 25 mL of a 10% (v/v) methylcyclopentane/hexanes solution. The brown solution was concentrated to ca. 15 mL and was placed in a –40 °C freezer for 1 day, resulting in the precipitation of dark brown needle crystals suitable for X-ray analysis. The crystals were isolated by filtration, washed with cold (–40 °C) pentane (3 × 2 mL) and dried under dinitrogen to afford the final product (13 mg, 0.014 mmol, 12%). Absorption spectrum (toluene): λ_{max} (ε_M) 317 (12300), 441 (10400), 543 (sh, 4100), 955 nm (6800 $M^{-1}\cdot cm^{-1}$). IR (solid, mineral oil): ν_{CC} 2027 cm^{-1}. Raman (solution in C_6H_6): ν_{NN} 1685 cm^{-1}. ^1H NMR (C_6D_6): δ 20.50 (br, 10H, Ar–*H*), –3.05 (br, 24H, –PCH_3), –4.56 (br, 8H, –PCH_2), –19.23 (br, 24H, –PCH_3), –22.51 ppm (br, 24H, –PCH_2). Anal calcd. for $C_{40}H_{74}N_2Cr_2P_8$: C, 51.38; H, 7.98; N, 3.00. Found: C, 51.70; H, 7.85; N, 2.67.

$[(dmpe)_4Cr_2(C_2Si^iPr_3)_2(\mu\text{-}N_2)]$ (4.2). A solution of $[(dmpe)_2CrCl_2]$ (515 mg, 1.22 mmol) in 10 mL of tetrahydrofuran at –78 °C was added to a mixture of triisopropylsilylacetylene (0.27 mL, 1.22 mmol) and *n*-BuLi (1.77 mL of a 1.59 molar solution on hexanes, 2.79 mmol) in 20 mL of pentane at –78 °C. As the green mixture

was slowly warmed to 293 K, the color changed to dark red-orange. After stirring for 1 hour, the solvent was removed *in vacuo* overnight and the residue was extracted with 20 mL of pentane and filtered through Celite. The red-orange solution was concentrated to ca. 10 mL and was placed in a –40 °C freezer for crystallization. After 1 day, dark red needle crystals formed. The crystals were isolated by filtration, washed with cold (–40 °C) pentane (2 × 2 mL) and dried under dinitrogen to afford 110 mg of the final product (0.100 mmol, 17%). Crystals suitable for X-ray analysis were obtained by cooling a dilute solution of 4.2 in pentane at –40 °C for 3 days. Absorption spectrum (toluene): λ_{max} (ε_M) 427 (44900), 940 nm (30300 $M^{-1}\cdot cm^{-1}$). IR (solid, mineral oil): ν_{CC} 1944, ν_{CSi} 833 cm^{-1}. Raman (solution in C_6H_6): ν_{NN} 1680 cm^{-1}. ^1H NMR (C_6D_6): δ 2.16 (br, 50H, –PC*H*$_2$ and –Si(C$_3$*H*$_7$)$_3$), –3.71 (br, 24H, –PC*H*$_3$), –4.60 (br sh, 8H, –PC*H*$_2$), –19.95 ppm (br, 24H, –PC*H*$_3$). Anal. calcd. for $C_{46}H_{106}N_2Cr_2P_8Si_2$: C, 50.44; H, 9.75; N, 2.56. Found: C, 50.28; H, 9.68; N, 2.28.

[(dmpe)$_4$Cr$_2$(C$_2$Si^{i}Pr$_3$)$_2$(μ-N$_2$)]BAr$^F_4$ (4.3). To a stirred solution of **4.2** (30 mg, 0.027 mmol) in 3 mL of diethyl ether was added a solution of [Cp$_2$Co]BAr$^F_4$ (28.8 mg, 0.027 mmol) in 3 mL of diethyl ether. The solution immediately turned dark green. After stirring for 5 min, the solution was filtered through a plug of Celite. Pentane (10 mL) was added and the solution was cooled to –40 °C. After 1 day, dark green needle crystals formed. The crystals were isolated by filtration, washed with pentane (2 × 10 mL) and dried under dinitrogen to afford 38 mg (0.019 mmol, 71%) of product. X-ray quality parallelepiped crystals of **4.3**·2 Et$_2$O were grown by layering pentane over a concentrated solution of **4.3** in diethyl ether in a –40 °C freezer for 2 days. Absorption spectrum (diethyl ether): λ_{max} (ε_M) 343 (10410), 361 (10590), 408 (8850), 607 (780), 914 nm (3180

$M^{-1}\cdot cm^{-1}$). IR (solid, mineral oil): ν_{CC} 1963, ν_{CSi} 838 cm^{-1}. Anal. calcd. for $C_{82}H_{128}N_2Cr_2BF_{24}P_8Si_2O$ (**4.3**·Et_2O): C, 48.45; H, 6.35; N, 1.38. Found: C, 48.34; H, 6.41; N, 1.23. Crystals maintained at room temperature release varying amounts of Et_2O; samples used for magnetic studies were ground finely, releasing all solvate molecules.

[(dmpe)$_4$Cr$_2$(C$_2$Si^{i}Pr$_3$)$_2$(μ-N$_2$)](BAr$^F{}_4$)$_2$ (4.4). To a stirred solution of **4.2** (40 mg, 0.037 mmol) in 10 mL of diethyl ether was added a solution of [Cp*$_2$Fe]BAr$^F{}_4$ (86.9 mg, 0.073 mmol) in 5 mL of diethyl ether. The solution first turned green, then dark brown. After stirring for 5 min, the solution was filtered through Celite. Pentane (ca. 20 mL) was added to precipitate a brown solid. The solid was isolated by filtration and washed with pentane (2 × 10 mL) to remove any trace of [Cp*$_2$Fe], yielding 75 mg (0.027 mmol, 73%) of product. X-ray quality parallelepiped crystals of **4.4**·3.5 THF were grown by layering pentane over a concentrated solution of **4.4** in tetrahydrofuran in a –40 °C freezer for 2 days. Absorption spectrum (diethyl ether): λ_{max} (ε_M) 349 (10440), 446 (5280), 904 nm (7000 $M^{-1}\cdot cm^{-1}$). IR (solid, mineral oil): ν_{CC} 1982, ν_{CSi} 838 cm^{-1}. Raman (tetrahydrofuran): ν_{NN} 1710 cm^{-1}. Anal. calcd. for $C_{110}H_{130}N_2B_2Cr_2F_{48}P_8Si_2$: C, 46.80; H, 4.65; N, 0.99. Found: C, 46.67; H, 4.74; N, 0.90.

4.3.2 X-ray Structure Determinations. All compounds reported herein were characterized by single crystal X-ray analysis (Table 4.1). Single crystals were coated in Paratone oil prior to removal from the glovebox. Crystals to be investigated at low temperature were supported on Cryoloops, then mounted on a Bruker Kappa Apex 2 CCD diffractometer under a stream of cold dinitrogen. For the room-temperature data set for **4.3**, the crystal was encased in epoxy and supported on a glass fiber before being mounted on the diffractometer under a stream of dinitrogen maintained at 296 K. All data

collections were performed with Mo Kα radiation and a graphite monochromator. Initial lattice parameters were determined from a minimum of 189 reflections harvested from 36 frames, and data sets were collected with complete coverage and four-fold redundancy. Data were integrated and corrected for absorption effects with the Apex 2 software package.[39] Structures were solved by direct methods and refined with the SHELXTL software package.[40] Displacement parameters for all non-H atoms were refined anisotropically with the exception of disordered C, P and F atoms as noted in the respective cif files. Hydrogen atoms were added at the ideal positions and were refined using a riding model where the isotropic displacement parameters were set at 1.2 times those of the attached carbon atom (1.5 times the attached carbon atom for methyl groups).

4.3.3 Magnetic Susceptibility Measurements. Magnetic susceptibility data were collected with a Quantum Design MPMS-XL SQUID magnetometer. Samples were loaded into gelatin capsules and inserted into straws prior to analysis. The straws were sealed in plastic bags prior to removal from the glovebox, and were quickly loaded into the instrument to minimize exposure to air. Diamagnetic corrections were applied by using Pascal's constants and by subtracting the diamagnetic susceptibility from an empty sample holder. Susceptibility data were fit with theoretical models using a relative error minimization routine (julX 1.41).[41] Zero field splitting parameters obtained with julX are based on the spin Hamiltonian $\hat{H} = \sum_{i=1}^{ns} D_i[S_{z,i}^2 - 1/3 S_i(S_i+1) + E_i/D_i(S_{x,i}^2 - S_{y,i}^2)] + \sum_{i=1}^{ns} g\beta\vec{S}_i \cdot \vec{B}$.

Fits of the magnetization data were obtained with the ANISOFIT[42] program and are based on the spin Hamiltonian $\hat{H} = D\hat{S}_z^2 + E(\hat{S}_x^2 + \hat{S}_y^2) + g_{iso}\beta\vec{S} \cdot \vec{B}$.

Table 4.1. Crystallographic data[a] for compounds $[(dmpe)_4Cr_2(PhC_2)_2(\mu\text{-}N_2)]\cdot C_6H_{12}$ (**4.1**·C_6H_{12}), $[(dmpe)_4Cr_2(^iPr_3SiC_2)_2(\mu\text{-}N_2)]$ (**4.2**), $[(dmpe)_4Cr_2(^iPr_3SiC_2)_2(\mu\text{-}N_2)]BAr^F{}_4\cdot 1.5\ Et_2O$ (**4.3**·$1.5Et_2O$), $[(dmpe)_4Cr_2(^iPr_3SiC_2)_2(\mu\text{-}N_2)]BAr^F{}_4$ (**4.3**) and $[(dmpe)_4Cr_2(^iPr_3SiC_2)_2(\mu\text{-}N_2)](BAr^F{}_4)_2\cdot 3.5$ THF (**4.4**·3.5THF).

	4.1·C_6H_{12}	**4.2**	**4.3**·$1.5Et_2O$ (100 K)	**4.3** (296 K)	**4.4**·3.5THF
formula	$C_{46}H_{86}Cr_2N_2P_8$	$C_{46}H_{104}Cr_2N_2P_8Si_2$	$C_{84}H_{133}BCr_2F_{24}N_2P_8Si_2O_{1.5}$	$C_{78}H_{118}BCr_2F_{24}N_2P_8Si_2$	$C_{124}H_{158}B_2Cr_2F_{48}N_2P_8Si_2O_{3.5}$
M_r	1018.93	1093.25	2069.67	1958.49	3072.98
T (K)	100(2)	100(2)	100(2)	296(2)	100(2)
space group	$P2_1/c$	$Pbca$	$P2_1/c$	$P2_1/c$	$P\bar{1}$
a (Å)	12.3602(2)	18.0902(5)	14.5070(4)	14.6116(6)	14.2386(5)
b (Å)	12.7197(2)	19.6306(5)	29.6682(9)	30.4203(13)	17.1753(6)
c (Å)	34.7651(6)	34.351(1)	24.1919(7)	24.9312(10)	31.8445(11)
α (°)	90	90	90	90	88.101(2)
β (°)	93.298(1)	90	96.531(2)	96.848(2)	86.562(2)
γ (°)	90	90	90	90	69.587(2)
V (Å^3)	5457.0(2)	12198.8(6)	10344.5(5)	11002.6(8)	7248.8(4)
Z	4	8	4	4	2
R_{int}	0.075	0.094	0.063	0.060	0.068
R_1[b] ($I>2\sigma(I)$)	0.046	0.062	0.065	0.077	0.093
wR_2[c] (all data)	0.113	0.180	0.209	0.220	0.277

[a] Obtained with graphite-monochromated Mo Kα (λ = 0.71073 Å) radiation. [b] $R_1 = \Sigma||F_o| - |F_c||/ \Sigma|F_o|$. [c] wR2 = $\{\Sigma[w(F_o^2 - F_c^2)^2/ \Sigma[w(F_o^2)^2]\}^{0.5}$.

4.3.4 Other Physical Measurements. UV-Vis absorption spectra were obtained in airfree cuvettes with a Hewlett-Packard 8453 spectrophotometer. Vis-Near IR spectra were recorded using a Cary 500 spectrophotometer. Infrared spectra were measured with a Nicolet 380 FT-IR using mineral oil mulls sandwiched between NaCl plates. ^{1}H NMR spectra were recorded using a Varian INOVA instrument operating at 300 MHz. EPR spectra were obtained using a continuous wave X-band Bruker EMX 200U instrument outfitted with a liquid nitrogen cryostat. Raman spectra were acquired with a Nicolet 760 spectrometer equipped with an FT-Raman module using an incident laser wavelength of 1064 nm. Cyclic voltammetry was done in 0.1 M solutions of $(Bu_4N)PF_6$ in tetrahydrofuran unless otherwise noted. The voltammograms were recorded with a CH Instruments potentiostat (either model 1230A or 660C) using a 0.25 mm Pt disk working electrode, Ag/Ag^+ reference electrode, and a Pt mesh auxiliary electrode. All voltammograms shown were measured with a scan rate of 0.1 V/s. Reported potentials are referenced to the $[Cp_2Fe]^+/[Cp_2Fe]$ redox couple and were determined by adding ferrocene as an internal standard at the conclusion of each electrochemical experiment. Elemental analyses for compounds **4.1**, **4.2**, and **4.4** were performed by Robertson Microlit Laboratories in Madison, NJ. The elemental analysis for **4.3** was performed by the microanalytical laboratory at the University of California at Berkeley.

4.3.5 Electronic Structure Calculations. Restricted and unrestricted B3LYP hybrid density functional studies[43] were carried out in the G03 suite of electronic structure codes.[44] Geometry optimized structures for the triplet, quartet, and quintet states of **4.2**, 4.3, and 4.4 utilized the X-ray coordinates for **4.2**, **4.3**·1.5 Et_2O, and **4.4**·3.5 THF as initial input (sp^3 C–H bond distances adjusted to 1.096 Å and sp^2 C–H bonds adjusted to

1.090 Å). Metric parameters are collected in Table 4.2 and calculated coordinates are provided as supplemental material. The LANL2[45] basis sets and effective core potentials were used for Si, P and Cr; H, C, and N were described with a 6-31g* model.[46-49] ORCA[50] CAS-SORCI computations used smaller models of compounds **4.3** and **4.4** (**4.3***, **4.4***) wherein the dmpe methyl and acetylide $^{i}Pr_3Si$ susbtituents were replaced with hydrogens directed along the P–C and C–Si bond vectors with P–H and C–H bond distances of 1.42 and 1.06 Å, respectively. The CAS-SORCI computations did not utilize effective core potentials and the 6-31g basis set was used for all atoms except Cr. For Cr the Ahlrichs-DZ basis[51] was used and for the bridging nitrogen atoms a set of polarization functions were added. B3LYP UKS quintet spin natural orbitals for **4.4*** were used as a starting guess for a [9,11] CAS calculation on **4.3*** that equally weighted the lowest two doublet states as well as the lowest two quartets. This model was chosen to prevent artificial symmetry breaking and provide an unbiased reference space for the subsequent CI/perturbation theory step.

4.4 Results

4.4.1 Syntheses and characterizations of the $[RC_2Cr(\mu\text{-}N_2)CrC_2R]^{n+}$ complexes. It has been shown that $[(dmpe)_2Cr^{II}(C_2R)_2]$ complexes can be prepared by addition of two equivalents of LiC_2R to $[(dmpe)_2CrCl_2]$.[18,52] However, Berben demonstrated that a dinuclear Cr^{I} dinitrogen-bridged acetylide complex could be synthesized by mixing $[(dmpe)_2CrCl_2]$ with stoichiometric LiC_2SiMe_3 and excess *n*-butyllithium; the latter acts as a reducing agent. Dinitrogen dissolved in the solvents caps and bridges the reduced $Cr(dmpe)_2(C_2R)$ moieties. The syntheses of **4.1** and **4.2** were adapted from Berben's

Table 4.2. Selected measured and calculated (comp) interatomic distances (Å) and angles (deg) for the structures of $[(dmpe)_4Cr_2(^iPr_3SiC_2)_2(\mu\text{-}N_2)]$ (**4.2**), $[(dmpe)_4Cr_2(^iPr_3SiC_2)_2(\mu\text{-}N_2)](BAr^F{}_4)\cdot 1.5Et_2O$ (**4.3**$\cdot 1.5Et_2O$), **4.3**, and $[(dmpe)_4Cr_2(^iPr_3SiC_2)_2(\mu\text{-}N_2)](BAr^F{}_4)_2\cdot 3.5THF$ (**4.4**$\cdot 3.5$THF).

	4.2	**4.2** (comp)	**4.3**$\cdot 1.5Et_2O$ (100 K)	**4.3** (296 K)	**4.3** (comp)	**4.4**$\cdot 3.5$THF	**4.4** (comp)
Cr–N	1.881[2][b]	1.929	1.857[7]	1.887[5]	2.05	1.88[1]	1.925
N≡N	1.187[5]	1.183	1.195[5]	1.164[3]	1.156	1.181[8]	1.185
Cr–C	2.053[2]	2.09	2.051[8]	2.041[6]	2.044	2.054[3]	2.054
Cr···Cr	4.946[3]	5.038	4.9083[10]	4.9362[8]	5.256	4.9313[15]	5.034
C≡C	1.231[4]	1.244	1.220[4]	1.223[6]	1.242	1.216[4]	1.24
C–Si	1.815[3]	1.842	1.85[1]	1.82[2]	1.838	1.842[1]	1.875
Cr–P	2.32[3]	2.32[a]	2.35[1]	2.37[2]	2.35[a]	2.42[2]	2.42[a]
P–Cr–N	96.1[8]	95.9	97[2]	96[2]	94.99	96[2]	96.58
P–Cr–C	84[1]	84.11	83[2]	84[1]	85.01	84[2]	83.42
C–Cr–N	178.2[5]	179.28	178.15[8]	177[1]	179.22	178.8[9]	179.12
Cr–N≡N	179.0[4]	179.34	178.0[3]	177.5[2]	179.66	178[1]	179.27
Cr–C≡C	178[2]	179.13	179.0[5]	178.9[8]	178.91	178.3[7]	178.78
C≡C–Si	176[1]	178.15	175.8[4]	178.7[3]	178.54	178[1]	178.61
dmpe–Cr(1)–N	97.8[5]		99.2[4]	98.2[5]		98.5[4]	
dmpe–Cr(2)–N	97.9[5]		99.8[4]	99[1]		98.5[4]	

[a] The Cr–P distances were constrained to be the same as those from the X-ray structure. [b] Square brackets[ ] represent esds for averaged metric parameters.

procedure; we find that quantitative removal of LiCl from the reaction mixture requires pentane extraction followed by filtration through Celite.[53]

Complexes **4.1** and **4.2** have been fully characterized structurally and spectroscopically. Despite the paramagnetism exhibited by these compounds (*vide infra*), resonances in the ^{1}H NMR spectra of **4.1** and **4.2** can be assigned on the basis of approximate integration (Figures 4.2 and 4.3, respectively). For brevity, and because of the structural similarities between **4.1** and **4.2**, we will focus discussion on the ^{i}Pr$_3$Si analogue **4.2**.

Shown in Figure 4.4, the cyclic voltammogram obtained for **4.2** in tetrahydrofuran shows two well defined, reversible waves centered at –1.37 V and –1.64 V (all potentials vs. Fc^+/Fc). These one-electron reversible redox waves are assignable to mono- and di-oxidation of the neutral compound to formally Cr^ICr^{II} and $Cr^{II}Cr^{II}$ complexes, respectively. The peak-to-peak separations in the cyclic voltammograms imply a comproportionation constant for the reaction $[RC_2Cr^I(\mu\text{-}N_2)Cr^IC_2R] + [RC_2Cr^{II}(\mu\text{-}N_2)Cr^{II}C_2R]^{2+} \rightleftharpoons 2[RC_2Cr^I(\mu\text{-}N_2)Cr^{II}C_2R]^+$ as $\sim 10^{4.5}$, a value which suggests Robin-Day Class II behavior for the mono-cationic species.[54] Diethyl ethereal solutions of **4.2** can be cleanly oxidized by stoichiometric $[Cp_2Co]^+$ or $[Cp^*_2Fe]^+$ to afford the one- and two-electron oxidized complexes **4.3** and **4.4**, respectively.

The solid state infrared spectra for all the dinitrogen-bridged complexes exhibit a single absorption in the acetylide stretching region. In redox-related **4.2**–**4.4**, the peak shifts higher in energy by 19 cm^{-1} with each successive oxidation. The solution Raman spectra of **4.2** and **4.4** show strong resonances for the dinitrogen symmetric stretch,[55] indicating that the homovalent complexes are stable and effectively centrosymmetric in solution.[56]

4.4.2 X-ray Crystallography. The crystal structures of dinitrogen complexes 4.2–4.4 (Figure 4.5) reveal essentially octahedral coordination geometries around each chromium ion. Selected bond distances and angles are presented in Table 4.2. The acetylide and bridging dinitrogen ligands are located trans to each other while the equatorial positions are occupied by the two bidentate dmpe ligands. Viewed along the Cr–N–N–Cr axis, the four dmpe ligands are offset rotationally such that the methyl substituents for the phosphine ligands surrounding one Cr atom fit snugly between the methyl substituents for the dmpe ligands coordinated to the other Cr atom. Notwithstanding, steric interactions between the methyl substituents cause the dmpe ligands to distort slightly from the center of the molecule. The R–C≡C–Cr–N–N–Cr–C≡C–R skeleton is nearly linear. The N–N bond distance of 1.187(5) Å for **4.2** suggests that the bridging ligand is mildly activated with respect to free dinitrogen (1.0971(2) Å).[57] The averaged Cr–P bond distances for **4.2** are similar to those reported for trans-$[Cr(dmpe)_2(CO)_2]BPh_4$,[58] which represents the only structurally characterized mono-valent $[Cr(dmpe)_2]$ complex prior to Berben and Kozimor's report.[18] The averaged Cr–N distance of 1.881(2) for **4.2** lies between the reported Cr–N distances observed for N_2–bridged zero-[59] and tri-valent[60] chromium complexes. Skeletal bond distances and angles are very similar to those reported for the trimethylsilyl analogue:[18] the N–N bond length for **4.2** is the same within experimental error, and the mean Cr–P distances differ by less than 0.01 Å. Comparing the oxidized complex salts **4.3** and **4.4** to the neutral complex **4.2**, the Cr–P interatomic distances are the same within experimental uncertainties for **4.2** and **4.3** and are slightly longer for **4.4** (Table 4.2). The dicationic complex **4.4** shows Cr–P distances that are comparable to $[Cr^{III}(dmpe)_2Cl_2]BPh_4$,[58] and distances for **4.3** are intermediate between **4.2**

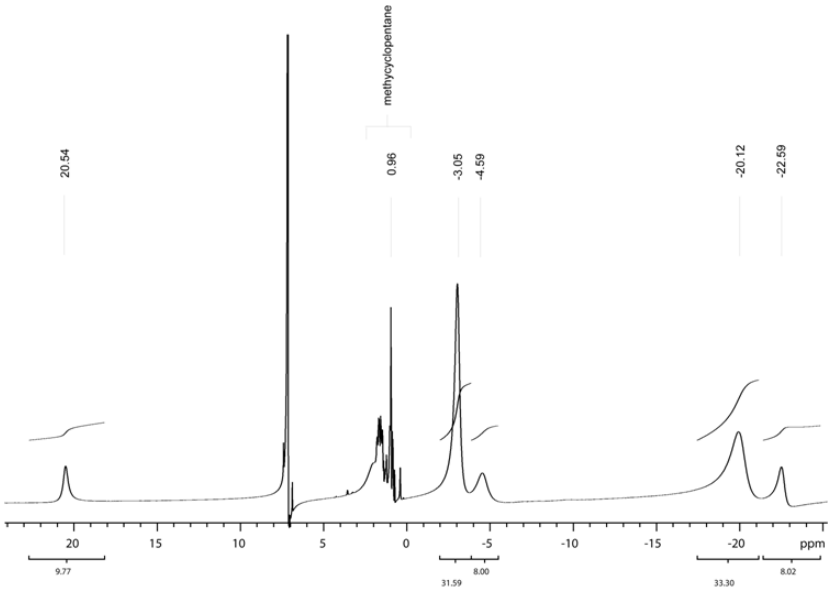

Figure 4.2. ^{1}H NMR spectrum of 4.1 taken in C_6D_6 at ambient temperature with a 300 MHz spectrometer (see experimental section in text). A minimum of 512 transients were recorded with an acquisition time of 0.5 s per transient with no acquisition delay time.

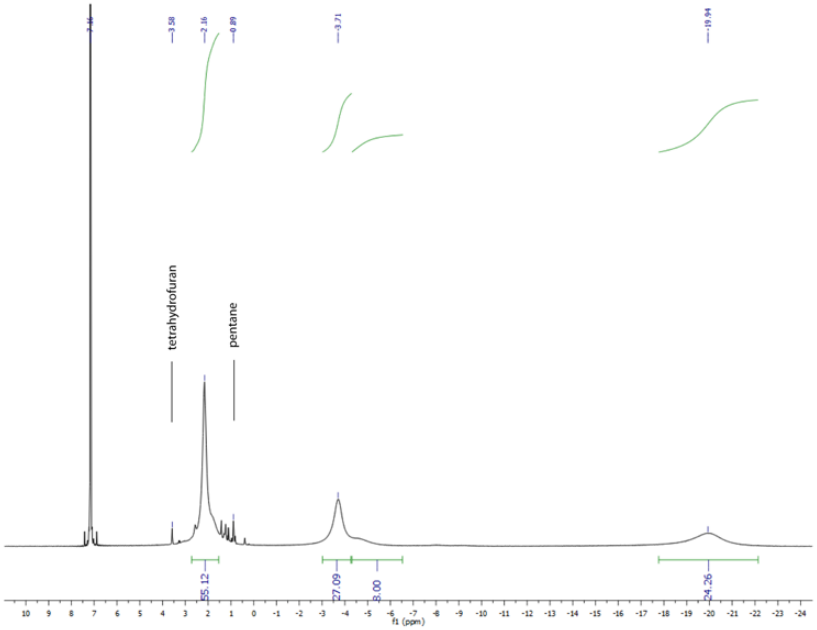

Figure 4.3. ^{1}H NMR spectrum of 4.2 taken in C_6D_6 at ambient temperature with a 300 MHz spectrometer (see experimental section in text). A minimum of 512 transients were recorded with an acquisition time of 0.5 s per transient with no acquisition delay time.

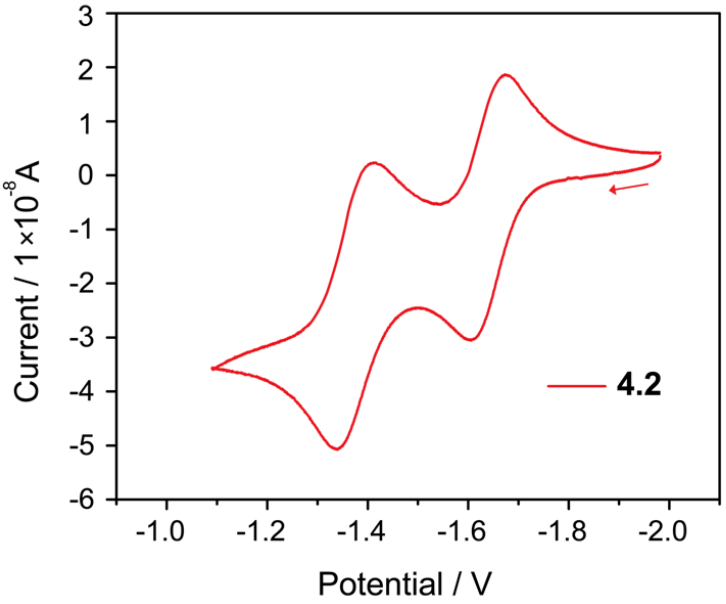

Figure 4.4. Cyclic voltammogram of the neutral dinuclear complex **4.2** obtained in tetrahydrofuran.

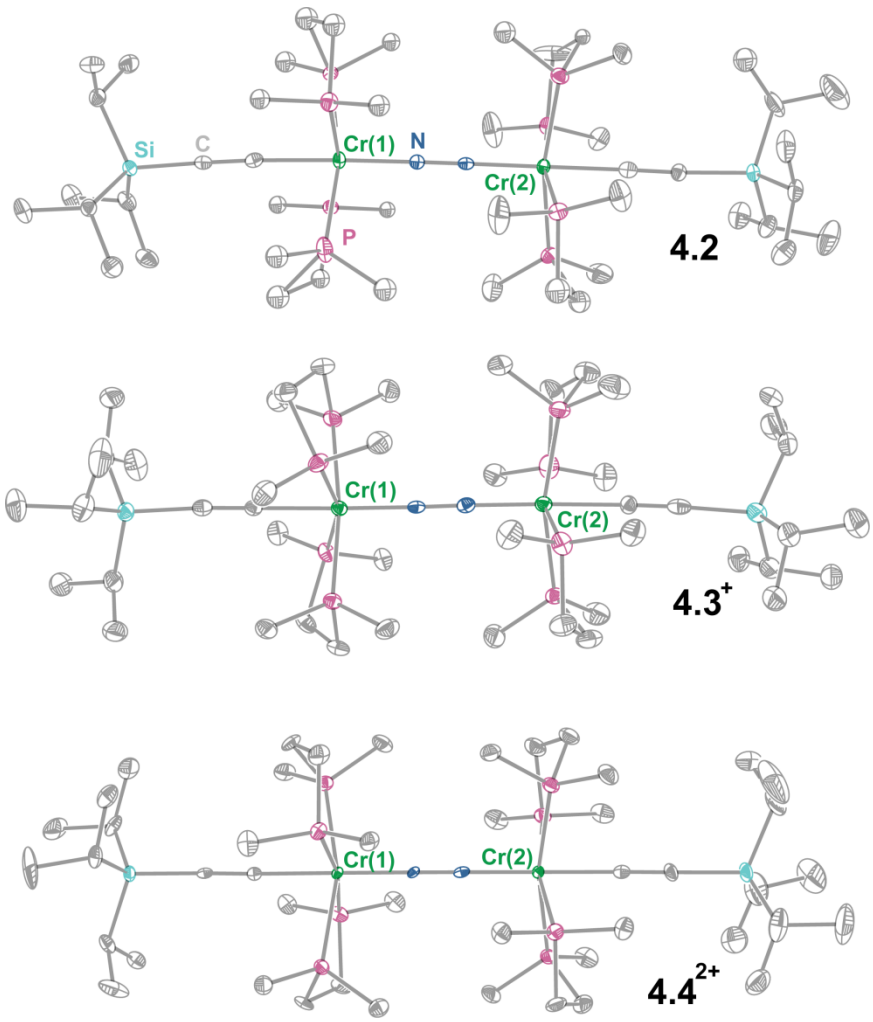

Figure 4.5. Crystal structures of the $[Cr_2(\mu\text{-}N_2)]^{n+}$ (n = 0, 1, 2) complexes in compounds **4.2**, **4.3**·1.5Et_2O and **4.4**·3.5THF, rendered with 40% ellipsoids. Green, violet, dark blue, light blue, and gray ellipsoids represent Cr, P, N, Si and C atoms, respectively. Hydrogen atoms, minor components of disordered atoms, charge balancing anions and solvent molecules are omitted for clarity. None of these complexes reside on sites of higher crystallographic symmetry.

and **4.4**. With the exception of the Cr–P bond distances, the structures are nearly superimposable despite the different formal oxidation states of the Cr ions. Significantly, we find that the Cr–N and N–N bond distances vary only slightly within this redox-related family.

Regarding monooxidized **4.3** specifically, we note only minor differences between the structures obtained at 100 and 296 K. First, where the low temperature structure contains diethyl ether solvate molecules; the high temperature structure exhibits void spaces. Second, the averaged Cr–P bond distances are the same for both Cr centers at 100 K (Cr(1)–P = 2.347(7) Å, Cr(2)–P = 2.35(1) Å), but are slightly different at the 1σ estimated standard deviation[61] at 296 K (Cr(1)–P = 2.365(9) Å, Cr(2)–P = 2.39(1) Å). Given the relatively large uncertainties in metric parameters and the difference in solvation, we do not find strong evidence for valence localization in the room temperature structure; however, bond distances in the low temperature structure are consistent with delocalization of chromium valence.

4.4.3 Magnetic Properties. Shown in Figure 4.6, the $\chi_M T$ product for **4.2** decreases only slightly upon cooling to 0.96 $cm^3 \cdot K \cdot mol^{-1}$ at 16 K, then drops off more precipitously to 0.34 $cm^3 \cdot K \cdot mol^{-1}$ at 2 K. Using julX[41] to fit the susceptibility data with a spin Hamiltonian that incorporates a zero-field splitting (ZFS) parameter, the downturn in susceptibility below 16 K can be reproduced to afford a D value of +8.34 cm^{-1} and a g value of 1.99. In contrast, fitting the susceptibility data to a model where the formally Cr^I centers couple antiferromagnetically affords unreasonably large g values (Table 4.3). The AF fits were generated by assuming two independent spin centers were present in the molecule. No zero-field splitting parameter was included in the refinement, but

temperature dependent susceptibility behavior could be reproduced by allowing an exchange parameter (J) to refine freely along with g and TIP. For each fit, the g values for each Cr center were forced to be equal. The g values listed below are all significantly higher than the Landé g value of 2.0023 in addition to being inconsistent for redox-related **4.2-4.4**, which is unusual for early transition metal ions. In the AF fit for **4.3**, the J value obtained is unreasonably high when compared alongside the other complexes, and TIP values for all complexes range seem either unreasonably low or high. Fixing the TIP value at an acceptable level (ca. 400 $\times 10^{-6}$ emu) resulted in poorer fits. The magnetization plot for **4.2** (Figure 4.6, right) exhibits non-superposition of the isofield data, a hallmark of a magnetically anisotropic ground state. Fitting the magnetization data with ANISOFIT[42] yields a ZFS parameter of D = +8.22 cm^{-1} with g = 1.95, values that are consistent with best fits to the magnetic susceptibility data.

Qualitatively, the susceptibility data for **4.4** is similar to that observed for **4.2**. At 300 K, the $\chi_M T$ product has a value of 3.09 $cm^3 \cdot K \cdot mol^{-1}$. This value hardly changes as the temperature is reduced, dropping to 2.95 $cm^3 \cdot K \cdot mol^{-1}$ at 2 K. Fits of this data to an $S = 2$ model afford a reasonable g value of 1.99. In contrast to **4.2**, the magnetic data for **4.4** does not appreciably decrease at low temperatures, and all the magnetization data collected at varying fields are superimposable upon the S = 2 Brillouin function, indicating the absence of ZFS in the di-oxidized compound (Figure 4.7).

In contrast to the nearly temperature invariant behavior of **4.2** and **4.4**, the susceptibility data for complex **4.3** show a steady decrease in $\chi_M T$ upon cooling, from 1.64 $cm^3 \cdot K \cdot mol^{-1}$ at 300 K to 0.75 $cm^3 \cdot K \cdot mol^{-1}$ at 105 K, followed by a milder decrease to 0.57 $cm^3 \cdot K \cdot mol^{-1}$ at 16 K. Below 16 K, the susceptibility drops sharply to 0.42 $cm^3 \cdot K \cdot mol^{-1}$

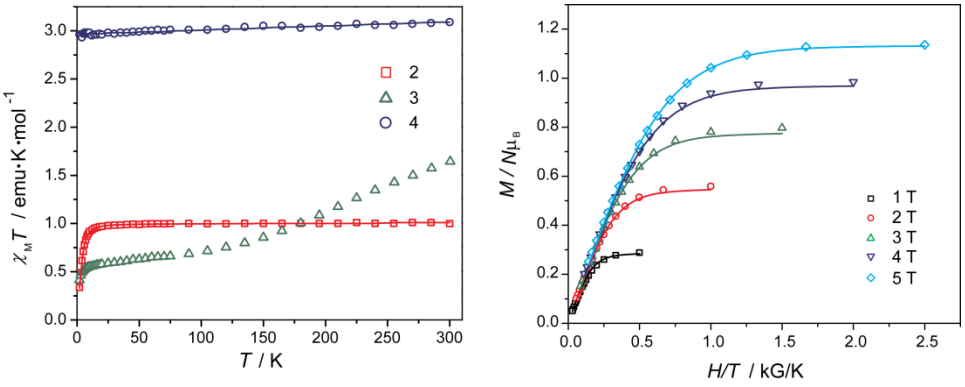

Figure 4.6. Left: temperature dependence of the magnetic susceptibility and best fits (solid lines) for compounds **4.2**, **4.3**, and **4.4**, obtained at a measuring field of 1000 G. Right: magnetization behavior and fit for compound **4.2**. See text for details of the fitting procedures.

Table 4.3. Antiferromagnetic (AF) fits to the DC susceptibility data for complexes **4.1**, **4.2**, **4.3**, and **4.4**.

	Data (K)	Range	g	J (cm^{-1})	TIP emu)	(1×10^{-6}	Relative error
AF model for **4.1**	2-300		2.36	–1.4	590		0.011
AF model for **4.2**	2-300		2.33	–1.6	0.0		0.015
AF model for **4.3**	18-300		2.38	–130	1800		0.027
AF model for **4.4**	2-300		2.46	–0.04	1.3		0.033

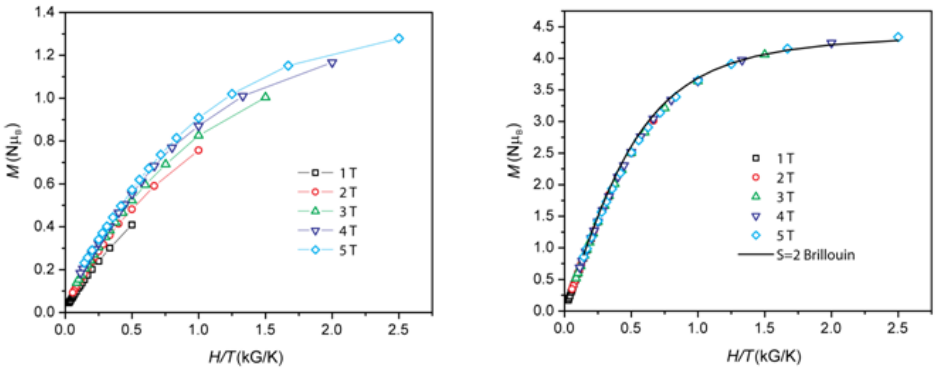

Figure 4.7. Magnetization behavior for **4.3** (left) and **4.4** (right). Colored lines between data points (i.e. not the Brillouin functions) are guides to the eye only.

at 2 K. As with **4.2**, the non-superposition of the isofield data in the reduced magnetization plot confirms the presence of ZFS (Figure 4.7), but satisfactory fits using ANISOFIT have not been obtained, likely owing to the lack of a well-defined ground state (*vide infra*). The low temperature/high field magnetization appears to saturate at approximately 1.3 $N\mu_B$,[6263] a value which is consistent with a mostly filled $S = ½$ ground state. The magnetization and low field susceptibility data agree within 0.02 $cm^3 \cdot K \cdot mol^{-1}$, and are slightly higher than what is predicted for an $S = ½$ ground state at low temperatures (1.0 $N\mu_B$ and 0.375 $cm^3 \cdot K \cdot mol^{-1}$ if $g = 2.00$). We note that the susceptibility and magnetization data obtained for all compounds, including **4.3**, are consistent from sample to sample.

X-band EPR spectra were collected for compounds **4.2**–**4.4** between 293 and 105 K to further investigate the magnetic properties of the complexes as well as to (attempt to) obtain independent measures of g values. Compounds **4.2** and **4.4** are effectively EPR-silent (Figures 4.8 and 4.9). The spectra feature only miniscule signals at $g \sim 2$ which vary in intensity from sample to sample, consistent with the formation of trace impurities during sample preparation. The low signal-to-noise ratios in the spectra of **4.2** and **4.4** relative to **4.3** indicate that any paramagnetic impurities are not making significant contributions to the magnetic susceptibility data (Figure 4.6). Meanwhile, in the solid state spectrum for **4.3** obtained at 293 K (Figure 4.10), a faint, broad signal centered at $g_{iso} = 2.00$ is observed. As the temperature is lowered to ca. 175 K, the intensity of the signal begins to increase. At 155 K, the signal begins to develop some rhombicity; at 105 K three resolved signals are observed at $g_\perp = 2.01$ and 1.96 and $g_\parallel = 1.74$. The appearance

of the $g_{\|}$ signal tracks with the susceptibility drop-off in the variable temperature magnetic data as well as the inflection point in the Weiss plot for **4.3** (Figure 4.11).

4.4.4 Electronic Structure Calculations. To better correlate oxidation state changes to the observed structural and magnetic properties, we undertook a series of electronic structure calculations on **4.2**–**4.4**, including geometry optimization. In order to enforce proper ligand-field effects, Cr–P distances were constrained to experimental values. The computed metrics of the triplet and quintet states of **4.2** and **4.4**, respectively, are in substantial agreement with experiment (Table 4.2). Computed Cr–X bond distances are systematically long. We are able to computationally reproduce the observed relative insensitivities of the N–N and Cr–N distances to di-oxidation. Angular metrics are in good agreement with the X-ray data.

The UKS[64] net spin density plots for **4.2**–**4.4** are presented in Figure 4.12. The parent complex **4.2** (Figure 4.12a) indicates orthogonal d-π* character in the singly occupied orbitals of the low spin d^5-d^5 electronic configuration–hence a triplet ground state, in agreement with the computations of Berben and Kozimor. A higher lying singlet state, wherein the d–π* orbitals are singlet coupled, is anticipated based on an O_2 bonding model. An $m_S = 0$ broken symmetry state solution is computed to be 17 kcal/mol above the triplet ground state. For reference, the $^1\Delta$ state of O_2 occurs 23 kcal/mol above the triplet ground state.[65] For **4.4**, the net spin density plot (Figure 4.12e) suggests oxidation occurs at each metal center, exposing orthogonal singly-occupied dδ orbitals. The staggered orientation of the dmpe ligands causes the cloverleaf pattern of one dδ to line

up with the nodal surface of the other when viewed down the Cr–Cr axis. A set of four mutually orthogonal d orbitals (two dδ, two dπ) gives rise to a quintet ground state. A

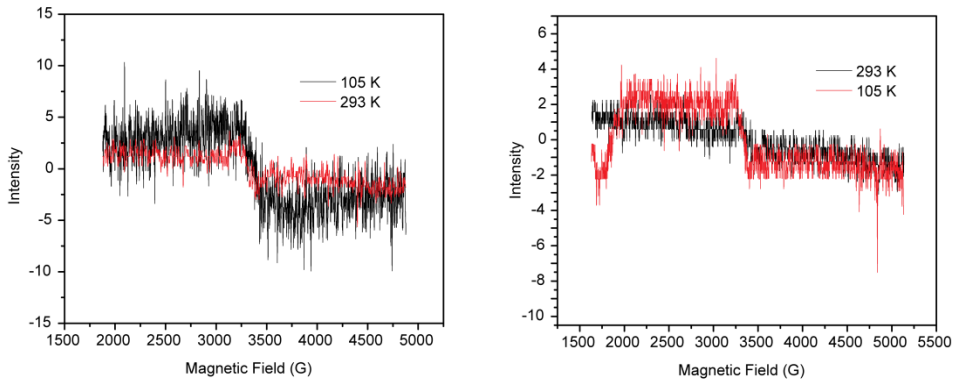

Figure 4.8. Solid state (left; S/N = 1.5 @ 293K, 1.8 @ 105K) and methylcyclopentane solution/glass (right; S/N = 1.7 @ 293 K, 2.1 @ 105 K) X-band EPR spectra of **4.2**. For comparison, the signal to noise ratio for the EPR spectrum of solid **4.3** is 437.7 at 105 K and is 13 at 293 K.

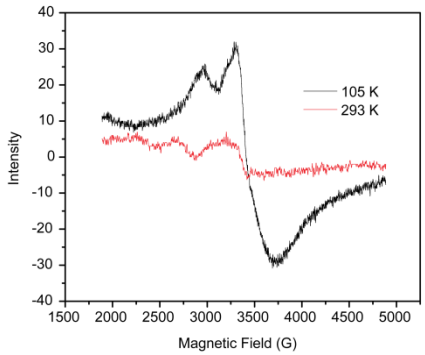

Figure 4.9. Solid state X-band EPR spectra for 4.4 at 105 K (S/N = 20) and 293 K (S/N = 13).

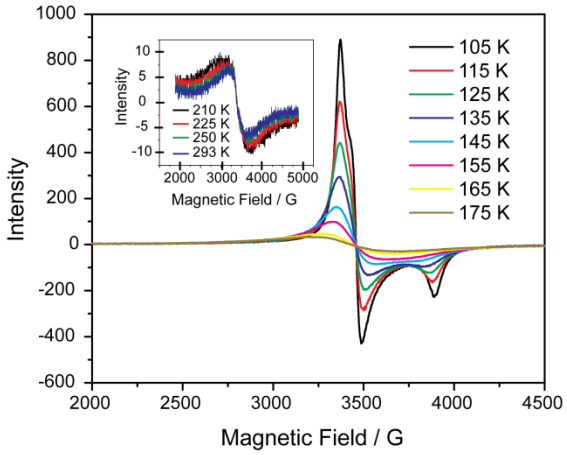

Figure 4.10. Solid state variable temperature EPR spectra of compound **4.3** (105–175 K). Inset: high temperature spectra of **4.3** (210–293 K).

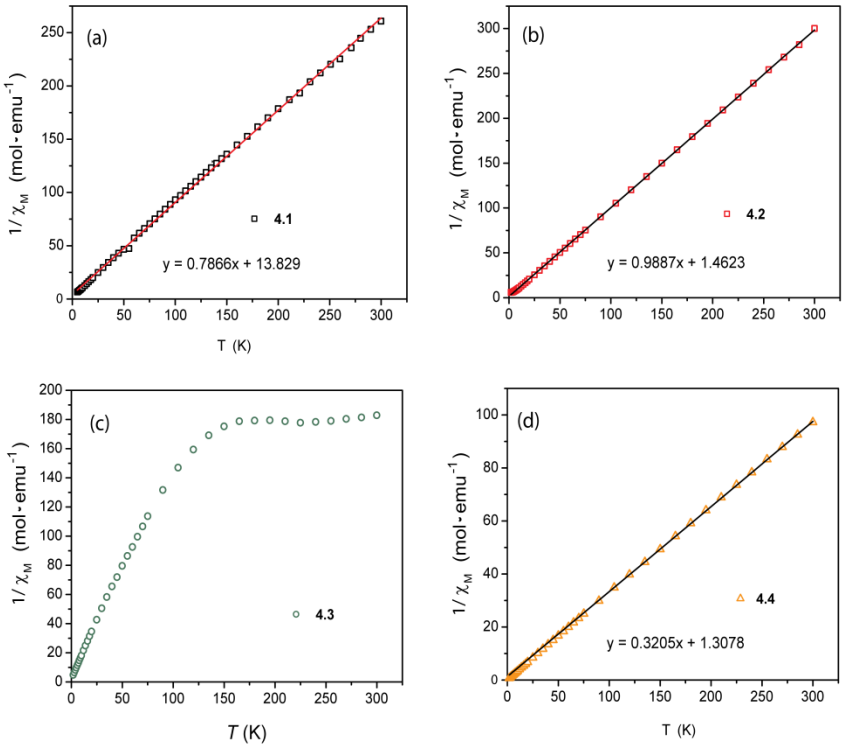

Figure 4.11. Weiss plots for **4.1** (a), **4.2** (b), **4.3** (c), and **4.4** (d). Linear regressions were calculated from data taken between 100 and 300 K. The Curie constants for **4.1** and **4.2** are 1.3 and 1.0 $cm^3 \cdot K \cdot mol^{-1}$, respectively. For **4.4**, the Curie constant was found to be 3.1 $cm^3 \cdot K \cdot mol^{-1}$.

broken symmetry $m_S = 0$ state model is computed to occur at 14 kcal/mol above the quintet.

These spin-density based descriptions of **4.2** and **4.4** are supported by the fractionally occupied UKS spin natural orbitals. For **4.2** the dδ orbitals are nearly doubly occupied (Figures 4.13a and 4.13b) whereas for **4.4** (Figures 4.14c and 4.14d) the dδ orbitals have occupancies near 1. Consistent with Berben's and Kozimor's report, the highest significantly occupied natural orbitals for **4.2** (Figures 4.13e and 4.13f) display N–N π bonding and Cr–N π* character. For **4.2**, the fractionally occupied UKS natural orbitals (Figures 4.13c, 4.13d, 4.13g, and 4.13h) are strongly suggestive of the first and second natural orbitals of a strongly correlated spin-paired bonding model for a pair of orthogonal Cr–N pi bonds. For **4.4**, a similar picture emerges; here the fractional occupancies are 1.88 and 0.12 (Figures 4.14a, 4.14b, 4.14g, and 4.14h). Although natural orbital analysis does not provide orbital energies, the absolute orbital occupations of **4.2** and **4.4** are suggestive of the relative energies. The Cr δ orbitals, having the highest occupancies of 1.99 electrons, appear to be lowest in energy in **4.2** whereas the Cr–N π orbitals show the highest occupancies in **4.4**. By including di-oxidized **4.4** in our study, we find that oxidation involves removal of an electron from each of the dδ orbitals in **4.2** and the highest occupied orbitals retain N–N π bonding character.

For the mixed-valent complex **4.3**, the B3LYP DFT model computes the quartet state (Figure 4.12b) to be significantly lower in energy than the lowest doublet, in contrast with the variable temperature magnetic susceptibility data. A symmetrically delocalized doublet wherein orthogonal dπ orbitals are antiferromagnetically coupled is computed to arise at 16 kcal/mol (Figure 4.12c), and a localized state where excess α spin density is

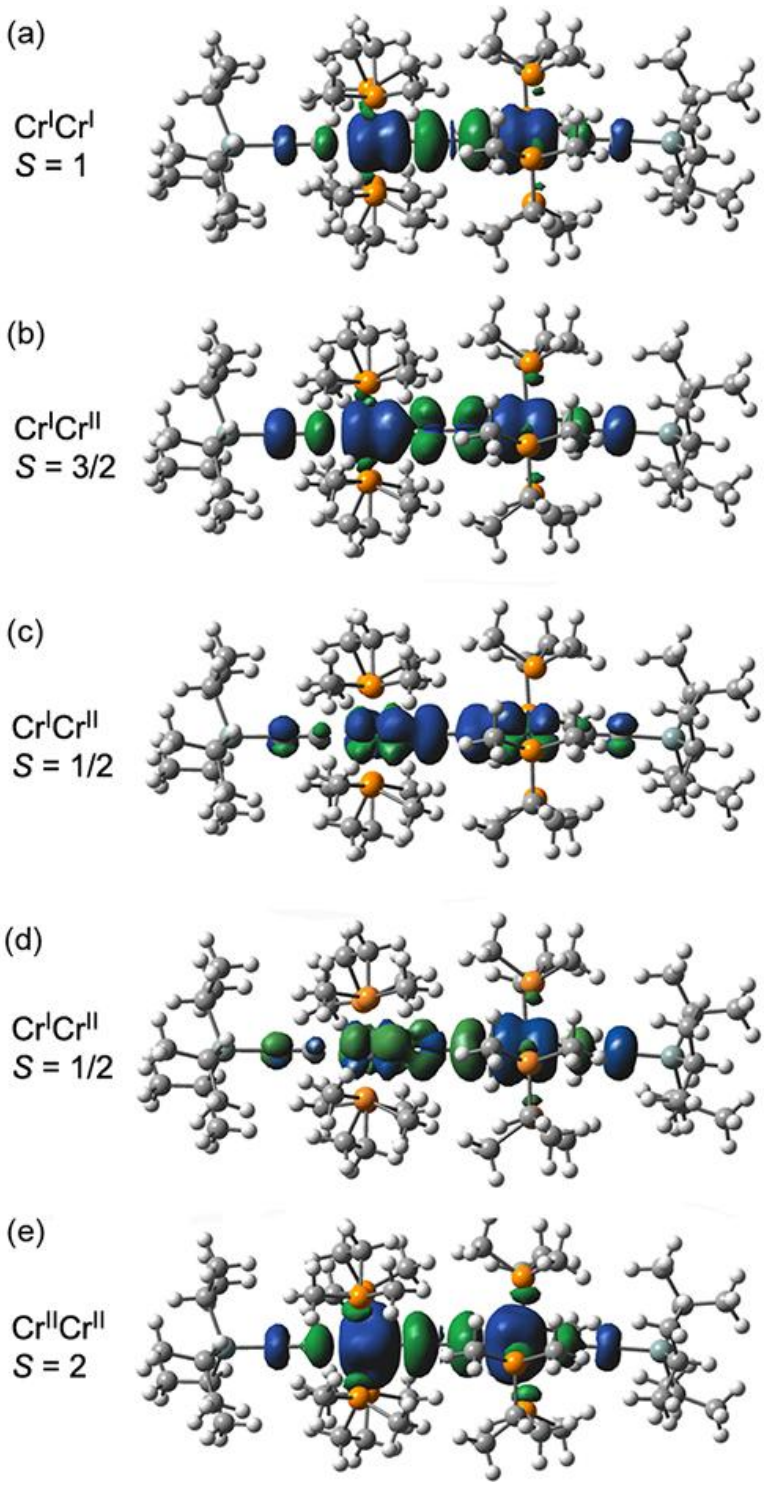

Figure 4.12. Net spin density plots (scaled at 0.0025 atomic units) for the: (a) triplet ground state in **4.2**; (b); quartet (computed) ground state for **4.3**; (c) symmetrically delocalized doublet for **4.3**; (d) localized doublet for **4.3**; (e) quintet ground state in **4.4**. Blue surfaces correspond to net α spin density and green to net β spin density.

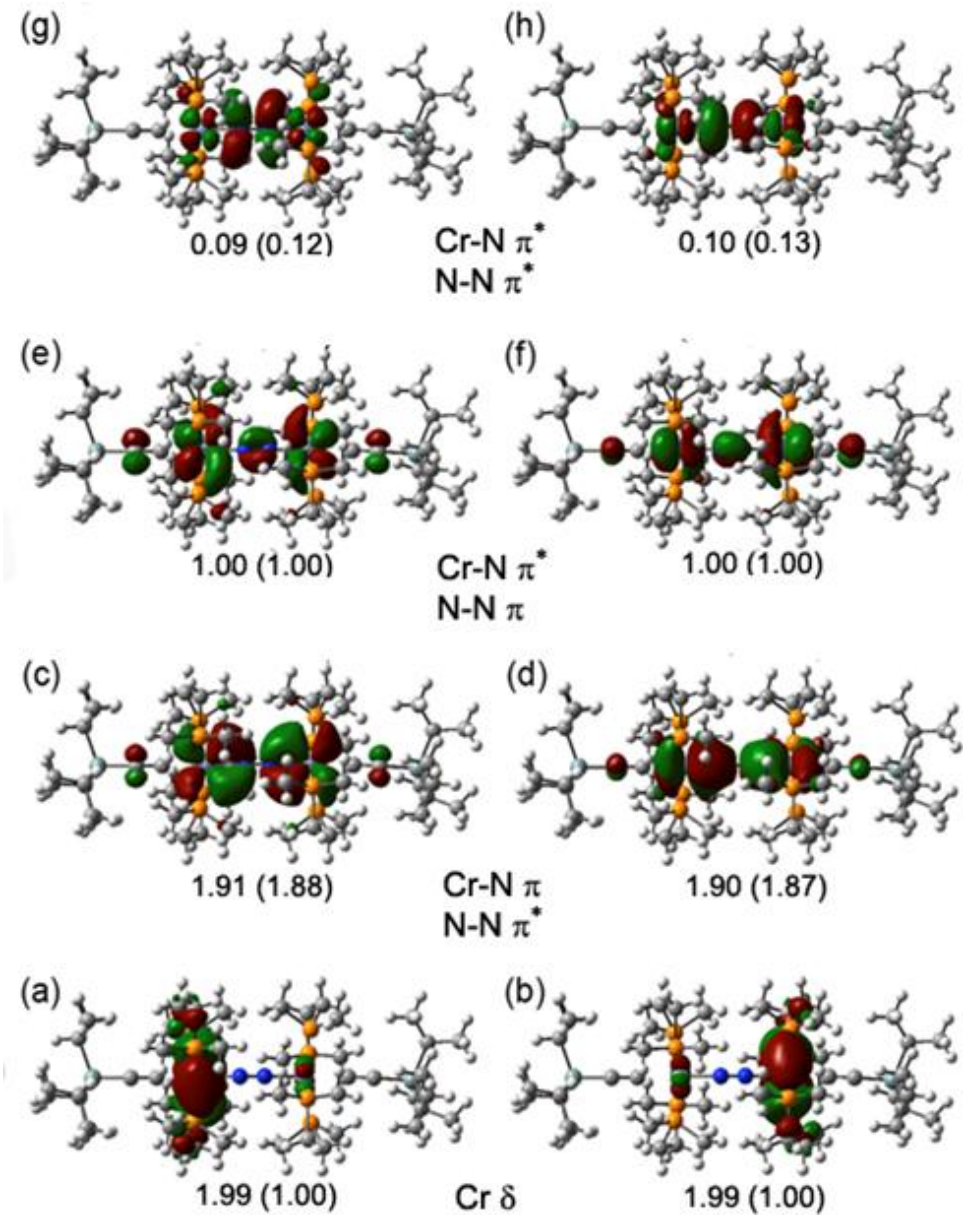

Figure 4.13. UKS frontier natural orbitals for **4.2** with corresponding electron occupancies. The electron occupancies for related orbitals in **4.4** are shown in parentheses.

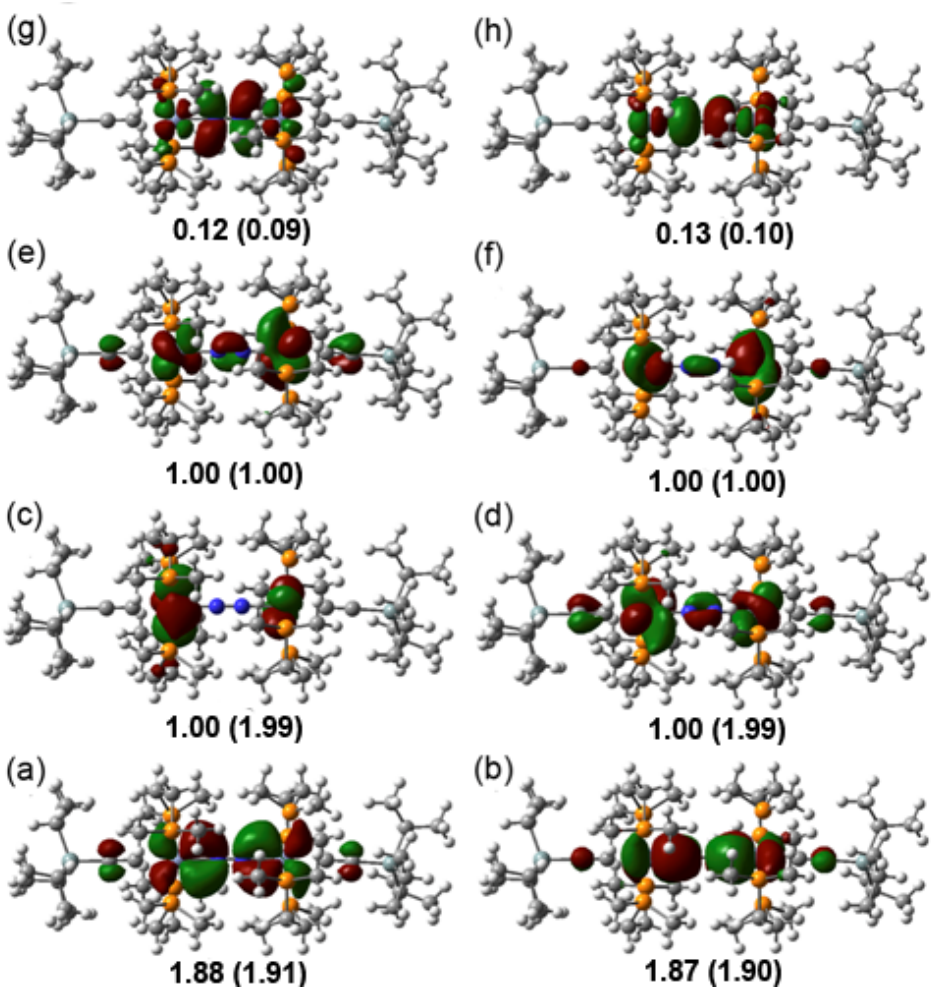

Figure 4.14. UKS frontier natural orbitals for **4.4** with corresponding electron occupancies. The electron occupancies for related orbitals in **4.2** are shown in parentheses.

localized on one end is found at 6 kcal/mol (Figure 4.12d). The Cr–N–N–Cr metrics for **4.3** are not well described by a quartet B3LYP model: the Cr–N distance is 0.16 Å long in **4.3** (compared to 0.05 Å long in **4.2** and **4.4**), the error in the N–N distance (0.04 Å)[66] is an order of magnitude larger than those found for **4.2** and **4.4**, and the computed N–N distance is short for **4.3** but long for **4.2** and **4.4**.

In contrast to the DFT model, we find the state averaged spectroscopy oriented restricted CI (CAS-SORCI) method[67] enjoys more success in accounting for the magnetic properties of the mixed valent compound **4.3**. The average field [9,11] CAS SCF computation on a model for **4.3** (**4.3***) finds a quartet ground state, followed by the second quartet at 2.45 kcal/mol, the lowest doublet at 2.23 kcal/mol, and the second doublet at 5.04 kcal/mol. Both doublets and quartets benefit from resonance stabilization. Due to the Fermi/exchange hole, there should be significantly more electron correlation for the doublets than for the quartets. The extra correlation of the SORCI places the doublets *lower* than the quartets. The second doublet is computed to occur 0.59 kcal/mol above the ground state doublet, and two quartet states reside at 1.45 kcal/mol and 2.81 kcal/mol above the ground state doublet. The CAS-SORCI total energy for the lowest doublet is –5394.834154395 hartree.

4.5 Discussion

4.5.1 N_2 Activation. Berben and Kozimor used the results of a UKS B3LYP study on the model complex $[(dpe)_4Cr^{I}_2(C_2H)_2(\mu\text{-}N_2)]$ (dpe = diphosphinoethane) to propose that oxidation of the dinuclear Cr^{I}–Cr^{I} compound (removal of an electron from each of the degenerate singly occupied molecular orbitals, SOMOs) should result in a weakened N–N bond and an increase in Cr–N bond character.[18] This reasonable suggestion was based

on the observation that the degenerate SOMOs each contained significant N–N π bonding character and significant Cr–N π* character. The demonstrated electrochemical (CV) stabilities of the mono- and dioxidized species implied that bulk quantities of the species could be produced for interrogation. Indeed, in this work we find that mono- and dioxidized **4.3** and **4.4** can be synthesized from neutral **4.2** by simple stoichiometric addition of appropriate organometallic oxidants. However, a comparison between the crystallographically determined N–N and Cr–C bond distances in **4.2** and **4.4** indicates that there is no significant change in the bond lengths upon oxidation (Table 4.2).[68] This is in contrast to what one would expect with regard to the similarity of the model complex on which the original calculations were performed. In addition, the N–N stretching frequency increases when the neutral complex **4.2** is oxidized by two electrons to **4.4**. The shift to higher energies relative to the neutral complexes is opposite to the behavior expected if the N–N bond order were to decrease upon oxidation, as predicted by DFT calculations carried out on the neutral complex.[18]

Based on the structural, magnetic and computational results we have acquired, we offer the following explanation: dinitrogen "activation" occurs, but only at the time of the neutral dinuclear complex formation. The natural orbitals generated for **4.2** (Figure 4.13), as well as the Berben/Kozimor calculations, are consistent with the formation of Cr=N moieties. The formation of Cr=N-type interactions implies that the N≡N bond order has been reduced; the apparent mild activation derived from X-ray structural data may be masked by ancillary ligand steric considerations—for example, the relatively tight packing of the dmpe ligands on neighboring Cr centers. Then, as the calculations for **4.4** suggest (Figure 4.14), subsequent oxidation of the neutral complex **4.2** does not follow

Koopman's theorem, a situation which is common for transition metal complexes. Upon oxidation, electrons are removed from the Cr dδ orbitals instead of dπ orbitals, Cr-N π-bonding remains intact, and retention of this bonding leads to the computed variable occupation of the dδ orbitals and the observation of non-diamagnetic ground states as discussed below. If the computed natural orbital occupations for neutral **4.2** and dioxidized **4.4** indicate a switch in relative orbital energies, it is reasonable to expect that the dπ and dδ orbitals in the intermediate complex **4.3** should be of nearly equal energies, which might afford novel magnetism.

4.5.2 Magnetic Properties. While it has been suggested that the N_2 ligand engenders (weak) antiferromagnetic coupling between metal centers in some cases,[17,18,24] others have reported paramagnetic, high-spin ground states for dicobalt,[20] and dimolybdenum[19] complexes. Münck and Bominaar have performed an extensive theoretical and Mössbauer study of on a diiron complex,[22] and conclude that the high spin behavior observed there originates from strong direct metal-ligand antiferromagnetic coupling. A similar mechanism has been cited to account for the diamagnetism found in a Ni^{I}_{2} complex.[24]

For the neutral compound **4.2**, the room temperature magnitude of $\chi_M T$, 1.00 $cm^3 \cdot K \cdot mol^{-1}$ at 300 K, evokes an $S = 1$ ground state rather than two uncoupled low spin d^5 centers (expected $\chi_M T \approx 0.75$ $cm^3 \cdot K \cdot mol^{-1}$), assuming a g value of 2 (Figure 4.6). The sharp downturn in susceptibility at low temperatures has been reasonably interpreted as weak antiferromagnetic coupling in the trimethylsilyl analogue,[18] but it is also consistent with significant ZFS, which is often associated with triplet ($S = 1$) ground states.[69] Fits of the susceptibility and magnetization data are both consistent with a triplet system,

whereas satisfactory fits based on metal-metal and metal-ligand antiferromagnetic coupling models could not be obtained. We also note here that the $S = 1$ ground state is consistent with our DFT calculations for **4.2** as well as Berben and Kozimor's original electronic structure model. Antiferromagnetic coupling of spins in the neutral complex would lead to a singlet ($S = 0$) ground state.

Similarly, a larger-than-expected susceptibility value at high temperature for two uncoupled $S = 1$ centers (expected $\chi_M T \approx 2$ $cm^3 \cdot K \cdot mol^{-1}$, but 3.09 $cm^3 \cdot K \cdot mol^{-1}$ is observed), leads us to classify dioxidized compound **4.4** as having an $S = 2$ ground state. A satisfactory fit based on an $S = 2$ model is obtained for the susceptibility data for **4.4**. Unlike **4.2**, the lack of a significant decrease in the magnitude of $\chi_M T$ at low temperatures implies that ZFS is not present in **4.2**. Supporting this, the isofield data in the magnetization plot overlay the $S = 2$ Brillouin function (Figure 4.7). Our electronic structure model does not provide an immediate explanation for the lack of ZFS: according to the calculations for **4.2** and **4.4**, there should be six electrons in the Cr-N π system, so orbital degeneracy should not change upon di-oxidation; however, the orbital energies are shifted significantly upon oxidation, based on the fact that Cr dδ are now SOMOs, and thus we might reasonably expect different amounts of spin-orbit coupling for **4.2** and **4.4**, leading to different zero-field magnetic behavior.

The magnetic behavior found for **4.2** bears some resemblance to the triplet ground states observed in paramagnetic $(C_4)^{2-}$-bridged complexes such as $[I_2(dmpe)_4Mn_2(\mu\text{-}C_4)]$.[70] Theoretical calculations for those complexes reveal that the HOMO is delocalized over the entire length of the bridging ligand. However, oxidation by two electrons of the formally d^5-d^5 $[Mn^{II}_2(\mu\text{-}C_4)]$ complex yields a *diamagnetic* d^4-d^4 complex. The

diamagnetic ground state for the $[Mn^{III}_2(\mu\text{-}C_4)]^{2+}$ species has been attributed to a significant contribution of the cumulenic resonance structure to the overall bonding picture. The fact that **4.4** is paramagnetic indicates that the electronic structure of **4.2** must be significantly different from the previously reported diyne-bridged dinuclear complexes.

For a dinitrogen bridged iron-diketiminate complex, Münck and co-workers observe a high spin ground state arising from a variable occupation of d orbitals due to N_2-induced Fe oxidation.[22] They attributed these observations to strong direct antiferromagnetism between the iron and nitrogen centers. Bonding and direct antiferromagnetism are limiting models on a continuum. We would suggest an operational model wherein interactions that can be disrupted by conventional temperatures and magnetic fields constitute direct antiferromagnetic interactions; otherwise, they represent M-L bonding.

For mixed-valent **4.3**, we believe the temperature dependence of the susceptibility data—a gradual decrease of $\chi_M T$ from 300 to 16 K, followed by a steeper drop at very low temperatures—is best understood as an incomplete quartet ⇌ doublet two-center spin equilibrium, where the doublet state is anisotropic. As with **4.2** and **4.4**, we cannot generate satisfactory fits to the data assuming weak exchange coupling of the two chromium spin centers: the room temperature $\chi_M T$ value is too high for uncoupled $S = 1$ and $S = ½$ spin centers (1.375 $cm^3 \cdot K \cdot mol^{-1}$ would be predicted for $g = 2$), and best fits to an antiferromagnetic coupling model give unreasonable g values (see Table 4.3). EPR spectroscopy further supports the assignment of a spin-crossover event for mixed-valent **4.3**. Whereas the featureless signal seen at higher temperatures (Figure 4.10 inset) is typical for isotropic quartet spin systems,[71] the intensification and development of

anisotropy in the *g* value upon temperature reduction is consistent with a spin state change.[72-74] Furthermore, the temperature dependence of the $g_{\|}$ signal is synchronized with the magnetic susceptibility drop-off.

Similar spin-crossover behavior has been observed before in mixed-valent diruthenium complexes in which the metal atoms are directly bound to one another.[75,76] Related, Bruce and coworkers have reported a diyne-bridged biradical diiron complex that exists in a thermally tunable mixture of singlet and triplet states.[77] To our knowledge, the magnetic behavior of **4.3** represents the first example of a ligand-mediated two-center spin crossover event in a mixed-valent species. In sum, the magnetic behavior of compounds **4.2**, **4.3** and **4.4** are consistent with extensive spin delocalization across the Cr–N–N–Cr backbone. Most significantly, the putative quartet ⇌ doublet transition is observed despite the fact that both homovalent complexes **4.2** and **4.4** show high spin (ferromagnetic) behavior at virtually all temperatures probed.

4.5.3 Electronic Structure of the Mixed-Valent Compound 4.3. The unprecedented magnetic properties of the monooxidized complex in **4.3** should be linked to the high spin/non-diamagnetic ground states of the homovalent compounds **4.2** and **4.4**, but also incorporate effects related to electron transfer/mixed valency. Thus, a deeper examination of the electronic structure of **4.3** is warranted.

The experimental data we have acquired for **4.3** does not allow for a clear-cut determination of mixed valency character. Analysis of electrochemical data (Figure 4.2) suggests partial electronic delocalization for **4.3** (Robin-Day Class II behavior).[54] From this, it should be possible to observe a difference in the stretching frequencies for the acetylide ligands bound to the formally Cr^{I} and Cr^{II} centers; however, the IR spectrum for

4.3 shows a single acetylide stretching resonance, suggesting that the Cr termini are equivalent on the IR time scale (10^{-13} s). Also, the Cr-ligand bond distances in the crystal structures of **4.3** are consistent with valence delocalization. The examination of the near-IR spectra of solutions of **4.3** in Et_2O shows no absorptions that could represent an IVCT band (Figure 4.15), and Hush analysis reveals that the observed bandwidth for the absorption peak at 914 nm is far too narrow to represent a IVCT process.[78,79] Intramolecular electron transfer rates have been correlated to the anisotropy in the *g* value of mixed-valent complexes ($\Delta g = g_{\perp} - g_{\|}$), where trapped ($\Delta g > 1.5$) or detrapped ($\Delta g < 1.1$) states give rise to slow and fast electron transfer, respectively.[80] For **4.3**, $\Delta g = 0.22$ at 105 K, which is consistent with a detrapped state, indicating that the odd electron is being shuttled between the Cr centers at a very fast rate ($>10^8$ s^{-1}). Similar observation of valence delocalization across a dinitrogen bridge has been observed before in mixed-valent Os^{III}/Os^{II} complexes.[81] In sum, whereas the electrochemical experiments suggest only partial electronic localization, structural, magnetic and spectroscopic data suggest that **4.3** possesses a delocalized electronic structure. This does not break new ground: others have noted that mixed-valent species can exhibit properties consistent with both localized and delocalized electronic structures, especially when multiple M–L–M orbital pathways can be involved.[3,82,83]

As might be expected from the multifaceted experimental results, the electronic structure calculations for **4.3** also reveal complexity. In going from **4.2** to **4.4**, one electron is removed from a dδ orbital on each chromium center. It would be reasonable to surmise that for **4.3**, one electron is removed from one of the doubly occupied dδ orbitals in **4.2**, generating a set of three orthogonal singly-occupied d orbitals and a resulting

quartet ground state.[84] Indeed, the quartet state (Figure 4.12b) is computed to be significantly lower in energy than the lowest doublet. Unfortunately, this B3LYP DFT model does not correspond to experimental observations: among other things, **4.3** displays the magnetism of a ground state doublet with a thermally accessible quartet excited state, and appears to be symmetric according to X-ray and IR experiments.

The DFT model does not take into account resonance stabilization. For the present Cr–N–N–Cr mixed-valent compound **4.3**, a resonance-stabilized localization model would involve a resonance between the localized state of Figure 4.12d, (where beta (blue) spin is localized on the right) with its counterpart (where beta spin is localized on the left). Molecular symmetry is restored, accompanied by an energetic stabilization, by use of two resonating wave functions wherein the electron is placed successively on each Cr atom. Compound **4.3** minimally comprises a resonating 3-electron/3-orbital doublet active space, for which there are two orthogonal spin eigenfunctions: (a) two electrons are singlet paired and the third electron is added on to create a doublet (↑↓·↑), and (b) two electrons are triplet coupled and the third is added with opposite spin to create a doublet (↑·↓·↑). *Spin unrestricted models such as UKS can only compute the average of these two spin eigenfunction states*. For **4.3** the second (triplet coupled) spin eigenfunction should be significantly favored, since one-center d-d exchange interactions approach 15 kcal/mol for first row transition metals, leading to a significant underestimation of the energy of the doublet state in **4.3** relative to the quartet. This extra lower-spin correlation is the accepted explanation for ground states that violate Hund's rule, as observed in organic chemistry.[85] Indeed, the more computationally demanding CAS-SORCI methods confirm this for a model of the mixed-valent complex in **4.3**. These results remind us that caution

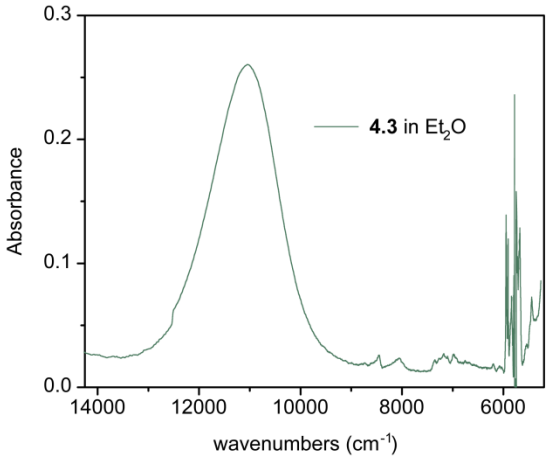

Figure 4.15. Vis-NIR absorption spectrum of **4.3** in diethyl ether. The peak at ca. 11000 cm^{-1} corresponds to the absorption at 914 nm in the UV-Visible spectrum.

must be taken when choosing computational methods to describe the electronic structures of complex spin systems. Questions of electronic structure continue to be of interest and Prof. Rappé will present a manuscript detailing the full account of the evolution in the computational methodology used herein in the future.

4.6 Conclusion

We have described the preparation, structural and magnetic characterization, and electronic structures of a redox-related family of $[RC_2Cr(\mu\text{-}N_2)CrC_2R]^{n+}$ (n = 0, 1, 2) acetylide complexes. Magnetic measurements performed on the n = 0 and n = 2 complexes are indicative of high-spin ground states at room temperature, which contrasts with the antiferromagnetic model presented by Berben and Kozimor for the Me_3Si analogue of **4.1** and **4.2**.[18] From the electronic structure calculations, the magnetic behaviors for neutral **4.2** and di-oxidized **4.4** originate from the population of doubly degenerate Cr–N π bonding orbitals; this in turn pins the orientation of the SOMOs to achieve an electronic structure reminiscent of dioxygen. The formation of Cr=N-type interactions implies that the N≡N bond order has been reduced; the apparent mild activation derived from X-ray structural data may be significantly masked by ancillary ligand steric considerations. The increase in Cr–N bond character is not inconsistent with the strong direct metal-ligand antiferromagnetic coupling advanced by Münck and Bominaar findings, though we would classify this particular Cr–N interaction as a bond under the operational model used herein.

Whereas an interpretation of previously reported DFT calculations performed on a model complex predicts a weakened dinitrogen bond upon oxidation of the low-spin d^5 Cr^I centers, we find that the Cr–N–N–Cr skeletal structures differ very little despite

alteration of the formal Cr oxidation states. The results of the calculations performed on $[^{i}Pr_3SiC_2Cr(\mu\text{-}N_2)CrC_2Si^{i}Pr_3]^{n+}$ suggest that the redox events proceeding from **4.2** to **4.4** are primarily metal-centered, which is perhaps not surprising if N_2 activation occurred only in the original formation of the neutral species. The mixed-valent $n = 1$ complex **4.3** exhibits magnetic behavior consistent with a thermally activated quartet ⇌ doublet two-center spin equilibrium. This phenomenon has not been reported in a mixed-valent system, and efforts to understand this behavior from a theoretical standpoint are ongoing. Importantly, while the characterization of the neutral complex alone allows for reasonable interpretations of magnetic properties, a more complete understanding of the contributing factors is attainable only when all three complex oxidation states are considered.

The $[RC_2Cr(\mu\text{-}N_2)CrC_2R]^{n+}$ complexes offer numerous handles for experimental interrogation; in addition, their moderate sizes allow for rigorous calculations to be carried out with a minimum of size reduction. They ultimately offer promise as a model system to address fundamental questions of electronic structure. Moving forward, these and related species can be used as a platform to test theory development in the fields of mixed-valency and electron transfer, areas where current DFT methods find difficulty.

4.7 Acknowledgment

This research was supported by Colorado State University and the ACS Petroleum Research Fund (44691-G3). We thank Prof. C. M. Elliott for assistance with electrochemical simulations and helpful discussions.

4.8 References and Notes

(1) Richardson, D. E.; Taube, H. *Coord. Chem. Rev.* **1984**, *60*, 107-129.

(2) Gunay, A.; Theopold, K. H. *Chem. Rev.* **2010**, *110*, 1060-1081.

(3) Demadis, K. D.; Hartshorn, C. M.; Meyer, T. J. *Chem. Rev.* **2001**, *101*, 2655-2686.

(4) *Single-Molecule Magnets and Related Phenomena.*; Springer: Berlin, 2006; Vol. 129.

(5) Goodenough, J. B. *Phys. Rev.* **1955**, *100*, 564.

(6) Weihe, H.; Gudel, H. U. *Inorg. Chem.* **1997**, *36*, 3632-3639.

(7) Kanamori, J. *J. Phys. Chem. Solids* **1959**, *10*, 87-98.

(8) Goldberg, D. P.; Caneschi, A.; Delfs, C. D.; Sessoli, R.; Lippard, S. J. *J. Am. Chem. Soc.* **1995**, *117*, 5789-5800.

(9) Miyasaka, H.; Julve, M.; Yamashita, M.; Clérac, R. *Inorg. Chem.* **2009**, *48*, 3420-3437.

(10) Toma, L. M.; Lescouezec, R.; Pasan, J.; Ruiz-Perez, C.; Vaissermann, J.; Cano, J.; Carrasco, R.; Wernsdorfer, W.; Lloret, F.; Julve, M. *J. Am. Chem. Soc.* **2006**, *128*, 4842-4853.

(11) Sokol, J. J.; Hee, A. G.; Long, J. R. *J. Am. Chem. Soc.* **2002**, *124*, 7656-7657.

(12) Entley, W. R.; Treadway, C. R.; Girolami, G. S. *Mol. Cryst. Liq. Cryst. Sci. Tech.* **1995**, *273*, 153-166.

(13) Berlinguette, C. P.; Vaughn, D.; Cañada-Vilalta, C.; Galán-Mascarós, J. R.; Dunbar, K. R. *Angew. Chem. Int. Ed.* **2003**, *42*, 1523-1526.

(14) Li, D.; Parkin, S.; Wang, G.; Yee, G. T.; Clérac, R.; Wernsdorfer, W.; Holmes, S. M. *J. Am. Chem. Soc.* **2006**, *128*, 4214-4215.

(15) Magnuson, R. H.; Taube, H. *J. Am. Chem. Soc.* **1972**, *94*, 7213-7214.

(16) Richardson, D. E.; Sen, J. P.; Buhr, J. D.; Taube, H. *Inorg. Chem.* **1982**, *21*, 3136-3140.

(17) Ferguson, R.; Solari, E.; Floriani, C.; Osella, D.; Ravera, M.; Re, N.; Chiesi-Villa, A.; Rizzoli, C. *J. Am. Chem. Soc.* **1997**, *119*, 10104-10115.

(18) Berben, L. A.; Kozimor, S. A. *Inorg. Chem.* **2008**, *47*, 4639-4647.

(19) Curley, J. J.; Cook, T. R.; Reece, S. Y.; Müller, P.; Cummins, C. C. *J. Am. Chem. Soc.* **2008**, *130*, 9394-9405.

(20) Ding, K.; Pierpont, A. W.; Brennessel, W. W.; Lukat-Rodgers, G.; Rodgers, K. R.; Cundari, T. R.; Bill, E.; Holland, P. L. *J. Am. Chem. Soc.* **2009**, *131*, 9471-9472.

(21) Smith, J. M.; Sadique, A. R.; Cundari, T. R.; Rodgers, K. R.; Lukat-Rodgers, G.; Lachicotte, R. J.; Flaschenriem, C. J.; Vela, J.; Holland, P. L. *J. Am. Chem. Soc.* **2006**, *128*, 756-769.

(22) Stoian, S. A.; Vela, J.; Smith, J. M.; Sadique, A. R.; Holland, P. L.; Münck, E.; Bominaar, E. L. *J. Am. Chem. Soc.* **2006**, *128*, 10181-10192.

(23) Holland, P. L. *Acc. Chem. Res.* **2008**, *41*, 905-914.

(24) Pfirrmann, S.; Limberg, C.; Herwig, C.; Stößer, R.; Ziemer, B. *Angew. Chem. Int. Ed.* **2009**, *48*, 3357-3361.

(25) Chatt, J.; Fay, R. C.; Richards, R. L. *J. Chem. Soc. A.* **1971**, 702-704.

(26) Treitel, I. M.; Flood, M. T.; Marsh, R. E.; Gray, H. B. *J. Am. Chem. Soc.* **1969**, *91*, 6512-6513.

(27) Sellmann, D. *Angew. Chem. Int. Ed. Engl.* **1974**, *13*, 639-649.

(28) Rappé, A. K. *Inorg. Chem.* **1984**, *23*, 995-996.

(29) Rappé, A. K. *Inorg. Chem.* **1986**, *25*, 4686-4691.

(30) Hart, J. R.; Rappé, A. K.; Gorun, S. M.; Upton, T. H. *Inorg. Chem.* **1992**, *31*, 5254-5259.

(31) Hart, J. R.; Rappe, A. K.; Gorun, S. M.; Upton, T. H. *J. Phys. Chem.* **1992**, *96*, 6255-6263.

(32) Hart, J. R.; Rappé, A. K.; Gorun, S. M.; Upton, T. H. *J. Phys. Chem.* **1992**, *96*, 6264-6269.

(33) Weyland, T.; Costuas, K.; Mari, A.; Halet, J. F.; Lapinte, C. *Organometallics* **1998**, *17*, 5569-5579.

(34) Sessoli, R.; Gatteschi, D.; Caneschi, A.; Novak, M. A. *Nature* **1993**, *365*, 141-143.

(35) Milios, C. J.; Vinslava, A.; Wernsdorfer, W.; Moggach, S.; Parsons, S.; Perlepes, S. P.; Christou, G.; Brechin, E. K. *J. Am. Chem. Soc.* **2007**, *129*, 2754-2755.

(36) Berben, L. A. Ph.D. Thesis, University of California, Berkeley, 2005.

(37) Girolami, G. S.; Wilkinson, G.; Galas, A. M. R.; Thorntonpett, M.; Hursthouse, M. B. *J. Chem. Soc. Dalton Trans.* **1985**, 1339-1348.

(38) Chávez, I.; Alvarez-Carena, A.; Molins, E.; Roig, A.; Maniukiewicz, W.; Arancibia, A.; Arancibia, V.; Brand, H.; Manríquez, J. M. *J. Organomet. Chem.* **2000**, *601*, 126-132.

(39) *APEX 2*; Bruker Analytical X-ray Systems, Inc.: Madison, WI, 2008.

(40) Sheldrick, G. M. *SHELXTL*; Bruker Analytical X-Ray Systems, Inc.: Madison, WI, 1999.

(41) Bill, E. *julX*; 1.41; Max Planck Institute for Bioinorganic Chemistry: Mulheim an der Ruhr, 2008 (http://ewww.mpi-muelheim.mpg.de/bac/logins/bill/julX_en.php).

(42) Shores, M. P.; Sokol, J. J.; Long, J. R. *J. Am. Chem. Soc.* **2002**, *124*, 2279-2292.

(43) Becke, A. D. *J. Chem. Phys.* **1993**, *98*, 5648.

(44) Frisch, M. J.; Trucks, G. W.; Schlegel, H. B.; Scuseria, G. E.; Robb, M. A.; Cheeseman, J. R.; Montgomery, J., J. A. ; Vreven, T.; Kudin, K. N.; Burant, J. C.; Millam, J. M.; Iyengar, S. S.; Tomasi, J.; Barone, V.; Mennucci, B.; Cossi, M.; Scalmani, G.; Rega, N.; Petersson, G. A.; Nakatsuji, H.; Hada, M.; Ehara, M.; Toyota, K.; Fukuda, R.; Hasegawa, J.; Ishida, M.; Nakajima, T.; Honda, Y.; Kitao, O.; Nakai, H.; Klene, M.; Li, X.; Knox, J. E.; Hratchian, H. P.; Cross, J. B.; Bakken, V.; Adamo, C.; Jaramillo, J.; Gomperts, R.; Stratmann, R. E.; Yazyev, O.; Austin, A. J.; Cammi, R.; Pomelli, C.; Ochterski, J. W.; Ayala, P. Y.; Morokuma, G. A.; Voth, G. A.; Salvador, P.; Dannenberg, J. J.; Zakrzewski, V. G.; Dapprich, S.; Daniels, A. D.; Strain, M. C.; Farkas, O.; Malick, D. K.; Rabuck, A. D.; Raghavachari, K.; Foresman, J. B.; Ortiz, J. V.; Cui, Q.; Baboul, A. G.; Clifford, S.; Cioslowski, J.; Stefanov, B. B.; Liu, G.; Liashenko, A.; Piskorz, P.; Komaromi, I.; Martin, R. L.; Fox, D. J.; Keith, T.; Al-Laham, M. A.; Peng, C. Y.; Nanayakkara, A.; Challacombe, M.; Gill, P. M. W.; Johnson, B.; Chen, W.; Wong, M. W.; Gonzalez, C.; Pople, J. A. *Gaussian 03*; Gaussian, Inc.: Wallingford, CT, 2004.

(45) Hay, P. J.; Dunning, T. H. *J. Chem. Phys.* **1976**, *64*, 5077.

(46) Ditchfield, R.; Hehre, W. J.; Pople, J. A. *J. Chem. Phys.* **1971**, *54*, 724.

(47) Hehre, W. J.; Ditchfield, R.; Pople, J. A. *J. Chem. Phys.* **1972**, *56*, 2257.

(48) Binkley, J. S.; Pople, J. A.; Hehre, W. J. *J. Am. Chem. Soc.* **1980**, *102*, 939.

(49) Francl, M. M.; Pietro, W. J.; Hehre, W. J.; Binkley, J. S.; Gordon, M. S.; DeFrees, D. J.; Pople, J. A. *J. Chem. Phys.* **1982**, *77*, 3654.

(50) ORCA is a modern electronic structure program package written by F. Neese, with contributions from U. Becker, D. Ganiouchine, S. Koßmann, T. Petrenko, C. Riplinger and F. Wennmohs.

(51) The Ahlrichs DZ basis set was obtained from the TurboMole basis set library under ftp.chemie.uni-karlsruhe.de/pub/basen.

(52) Lopez-Herdandez, A.; Venkatesan, K.; Schmalle, H. W.; Berke, H. *Monatsh. Chem.* **2009**, *140*, 845-857.

(53) In the presence of chloride (from adventitious LiCl), over a period of hours, intensely colored solutions of oxidized **4.2** turn pale yellow, and crystals of $[(^{i}Pr)_3SiC_2Cr^{III}Cl](BAr_4^F)$ can be isolated. Details concerning the reactivity of these species are under investigation.

(54) Robin, M. B.; Day, P. *Adv. Inorg. Chem. Radiochem.* **1967**, *10*, 247-422.

(55) MacKay, B. A.; Fryzuk, M. D. *Chem. Rev.* **2004**, *104*, 385-402.

(56) Attempts to collect Raman spectra of **4.3** have been thwarted by the propensity of **4.3** to undergo a reversible reaction upon irradiation with the 1064 nm incident laser. Dark green ethereal solutions of **4.3** turn golden brown upon insertion into the path of the laser; removal prompts the dark green color to reappear. We tentatively attribute this reactivity to reversible coordination of dinitrogen.

(57) Wilkinson, P. G.; Houk, N. B. *J. Chem. Phys.* **1956**, *24*, 528-534.

(58) Salt, J. E.; Wilkinson, G.; Motevalli, M.; Hursthouse, M. B. *J. Chem. Soc. Dalton Trans.* **1986**, 1141-1154.

(59) Denholm, S.; Hunter, G.; Weakley, T. J. R. *J. Chem. Soc. Dalton Trans.* **1987**, 2789-2791.

(60) Vidyaratne, I.; Scott, J.; Gambarotta, S.; Budzelaar, P. H. M. *Inorg. Chem.* **2007**, *46*, 7040-7049.

(61) The bond distances are different at 1 σ, but are indistinguishable at the 3 σ level.

(62) Kahn, O. *Molecular Magnetism*; Wiley-VCH: New York, 1993.

(63) This is not to be confused with the expected μ_{eff} for a single unpaired electron. As Kahn has noted, the Bohr magneton is better reserved as a unit of magnetization.

(64) Kohn, W.; Sham, L. J. *Phys. Rev.* **1965**, *140*, A1133-A1138.

(65) Huber, K. P.; Herzberg, G. *Constants of Diatomic Molecules*; Van Nostrand Reinhold: New York, 1979; Vol. 4.

(66) All structural comparisons related to **4.3** refer to the X-ray structure of **4.3**·1.5Et_2O.

(67) Neese, F. *J. Chem. Phys.* **2003**, *119*, 9428-9443.

(68) However, we note that the mono-oxidized compound **4.3** does show very slightly longer N–N and shorter Cr–N distances compared to neutral **4.2**.

(69) *Physical Methods in Bioinorganic Chemistry*; University Science: Sausalito, 2000.

(70) Kheradmandan, S.; Heinze, K.; Schmalle, H. W.; Berke, H. *Angew. Chem. Int. Ed.* **1999**, *38*, 2270-2273.

(71) Drago, R. S. *Physical Methods for Chemists*; 2nd ed.; Surfside: Gainesville, 1992.

(72) Le Stang, S.; Paul, F.; Lapinte, C. *Organometallics* **2000**, *19*, 1035-1043.

(73) Denis, R.; Toupet, L.; Paul, F.; Lapinte, C. *Organometallics* **2000**, *19*, 4240-4251.

(74) Roué, S.; Le Stang, S.; Toupet, L.; Lapinte, C. *C. R. Chimie* **2003**, *6*, 353-366.

(75) Angaridis, P.; Cotton, F. A.; Murillo, C. A.; Villagran, D.; Wang, X. *J. Am. Chem. Soc.* **2005**, *127*, 5008-5009.

(76) Tara, J. B.; Cameron, T. S.; Donal, H. M.; Laurence, K. T.; Manuel, A. S. A. *Eur. J. Inorg. Chem.* **2007**, *2007*, 4021-4027.

(77) Bruce, M. I.; Costuas, K.; Davin, T.; Ellis, B. G.; Halet, J.-F.; Lapinte, C.; Low, P. J.; Smith, M. E.; Skelton, B. W.; Toupet, L.; White, A. H. *Organometallics* **2005**, *24*, 3864-3881.

(78) At any rate, all the compounds studied here feature intense peaks between 900 and 950 nm; metal-to-ligand charge transfer or symmetry-allowed HOMO-SOMO transitions are more likely candidates for assignment based on literature precedent.

(79) Klein, A.; Lavastre, O.; Fiedler, J. *Organometallics* **2005**, *25*, 635-643.

(80) Lohan, M.; Ecorchard, P.; Ruffer, T.; Justaud, F.; Lapinte, C.; Lang, H. *Organometallics* **2009**, *28*, 1878-1890.

(81) Demadis, K. D.; El-Samanody, E.-S.; Coia, G. M.; Meyer, T. J. *J. Am. Chem. Soc.* **1999**, *121*, 535-544.

(82) Lapinte, C. *J. Organomet. Chem.* **2008**, *693*, 793-801.

(83) Creutz, C. In *Prog. Inorg. Chem.*; Lippard, S. J., Ed. 1983, p 1-73.

(84) Alternatively, one electron could be added to one of the singly occupied dδ orbitals in **4.4**, again generating a set of three orthogonal singly occupied d orbitals and a quartet ground state.

(85) Hrovat, D. A.; Borden, W. T. *J. Mol. Struct.: THEOCHEM* **1997**, *398-399*, 211-220.

Chapter 5. Syntheses and Characterizations of New Iron Oligo-yne Complexes

5.1 Introduction

An emerging area of materials research aspires to understand and exploit metal complexes bridged by carbon-rich ligands for molecule-based electronics.[1] Metal-containing dinodal endgroups joined by oligoynes can create highly delocalized electronic structures, a necessary condition for the realization of molecular wires.[2] This potential application of poly-yne-bridged complexes has attracted much attention, but the magnetic properties of these molecular species have been studied in relatively less detail. Despite this, the structural and electronic features imparted by poly-yne bridging ligands make them attractive targets for molecule-based magnets. Notably, the strong exchange coupling and topological anisotropy observed in paramagnetic $[M_2(\mu\text{-}C_4)]$ complexes are prerequisites for slow magnetic relaxation in molecular species,[3] and the combination of many of these units into a single assembly should produce highly interesting magnetism. However, as discussed in Chapter 1, synthetic hurdles confronting the controlled isolation of low-dimensional, high-spin organometallic complexes have yet to be cleared. Nonetheless, understanding the magnetic and electronic properties of the individual building blocks will aid future research in this area.

Related trinodal compounds are also appealing because additional functionalities may be introduced by the central metal ion(s). Conventionally, ligand rigidity and metal coordination preferences direct the connectivity of these trinodal complexes as

a more or less straight vector running through the axes of each metal-containing node.[4] A family of linear, diruthenium-based trinodal molecular wires recently reported by Ren and co-workers demonstrates that a central transition-metal-containing unit can mediate electron transfer through two adjacent butadiynyl bridging ligands.[5] Berke has also isolated a C_4-bridged tetranuclear complex with Fe–W–W–Fe connectivity and demonstrated electronic delocalization through the metal/ligand backbone.[6] Nevertheless, the relative paucity of tunable trinodal wire-like complexes points to the myriad challenges involved in the synthesis of these species.

Lapinte and coworkers have synthesized a family of redox-related complexes of the type $[(dppe)_2Fe_2(Cp^*)_2(\mu\text{-}C_4)]^{n+}$ (n = 0,1,2).[7] The delocalization of charge in the mixed valent and di-oxidized complexes demonstrates the ability of butadiynyl bridging ligands to produce strongly coupled di-iron systems. Further, Field and coworkers have reported the synthesis and electrochemical properties of myriad Fe mono- and bis-acetylides,[8] including a significant number of complexes with chloro and acetylide ligands *trans* to each other. Typically, these complexes are prepared using a dehydrohalogenation strategy starting with $[(dmpe)_2FeCl_2]$ and acetylenes in the presence of methanol and an organic base.

Based on these precedents, the hypothesis that $(dmpe)_2Fe^{II}$ (dmpe = 1,2-bis(dimethyl)phosphinoethane) units would offer synthetic access to interesting and novel oligoyne complexes due to the wide array of ligand substitution chemistry and redox activity of the metal unit was formed.[8d,8a, 9] We reasoned that halide abstraction from $[(dmpe)_2FeCl_2]$ in combination with fluoride-promoted desilylation of 1,4-

bis(trimethylsilyl)butadiyne would target a dimeric complex bridged by a C_4^{2-} ligand. During the course of this work, the discovery was made that this approach could be used to prepare wire-like complexes containing an ene-yne moiety, while isolation of the original synthetic target required an alternative methodology. Herein, the synthesis, characterization, and initial computational work on a series of wire-like di-and tri-nodal $(dmpe)_2Fe$-containng oligo-yne complexes is reported.

5.2 Division of Labor/Results Dissemination Statement

All experimental work was performed by Wesley Hoffert. Prof. Anthony Rappé carried out the DFT calculations and constructed the spin density plot shown in Figure 5.15. The portion of this work relating to the tri-nodal complexes **5.1** and **5.2** was published in *Chemical Communications* in 2010 with the following citation: Hoffert, W. A.; Rappé, A. K.; Shores, M. P., "Intramolecular Charge Transfer in a Trinuclear Iron Ene-Triyne Complex." *Chem. Commun.* **2010,** *46,* 4710-4712. Additional information relating to the supporting information for this chapter can be found in the Appendix.

5.3 Experimental Section

5.3.1 Preparation of Compounds. Manipulations were performed either inside a dinitrogen-filled glovebox (MBRAUN Labmaster 130) or using standard Schlenk techniques on a N_2/vacuum manifold. Anhydrous methanol was purchased from Aldrich and was used as received. All other solvents were sparged with dinitrogen, passed over alumina, and degassed prior to use. The preparations of $[(dmpe)_2FeCl_2]$ (dmpe = 1,2-bis(dimethylphoshino)ethane),[10] $[Cp_2Fe]BAr^F_4$ (BAr^F_4 = tetrakis-[(3,5-trifluoromethyl)phenyl]borate),[11] $[Cp_2Fe]PF_6$,[12] $[Cp^*_2Fe](PF_6)$,[12] and $Li_2C_4(THF)_n$[13] have

been described elsewhere. All other reagents were purchased commercially and were used without further purification.

$[(dmpe)_6Fe_3Cl_2(C_8H)](PF_6)$ (5.1).[$(dmpe)_2FeCl_2$] (262 mg, 0.625 mmol) and 1,4-bis(trimethylsilyl)butadiyne (81.01 mg, 0.417 mmol) in dichloromethane (18 mL) were added to a 50 mL Schlenk flask containing KPF_6 (85.64 mg, 0.465 mmol). Addition of potassium fluoride (49 mg, 0.84 mmol) in 2 mL of methanol caused the mixture color to become purple. After refluxing the mixture under dinitrogen for 24 hours, the mixture turned deep red-brown. After cooling, the solvent was removed and the residue was extracted with 10 mL dichloromethane to yield a dark red-brown filtrate. Diethyl ether vapor diffusion into a concentrated solution of the crude product in dichloromethane afforded dark red needle crystals after 1 day. The crystals were separated from the mother liquor by filtration, washed with diethyl ether (2 × 5 mL) and dried under dinitrogen to afford the final product (98 mg, 34%). Absorption spectrum (CH_2Cl_2): λ_{max} (ε_M): 287 (sh, 30610), 361 (20090), 414 (sh, 22480), 467 nm (27570 $M^{-1}\cdot cm^{-1}$). IR (solid, mineral oil): ν_{CC} 2022, 1992, and 1891 cm^{-1}, $\nu_{C=C}$ 1558 cm^{-1}. ^1H NMR (CD_2Cl_2): δ 5.54 (1H, s, C═C*H*C), 1.98 (12H, d, Me), 1.83 (12H, br s, Me), 1.43 (46H, br s, Me and *CH_2*), 1.38 (8H, s, *CH_2*), 1.13 (8 H, m, *CH_2*), 0.66 (3H, d, Me), 0.50 (3H, d, Me). $\{^1H\}^{31}P$ NMR (CD_2Cl_2): δ 68.60 (2P, br), 64.76–65.65 (4P, br), 64.09 (4P, s), 58.39–59.90 (1P, br) 49.11 (1 P, br), –143.47 (1P, septet, *J* 1755, *P*F_6). $\{^1H\}^{13}C$ NMR (CD_2Cl_2): δ 9.2 (1C, m, Me), 13.3 (4C, br s, Me), 15.9 (4C, br s, Me), 16.7 (1C, d, Me), 18.8 (1C, m, Me), 20.8 (1C, d, Me), 21.1 (1C, d, Me), 22.1 (1C, d, Me), 27.6 (1C, m, *C*H_2), 29.2 (1C, m, *C*H_2), 30.6 (8C, m, *C*H_2), 32.6 (1C, m, *C*H_2), 34.1 (1C, m, *C*H_2), 88.5 (1C, C≡C), 94.6 (1C, C≡C), 99.4 (1C, C≡C), 101.0 (1C, C≡C), 104.2 (1C, C≡C), 113.7 (1 C, C≡C), 129.0 (1C,

C═*C*HC), 166.7, (1C, Fe*C*═C); ES$^+$-MS (CH_2Cl_2): *m/z* 1234.93 ([**5.1**–PF_6]$^+$. Anal. Calcd. for $C_{44}H_{97}Cl_2F_6P_{13}Fe_3$: C, 38.26; H, 7.08. Found: C, 38.08; H, 6.80.

[(dmpe)$_6$Fe$_3$Cl$_2$(C$_8$H)](PF$_6$)$_2$ (5.2): A solution of 1 eq. [FeCp$_2$]PF_6 (12.6 mg, 0.038 mmol) in 5 mL dichloromethane was added to a solution of **5.1** (52.4 mg, 0.038 mmol), causing the solution to immediately turn dark green. The solution was concentrated to *ca.* 1 mL and 15 mL diethyl ether was added. The mixture was placed in a –40 °C freezer, causing a dark green solid to precipitate after 3 hours. The solid was separated from the mixture by filtration and was washed with diethyl ether (2 × 5 mL) and dried under dinitrogen to afford the final product (48 mg, 83%). Absorption spectrum (CH_2Cl_2): λ_{max} (ε_M): 308 (sh, 26940), 344 (sh, 18510), 431 (22970), 577 (11200), 635 (10250), 1148 nm (9400 $M^{-1}cm^{-1}$). IR (solid, mineral oil): ν_{CC} 2023, 1905, and 1861; $\nu_{C=C}$ 1552. ES$^+$-MS (CH_2Cl_2): 1379.80 ([**5.2**–PF_6]$^+$).

[(dmpe)$_4$Fe$_2$Cl$_2$(μ-C$_4$)](PF$_6$) (5.3). A green solution of [(dmpe)$_2$FeCl$_2$] (102 mg, 0.239 mmol) in tetrahydrofuran (5 mL) was added to a slurry of $Li_2C_4(THF)_n$ (33 mg) in tetrahydrofuran (5 mL). The mixture was stirred for 15 hours, during which time its color turned to dark red. The solvent was removed *in vacuo*, and the residue was extracted with 10 mL of toluene. Evaporation of the solvent afforded 77 mg crude [(dmpe)$_4$Fe$_2$Cl$_2$(μ-C$_4$)] as a brick red solid. A solution of [Cp*$_2$Fe](PF_6) (38.9 mg, 0.083 mmol) in dichloromethane (3 mL) was added to a solution of crude [(dmpe)$_4$Fe$_2$Cl$_2$(μ-C$_4$)] (137 mg, ca. 0.165 mmol) in dichloromethane (5 mL). The solution color immediately turned to dark green. The solvent was removed *in vacuo* and diethyl ether (10 mL) was added. Solid 5.3 was isolated by filtration and washed with diethyl ether (3 × 3 mL) to remove residual [Cp*$_2$Fe]. The solid was recrystallized by slow diffusion of diethyl ether vapor

into a concentrated solution of the crude product in dichloromethane. After 1 day, dark green needle crystals were isolated by filtration, washed with diethyl ether (2 × 3 mL) and dried under dinitrogen for 1 hr at 293 K to afford 89 mg of product (0.091 mmol, 43% based on [(dmpe)$_2$FeCl$_2$]). Absorption spectrum (CH_2Cl_2) λ_{max} (ε_M): 313 (70600), 384 (5780), 414 (6010) 580 (3180), 1100 (sh, 8370), 1458 nm (36130 $M^{-1}\cdot cm^{-1}$). IR (ATR): ν_{CC} 1980, 1963 (sh), 1932 (sh), 1882 cm^{-1}. ^{1}H NMR (CD_2Cl_2) δ –5.57 (br, 12H, –PC*H*$_3$), –7.32 (br, 4H, –PC*H*$_2$), –10.87 (br, 12H, –PC*H*$_3$), –11.28 (br, 4H, –PC*H*$_2$). ES$^+$-MS (CH_2Cl_2): m/z 830.00 ([**5.3**–PF_6]$^+$). Anal. Calcd. for $C_{28}H_{64}Cl_2F_6P_9Fe_2$: C, 34.45; H, 6.61. Found: C, 34.18; H, 6.28. Although analytically pure (*vide infra*), X-ray quality single crystals of 5.3 could not be grown, the triflate salt (**5.3b**) lent itself to crystallographic analysis. It was synthesized by substituting [Cp*$_2$Fe](OTf) for [Cp*$_2$Fe](PF_6) in the procedure described above.

[(dmpe)$_4$Fe$_2$Cl$_2$(μ-C$_4$)](PF$_6$)$_2$ (5.4). A solution of [Cp$_2$Fe](PF_6) (7.8 mg, 0.024 mmol) in dichloromethane (2 mL) was added to a solution of **5.3** (22.9 mg, 0.024 mmol) in dichloromethane (3 mL). The solution color immediately became forest green. The solvent was removed *in vacuo*. The green solid was washed with diethyl ether (3 × 3 mL) to remove residual [Cp$_2$Fe]. The solid was recrystallized by slow diffusion of diethyl ether vapor into a solution of the crude product in dichloromethane. After 1 day, dark green needle crystals were isolated by filtration, washed with diethyl ether (2 × 3 mL) and dried under dinitrogen to afford 20 mg of product (0.018 mmol, 76%). Absorption spectrum (CH_2Cl_2) λ_{max} (ε_M): 333 (53080), 346 (sh, 51490), 447 (5070), 656 (4250), 896 nm (61670 $M^{-1}\cdot cm^{-1}$). IR (ATR): ν_{CC} 1969, 1884 cm^{-1}. ^{1}H NMR (CD_2Cl_2): δ –13.24 (br, 4H, –PC*H*$_2$), –14.76 (br, 12H, –PC*H*$_3$), –16.10 (br, 12H, –PC*H*$_3$), –20.34 (br, 4H,

–PCH_2). ES$^+$-MS (CH_2Cl_2): m/z 974.80 ([5.4–PF_6]$^+$). Anal. Calcd. for $C_{29}H_{66}Cl_4F_{12}P_{10}Fe_2$ (**5.4**·CH_2Cl_2): C, 28.88; H, 5.52. Found: C, 28.87; H, 5.00.

5.3.2 X-ray Structure Determinations. When possible, compounds were characterized by single crystal X-ray analysis (Table 5.1). Single crystals were coated in Paratone oil prior to removal from the glovebox. The crystals were supported on cryoloops before being mounted on a Bruker Kappa Apex 2 CCD diffractometer under a stream of dinitrogen. Data collection was performed between 115 K and 120 K with MoKα radiation and a graphite monochromator. Initial lattice parameters were determined from a minimum of 190 reflections harvested from 36 frames, and a full data set was collected targeting complete coverage and four-fold redundancy. Data were integrated and corrected for absorption effects with the Apex 2 software package.[14] The structures were solved by direct methods and refined with the SHELXTL software package.[15] For compound **5.1**, the initial space group determination using XPREP was ambiguous as to whether the space group was centrosymmetric (*Pnma*) or non-centrosymmetric ($Pna2_1$). The figure of merit was slightly lower for *Pnma*, and the correct connectivity could be observed in that solution. However, the only reasonable disorder model for the ene–triyne backbone and central Fe(dmpe)$_2$ unit in this space group is to keep the disordered parts at 50% occupancy. The *Pnma* solution was refined with a final residual R_1 value of 0.176. The presence of systematic absences and much higher F_o values than F_c values in *Pnma* led us to believe that twinning was present in the non-centrosymmetric space group. By solving the structure in $Pna2_1$ with a racemic TWIN refinement, the occupancies of the disordered parts were allowed to freely refine. All atoms for the minor disordered component could not be found in the difference map,

so a set of coordinates for each disordered atom was generated by reflecting the relevant atomic coordinates through the pseudo mirror plane between Fe(3) and Fe(3a), then allowing the new atoms to refine under the SAME command with reference to the pseudo–mirror plane counterpart. After refinement, the occupancies for the major and minor components of the $Fe(dmpe)_2C_8H$ group were 82% and 18%, respectively. Thermal parameters for the atoms in the major disordered component were refined anisotropically, as were all other non-disordered atoms.

The structure for **5.3b** was solved in $P\bar{1}$, and two complexes and two anions were present in the asymmetric unit. Unit cell angles are close to 90°, and the two complexes appear to be symmetry related. However, ADDSYM[16] does not find any additional symmetry, so the triclinic solution is presented.

Initial attempts at solving the structure of **5.4**·CH_2Cl_2 were made in $P\bar{1}$. It was apparent from the high refinement residuals and unit cell parameters that pseudo merohedral twinning was a possibility. Thus, the TwinRotMat and ADDSYM routines[16] were applied to the triclinic solution. Inclusion of a [–1 0 0 0 –1 0 2 0 1] twin law and solving in $P2_1/c$ led to a solution with much lower residual values.

In all structures, thermal parameters for minor disordered components were refined isotropically. Hydrogen atoms were added at the ideal positions and were refined using a riding model where the thermal parameters were set at 1.2 times those of the attached carbon atom (except for methyl protons, whose thermal parameters were set at 1.5 times that of the attached C atom).

5.3.3 Other Physical Measurements. Near infrared spectra for **5.1**-**5.4** were obtained with a Varian Cary–500 UV–Vis–NIR spectrophotometer using an airfree cuvette.

Table 5.1. Crystallographic data[a] for compounds $[(dmpe)_6Fe_3Cl_2(C_8H)](PF_6)$ (**5.1**), $[(dmpe)_4Fe_2Cl_2(\mu\text{-}C_4)](OTf)$ (**5.3b**), and $[(dmpe)_4Fe_2Cl_2(\mu\text{-}C_4)](PF_6)_2 \cdot CH_2Cl_2$ (**5.4**·CH_2Cl_2).

	5.1	**5.3b**	**5.4**·CH_2Cl_2
Crystal ID code	msn224	msn230	msn237
formula	$C_{44}H_{97}Cl_2Fe_3P_{13}F_6$	$C_{29}H_{64}Cl_2F_3Fe_2O_3P_8S$	$C_{29}H_{66}Cl_4F_{12}Fe_2P_{10}$
fw	1381.28	980.22	1206.02
color, habit	red needle	green needle	green needle
T, K	115(2)	120(2)	120(2)
crystal system	orthorhombic	triclinic	monoclinic
space group	$Pna2_1$ (no. 33)	$P\bar{1}$ (no. 2)	$P2_1/c$ (no. 14)
reflections measured	35753	70022	32613
independent reflections	12909	15387	7150
R_{int}	0.0313	0.0454	0.0328
theta range	$1.44° \le \theta \le 28.57°$	$1.02° \le \theta \le 24.71°$	$1.15° \le \theta \le 23.26°$
maximum *h, k, l*	21, 30, 18	13, 19, 23	11, 15, 40
minimum *h, k, l*	–21, –23, –24	–16, –19, –23	–11, –14, –40
parameters	691	865	515
restraints	83	0	0
highest peak/deepest hole	1.309 / –1.002	1.136/ –0.883	0.670/–0.604
Z	4	4	4
a, Å	15.9440(6)	13.7642(2)	10.4042(5)
b, Å	22.8376(7)	16.7872(3)	14.1040(7)
c, Å	18.0016(7)	19.9731(3)	36.861(2)
α, deg	90	89.5390(10)	90
β, deg	90	89.0680(10)	106.3950(10)
γ, deg	90	78.3860(10)	90
V, Å^3	6554.8(4)	4519.9(1)	5189.1(4)
d_{calc}, g/cm^3	1.400	1.440	1.544
GOF	1.07	1.061	1.099
R_1 (wR_2)[b], %	6.88 (15.08)	4.79 (12.68)	3.70 (10.08)

[a] Obtained with graphite-monochromated Mo Kα (λ = 0.71073 Å) radiation.
[b] $R_1 = \sum||F_o| - |F_c||/\sum|F_o|$, $wR_2 = \{\sum[w(F_o^2 - F_c^2)^2]/\sum[w(F_o^2)^2]\}^{1/2}$ for $I>2\sigma(I)$

Electronic absorption spectra for **5.3** and **5.4** were recorded with a Hewlett-Packard 8453 spectrophotometer. Infrared spectra were measured with a Nicolet 380 FT-IR spectrometer using mineral oil mulls sandwiched between NaCl plates. ^{1}H, $\{^{1}H\}^{31}P$, and $\{^{1}H\}^{13}C$ NMR spectra were recorded using a Varian INOVA instrument operating at 300 MHz. EPR spectra were obtained with a continuous wave X-band Bruker EMX 200U EPR outfitted with a liquid nitrogen cryostat. Mass spectroscopy was performed by injecting a dilute solution of the compound of interest directly into a Finnigan LCQ-DUO instrument outfitted with an ion trap. Cyclic voltammetry was done in 0.1 M solutions of $(Bu_4N)PF_6$ in dichloromethane or acetonitrile. The voltammograms were recorded with either a CH Instruments 1230A or 660C potentiostat, Ag/Ag^{+} reference electrode, and a Pt mesh auxiliary electrode. The working electrode was either a 0.25 mm or 1 mm Pt disk. Reported potentials are referenced to the $[Cp_2Fe]^{+}/[Cp_2Fe]$ redox couple and were determined by adding ferrocene as an internal standard at the conclusion of each electrochemical experiment. Elemental analyses were performed by Robertson Microlit Laboratories in Madison, NJ.

5.3.4 Magnetic Susceptibility Measurements. Magnetic susceptibility data were collected with a Quantum Design MPMS-XL SQUID magnetometer. In the glovebox, finely ground samples were loaded into gelatin capsules and inserted into straws. The straws were sealed in plastic bags prior to removal from the glovebox, and were quickly loaded into the SQUID to minimize exposure to air. Data were corrected for the magnetization of the sample holder by subtracting the susceptibility of an empty container and for diamagnetic contributions of the sample using Pascal's constants.[17] Theoretical fits to the susceptibility data were obtained using a relative error

minimization routine (julX 1.4.1)[18] using Hamiltonians of the form $\hat{H}_{ex} = -2J_{ab}S_a \cdot S_b$ and $\hat{H}_{ZFS} = \sum_{i=1}^{ns} D_i[S_{z,i}^2 - 1/3S_i(S_i+1) + E_i/D_i(S_{x,i}^2 - S_{y,i}^2)] + \sum_{i=1}^{ns} g\beta\vec{S}_i \cdot \vec{B}$. Fits of the magnetization data were obtained with the ANISOFIT[19] program and are based on the Hamiltonian $\hat{H} = D\hat{S}_z^2 + E(\hat{S}_x^2 + \hat{S}_y^2) + g_{iso}\beta\vec{S} \cdot \vec{B}$.

5.3.4 Electronic Structure Calculations. Restricted and unrestricted B3LYP hybrid density functional studies were carried out on the one-electron oxidized complex in **5.1** in the G03 suite of electronic structure codes.[20] X-ray coordinates were used for Fe, P, F, and C_8H centers. The coordinates for the remaining C and H centers were relaxed from the X-ray structure using the APT force field model.[21] The LANL2 basis sets[22] and effective core potentials were used for P and Fe; H, C, and F were described with a 6-31g* model.[23]

5.4 Results

5.4.1 Synthesis and Characterization of Tri-Nodal Complexes. Intending to prepare [$(dmpe)_4Fe_2Cl_2(\mu$-C4)], it was reasoned that halide abstraction from [$(dmpe)_2FeCl_2$] combined with fluoride-promoted desilylation of 1,4-bis(trimethylsilyl)butadiyne would target the dimeric complex bridged by a C_4^{2-} ligand (Scheme 5.1). Indeed, mass spectra obtained for the CH_2Cl_2/MeOH reaction mixture (the latter solvent used to solubulize KF) suggest that the expected 2:1 Fe:ligand complex, [$(dmpe)_4Cl_2Fe_2(\mu-C_4)$], is present in solution, albeit as the minor product (*m/z* = 830.00). The most intense peak (*m/z* = 1234.93) corresponds to a compound with a 3:2 Fe:ligand ratio. Since $(dmpe)_2Fe$ units are known to axially coordinate either one or two acetylide ligands,[8a, 8d] we suspected that a trinuclear wire-type complex was present in solution, and thus refined the synthetic procedure for that compound.

Indeed, after optimization of the stoichiometry and reaction conditions, the trinuclear Fe^{II} complex **5.1** is isolated in 34% isolated yield as deep red needle crystals (Scheme 5.1). Single crystal X-ray analysis (*vide infra)* indicates that a tri-nodal complex was indeed formed, albeit with unprecedented C_8H connectivity (Figure 5.1). Mononuclear Fe^{II} ene-yne complexes have been previously isolated,[8a, 8d, 24] and their spectroscopic signatures were comparable to those for **5.1**. All of the resonances in the ^1H NMR spectrum were assignable; the vinylic proton resonance appears as a broad singlet at 5.54 ppm, consistent with literature precedent (Figure 5.2). Cyclic voltammetry was used to probe the redox activity of **5.1**. The complex exhibits two one electron oxidations at –0.61 V and –0.81 V versus Fc^+/Fc (Figure 5.3). These redox waves are attributable to the Fe^{III}/Fe^{II} couples at the $Fe(dmpe)_2$ termini based on the similarity in potentials to previously characterized Fe complexes with comparable coordination environments.[25] We assign a third one electron redox wave at +0.13 V vs. Fc^+/Fc to the Fe^{III}/Fe^{II} couple on the central *cis*-$(dmpe)_2Fe$ unit. Applying more positive potentials to solutions of **5.1** during the anodic scan brings about a fourth and irreversible redox event at +0.78 V vs Fc^+/Fc (Figure 5.4), and is tentatively ascribed to a Fe^{IV}/Fe^{III} process.[8d] This wave is somewhat larger than those at lower potentials, suggesting that multiple electrons are involved. Subsequent scans lack reversible waves for the processes at –0.61 V and +0.13 V vs. Fc^+/Fc, suggesting complex dissociation. Cyclic voltammograms taken in acetonitrile show that the redox wave corresponding to the central Fe ion is irreversible at all times, indicating that oxidation of the *cis*-Fe unit in polar solvents also causes the

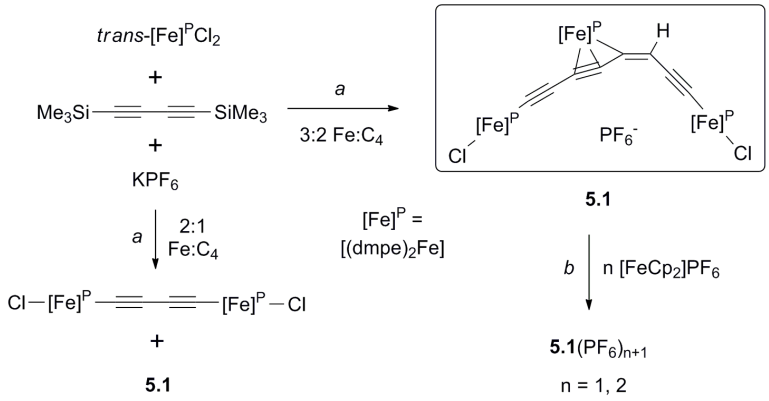

Scheme 5.1. Synthetic conditions used for the preparation of complexes **5.1** and **5.2**. Reaction conditions: *a* = CH_2Cl_2, MeOH, KF, reflux 24 hours; *b* = CH_2Cl_2.

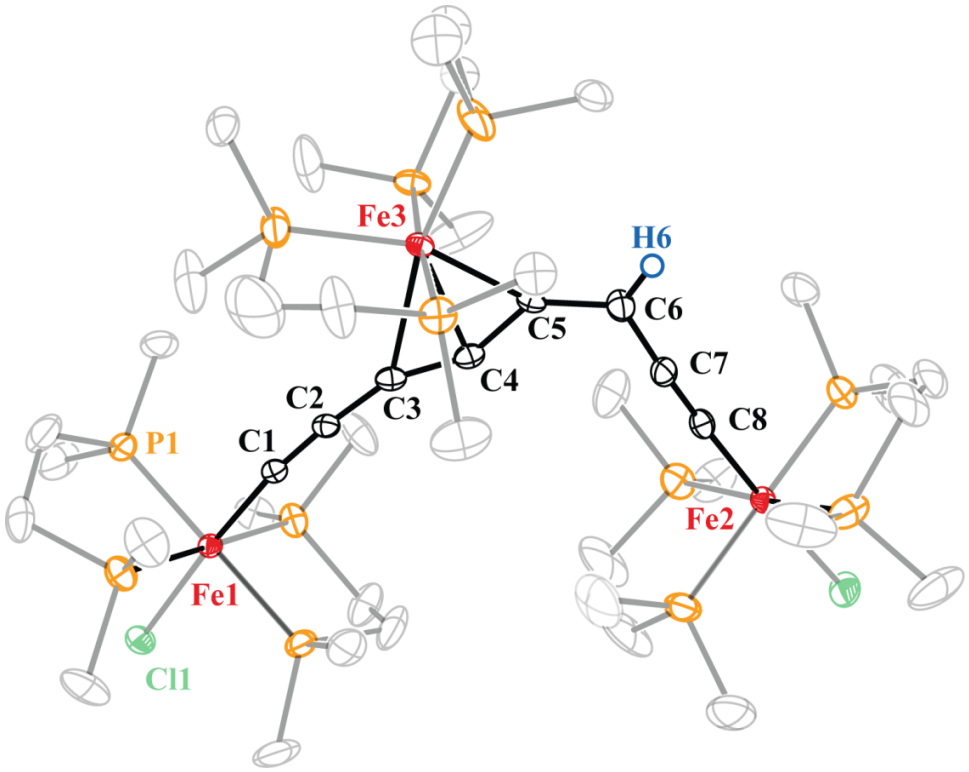

Figure 5.1. X–ray crystal structure of the complex cation in **5.1** with thermal ellipsoids rendered at 40% probability. With the exception of the vinylic hydrogen, H atoms have been omitted for clarity. Fe(1)–C(1) 1.890(8) Å, C(1)–C(2) 1.24(1) Å, C(2)–C(3) 1.352(9) Å, C(3)–C(4) 1.28(2) Å, C(4)–C(5) 1.36(2) Å, C(5)–C(6) 1.376(9) Å, C(6)–C(7) 1.425(9) Å, C(7)–C(8) 1.21(1) Å, C(8)–Fe(2) 1.878(8) Å.

complex to dissociate. In accord with the measured redox potentials obtained from the voltammetry experiment, the mono-oxidized complex **5.2** can be prepared by mixing equimolar amounts of **5.1** and $[FeCp_2]PF_6$ in dichloromethane (Scheme 5.1). Removal of the solvent, followed by washing the product with diethyl ether, leads to the isolation of analytically pure **5.2** in 83% yield. The dichloromethane/dichloroethane frozen glass EPR spectrum (Figure 5.5) taken at 100 K shows an axial signal (g_{iso} = 2.07), which indicates the formation of a LS Fe^{III} ion in solution. The near-IR spectrum of **5.2** shows the appearance of an intense, broad peak at 8711 cm^{-1} (1148 nm) which is consistent with an intervalence charge transfer process along the ene-yne backbone of **5.2** (Figure 5.6**)**. This band is not present for solutions of "$[(dmpe)_6Fe_3C_8HCl_2]^{3+}$" generated by mixing 2.5 eq. $[FeCp_2]PF_6$ with **5.1**, which supports the assignment of the low energy absorption as a photo-induced intervalence charge transfer (IVCT) process.

5.4.2 Synthesis and Characterization of Di-Nodal Complexes. In order to avoid ene-yne complex formation during the preparation of **5.3**, we employed methods in which protons were rigorously absent. Berke has recently reported the synthesis and properties of C_4-bridged ditungsten complexes in which $Li_2C_4(THF)_x$ was used as a precursor.[13] Compound 5.3 was synthesized using this material in two steps (Scheme 5.2). The first step occurs by straightforward ligand substitution where approximately one half equivalent of Li_2C_4 reacts with $[(dmpe)_2FeCl_2]$ in THF to form crude $[(dmpe)_4Fe_2Cl_2(\mu\text{-}C_4)]$ and 2 equivalents of LiCl Since the exact amount of tetrahydrofuran associated with solid $Li_2C_4(THF)_x$ is unknown, the formation of $[(dmpe)_4Fe_2Cl_2(\mu\text{-}C_4)]$ is accompanied by an unknown Fe^{II}-containing impurity. Both compounds have similar solubility, which precludes a solvent wash as a purification method. A cyclic voltammogram of the crude

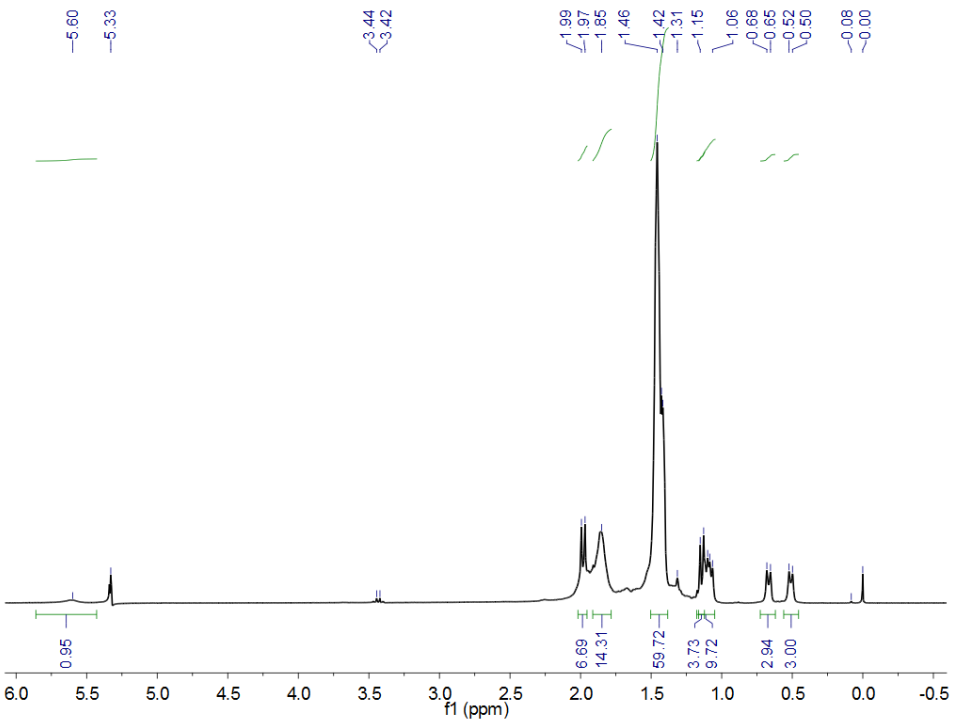

Figure 5.2. ^{1}H NMR spectrum of **5.1** in CD_2Cl_2.

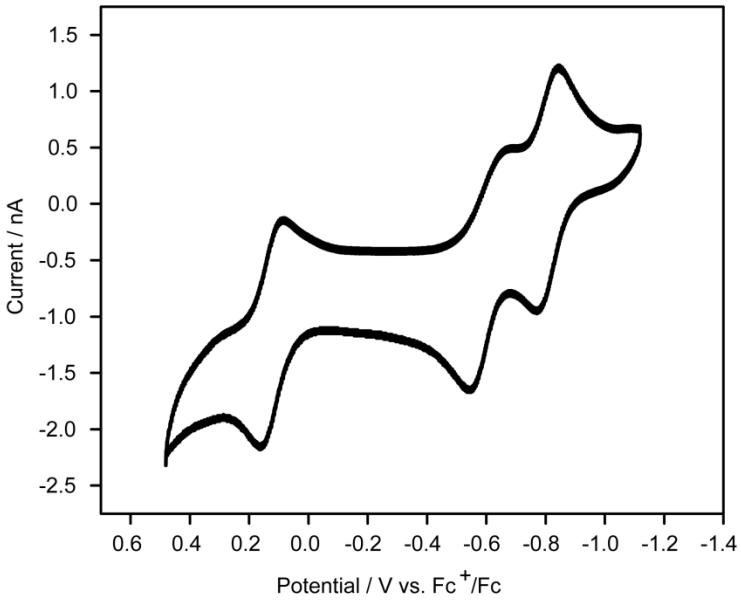

Figure 5.3. Cyclic voltammogram of **5.1** in dichloromethane The CV was obtained with a 0.25 mm Pt disk electrode at a 0.1 V/s scan rate.

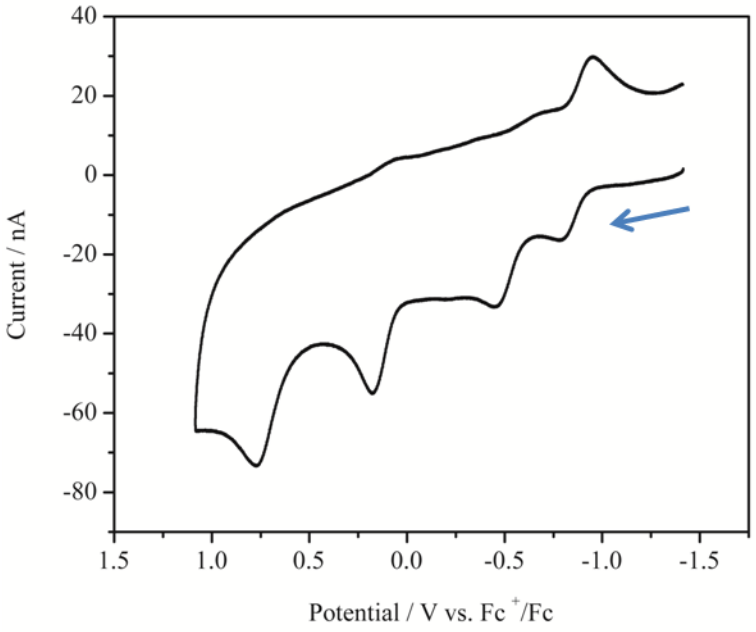

Figure 5.4. Cyclic voltammogram of **5.1** in dichloromethane showing the probable dissociation of the complex cation as a result of a fourth redox event at higher applied potentials.

THF reaction mixture indicated the presence of two oxdidation waves at −0.82 V and −1.42 V vs. Fc^+/Fc (Figure 5.7). The wave at −0.82 V is approximately twice as large as the wave at lower potentials. It represents the combined oxidation of one of the Fe centers from $[(dmpe)_4Fe_2Cl_2(\mu\text{-}C_4)]$ and an unknown mononuclear Fe-containing impurity. Since we anticipated that mixed-valent **5.3** would exhibit different solubility in non-polar solvents relative to the Fe^{II} impurity, **5.3** was formed by adding half an equivalent of $[Cp^*_2Fe](PF_6)$, allowing the impurity and Cp^*_2Fe to be washed away with diethyl ether. The choice of $[Cp^*_2Fe]^+$ as a chemical oxidant was made because the oxidation potential falls between those from $[(dmpe)_4Fe_2Cl_2(\mu\text{-}C_4)]$ and the impurity.[12] Following recrystallization, the cyclic voltammogram of clean **5.3** in dichloromethane shows two well-separated one-electron redox waves at −0.47 V and −1.08 V versus Fc^+/Fc (Figure 5.8). Accordingly, the preparation of homo-valent **5.4** was accomplished by straightforward, stoichiometric addition of one equivalent of $[Cp_2Fe](PF_6)$ to **5.3** followed by recrystallization.

The ^1H NMR spectra of **5.3** and **5.4** exhibit broad, paramagnetically shifted resonances that can be assigned to methylene, ethylene, or aromatic protons on the basis of integration (Figure 5.9). The ^1H NMR spectrum of mixed valent **5.3** contains four distinct resonances between −5.6 and −11.3 ppm, corresponding to a uniform chemical environment for both sets of dmpe protons on the NMR time scale (10^{-6} s). Similarly, the spectrum for homo-valent **5.4** contains four shifted resonances that are bunched between −13.2 and −20.3 ppm. For comparison, the dmpe resonances in the d_8-toluene ^1H NMR spectrum of isoelectronic $[(dmpe)_4Mn_2I_2(\mu\text{-}C_4)]$ are spread out between −9.5 and −21.4 ppm at 25° C.[26]

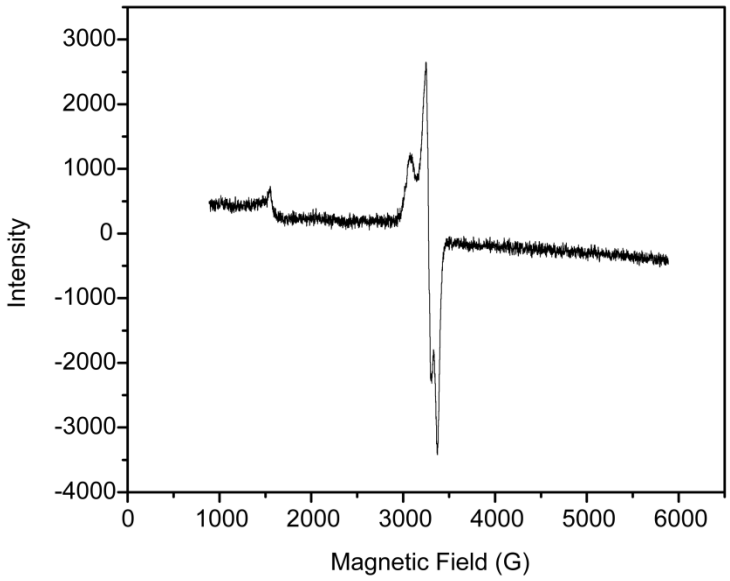

Figure 5.5. X-band EPR spectrum of **5.2** at 100 K in frozen dichloromethane/dichloroethane glass. $\Delta g = 0.36$.

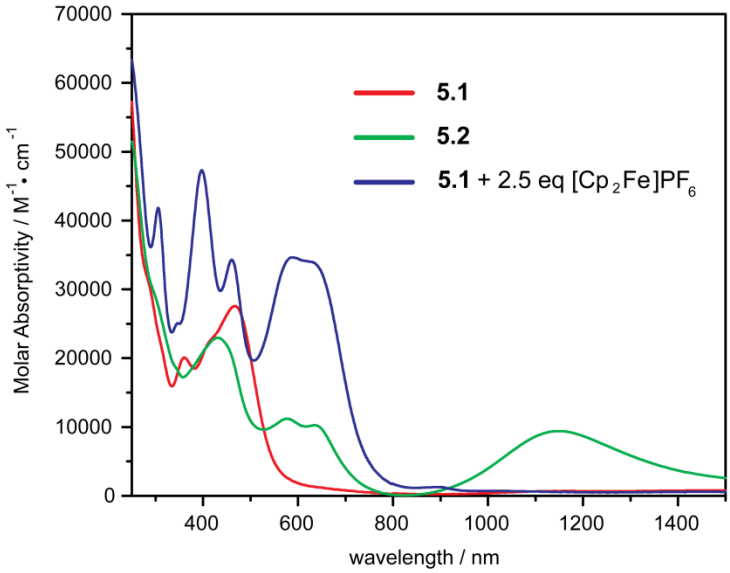

Figure 5.6. UV–Vis–NIR absorption spectra recorded in dichloromethane for **5.1**, **5.2**, and a combination of **5.1** with 2.5 equivalents of $[Cp_2Fe]^+PF_6^-$.

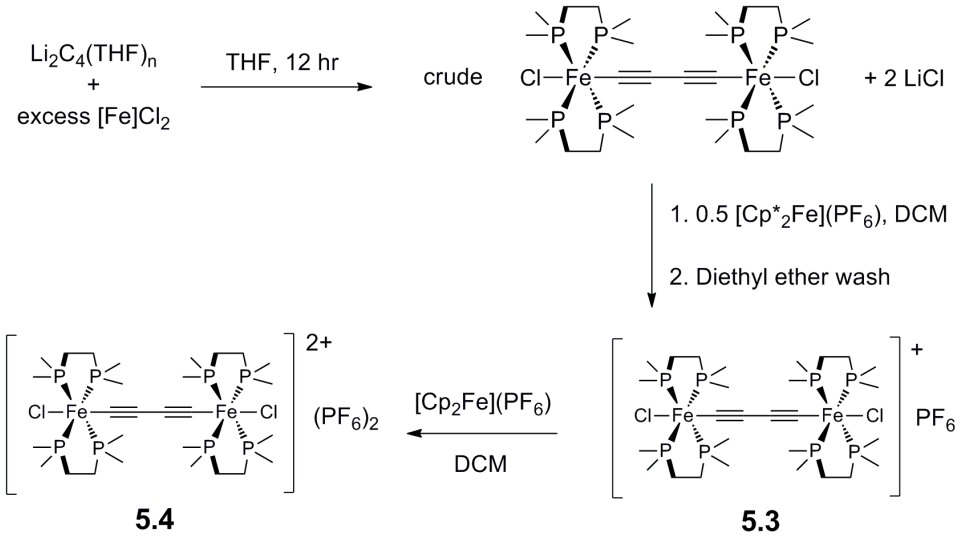

Scheme 5.2. Syntheses of C_4-bridged complexes **5.3** and **5.4**.

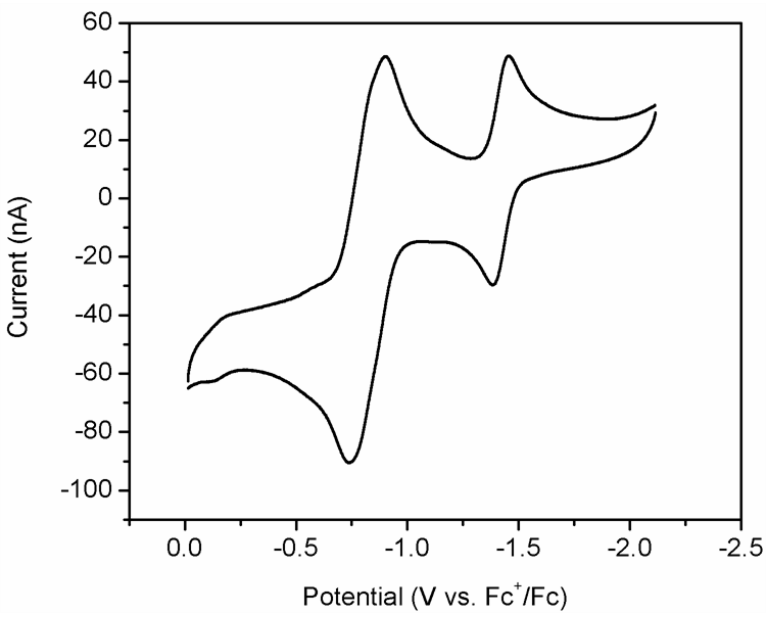

Figure 5.7. Cyclic voltammogram in tetrahydrofuran of the reaction mixture containing $[(dmpe)_4Fe_2Cl_2(\mu\text{-}C_4)]$ and an unknown, mononuclear Fe-containing impurity.

In dichloromethane, the near infrared (NIR) spectrum of **5.3** contains a broad, intense absorption centered at 1465 nm (6826 cm^{-1}) that is not present in the spectrum of homo-valent **5.4** (Figures 5.10 and 5.11). Because the absorption appears to have a shoulder at higher energy, the NIR portion of the spectrum was deconvoluted, assuming that two overlapping bands with Gaussian band shapes were present (Figure 5.11). This sort of complexity in NIR bands is common for oligoyne-bridged complexes of Fe, Ru, and Os.[27] Typically, the more intense band (band B) is attributed to direct superexchange between terminal metal centers. The weaker band is thought to originate from alternate processes such as spin-orbit coupling, double exchange mechanisms, or HOMO-SOMO transitions.[28] In the case of **5.3**, the exact processes that give rise to multiple bands are unknown.

5.4.3 X-ray structures. Single crystal X–ray analysis for compound 5.1 (Figure 5.1) reveals that a monocationic complex is formed (as the PF_6^- salt) instead of the expected neutral species. Further, the three Fe(II) ions in **5.1** are arranged in an unusual structural motif. A bent $(C_8H)^{3-}$ ligand connects two Fe atoms, while the central *cis*-$(dmpe)_2Fe^{II}$ group coordinates the ene-triyne moiety in an η^3 fashion. The terminal Fe(II) ions display pseudo-octahedral first coordination spheres comprising four dmpe-based phosphorus atoms at the equatorial positions plus axially coordinated chloride and carbon atoms. Crystallographic disorder of the ene-triyne moiety in the X-ray structure of **5.1** precludes highly precise measurements of carbon–carbon bond distances in the C_8H ligand. We note that η^3 connectivity of a $(C_4HR_2)^-$ (R = Me, ^{t}Bu, Ph, 4-(HC≡C)Ph, 3,5-$(HC{\equiv}C)_2$Ph) ligand to a $(dmpe)_2Fe^{II}$ ion has been previously documented by Field and coworkers,[8d]

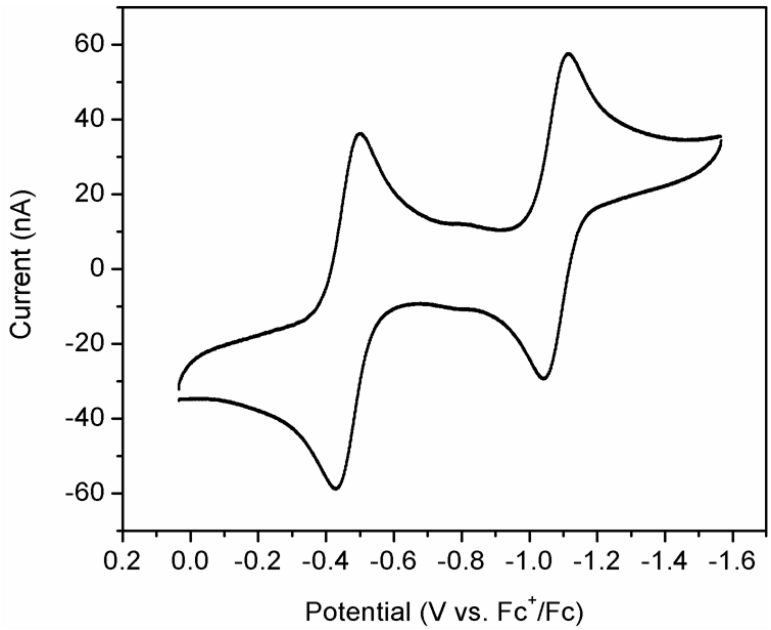

Figure 5.8. Cyclic voltammogram in dichloromethane of **5.3**. The open circuit potential falls directly between the redox waves, confirming the mixed-valent nature of **5.3** in solution.

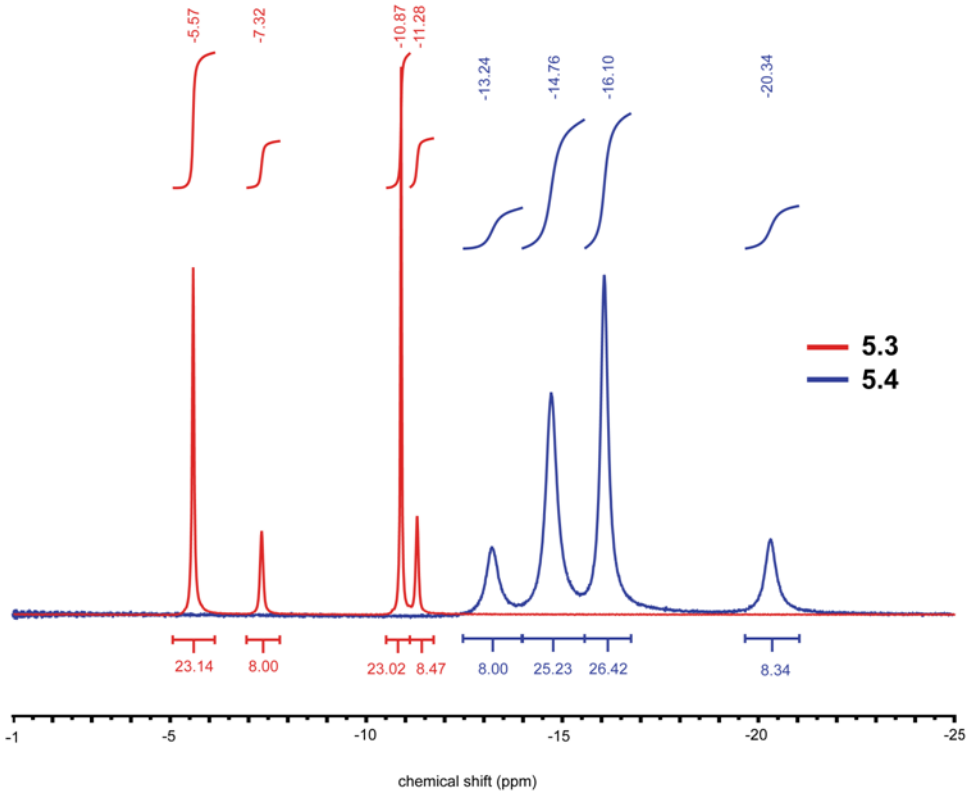

Figure 5.9. Overlaid ^{1}H NMR spectra of **5.3** and **5.4** in CD_2Cl_2.

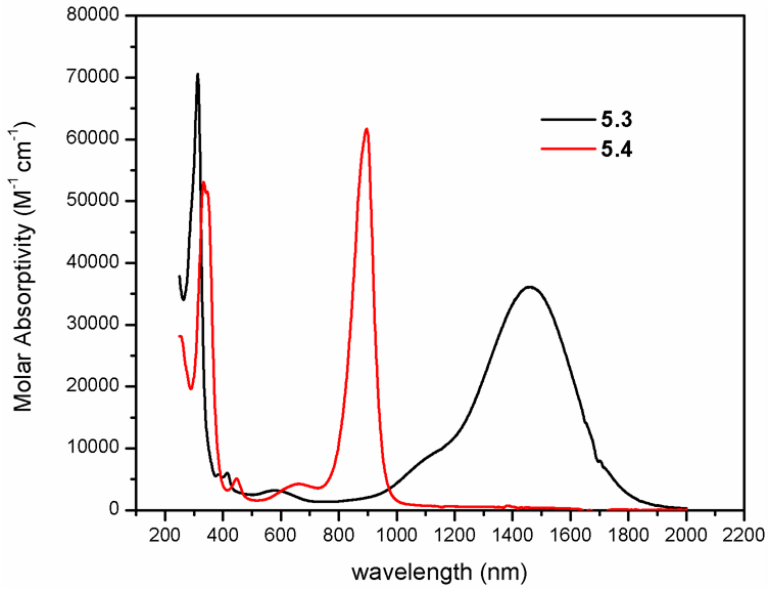

Figure 5.10. UV-Vis_NIR spectra of compounds **5.3** and **5.4** in dichloromethane.

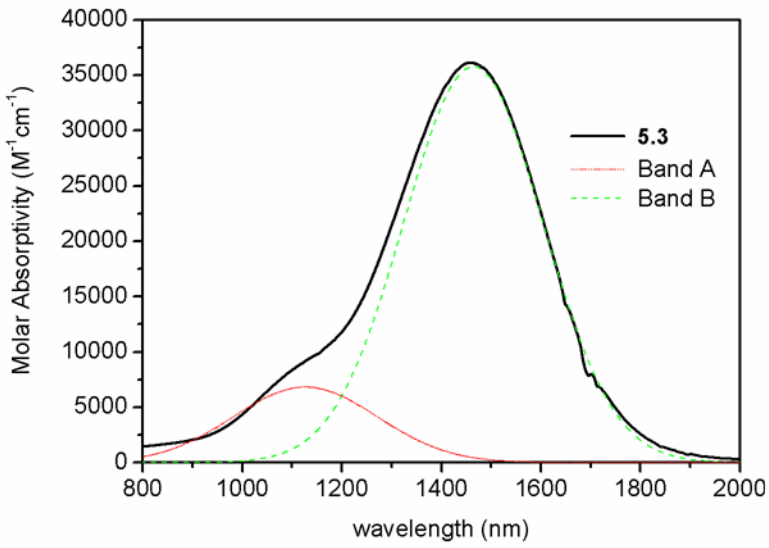

Figure 5.11. Deconvoluted NIR spectrum of **5.3** in dichloromethane.

but appending the ene-yne moiety with transition metal acetylide groups gives rise to a heretofore unprecedented trinuclear complex cation.

The structure of mixed valent **5.3b** contains two [Fe_2C_4] molecules and two triflate anions in the asymmetric unit (Figure 5.12, top). The Cl–Fe–C bond angle in one of the crystallographically independent cations is slightly smaller (176.5° versus 177.3°) and is likely the result of either weak intermolecular Cl···H–C hydrogen interactions or packing forces. Otherwise, the two cations are essentially superimposable, and both show linear Cl–Fe–C≡C–C≡C–Fe–Cl skeletal structures. A comparison of the interatomic Fe-X distances (Table 5.2) shows no significant differences between Fe species, which is consistent with delocalization of iron valence. Comparing the cation in the structure of mixed valent **5.3b** with **5.4**, the mean Fe–P distance increases slightly, which is consistent with metal oxidation. However, the iron-iron distance undergoes a contraction: the C≡C distances remain constant, but the other distances decrease. These changes are consistent with a partial contribution of a cumulenic-type bond structure to the overall bonding picture. The structure of **5.4** is reminiscent of isoelectronic [$(dmpe)_4Mn_2Cl_2(\mu\text{-}C_4)$],[26] and the carbon-carbon bond lengths in the bridging ligands for the iron and manganese complexes are the same within experimental error.

5.4.4 Magnetic Properties. The magnetic susceptibility of **5.3** at 300 K is 0.73 emu·K·mol^{-1}, consistent with a S = ½ system with significant temperature independent paramagnetism (TIP) (Figure 5.13, left). The EPR spectrum of this compound in a DCM/DCE frozen glass at 110 K shows a rhombic signal with a resonance centered at g = 4.36 corresponding to a $\Delta m_s = 2$ transition, and an anisotropic $\Delta m_s = 1$ signal at g_{iso} = 2.04 (Figure 5.14). These features are consistent with the presence of a LS octahedral

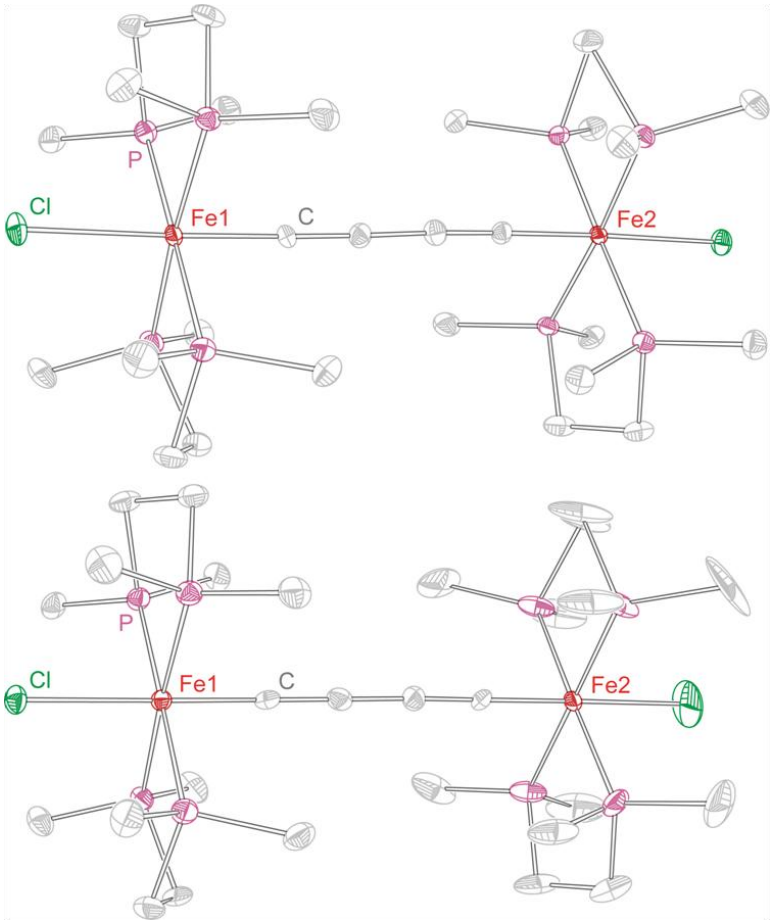

Figure 5.12. X-ray structures of the complex cations in **5.3** (OTf salt) (top) and **5.4** (bottom) with thermal ellipsoids rendered at 40% probability. Hydrogen atoms are removed for clarity.

Fe^{3+} center in the complex. The resonance centered at g = 2.04 contains three well separated signals at g = 2.09, g = 2.03, and g = 1.92 which represent the x, y, and z components of the g tensor. The extent of tensorial anisotropy in mixed valent systems has been correlated to the rate of intramolecular electron transfer, with $\Delta g < 1.1$ indicating fast electron transfer on the EPR time scale (10^{-8} s).[29] For **5.3**, Δg = 0.19 at 105 K; this is consistent with a detrapped MV state. Based on magnetic and theoretical investigations of dinuclear C_4-bridged LS d^5 complexes, the temperature-dependent susceptibility of **5.4** would be expected to show behavior consistent with a temperature dependent triplet (S = 1) ⇌ singlet (S = 0) equilibrium. Upon cooling, the raw susceptibility of **5.4** decreases monotonically from 1.88 emu·K·mol^{-1} at 300 K to 1.25 emu·K·mol^{-1} at 90 K. This is followed by an abrupt decrease to 0.07 emu·K·mol^{-1} at 2 K. Fits of the raw data to a single spin model yield D = +58 cm^{-1}, E/D fixed at 0, and TIP = 1.6 × 10^{-6} emu with g fixed at 2.02. In order to subtract the masking effects of the unquenched orbital angular momentum present for LS Fe^{III} ions, the magnetic data were also subjected to a correction procedure to isolate the spin-only and exchange coupling contributions to the susceptibility (Figure 5.13, right).[30] The adjusted susceptibility-temperature product at 300 K is 0.95 emu·K·mol^{-1}. Upon cooling, $\chi_M T$ begins a gradual decrease at approximately 200 K, then drops more precipitously below 50 K. At 5 K, $\chi_M T$ is 0.05 emu·K·mol^{-1}. This data was fit with julX to obtain D = +78 cm^{-1}, E/D fixed at 0, TIP = 0 emu, and g = 1.97. To gain further insight into the parameters of the spin equilibrium in **5.4**, magnetization data were collected (Figure 5.13, left inset). The non-superposition of the isofield data is consistent with significant zero-field splitting, and the data were fit with ANISOFIT to afford a D value of +43 cm^{-1} with g = 2.09, in

Table 5.2. Selected interatomic distances (Å) and angles (deg) for both $[Fe_2C_4]^+$ residues in the structure of $[(dmpe)_4Fe_2Cl_2(\mu\text{-}C_4)]^+$ in **5.3b** and the measured angles and distances for the $[Fe_2C_4]^{2+}$ complex in **5.4**.

	5.3 (OTf salt)	**5.4**
Fe(1)–C	1.805(5)	1.775(4)
Fe(2)–C	1.815(5)	1.763(4)
Fe(3)–C	1.822(5)	
Fe(4)–C	1.818(5)	
C(1)≡C(2)	1.250(7)	1.250(6)
C(3)≡C(4)	1.236(7)	1.256(6)
C(29)≡C(30)	1.249(7)	
C(31)≡C(32)	1.240(7)	
C2–C3	1.356(7)	1.323(6)
C30–C31	1.345(7)	
Fe(1)–P	2.248(7)	2.274(1)
Fe(2)–P	2.244(6)	2.266(2)
Fe(3)–P	2.243(8)	
Fe(4)–P	2.250(5)	
Fe(1)–Cl	2.347(1)	2.234(1)
Fe(2)–Cl	2.353(1)	2.303(2)
Fe(3)–Cl	2.349(1)	
Fe(4)–Cl	2.349(1)	

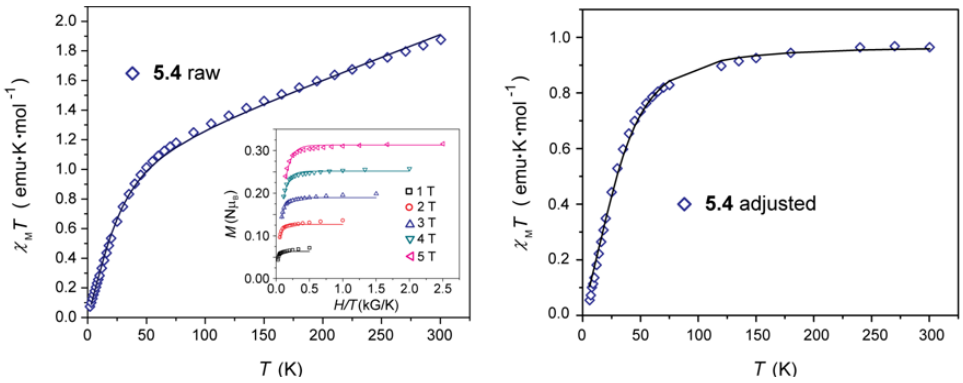

Figure 5.13. Left: Raw temperature dependence of the magnetic susceptibility data (open diamonds, measured at 1000 G) and fit (solid black line) for **5.4.** Inset: reduced magnetization data and fit for **5.4**. Right: Temperature dependent susceptibility data and fit that is corrected for the presence of unquenched orbital angular momentum on the Fe^{III} ions. See text for details of the fitting procedures.

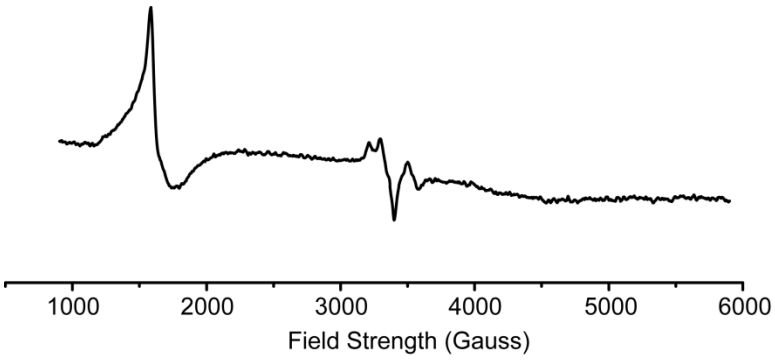

Figure 5.14. X-band EPR spectrum of **5.3** in a dichloromethane/dichloroethane frozen glass at 100 K.

reasonable agreement with the fit to the susceptibility data. Here, the magnitude of the ZFS parameter *D* corresponds to the singlet-triplet energy gap that is present for **5.4**. Thus, the triplet state lies higher in energy than the singlet by at least 43 cm^{-1} and is fully populated at room temperature.

5.5 Discussion

5.5.1 Formation of the Ene-Triyne Complex. The reaction to form **5.1** is believed to proceed by the following (Scheme 5.3): methanolic $[(dmpe)_2FeCl_2]$ forms a cationic solvento complex;[9] this may be aided by the presence of KPF_6, a reported Cl^-abstraction agent.[31] Sequential replacement of solvent by fluoride-deprotected alkynyl ligands, likely via vinylidene intermediates,[8a] leads to a *trans*-triiron species. Protonation by methanol of one butadiyne ligand at the β-carbon affords a vinylidene. A *trans-cis* isomerization, proposed by Field in the formation of *cis*-$[(dmpe)_2Fe(C_4HR_2)]^+$ complexes where methanol was the only proton source,[8d] combined with coupling of the other butadiyne ligand to the α-carbon atom of the vinylidene would form **5.1**.

5.5.3 Electronic Delocalization in Tri-Nodal Complexes. Cyclic voltammetry experiments on **5.1** in dichloromethane were employed to investigate the extent of electron delocalization possible for Fe(III) congeners (Figure 5.2). Applying Taube's method[32] to the difference in redox potentials for the Fe termini leads to a comproportionation constant of 2.1×10^3 for the reaction, $\{Fe^{III}–Fe^{II}–Fe^{III}\} + \{Fe^{II}–Fe^{II}–Fe^{II}\} \rightleftharpoons 2\{Fe^{II}–Fe^{II}–Fe^{III}\}$. This value signifies that the partial electronic delocalization present in the mixed valent congener is typical of Robin–Day Class II behavior.[33]

The preceeding experimental data suggests that valence delocalization occurs in

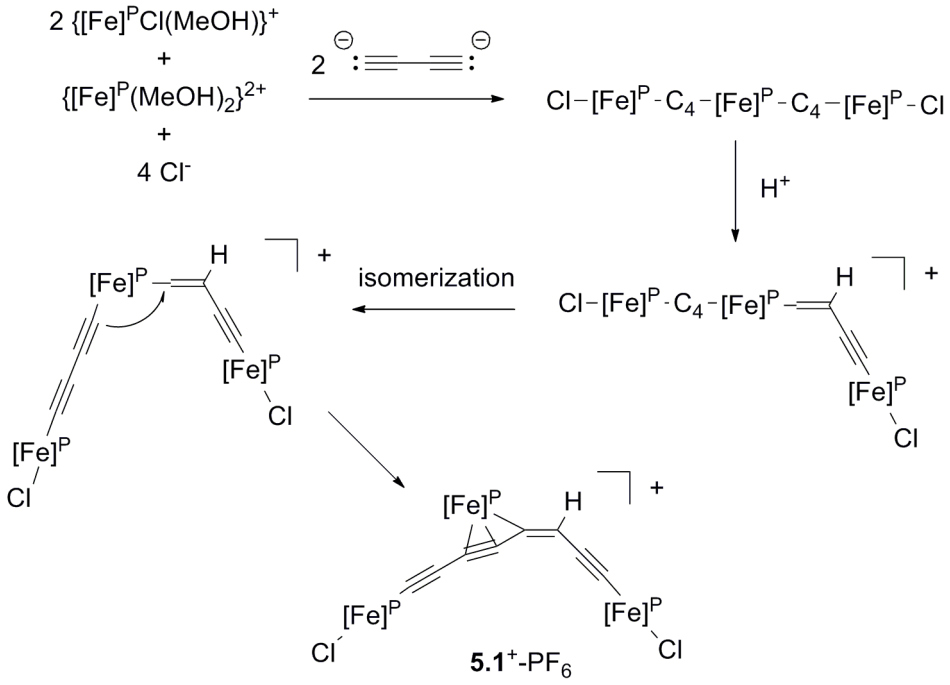

Scheme 5.3. Proposed mechanism for the formation of **5.1**.

5.2. To understand this more quantitatively, an attempt was made to apply Hush theory[14] to the near-IR data, fully aware that the asymmetric nature of the species and its IVCT band preclude a rigorous theoretical analysis. The extent of interaction in a weakly interacting donor/acceptor system (V_{ab}) can be calculated by Equation. 5.1

$$V_{ab} = (2.05\times10^{-2} / r)\sqrt{\varepsilon_{max}\nu_{max}\Delta\nu_{1/2}} \qquad \text{(Equation. 5.1)}$$

where $\Delta\nu_{1/2}$ and ν_{max} are in cm^{-1}, ε_{max} is in $M^{-1}cm^{-1}$, and r is the distance (in Å) between donor and acceptor sites. Taking values from the spectral data for **5.2**, and assuming that the electron transfer distance is approximately the same as the through-bond distance between Fe termini from the X-ray structure, V_{ab} is estimated to be 703 cm^{-1}. This compares favorably to previously characterized mixed-valent Fe-containing asymmetric C_4-bridged compounds,[15-17] where V_{ab} is estimated to be at least twice as large for **5.2** despite having a much longer through-bond connection. However, Hush theory also predicts (for symmetric complexes) the half width ($\Delta\nu_{1/2}$) of the IVCT band to be related to ν_{max} by Equation. 5.2.

$$\Delta\nu_{1/2} = \sqrt{2310\nu_{max}} \qquad \text{(Equation. 5.2)}$$

Applying this equation to the spectrum of **5.2** gives an expected $\Delta\nu_{1/2}$ = 4503 cm^{-1}, which is signicantly larger than the observed $\Delta\nu_{1/2}$ of 2430 cm^{-1}. This discrepancy is common, and has been previously observed for Fe^{III}-containing complexes under near-ideal conditions.[18] Thus, the value for V_{ab} calculated herein must be treated as approximate.

To further sustantiate the spin delocalization in **5.2**, DFT/B3LYP calculations were performed on a one–electron oxidized analogue of **5.1**. The B3LYP UKS spin density (Figure 5.15) is consistent with the partial spin delocalizitation derived from the

experimental data. The first one-electron oxidation likely occurs at the ene-ynl terminal iron (Fe2 in Figure 5.1) based on its proximity to relatively high concentrations of unpaired electron density. In addition, we note the presence of α spin density at the central *cis*-Fe^{II} ion, which suggests that the intramolecular electron transfer properties in this system could be tuned by altering the transition metal environment at the center of the ene-triyne backbone.

5.5.4 Electronic Delocalization in Di-Nodal Complexes. For the di-nodal C_4-bridged complexes, the difference in redox potentials from the two Fe^{III}/Fe^{II} couples led to an estimation of the comproportionation constant as 4×10^{10} for the reaction $[Fe_2C_4] + [Fe_2C_4]^{2+} \rightleftharpoons 2[Fe_2C_4]^{+}$. This value is consistent with a high degree of electronic delocalization in **5.3**, and the electrochemical data are consistent with the NIR spectroscopic data as well as literature precedent.[7b] The spectroscopic signatures of **5.3** were analyzed in turn, and an intense band appeared in the near infrared (1465 nm) that was not present for compound **5.4**. As with **5.2**, the observed bandwidths of both deconvoluted bands were too narrow to qualify for rigorous Class II Hush analysis. However, we note that the most intense band in the spectrum (band A) is significantly narrower than the assigned IVCT band for **5.2**. This observation, along with the large K_c value for **5.3** suggests a Class III mixed valence treatment to interpret the NIR spectrum for **5.3**. Shown in Table 5.3, the V_{ab} values for the deconvoluted spectrum are presented, and the increased electronic delocalization relative to **5.2** is consistent with the shorter, more direct ligand bridge. Furthermore, the value of V_{ab} for **5.3** obtained from band A (3716 cm^{-1}) compares favorably with the value for $[(dppe)_2Cp^*_2Fe_2(\mu\text{-}C_4)](PF_6)]$ (3791 cm^{-1}).[7b37]

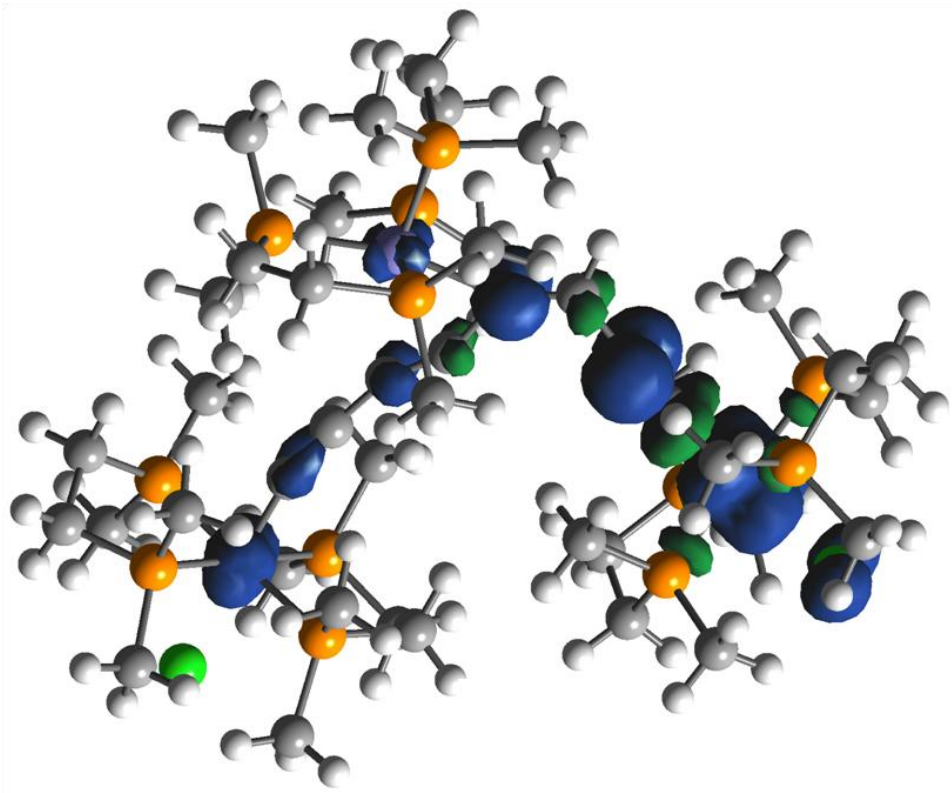

Figure 5.15. Net spin density plot (scaled at 0.001 atomic units) for the monooxidized species (**5.2**) based on the crystallographic coordinates for **5.1**. Blue surfaces correspond to net α spin density and green to net β spin density.

The fast timescale of the IR experiment (10^{-13} s) allows us to probe the relative rate of electron transfer in mixed-valent compounds. The spectrum for **5.3** contains two prominent absorptions at 1981 cm^{-1} and 1882 cm^{-1} with two shoulders protruding from the higher energy resonance at 1963 cm^{-1} and 1932 cm^{-1}. The presence of the shoulders probably indicates that non-equivalence between the Fe termini can be observed in the time-scale of IR spectroscopy, implying that the electron transfer rate is < 10^{-13} s^{-1}. For the spectrum of homo-valent $[(dmpe)_4Fe_2Cl_2(\mu\text{-}C_4)](PF_6)_2$ (**5.4**), two symmetrically shaped acetylide stretching bands are observed at 1969 cm^{-1} and 1884 cm^{-1}, consistent with a uniform bond structure along the C_4 bridging ligand.

5.5.4 Solid State Magnetic Properties of the C_4-Bridged Complex. The presence of singlet/triplet equilibria in C_4-bridged complexes has been previously noted.[38] Lapinte has reported an energy difference between these states for $[(dppe)_2Cp^*Fe_2(\mu\text{-}C_4)](PF_6)_2$ as 18 cm^{-1}.[39] Here, fits to the susceptibility data are consistent with an even larger singlet-triplet energy gap. Using julX, the fit to the raw susceptibility data is consistent with a zero field splitting parameter (and singlet-triplet energy gap) of 58 cm^{-1} while the energy gap obtained from the corrected data fit is 78 cm^{-1}. Since the masking effects of the LS Fe^{III} ion are removed from the latter data set, the fitted parameters are likely closer to reality. Alternatively, the magnitude of zero-field splitting can be evaluated from fits to the reduced magnetization data. The non-superposition of the isofield data shown in Figure 5.11 (inset) signifies the presence of magnetic anisotropy (ANISOFIT: D = 43 cm^{-1}). However, a mixture of electronic states (S=0 and S=1) is being sampled during this experiment, so the parameters obtained with ANISOFIT are less reliable.[40]

Table 5.3. NIR spectral data and Gaussian analysis for the deconvoluted IVCT bands in **5.4.**

Band	ν_{max} (cm^{-1})	ε_{max} (M^{-1} cm^{-1})	$\Delta\nu_{1/2}^{exp}$ (cm^{-1})	$\Delta\nu_{1/2}^{calc}$ (cm^{-1}) [a]	$H_{ab}^{class\ III}$ (cm^{-1}) [b]
A	8873	6828	2750	4527	4437
B	6831	35757	1560	3972	3416

[a] Calculated from Hush theory class II equation $\Delta\nu = (2310\nu_{max})^{1/2}$. [b] Calculated from $H_{ab} = \nu_{max} / 2$

The origin of the triplet state at high temperatures suggests strong ferromagnetic coupling between Fe ions. This is not intuitive with regard to the direct π*-orbital pathway between the Fe^{III} ions. However, good metal-ligand overlap allows for leakage of spin density from the metal centers onto orthogonal p_x and p_y π systems on the C_4 ligand. This orthogonality would provide a mechanism for strong ferromagnetic coupling. An alternative (but technically indistinguishable) interpretation involves the formation of a bond originating from neighboring radicals on the Fe^{III} and C^{-} atoms, leaving two unpaired electrons on the C_4 ligand and a cumulenic bonding structure. In both cases, the triplet state observed at room temperature contains a significant contribution from the ligand. The degeneracy of this state is broken at low temperature, leading to a singlet ground state.

5.6 Conclusion

The preparation, structural, magnetic, and spectroscopic characterizations of a series of tri- and di-nodal oligo-yne complexes of Fe^{III} and Fe^{II} ions have been described. The use of dehydrohalogenation conditions with a $[(dmpe)_2FeCl_2]$ starting material leads to the formation of a novel redox-active Fe-based ene-triyne complex. By using more forcing conditions under a proton-free environment, redox-active di-nodal complexes can be prepared. Spectroscopic studies of the trinuclear complex indicate significant electronic delocalization along the C_8H backbone, a property that is desirable for molecular electronics applications. Furthermore, initial computational work shows that the central Fe ion is involved in the delocalization pathway. This property opens the door for tunability if further reactivity could be focused at the central Fe^{II} site.

The extent of electronic delocalization in the C_4-bridged mixed valent complex **5.3** was found to be much greater than for the bent C_8H-bridged complex. This comes as no surprise, since the delocalization pathway is half as long and occurs along a straight vector. Further oxidation yields the di-ferric complex **5.4**, and magnetic measurements are consistent with $S = 1$ behavior at high temperatures. This high spin state likely originates from the presence of orthogonal pπ systems on the bridging ligand. Upon cooling the compound, the degeneracy that is responsible for the triplet state is broken, which leads to a singlet ground state. Fitting the variable temperature magnetic data to a $S = 1$ model with zero field splitting allows us to estimate the singlet-triplet energy gap as 78 cm^{-1}, a value that compares quite favorably to a previously characterized di-ferric C_4-bridged complex.[39]

Moving forward, the lessons learned here will be applied to the problem of increasing the number of nodes in paramagnetic carbon-bridged complexes. The results presented here suggest that larger complexes should display strong magnetic coupling while maintaining a low-dimensional topology. Both of these characteristics are attractive for advancing the state of the art in the fields of molecular magnetism and molecular electronics.

5.7 Acknowledgement

This work was supported by Colorado State University and ACS-PRF (44691-G3). We thank Profs. C. M. Elliott and O. P. Anderson for valuable discussions related to NIR and X-ray experiments, respectively.

5.8 References and Notes

1. (a) Ren, T., *Organometallics* **2005,** *24*, 4854-4870; (b) Le Stang, S.; Paul, F.; Lapinte, C., *Organometallics* **2000,** *19*, 1035-1043.

2. Schwab, P. F. H.; Smith, J. R.; Michl, J., *Chem. Rev.* **2005,** *105*, 1197-1280.

3. *Single-Molecule Magnets and Related Phenomena.* Springer: Berlin, 2006; Vol. 129, p 262.

4. Field, L. D.; Turnbull, A. J.; Turner, P., *J. Am. Chem. Soc.* **2002,** *124*, 3692-3702.

5. Ying, J.-W.; Liu, I. P.-C.; Xi, B.; Song, Y.; Campana, C.; Zuo, J.-L.; Ren, T., *Angew. Chem. Int. Ed.* **2010,** *49*, 954-957.

6. Semenov, S. N.; Taghipourian, S. F.; Blacque, O.; Fox, T.; Venkatesan, K.; Berke, H., *J. Am. Chem. Soc.* **2010,** *132*, 7584-+.

7. (a) Le Narvor, N.; Lapinte, C., *C. R. Acad. Sci., Ser. IIC: Chim.* **1998,** *1*, 745-749; (b) Le Narvor, N.; Toupet, L.; Lapinte, C., *J. Am. Chem. Soc.* **1995,** *117*, 7129-7138.

8. (a) Field, L. D.; George, A. V.; Hambley, T. W., *Inorg. Chem.* **1990,** *29*, 4565-4569; (b) Field, L. D.; George, A. V.; Laschi, F.; Malouf, E. Y.; Zanello, P., *J. Organomet. Chem.* **1992,** *435*, 347-356; (c) Field, L. D.; George, A. V.; Malouf, E. Y.; Slip, I. H. M.; Hambley, T. W., *Organometallics* **1991,** *10*, 3842-3848; (d) Field, L. D.; George, A. V.; Purches, G. R.; Slip, I. H. M., *Organometallics* **1992,** *11*, 3019-3023; (e) Field, L. D.; Turnbull, A. J.; Turner, P., *J. Am. Chem. Soc.* **2002,** *124*, 3692-3702.

9. Bellerby, J. M.; Mays, M. J.; Sears, P. L., *J. Chem. Soc. Dalton Trans.* **1976**, 1232 - 1236.

10. Girolami, G. S.; Wilkinson, G.; Galas, A. M. R.; Thorntonpett, M.; Hursthouse, M. B., *J. Chem. Soc. Dalton Trans.* **1985**, 1339-1348.

11. Chávez, I.; Alvarez-Carena, A.; Molins, E.; Roig, A.; Maniukiewicz, W.; Arancibia, A.; Arancibia, V.; Brand, H.; Manríquez, J. M., *J. Organomet. Chem.* **2000,** *601*, 126-132.

12. Connelly, N. G.; Geiger, W. E., *Chem. Rev.* **1996,** *96*, 877-910.

13. Semenov, S. N.; Blacque, O.; Fox, T.; Venkatesan, K.; Berke, H., *J. Am. Chem. Soc.* **2010,** *132*, 3115-3127.

14. *APEX 2*, Bruker Analytical X-ray Systems, Inc.: Madison, WI, 2008.

15. Sheldrick, G. M. *SHELXTL*, Bruker Analytical X-Ray Systems, Inc.: Madison, WI, 1999.

16. Spek, A. L. *PLATON, A Multipurpose Crystallographic Tool*, Utrecht University: Utrecht, The Netherlands, 2005.

17. Kahn, O., *Molecular Magnetism*. VCH: New York: 1993.

18. Bill, E. *julX*, 1.41; Max Planck Institute for Bioinorganic Chemistry: Mulheim an der Ruhr, 2008 (http://ewww.mpi-muelheim.mpg.de/bac/logins/bill/julX_en.php).

19. Shores, M. P.; Sokol, J. J.; Long, J. R., *J. Am. Chem. Soc.* **2002,** *124*, 2279-2292.

20. Frisch, M. J.; Trucks, G. W.; Schlegel, H. B.; Scuseria, G. E.; Robb, M. A.; Cheeseman, J. R.; Montgomery, J., J. A. ; Vreven, T.; Kudin, K. N.; Burant, J. C.; Millam, J. M.; Iyengar, S. S.; Tomasi, J.; Barone, V.; Mennucci, B.; Cossi, M.; Scalmani, G.; Rega, N.; Petersson, G. A.; Nakatsuji, H.; Hada, M.; Ehara, M.; Toyota, K.; Fukuda, R.; Hasegawa, J.; Ishida, M.; Nakajima, T.; Honda, Y.; Kitao, O.; Nakai, H.; Klene, M.; Li, X.; Knox, J. E.; Hratchian, H. P.; Cross, J. B.; Bakken, V.; Adamo, C.; Jaramillo, J.; Gomperts, R.; Stratmann, R. E.; Yazyev, O.; Austin, A. J.; Cammi, R.; Pomelli, C.; Ochterski, J. W.; Ayala, P. Y.; Morokuma, G. A.; Voth, G. A.; Salvador, P.; Dannenberg, J. J.; Zakrzewski, V. G.; Dapprich, S.; Daniels, A. D.; Strain, M. C.; Farkas, O.; Malick, D. K.; Rabuck, A. D.; Raghavachari, K.; Foresman, J. B.; Ortiz, J. V.; Cui, Q.; Baboul, A. G.; Clifford, S.; Cioslowski, J.; Stefanov, B. B.; Liu, G.; Liashenko, A.; Piskorz, P.; Komaromi, I.; Martin, R. L.; Fox, D. J.; Keith, T.; Al-Laham, M. A.; Peng, C. Y.; Nanayakkara, A.; Challacombe, M.; Gill, P. M. W.; Johnson, B.; Chen, W.; Wong, M. W.; Gonzalez, C.; Pople, J. A. *Gaussian 03*, Gaussian, Inc.: Wallingford, CT, 2004.

21. Rappé, A. K.; Bormann-Rochotte, L. M.; Wiser, D. C.; Hart, J. R.; Pietsch, M. A.; Casewit, C. J.; Skiff, W. M., *Mol. Phys.* **2007,** *105*, 301 - 324.

22. Hay, P. J.; Wadt, W. R., *J. Chem. Phys.* **1985,** *82*, 299-310.

23. (a) Ditchfield, R.; Hehre, W. J.; Pople, J. A., *J. Chem. Phys.* **1971,** *54*, 724; (b) Francl, M. M.; Pietro, W. J.; Hehre, W. J.; Binkley, J. S.; Gordon, M. S.; DeFrees, D. J.; Pople, J. A., *J. Chem. Phys.* **1982,** *77*, 3654.

24. Field, L. D.; Magill, A. M.; Pike, S. R.; Turnbull, A. J.; Dalgarno, S. J.; Turner, P.; Willis, A. C., *Eur. J. Inorg. Chem.* **2010,** *2010*, 2406-2414.

25. Colbert, M. C. B.; Lewis, J.; Long, N. J.; Raithby, P. R.; Younus, M.; White, A. J. P.; Williams, D. J.; Payne, N. N.; Yellowlees, L.; Beljonne, D.; Chawdhury, N.; Friend, R. H., *Organometallics* **1998,** *17*, 3034-3043.

26. Kheradmandan, S.; Heinze, K.; Schmalle, H. W.; Berke, H., *Angew. Chem. Int. Ed.* **1999,** *38*, 2270-2273.

27. (a) D'Alessandro, D. M.; Keene, F. R., *Chem. Rev.* **2006,** *106*, 2270-2298; (b) Bruce, M. I.; Costuas, K.; Davin, T.; Ellis, B. G.; Halet, J.-F.; Lapinte, C.; Low, P. J.; Smith, M. E.; Skelton, B. W.; Toupet, L.; White, A. H., *Organometallics* **2005,** *24*, 3864-3881.

28. Klein, A.; Lavastre, O.; Fiedler, J., *Organometallics* **2005,** *25*, 635-643.

29. Lohan, M.; Ecorchard, P.; Rüffer, T.; Justaud, F. d. r.; Lapinte, C.; Lang, H., *Organometallics* **2009,** *28*, 1878-1890.

30. (a) Lescouĕzec, R.; Lloret, F.; Julve, M.; Vaissermann, J.; Verdaguer, M., *Inorg. Chem.* **2002,** *41*, 818-826; (b) Toma, L. M.; Lescouezec, R.; Pasan, J.; Ruiz-Perez, C.; Vaissermann, J.; Cano, J.; Carrasco, R.; Wernsdorfer, W.; Lloret, F.; Julve, M., *J. Am. Chem. Soc.* **2006,** *128*, 4842-4853.

31. Bruce, M. I., *Chem. Rev.* **1991,** *91*, 197-257.

32. Richardson, D. E.; Taube, H., *Inorg. Chem.* **1981,** *20*, 1278-1285.

33. Robin, M. B.; Day, P., *Adv. Inorg. Chem. Radiochem.* **1967,** *10*, 247-422.

34. Hush, N. S., *Prog. Inorg. Chem.* **1967,** *8*, 391.

35. Elliott, C. M.; Derr, D. L.; Matyushov, D. V.; Newton, M. D., *J. Am. Chem. Soc.* **1998,** *120*, 11714-11726.

36. (a) Coat, F.; Guillevic, M.-A.; Toupet, L.; Paul, F.; Lapinte, C., *Organometallics* **1997,** *16*, 5988-5998; (b) Paul, F.; Meyer, W. E.; Toupet, L.; Jiao, H.; Gladysz, J. A.; Lapinte, C., *J. Am. Chem. Soc.* **2000,** *122*, 9405-9414.

37. Interestingly, the comproportionation constant is essentially the same as that observed for the $[(dmpe)_4Mn_2I_2(\mu\text{-}C_4)]^+$, but V_{ab} for **5.3** is seven times greater.

38. Lapinte, C., *J. Organomet. Chem.* **2008,** *693*, 793-801.

39. Le Narvor, N.; Lapinte, C., *C. R. Acad. Sci., Ser. IIC: Chim.* **1998,** *1*, 745-749.

40. A low error in the fit is only possible because one of the states is diamagnetic. This accounts for the lower than expected saturation values at high field/low temp. Therefore, little weight should be placed on the extracted values from this fit.

Appendix

A.1 Supporting Information for Chapter 4

X-ray structural data for compounds **4.1**-**4.4** are available on the Internet as a crystallographic information file at:

http://pubs.acs.org/doi/suppl/10.1021/ic101528d/suppl_file/ic101528d_si_002.cif

Besides the compounds presented in Chapter 4, additional chromium acetylide complexes were synthesized and characterized in the course of my research.

A.1.1 Preparation of Compounds

$[(dmpe)_2Cr(C_2Si^iPr_3)_2]$ (A.1.1). Under an argon atmosphere, a solution of $[Cr(dmpe)_2Cl_2]$ (250 mg, 0.591 mmol) in 10 mL of freshly degassed diethyl ether was added to a solution of triisopropylsilylacetylene (0.27 mL, 1.21 mmol) and *n*-BuLi (0.78 mL of a 1.54 M solution in hexanes, 1.21 mmol) in 5 mL of diethyl ether at room temperature. After stirring for 12 hours, the solvent was removed *in vacuo*. The orange residue was extracted with 15 mL of pentane under dinitrogen. Concentration of the solution to 5 mL and placement in a –40°C freezer afforded 155 mg $[(dmpe)_2Cr(C_2Si^iPr_3)]$ as an orange crystalline solid (0.217 mmol, 37%). The compound was sufficiently stable to collect X-ray data, but decomposed after *ca.* one week of standing in the dinitrogen-filled glovebox. A cyclic voltammogram obtained on this material indicated that the complex could be oxidized by ferrocenium to yield the Cr^{III} congener. After we isolated **A.1.1** in 2008, it was reported by Berke and coworkers in 2010.[1]

[(dmpe)$_2$Cr(C$_2$Si^{i}Pr$_3$)$_2$](PF$_6$) (A.1.2). In the glovebox, a solution of A.1.2 (35 mg, 0.049 mmol) in 5 mL of tetrahydrofuran was added to a solution of [Cp$_2$Fe]PF$_6$ (17 mg, 0.05 mmol) in 2 mL of tetrahydrofuran. After stirring for 2 hours, the solvent was removed *in vacuo*, leaving a yellow solid. The solid was washed with diethyl ether (3 × 5 mL), affording 38 mg of A.1.2 as a yellow solid (0.044 mmol, 90% based on A.1.1). Needle shaped crystals suitable for X-ray diffraction studies were grown by the slow diffusion of diethyl ether into a concentrated dichloromethane solution of A.1.2. IR (mineral oil): ν_{CC} 1991 cm^{-1}, ν_{CSi} 837 cm^{-1}. Absorption spectrum (dichloromethane): λ_{max} (ε_M) 382 (20800), 397 nm (21700 L·mol^{-1}·cm^{-1}). Magnetic susceptibility (SQUID, 293 K): 1.91 emu·K·mol^{-1}. Anal. Calcd. for $C_{34}H_{74}CrF_6P_5Si_2$: C, 47.48; H, 8.68. Found: C, 47.36; H, 8.31.

[(dmpe)$_2$Cr(C$_2$Si^{i}Pr$_3$)(MeCN)]BPh$_4$ (A.1.3). In a dinitrogen-filled glovebox, solid [Cp*$_2$Fe]BPh$_4$ (39 mg, 0.060 mmol) was added to a solution of [(dmpe)$_4$Cr$_2$(C$_2$Si^{i}Pr$_3$)$_2$(μ-N$_2$)] (4.2) (33 mg, 0.030 mmol) in 10 mL of diethyl ether. Then, 0.5 mL of acetonitrile was added to the mixture, causing the solid green [Cp*$_2$Fe]BPh$_4$ to be replaced by a golden yellow solid over 2 hours of stirring. The yellow solid was isolated by filtration to yield 44 mg of product (0.049 mmol, 82%). Plate-shaped single crystals of this compound were grown by diffusion of diethyl ether vapor into a concentrated solution of the compound in tetrahydrofuran. IR (mineral oil): ν_{CC} 1964 cm^{-1}, ν_{CN} 2253, 2305 cm^{-1}. Absorption spectrum (dichloromethane): λ_{max} (ε_M) 337 (4120), 353 (4830), 372 (sh, 3530), 418 nm (sh, 1090 L·mol^{-1}·cm^{-1}). Anal. Calcd. for $C_{49}H_{76}NBCrP_4Si$: C, 65.84; H, 8.57; N, 1.57. Found: C, 65.58; H, 8.30; N, 1.42.

[(dmpe)$_2$Cr(C$_2$Si^{i}Pr$_3$)Cl](BAr$_4^F$) (A.1.4). Crystals of this compound were first obtained by allowing a tetrahydrofuran solution of [(dmpe)$_4$Cr$_2$(C$_2$Si^{i}Pr$_3$)$_2$(μ-N$_2$)](BAr$_4^F$) and trace amounts of LiCl (from the synthesis of [(dmpe)$_4$Cr$_2$(C$_2$Si^{i}Pr$_3$)$_2$(μ-N$_2$)]) to stand at room temperature, followed by slow diffusion of pentane vapor to yield crystals of A.1.4. I have since attempted to devise a more optimum set of reaction conditions, which I report below.

A solution of tetrabutylammoniun chloride (25 mg, 0.090 mmol) and [Cp$_2$Fe](BAr$_4^F$) (4 eq., 187 mg, 0.18 mmol) in tetrahydrofuran (3 mL) was added to a solution of **4.2** (48 mg, 0.044 mmol) in tetrahydrofuran. The solution quickly turned yellow. After stirring for 10 minutes, the solvent was concentrated. Pentane was slowly diffused into the reaction solution to afford yellow crystals of **A.1.4**. The crystals were isolated by filtration, washed with pentane (2 × 3 mL), and dried under dinitrogen. IR (ATR): ν_{CC} 1994 cm^{-1}. Anal. Calcd. for $C_{64.6}H_{86.6}BClCrF_{24}N_{0.6}P_4Si$ (**A.1.4** · 0.6 Bu$_4$NCl): C, 49.17; H, 5.53; N, 0.53. Found: C, 49.11; H, 4.08; N, 0.67. The discrepancy in the hydrogen value indicates the presence of an additional impurity whose idendity has not been determined.

A.1.2 X-Ray Structure Determinations

Structural characterization for **A.1.1-A.1.4** was done by X-Ray analysis (Table A.1.1). The data quality for **A.1.2** was hampered by the thin plate-like nature of the crystals, which caused weak diffraction in certain crystal orientations. Two crystallographically independent molecules were present in the unit cell of **A.1.2**. Attempts to refine two carbon atoms on a tetraphenylborate anion and C$_2$Si^{i}Pr$_3$ ligand

Table A.1.1. Crystallographic data[a] for $[(dmpe)_2Cr(C_2Si^iPr_3)_2]$ (**A.1.1**), $[(dmpe)_2Cr(C_2Si^iPr_3)_2](PF_6)$ (**A.1.2**), $[(dmpe)_2Cr(C_2Si^iPr_3)(MeCN](BPh_4)$ (**A.1.3**), $[(dmpe)_2Cr(C_2Si^iPr_3)Cl](BAr_4^F)$ (**A.1.4**).

	A.1.1	**A.1.2**	**A.1.3**	**A.1.4**
crystal ID	msn132	msn133	msn155	msn210
formula	$C_{34}H_{74}Si_2P_4Cr$	$C_{34}H_{74}CrF_6P_5Si_2$	$C_{49}H_{76}BCrNP_4Si$	$C_{59}H_{65}BClCrF_{24}P_4Si$
fw	714.99	859.96	893.89	1480.34
color, habit	orange plate	yellow needle	yellow plate	yellow prism
T, K	100(2)	100(2)	100(2)	120(2)
space group	$P2_1/n$	$P\bar{1}$	$P\bar{1}$	$P\bar{1}$
Z	2	4	4	8
a, Å	15.5725(7)	14.0510(4)	10.3412(6)	18.888(2)
b, Å	9.1025(4)	17.3313(5)	20.8317(12)	19.118(2)
c, Å	16.2657(7)	20.3096(6)	24.4851(14)	36.263(4)
α, deg	--	74.513(2)	74.766(3)	90.004(4)
β, deg	113.525(2)	76.433(2)	89.747(4)	92.752(4)
γ, deg	--	79.269(2)	88.759(4)	91.377(4)
V, Å^3	2114.01(16)	4587.5(2)	5088.2(5)	13076(2)
d_{calc}, g/cm^3	1.123	1.245	1.167	1.504
GOF	1.00	1.04	1.08	1.109
$R_1(wR_2)$[b], %	3.11 (7.76)	5.25 (14.72)	8.51(24.30)	17.63(43.88)

[a] Obtained with graphite-monochromated Mo Kα (λ = 0.71073 Å) radiation.
[b] $R_1 = \sum||F_o| - |F_c||/\sum|F_o|$, $wR_2 = \{\sum[w(F_o^2 - F_c^2)^2]/\sum[w(F_o^2)^2]\}^{1/2}$ for $I > 2\sigma(I)$.

gave non-positive definite results, so the thermal parameters for these carbon atoms remained isotropic.

In the structure of **A.1.3**, positional disorder for one isopropyl substituent was modeled at a 55:45 occupancy ratio.

The structure solution for **A.1.4** was hindered by high R_{int} values despite the crystals having a large and well-formed morphology. However, the structure solution described here was sufficient to establish atomic connectivity.

A.1.3 Results and Discussion. As Berben and Berke have noted,[1,2] the synthesis of chromium bis-acetylide complexes can be achieved by reacting two equivalents of a lithiated acetylide ligand with $[(dmpe)_2CrCl_2]$. The synthesis of **A.1.1** was done in this fashion under an argon atmosphere as an added measure to prevent the formation of dinitrogen bridged **4.2**. This complex can be cleanly oxidized by ferrocenium to afford complex **A.1.2**. The X-ray structures of both **A.1.1** (Figure A.1.1, top left) and **A.1.2** (Figure A.1.1, top right) clearly show that the Cr ions coordinate the dmpe and acetylide ligands in an octahedral fashion, with the acetylide ligands located at the axial positions. Upon oxidation, the average Cr–P bond lengths increase from 2.338(4) Å in **A.1.1** to 2.43(1) Å in **A.1.2** while the Cr–C bond contracts from 2.045(2) Å to 2.027(4) Å. The latter effect likely results from a stronger electrostatic interaction between the anionic acetylide ligands and the tri-valent Cr ion.

Our original attempts at isolating oxidized analogues of **4.2** were performed in acetonitrile, which resulted in the isolation of crystals of **A.1.3** (Figure A.1.1, bottom left). Although the neutral dinitrogen complex is relatively stable in the presence of strong σ-donor ligands, it is clear that the $Cr–N_2$ bond becomes weaker upon oxidation,

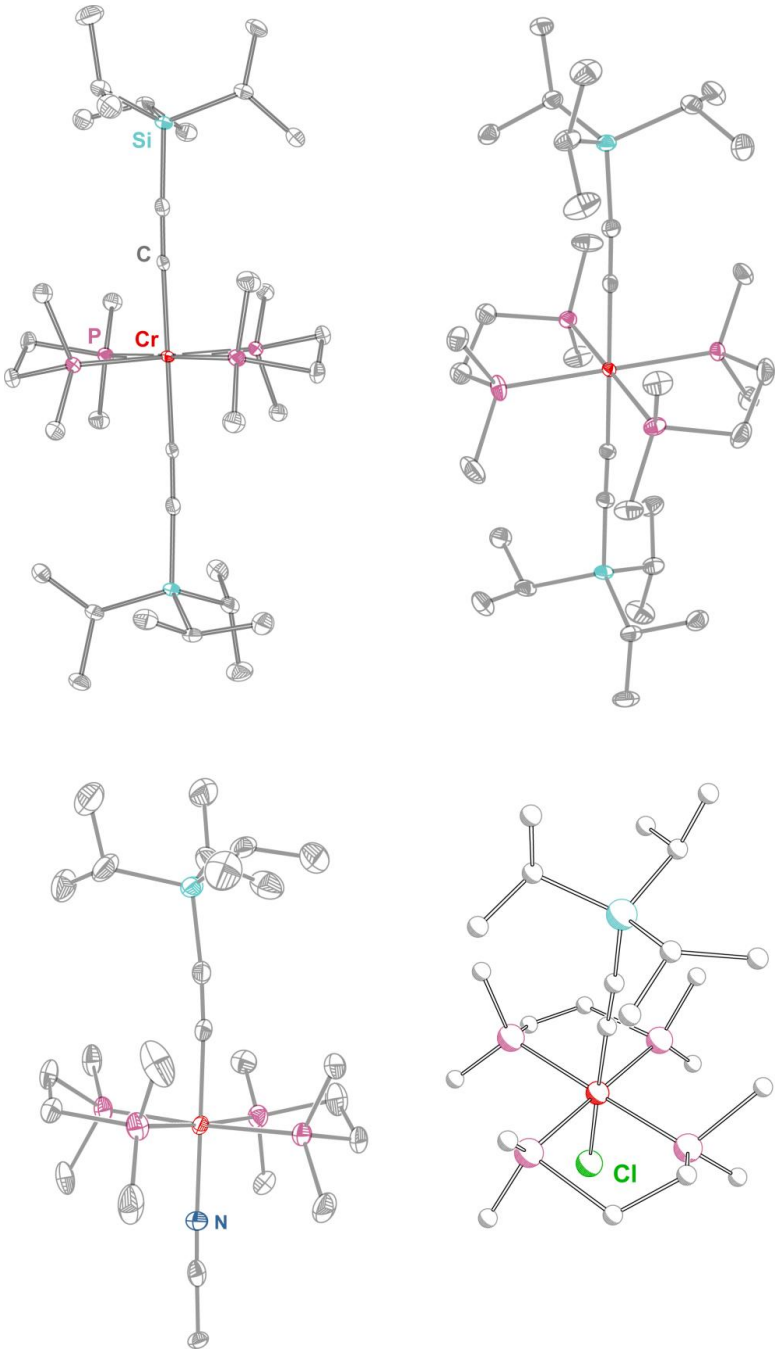

Figure A.1.1. X-ray crystal structures of the complexes in **A.1.1** (top left), **A.1.2** (top right), **A.1.3** (bottom left), and **A.1.4** (bottom right) with thermal ellipsoids rendered at 40% probability. Red, purple, cyan, blue, green, and gray ellipsoids/spheres represent chromium, phosphorus, silicon, nitrogen, chlorine, and carbon atoms respectively. Hydrogen atoms have been omitted for clarity. Thermal ellipsoids for **A.1.4** could not be rendered because of the presence of non-positive definite atoms in the complex.

and the dinitrogen ligand can be displaced. This result offers the possibility of using **4.2** as a synthon for the preparation of nitrile-bridged clusters containing $S = 1$ Cr^{II} centers. However, recent work by Saillard and coworkers indicates that electronic communication between Fe^{III} centers through aromatic nitrile ligands is weak,[10] so the pursuit of nitrile bridged assemblies would appear to have a small return on investment.

A.2 Supporting Information for Chapter 5

X-ray structural data for compound **5.1** is available on the Internet as a crystallographic information file at:

http://www.rsc.org/suppdata/CC/C0/C0CC00202J/C0CC00202J.TXT

A.3 Syntheses and Structures of Additional Coordination Compounds

While exploring possible routes for the preparation of paramagnetic acetylide compounds, I synthesized several other compounds that were not fully characterized. However, some of these compounds were structurally characterized, and the experimental procedures and crystal structures are presented here.

A.3.1 Preparation of Compounds

***trans*-[(cyclam)CrCl(CF_3SO_3)](CF_3SO_3) (A.3.1)**. In a 250 mL Schlenk flask, neat triflic acid (ca. 3 mL) was added to solid *trans*-[(cyclam)$CrCl_2$]Cl_2[3] (345 mg, 0.962 mmol) under an atmosphere of dinitrogen. The resulting purple solution was heated at 70° C overnight with stirring. The solution was chilled in an ice bath, and 75 mL diethyl ether was carefully added to precipitate a gray/purple solid. The solid was isolated by filtration, washed with diethyl ether (3× 5 mL), and dried under vacuum to afford 527 mg of product (0.899 mmol, 93%). Crystals of **A.3.1** were grown by diffusion of diethyl ether vapor into concentrated solutions of **A.3.1** in methanol.

[(cyclen)Cu(CH_3CN)](CF_3SO_3)$_2$ (A.3.2). In a 100 mL Schlenk flask, neat triflic acid was added to solid [(cyclen)CuCl]Cl·H_2O[4] under dinitrogen. Acetonitrile (5 mL) was added to facilitate stirring, and the purple solution was heated at 70° C overnight with stirring. During the reaction, the solution turned yellow-green. The solution was chilled in an ice bath, and diethyl ether (80 mL) was added to precipitate a yellow-green solid. Addition of acetonitrile caused a yellow solid to separate from a green soluble component. Crystals of **A.3.2** could be grown by diffusion of diethyl ether vapor into concentrated solutions of **A.3.2** in acetonitrile.

[(dmpe)Mn(CpMe)($C_2Si^iPr_3$)] (A.3.3). The trimethylsilyl analogue of this compound was reported earlier.[2] In a 50 mL Schlenk flask, dmpe (0.225 mg, 0.25 mL, 1.50 mmol) and tri(isopropyl)silylacetylene (0.279 mg, 0.34 mL, 1.53 mmol) were added to a solution of dimethylmanganocene[5] (323 mg, 1.52 mmol) in benzene (12 mL). The solution was refluxed under dinitrogen for 17 hr, during which time it turned orange. The solvent was removed *in vacuo*, and the residue was extracted with pentane (8 mL). The pentane extract was concentrated to 2 mL and cooled to −35° C for 4 hr to afford red-brown crystals. The crystals were isolated by filtration, washed with cold (−35° C) pentane (2 × 2 mL), and dried under dinitrogen to afford 180 mg of product (0.387 mmol, 25 %). IR (mineral oil): ν_{CC} 1943 cm^{-1}. ^{1}H NMR (C_6D_6) δ 6.15, 2.86 (br, 21H, −SiC_3H_7), 2.02 (br, 3H, CpCH_3), −5.00 (br, Cp−*H*), −15.00 (br, −PCH_2), −21.32 (br, −PCH_3).

[(dmpe)$_2$FeCl(*p*-^{i}Pr$_3$SiDEBH)] (A.3.4). Triethylamine (1 mL, 7.15 mmol) was added to solution of [(dmpe)$_2$$FeCl_2$][6] (390 mg, 0.915 mmol) and *p*-^{i}Pr_3SiDEBH[7] (280.3 mg, 0.915 mmol) in methanol (10 mL). The solution immediately turned orange. After 10 minutes, an orange solid precipitated which was isolated by filtration, washed with

methanol (2 × 5 mL) then dried under vacuum for 1 hr at 293 K to afford 400 mg of product (0.574 mmol, 63%). IR (ATR) ν_{CCSi} 2148 cm^{-1}, ν_{CCFe} 2035 cm^{-1}. ^1H NMR (C_6D_6) δ 7.44 (d, 2H, Ar–*H*), 6.94 (d, 2H, Ar–*H*), 1.55 (m, 8H, –PCH_2), 1.34 (s, 12H, –PCH_3), 1.27 (s, 12H, –PCH_3), 1.21 ppm (s, 21H, –SiC$_3H_7$). Anal. Calcd. for $C_{31}H_{57}ClFeP_4Si$: C, 55.32; H, 8.54. Found: C, 55.20; H, 8.59.

[(dmpe)$_2$FeCl(*p*-DEBH)] (A.3.5). Slightly wet (ca. 5% H_2O) tetrabutylammonium fluoride (0.51 mL of a 1M THF solution, 0.51 mmol) was added to solution of A.3.4 (355 mg, 0.509 mmol) in THF (5 mL). After stirring for 3 hours at room temperature, the solution was evaporated, and the orange residue was treated with methanol (5 mL). The mixture was placed in a –40 °C freezer for 1 hour. The orange solid was isolated by filtration, washed with cold (–40 °C) methanol (2 × 5 mL) then dried under vacuum for 1 hr at 293 K to afford 202 mg of product (0.391 mmol, 76%). IR (ATR) ν_{CC} 2040, 2021, 2011 cm^{-1}. ^1H NMR (C_6D_6) δ 7.40 (d, 2H, Ar–*H*), 6.92 (d, 2H, Ar–*H*), 2.83 (s, 1H, –CC*H*), 1.55 (m, 8H, –PCH_2), 1.34 (s, 12H, –PCH_3), 1.27 ppm (s, 12H, –PCH_3). ^{13}C NMR (CD_2Cl_2) δ 131.89 (s, 2C, C_{Ar}–H), 130.97 (s, 1C, Fe–C*C*–Ar), 129.65 (C_{Ar}–H), 120.23 (s, 1C, C_{Ar}–C_2H), 114.85 (s, 1C, C_{Ar}–C_2Fe), 84.85 (s, 1C, *C*CH), 76.92 (s, 1C, C*C*H), 30.30 (p, 4C, P*C*H$_2$), 15.59 (m, 4C, P*C*H$_3$), 13.28 ppm (m, 4C, P*C*H$_3$). The resonance for the carbon atom ligated to Fe^{II} was not observed. Absorption spectrum (toluene): λ_{max} (ε_M) 405 nm (47340 $M^{-1}\cdot cm^{-1}$). Anal. Calcd. for $C_{22}H_{37}ClFeP_4$: C, 51.14; H, 7.22. Found: C, 51.12; H, 6.99.

A.3.2 X-Ray Structure Determinations. Structural characterization for **A.3.1-A.3.3** was done by X-Ray analysis (Table A.3.1 and Figure A.3.1). For data collection and refinement details, see section 4.3.2. All of the atoms in the structures in of **A.3.1** and

Table A.3.1. Crystallographic data[a] for *trans*-[(cyclam)CrCl(CF_3SO_3)]-(CF_3SO_3) **(A.3.1)**, [(cyclen)Cu(CH_3CN)](CF_3SO_3)$_2$ **(A.3.2)**, and [(dmpe)Mn-(CpMe)($C_2Si^iPr_3$)] **(A.3.3)**.

	A.3.1	**A.3.2**	**A.3.3**
crystal ID	ms08m	ms09m	msn190b
formula	$C_{12}H_{24}ClCrF_6N_4O_6S_2$	$C_{10}H_{20}CuF_6N_4O_6S_2$	$C_{23}H_{44}MnP_2Si$
fw	585.92	533.96	465.55
color, habit	purple block	green prism	brown prism
T, K	100(2)	100(2)	120(2)
space group	$P2_1/c$	$P2_1/n$	$P2_1/n$
Z	4	4	4
a, Å	8.9240(5)	8.1607(7)	16.9657(7)
b, Å	17.7016(10)	12.849(1)	8.5620(3)
c, Å	14.4230(9)	22.023(2)	18.7105(7)
α, deg	90	90	90
β, deg	102.672(1)	97.662(2)	103.008(1)
γ, deg	90	90	90
V, Å^3	2222.9(2)	4587.5(2)	2648.2(2)
d_{calc}, g/cm^3	1.751	1.669	1.168
GOF	0.931	1.015	1.104
$R_1(wR_2)$[b], %	3.11 (10.45)	7.54 (20.15)	2.77 (7.50)

[a] Obtained with graphite-monochromated Mo Kα (λ = 0.71073 Å) radiation.
[b] $R_1 = \sum||F_o| - |F_c||/\sum|F_o|$, $wR_2 = \{\sum[w(F_o^2 - F_c^2)^2]/\sum[w(F_o^2)^2]\}^{1/2}$ for $I > 2\sigma(I)$.

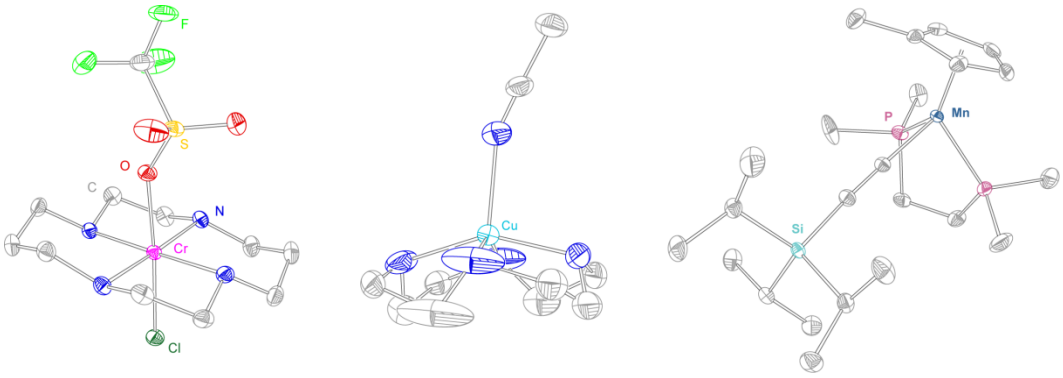

Figure A.3.1. X-ray structure of the complexes in **A.3.1** (left), **A.3.2** (middle), and **A.3.3** (right) with thermal ellipsoids rendered at 40% probability. Transition metal ions are labeled in the thermal ellipsoid plots. Light green, gray, red, blue, purple, cyan, and dark green ellipsoids represent fluorine, carbon, oxygen, nitrogen, silicon, and phosphorus atoms, respectively. Hydrogen atoms have been omitted for clarity.

A.3.3 were well ordered, and the structure solutions were straightforward. The N_4 macrocycle in **A.3.2** appears to be rotationally disordered, but due to a lack of time, the disorder was not modeled.

A.4 Strategies for Incorporating Paramagnetic Ions in Ethynylbenzene Frameworks

The synthesis of paramagnetic metallodendrimers based on ethynylbenzene frameworks is a difficult endeavor. The primary source of frustration is finding a system that is amenable to *stepwise* acetylide substitution at the axial sites of an octahedral metal ion. The low-spin d^6 ions like the Fe^{II} and Co^{III} systems discussed in Chapters 2 and 3 fulfill this criterion, but they lack the high-spin ground states and magnetic anisotropy that is required for SMM behavior. The isolation of the dinitrogen-bridged Cr acetylide complexes emanated from my attempts to directly react an octahedral d^4 Cr^{II} complex ($[(dmpe)_2CrCl_2]$) with stoichiometric amounts of lithium phenylacetylide. Furthermore, the presence of excess lithium phenylacetylide has been shown to afford ($[(dmpe)_2Cr(CCPh)_2]$). These results demonstrate that using reaction stoichiometry is not an effective method for preparing asymmetrically substituted, high spin metal acetylide complexes. In order to help future graduate students and post docs in the Shores group, I present the most promising results involving Mn^{II} and several schemes that could provide a good place to start for the next person who wishes to take up this project.

One approach for incorporating redox active, low-spin d^5 Mn^{II} ions into acetylide-bridged assemblies draws on the work of Prof. Heinz Berke.[8] The versatility of 1,1'-dimethylmanganocene ($MnCp'_2$, Cp' = 1-methylcyclopentadienide) as a starting material has been demonstrated by the isolation of a variety of asymmetric complexes. During my time at CSU, I explored the possibility of adapting Berke's methods to prepare

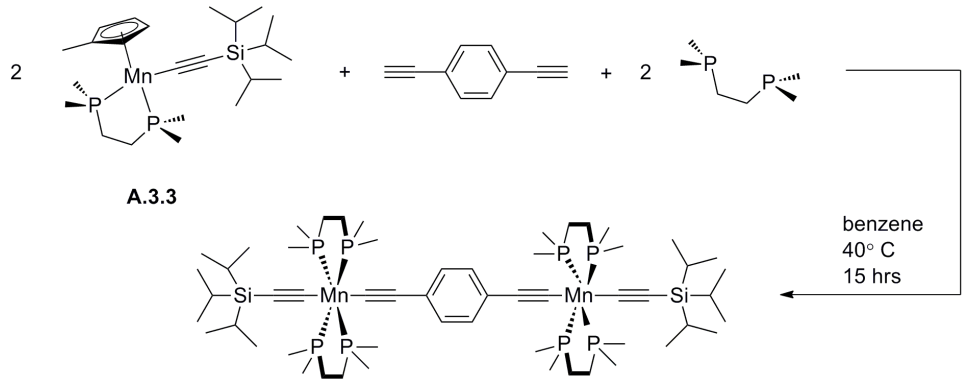

Scheme A.3.1. Reaction conditions used for the attempted synthesis of $[(dmpe)_4Mn_2(TIPS)_2(\mu\text{-DEB})]$.

ethynylbenzene-bridged Mn^{II} assemblies (wh8-119, Scheme A.4.1). Here, the presence of a strong σ donor (dmpe) drives the dissociation of Cp' from the Mn^{II} ion from **A.3.3**. The relatively acidic acetylenic proton from 1,4-diethynylbenzene (H_2DEB) can then combine with anionic Cp' to form methylcylopentadiene, leaving DEB^{2-} to ligate at the vacant coordination sites on the Mn^{II} ions. Proton NMR and infrared spectra obtained on the reaction product are both consistent with the expected structure (Figures A.4.1 and A.4.2, respectively). However, single crystals of this compound could not be grown. Cyclic voltammograms of the material indicate the presence of a quasi-reversible, two electron oxidation process, which I assign as two overlapping Mn^{III}/Mn^{II} redox couples.

A similar reaction was tried with 1,3,5-trithynylbenzene (H_3TEB) (see wh8-127), but ^{1}H NMR spectra of the product indicate that the reaction did not proceed as cleanly. An attempt at isolating the tri-oxidized product was also attempted (wh8-143).

Provided that the reactions can get cleaned up, these results suggest that the preparation of building blocks for metallodendrimers that contain redox-active Mn^{II} centers is within reach.

Below, I propose divergent (Schemes A.4.2- A.4.5) and convergent (Schemes A.4.6-A.4.8) syntheses for a nonanuclear Mn^{II}-containing dendrimer based on 1,3,5-triethynylbenzene. The Mn^{II} centers should be redox-active, allowing for conversion to Mn^{III}-containing molecules.

Recent work from Berke and coworkers[9] inspired me to outline an alternative scheme for preparing metallodendrimers based on early second and third row transition metals. Ions such as Mo^{II} and W^{II} are expected to display enhanced magnetic anisotropy relative

to their first row counterparts, so future students and post docs may want to consider the merits of the following schematic pathway (Schemes A.4.9-A.4.15).

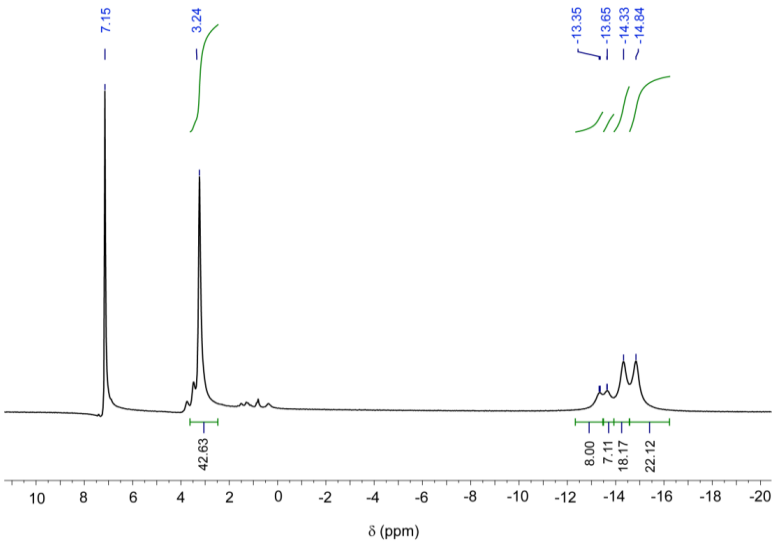

Figure A.4.1. ^{1}H NMR spectrum of [(dmpe)$_4$Mn$_2$(TIPSA)$_2$(μ-DEB)] in C_6D_6. The resonance at 7.15 ppm is from trace amounts of benzene.

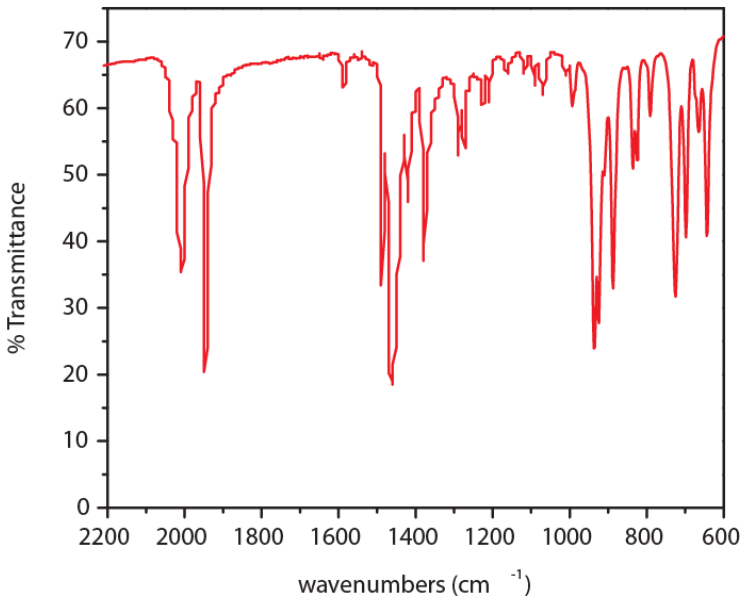

Figure A.4.2. Mineral oil IR spectrum of [(dmpe)$_4$Mn$_2$(TIPS)$_2$(μ-DEB)]. The absorbance at 2007 cm^{-1} is due to DEB and the absorbance at 1946 cm^{-1} is assigned to the carbon-carbon triple bond from TIPSA.

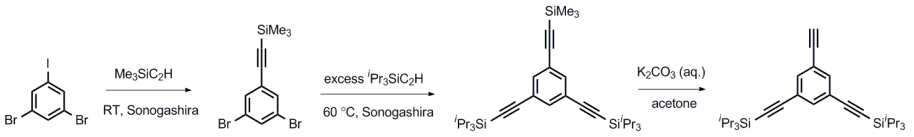

Scheme A.4.2. Synthesis of 1-ethynyl-3,5-(triisopropylsilyl-ethynyl)benzene.

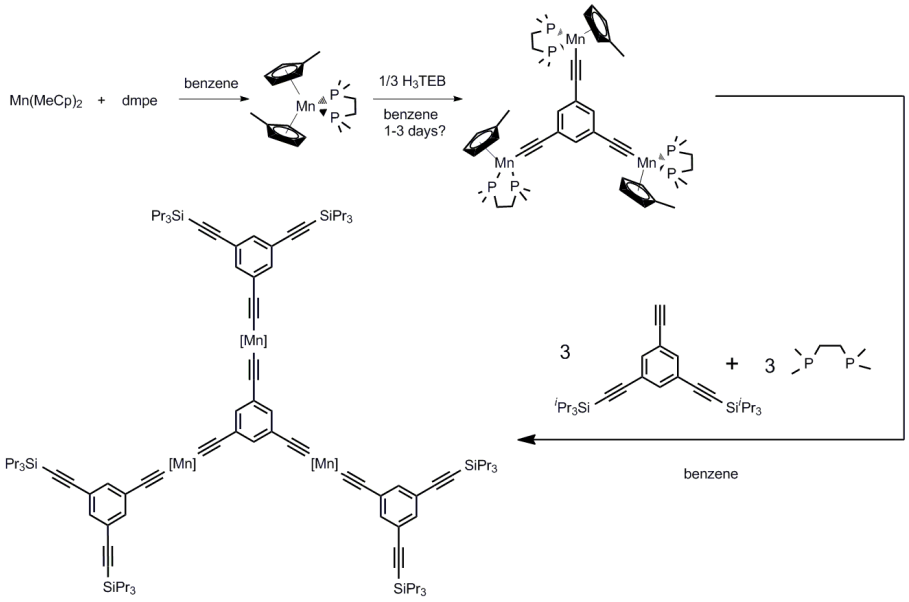

Scheme A.4.3. Step 1 of proposed divergent synthesis of a mangano-dendrimer. The formation of $[(dmpe)(Cp')_2Mn]$ is fast, but subsequent acetylide coordination is relatively slow and may require heating. Here, and in the schemes to follow, $[Mn] = (dmpe)_2Mn$.

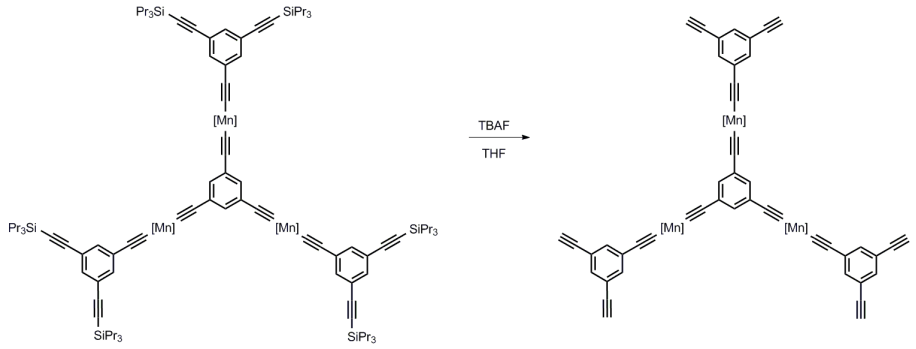

Scheme A.4.4. Step 2 of proposed divergent mangano-dendrimer synthesis. Separation of the desired product from tetrabutylammoniun side products can be achieved by extraction with non polar organic solvents.

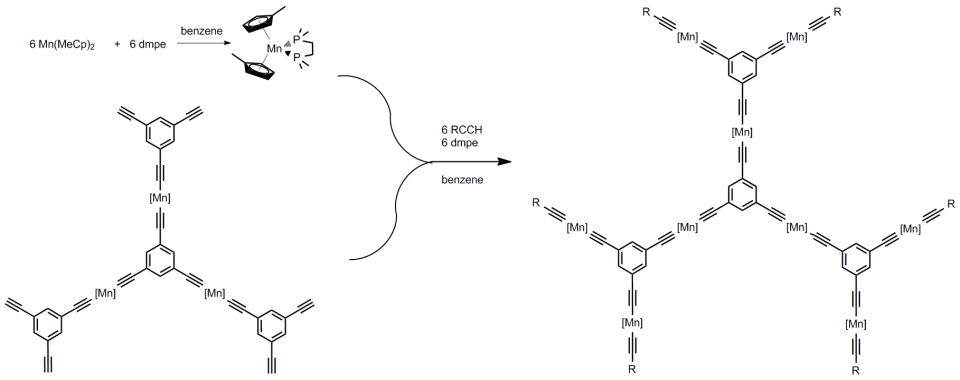

Scheme A.4.5. Step 3 of proposed divergent mangano-dendrimer synthesis.

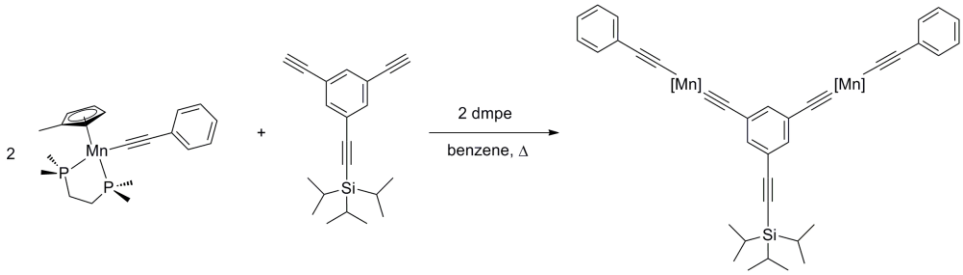

Scheme A.4.6. Step 1 of proposed convergent magnano-dendrimer synthesis.

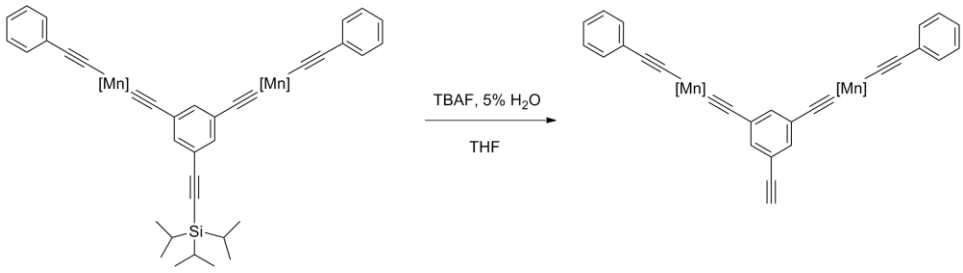

Scheme A.4.7. Step 2 of proposed convergent mangano-dendrimer synthesis. Purification should be possible by non-polar organic solvent extraction.

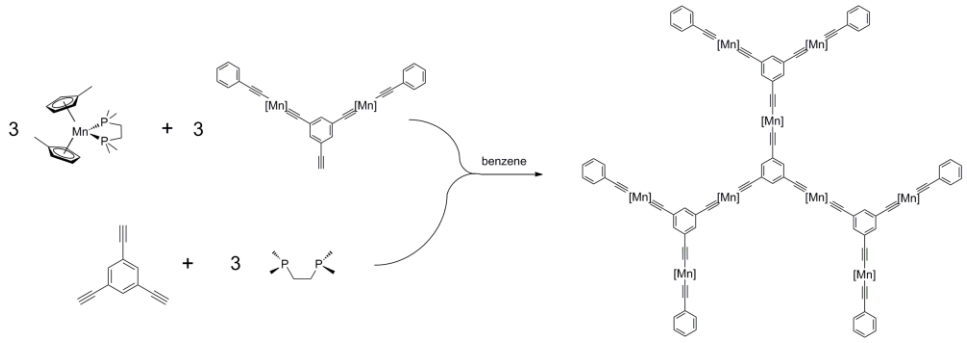

Scheme A.4.8. Step 3 of proposed convergent mangano-dendrimer synthesis.

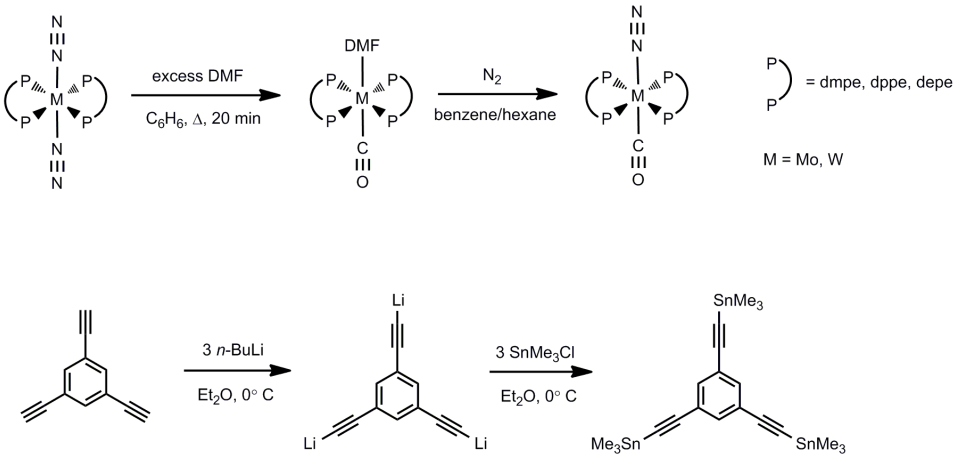

Scheme A.4.9. Syntheses of starting metal complexes (top) and stannylated ligand precursors (bottom) required for proposed synthesis of Mo and W-containing metallodendrimers. An alternative preparation of 1,3,5-(trimethyltinethynyl)benzene involves the direct reaction of Me_3SnNEt_2 with H_3TEB. For the preparation of the *trans*-CO/NN complex, see Ishida, T.; Mizobe, Y.; Tanase, T.; Hidai, M. *J. Organomet. Chem.* 1991, *409*, 355.

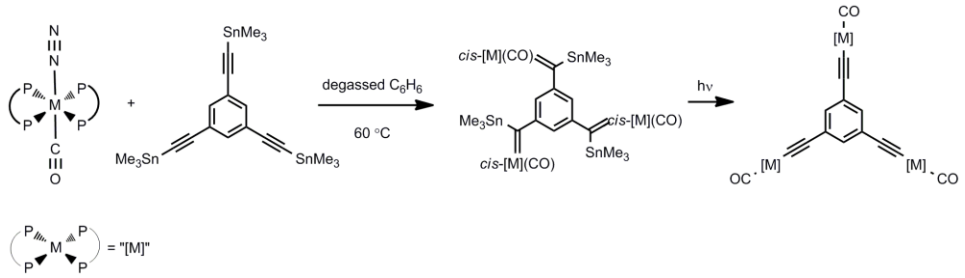

Scheme A.4.10. Step 1 of proposed synthesis of Mo and W- containing metallodendrimers.

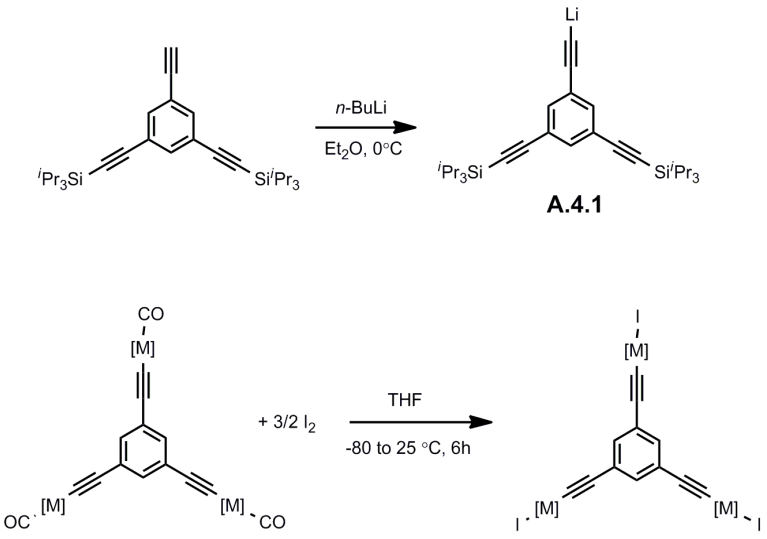

Scheme A.4.11. Synthesis of ligand intermediate **A.4.1** (top) and step 2 of proposed W/Mo metallodendrimer synthesis (bottom).

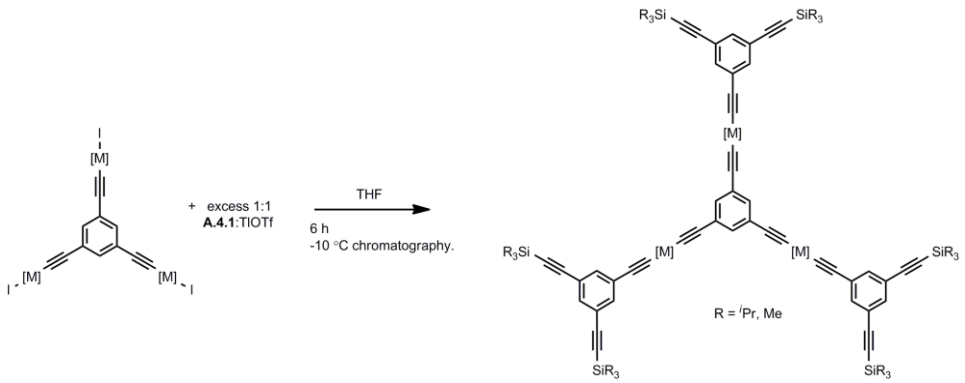

Scheme A.4.12. Step 3 of proposed synthesis of Mo and W- containing metallodendrimers.

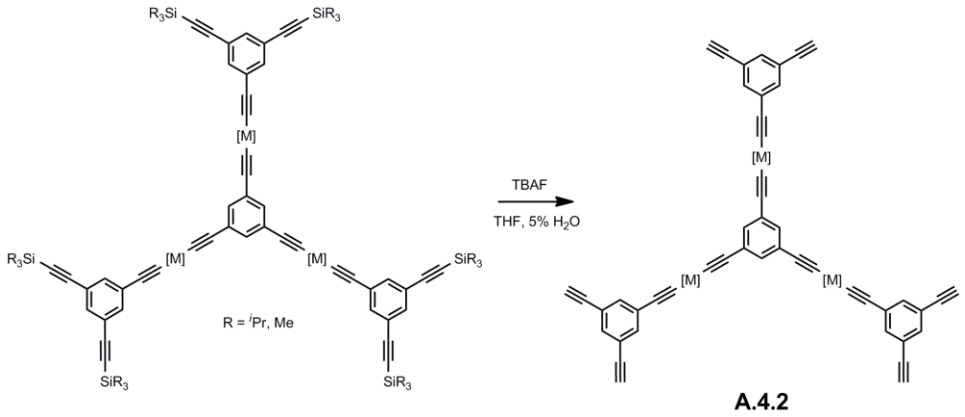

Scheme A.4.13. Step 4 of proposed synthesis of Mo and W- containing metallodendrimers.

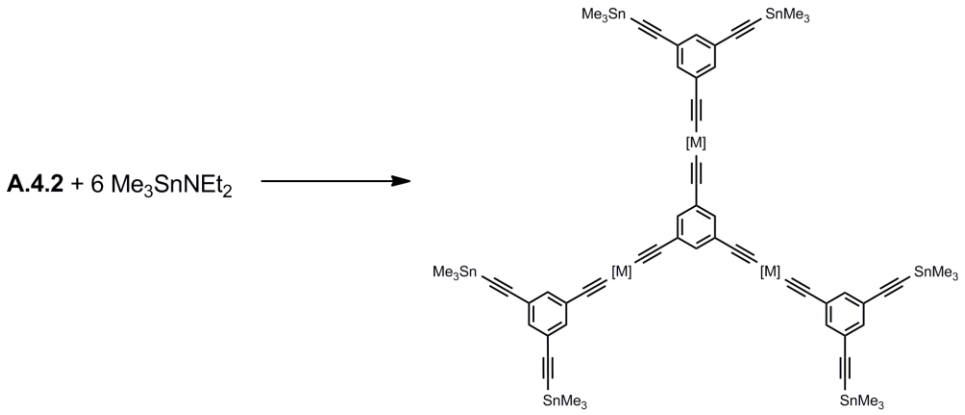

Scheme A.4.14. Step 5 of proposed synthesis of Mo and W- containing metallodendrimers.

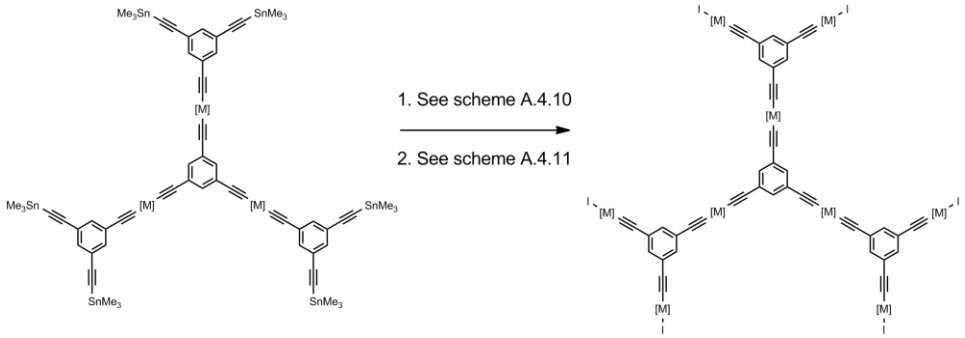

Scheme A.4.15. Step 6 of proposed synthesis of Mo and W- containing metallodendrimers.

A.5 Cross referenced collection of notebook pages and crystal structure data sets for relevant compounds. Included notebook IDs emanate from the notebooks belonging to Ms. Sara Mosley (SM), Dr. Md. K. Kabir (MK) and Wesley Hoffert (WH).

Compound	Dissertation ID	Relevant Notebook IDs	Crystal ID
trans-[(cyclam)CoCl(C_2Ph)]Cl	**2.1**Cl_2	SM1-57	N/A
trans-[(cyclam)CoCl(C_2Ph)]BPh_4	**2.1**	SM1-57 WH9-81	msn209
trans-[(cyclam)CoCl(DEBH)]Cl	N/A	MK2-64	ms12
trans, trans-[(cyclam)$_2$$Co_2Cl_2$(μ-p-DEB)]$Cl_2$	**2.2**Cl_2	MK1-44B MK3-84 WH9-69 WH9-89	mk001
trans, trans-[(cyclam)$_2$$Co_2Cl_2$(μ-p-DEB)]$(BPh_4)_2$	**2.2**	WH9-69	N/A
trans, trans, trans-[(cyclam)$_3$$Co_3Cl_3$(TEB)]$Cl_3$	**2.3**Cl_3	WH2-29 WH2-113 WH2-141 WH3-37 WH9-79	msn214 msn214b
trans, trans, trans-[(cyclam)$_3$$Co_3Cl_3$(TEB)]$(BPh_4)_3$	**2.3**	WH3-95 WH9-79	N/A
trans, trans-[(cyclam)$_2$$Co_2Cl_2$(HTEB)]$Cl_2$	**2.4**	WH2-57 WH9-97 WH9-135	ms07
trans, trans-[(cyclam)$_2$$Co_2Cl_2$(HTEB)]$(BPh_4)_2$	**2.4**$(BPh_4)_2$	WH10-43	msn229
trans-[(cyclam)Co(C_2Ph)$_2$](BPh_4)	**2.5**	WH9-119	msn216
[(dmpe)$_2$FeCl(C_2Ph)]OTf	**3.1**	WH7-29	msn142
[(dmpe)$_4$$Fe_2Cl_2$(μ-*p*-DEB)]$(BAr^F{}_4)_2$	**3.2**	WH7-133 WH10-85 WH10-99	msn171
[(dmpe)$_3$$Fe_3Cl_3$(TEB)]	**3.3**	WH6-61 WH6-59 WH7-23 WH7-127 WH7-137 WH10-105	N/A
[(dmpe)$_3$$Fe_3Cl_3$(TEB)](OTf)$_3$	**3.4**	WH7-127 WH7-137 WH10-85 WH10-87 WH10-91	msn232
[(dmpe)$_4$$Fe_2Cl_2$(μ-*m*-DEB)]$(BAr^F{}_4)_2$	**3.5**	WH10-101	msn259r
[(dmpe)$_4$$Cr_2$($C_2$Ph)$_2$(μ-$N_2$)]	**4.1**	WH5-131 WH5-149 WH6-33 WH6-83 WH6-131 WH7-9 WH7-21	msn131
[(dmpe)$_4$$Cr_2$($C_2Si^iPr_3$)$_2$(μ-$N_2$)]	**4.2**	WH6-155 WH7-15 WH7-101 WH7-125	msn135

		WH9-25 WH9-87	
$[(dmpe)_4Cr_2(C_2Si^iPr_3)_2(\mu\text{-}N_2)]BAr^F{}_4$	**4.3**	WH7-85 WH7-145 WH9-87	msn173 msn203
$[(dmpe)_4Cr_2(C_2Si^iPr_3)_2(\mu\text{-}N_2)](BAr^F{}_4)_2$	**4.4**	WH7-99 WH7-139 WH9-87	msn169r
$[(dmpe)_6Fe_3Cl_2(C_8H)](PF_6)$	**5.1**	WH8-93 WH8-147 WH8-149 WH9-21 WH9-65 WH9-93 WH9-141	msn188 msn224
$[(dmpe)_6Fe_3Cl_2(C_8H)](PF_6)_2$	**5.2**	WH9-21 WH9-65 WH9-141	N/A
$[(dmpe)_4Fe_2Cl_2(\mu\text{-}C_4)](PF_6)$	**5.3**	WH10-59	msn230
$[(dmpe)_4Fe_2Cl_2(\mu\text{-}C_4)](PF_6)_2$	**5.4**	WH10-63	msn237r
$[(dmpe)_2Cr(C_2Si^iPr_3)_2]$	**A.1.1**	WH6-39 WH6-101	msn132
$[(dmpe)_2Cr(C_2Si^iPr_3)_2](PF_6)$	**A.1.2**	WH6-127	msn133
$[(dmpe)_2Cr(C_2Si^iPr_3)(MeCN)]BPh_4$	**A.1.3**	WH7-87 WH7-109	msn155
$[(dmpe)_2Cr(C_2Si^iPr_3)Cl]BAr_4{}^F$	**A.1.4**	WH9-73 WH10-45 WH10-89	msn210
trans-$[(cyclam)CrCl(CF_3SO_3)](CF_3SO_3)$	**A.3.1**	WH2-71 WH3-17 WH3-87	ms08
$[(cyclen)Cu(CH_3CN)](CF_3SO_3)_2$	**A.3.2**	WH2-77	ms09
$[(dmpe)Mn(CpMe)(C_2Si^iPr_3)]$	**A.3.3**	WH8-125	msn190
$[(dmpe)_2FeCl(^iPr_3SiDEB)]$	**A.3.4**	WH9-145	N/A
$[(dmpe)_2FeCl(DEBH)]$	**A.3.5**	WH9-145	N/A
$[(dmpe)_4Mn_2(TIPS)_2(\mu\text{-}DEB)]$ (attempted)	N/A	WH8-119	N/A
$[(dmpe)_6Mn_3(TIPS)_3(\mu\text{-}TEB)]$ (attempted)	N/A	WH8-127 WH8-141 WH8-153	N/A
$[(dmpe)_2Mn(DEBTMSA)_2]$	N/A	WH8-11	N/A
$[(dmpe)_2Mn(DEBTMSA)_2](BF_4)$	N/A	WH8-11	N/A
$[(dmpe)_2Mn(DEBH)_2](BF_4)$	N/A	WH9-23	N/A
$[(dmpe)_6Mn_3(TIPS)_3(\mu\text{-}TEB)](PF_6)_3$ (attempted)	N/A	WH8-127 WH8-141	N/A
$[(dmpe)_2CrCl(CH_3)]$	N/A	WH5-101 WH5-105	msn120m

A.6 References

1. Lopez-Herdandez, A.; Venkatesan, K.; Schmalle, H. W.; Berke, H., *Monatsh. Chem.* **2009,** *140*, 845-857.

2. (a) Berben, L. A. Toward acetylide- and N-heterocycle-bridged materials with strong electronic and magnetic coupling. Ph.D., University of California, Berkeley, 2005; (b) Berben, L. A.; Kozimor, S. A., *Inorg. Chem.* **2008,** *47*, 4639-4647.

3. Bakac, A.; Espenson, J. H., *Inorg. Chem.* **1992,** *31*, 1108-1110.

4. Styka, M. C.; Smierciak, R. C.; Blinn, E. L.; DeSimone, R. E.; Passariello, J. V., *Inorg. Chem.* **1978,** *17*, 82-86.

5. Wilkinson, G.; Cotton, F. A.; Birmingham, J. M., *J. Inorg. Nucl. Chem.* **1956,** *2*, 95-113.

6. Girolami, G. S.; Salt, J. E.; Wilkinson, G.; Thorntonpett, M.; Hursthouse, M. B., *J. Am. Chem. Soc.* **1983,** *105*, 5954-5956.

7. Onitsuka, K.; Fujimoto, M.; Kitajima, H.; Ohshiro, N.; Takei, F.; Takahashi, S., *Chem. Eur. J.* **2004,** *10*, 6433-6446.

8. (a) Fernandez, F.; Blacque, O.; Alfonso, M.; Berke, H., *Chem. Comm.* **2001**, 1266-1267; (b) Kheradmandan, S.; Heinze, K.; Schmalle, H. W.; Berke, H., *Angew. Chem. Int. Ed.* **1999,** *38*, 2270-2273; (c) Kheradmandan, S.; Venkatesan, K.; Blacque, O.; Schmalle, H. W.; Berke, H., *Chem. Eur. J.* **2004,** *10*, 4872-4885; (d) Unseld, D.; Krivykh, V. V.; Heinze, K.; Wild, F.; Artus, G.; Schmalle, H.; Berke, H., *Organometallics* **1999,** *18*, 1525-1541; (e) Venkatesan, K.; Blacque, O.; Fox, T.; Alfonso, M.; Schmalle, H. W.; Berke, H., *Organometallics* **2004,** *23*, 1183-1186; (f) Venkatesan, K.; Fox, T.; Schmalle, H. W.; Berke, H., *Organometallics* **2005,** *24*, 2834-2847.

9. (a) Semenov, S. N.; Blacque, O.; Fox, T.; Venkatesan, K.; Berke, H., *J. Am. Chem. Soc.* **2010,** *132*, 3115-3127; (b) Semenov, S. N.; Taghipourian, S. F.; Blacque, O.; Fox, T.; Venkatesan, K.; Berke, H., *J. Am. Chem. Soc.* **2010,** *132*, 7584-7585.

10. Bonniard, L. l.; Kahlal, S.; Diallo, A. K.; Ornelas, C. t.; Roisnel, T.; Manca, G.; Rodrigues, J. o.; Ruiz, J.; Astruc, D.; Saillard, J.-Y., *Inorg. Chem.* **2010,** *50*, 114-124.